ON PLASMONIC SUPERRADIANCE, THE SCALING LAWS OF SPONTANEOUS PARAMETRIC DOWNCONVERSION, AND THE PRINCIPLES AND RECENT ADVANCES IN NONLINEAR OPTICS

by

Saumya Choudhary

A thesis submitted to the Faculty of Graduate and Postdoctoral studies,
University of Ottawa,
in partial fulfillment of the requirements for the degree of
Master of Applied Sciences in Electrical and Computer Engineering

uOttawa

Ottawa-Carleton Institute for Electrical Engineering
Faculty of Engineering
Department of Electrical Engineering
University of Ottawa, Ottawa
Canada

Abstract

This thesis covers three different topics. The first part is a pedagogical review of the basic principles and recent advances in nonlinear optics. It was originally written as a chapter for the proceedings of the "International School of Physics (Enrico Fermi)" summer school on Photonics held in June, 2014. It is included to provide some background information about nonlinear optical processes in general, and is particularly relevant for the third part of this thesis which is based on the second-order nonlinear optical process of spontaneous parametric downconversion.

The second part is based on original research, and deals with superradiance in plasmonic nanostructures. The process of superradiance, as introduced by Dicke in 1954, entails the shortening of the spontaneous emission lifetime of a collection of N quantum emitters as a consequence of the development of a macroscopic dipole moment. Specifically, the lifetime is shortened by a factor of $1/N$, and the linewidth is broadened by a factor of N. Such a linewidth dependence has been previously observed in systems of several plasmonic 'emitters'. However, a clear physical insight into this phenomenon and how it relates to Dicke superradiance has not been shown yet. In this part, we demonstrate by experiment, simulation, and a simple analytical model that Dicke's superradiance can indeed be observed in a planar array of plasmonic nanoantennas, with a linewidth that scales linearly with the number of nanoantennas within a square wavelength.

The third part is also based on original research, and is based on the scaling laws of spontaneous parametric downconversion (SPDC) for a type-I phase-matching configuration. The variation of bi-photon generation rate, heralding efficiency and radiance with parameters such as crystal length, pump focussing and collection waist sizes are examined for collinear and non-collinear emission. The results can be used to maximize the brightness of the SPDC source or increase the heralding efficiency depending on the application.

Acknowledgements

First and foremost, I would like to thank my supervisor Prof. Robert Boyd for his guidance and help throughout my degree. I am highly indebted to him for his encouragement and support. I also extend my gratitude to my committee members Prof. Jacques Albert and Dr. Ksenia Dolgaleva for agreeing to be on my examining committee and for their very helpful comments regarding this thesis. I am also very grateful to Prof. John Sipe for his valuable collaboration and helpful insight.

Secondly, I thank all the members in Prof. Boyd's group who helped me with various parts of my research. I am very grateful to Israel de Leon for his efficient guidance and for helping me with the nitty-gritty of my research, from learning Lumerical to working in the lab. I am thankful to Filippo Miatto, Jeremy Upham, Sebastian Schulz, Ebrahim Karimi and Peter Banzer for valuable discussions and help. I have also benefitted immensely from discussions with my fellow graduate students in the group, particularly Zahirul Alam, Akbar Safari and Marie-Claude Dicaire. I also thank Sylvia Swiecicki for the very valuable collaboration and helpful discussions.

Lastly, but not the least, I would like to express my appreciation for my immensely supportive and loving parents, and brother. I would have never been where I am now without their encouragement and confidence in me.

Contents

List of Figures

List of Tables

List of Symbols

A_i Shape factors of the ellipsoid.

A_j Plane-wave electric field amplitude of the j-th frequency contribution.

α xx and yy components of the $\overleftrightarrow{\alpha}$ tensor; $\alpha_{xx} = \alpha_{yy} = \alpha$.

α Molecular polarizability along the transverse axis (1) and along the molecular axis (3).

α_l Linear absorption coefficient.

$\tilde{\alpha}$ Effective polarizability which characterizes the response of the dipole to only the incident field $\mathbf{E}_{\text{inc}}$.

α Diagonal elements of the polarizability tensor $\overleftrightarrow{\alpha}$ of the ellipsoid.

$\overleftrightarrow{\boldsymbol{\beta}}$ Dynamic interaction constant.

β xx and yy components of the $\overleftrightarrow{\boldsymbol{\beta}}$ tensor; $\beta_{xx} = \beta_{yy} = \beta$.

c Speed of light in vacuum.

d_{eff} Contracted second-order nonlinearity.

$\mathbf{p}$ Dipole moment.

Δk Wave-vector or phase-mismatch.

ϵ_0 Vacuum Permittivity.

Ee Energy of the excited state.

Eg Energy of the ground state.

$\hat{\mathbf{E}}$ Quantized electric-field within a cavity of volume V.

$\mathbf{E}_{\text{inc}}$ Incident electric field at the dipole.

$\mathbf{E}_{\text{int}}$ Electric field at the dipole due to all the other dipoles in the array.

E_j Electric field of the j-th frequency contribution in frequency domain.

$\mathbf{e}_\Lambda$ Polarization vector.

$\tilde{E}$ Electric field in time domain.

$\mathbf{E}_{\text{tot}}$ Total electric field at the dipole.

g_m Transverse mode-function including the phase for the m-th beam.

$\overleftrightarrow{\boldsymbol{G}}(\mathbf{r})$ Green's tensor for a dipole; $\overleftrightarrow{\boldsymbol{G}}(\mathbf{r}) \cdot \mathbf{p}$ is the response at position $\mathbf{r}$ for a dipole $\mathbf{p}$placed at the origin.

$\hat{H}_A$ Atomic Hamiltonian.

$\hbar$ Reduced Planck's constant.

$\hat{H}_F$ Field Hamiltonian.

$\hat{H}_I$ Interaction Hamiltonian.

I Intensity of emitted spontaneous radiation from the collection of N emitters.

I_k Intensity of emitted radiation in a particular direction k.

$\mathbf{p}$ Dipole moment of a single emitter.

I_{sp} Intensity of emitted spontaneous radiation from a single emitter.

$\mathbf{J}$ Averaged surface current density.

L_{rad} Spectral radiance of the SPDC source.

m_N Index signifying population inversion; eigen-value of $\hat{R}_3$ operator.

μ Shape-factor associated with the arrangement of emitters.

μ_0 Permeability of a non-magnetic medium.

N Number of emitters.

n_0 Linear refractive index.

n_2 Intensity-dependent refractive index.

N_0 Number density of dipoles in the medium.

N_{eff} Effective number of dipoles enclosed within a radius equal to the resonance wavelength λ_0.

n_- Number of emitters in ground state.

n_+ Number of emitters in excited state.

ω Angular frequency of optical field.

$\Phi(\Delta k)$ Overlap function for the overlap between pump, signal and idler beams within a crystal.

P_0 Power of the pump beam.

P_{ext} Total power lost due to absorption and scattering in each dipole.

$\hat{\mathbf{p}}$ Electric dipole moment operator (vector form).

$\tilde{P}$ Induced polarization in time domain.

$\tilde{P}^{NL}$ Nonlinear contribution to Induced polarization in time domain.

P_{rad} Radiated power by each dipole.

$\mathbf{p}_s$ Surface density of dipole moments.

$\tilde{P}(t)$ Induced polarization in time domain.

r Co-operation number; $r(r+1)$ is the eigen-value of the collective transition operator $\hat{R}^2$.

$\hat{R}^2$ Collective transition operator analogous to the angular momentum operator $\hat{L}^2$.

$\hat{R}_3$ Collective population inversion operator.

$\hat{R}_-^{(i)}$ Transition operator for the radiative decay of i-th emitter from excited state to ground state.

$\hat{R}_+^{(i)}$ Transition operator for the transition of the i-th emitter from ground state to excited state on absorption of a single resonant photon.

$R(k_s)$ Transition rate from an initial two-mode vacuum state to the final state with one photon each in signal and idler for a fixed signal state.

$\hat{R}_-$ Collective transition operator for the radiative decay of one emitter among a collection of N emitters.

$\hat{R}_+$ Collective transition operator for the absorption of a single photon by a collection of N emitters.

R_T Total bi-photon generation rate.

$\hat{\sigma}$ Pauli spin matrices.

t_0 Time delay required for the emitted radiation to reach peak intensity due to superfluorescence.

τ_0 Radiative lifetime of spontaneous emission from a single emitter.

τ_c Characteristic decay time of a co-operatively emitting system of N emitters.

θ Half-angle of the emission cone of signal and idler.

$\tilde{R}$ Reflectance of the array.

$\tilde{r}$ Reflection coefficient of the array.

$\tilde{T}$ Transmittance of the array.

$\tilde{t}$ Transmission coefficient of the array.

U Spatial mode amplitude functions of the pump, signal and idler.

χ Susceptibility.

Z_0 Characteristic impedance of free space ($= 377\Omega$).

Z_a Impedance of the dipole array.

Chapter 1

Introduction

This thesis is divided in three parts and each part deals with a different topic. The first part was written as a chapter for the proceedings of the "International School of Physics (Enrico Fermi)" summer school on Photonics held in June, 2014. The second and third parts are contributions of original research conducted by me.

Chapter 2 comprises the first part of this thesis and is a very pedagogical overview of the field of non-linear optics and some of the recent advances in its research. Nonlinear optics deals with phenomena that occur when a very intense light interacts with a material medium, modifying its optical properties. Shortly after the demonstration of first working laser in 1960 by Maiman [1], the field of nonlinear optics began with the observation of second-harmonic by Franken et al. in 1961 [2]. Since then, the interest in this field has grown and various nonlinear optical effects are utilized for purposes such as nonlinear microscopy, switching, harmonic generation, parametric downconversion, filamentation, and so on. This chapter serves as a prelude to part three, which is the study of spontaneous parametric downconversion, a second-order nonlinear process.

The second part deals with Dicke superradiance in plasmonic nanostructures. Robert Dicke introduced superradiance in 1954 [3] as a co-operative many-body effect in a collection of emitters. While there are a wide range of phenomena that can result, essentially as a consequence of all emitters interacting with the same radiation field, very often the N emitters will radiate at a rate N times what one would expect for a single emitter, and thus lead to a linewidth N times that which would result from a single emitter. This occurs when these emitters are maximally correlated with each other. This implies that in the electric dipole approximation, the system has a macroscopic dipole moment equal to the sum of dipole moments of the individual emitters [3–7]. This effect, although generally associated with quantum systems, can be described classically [6]. It has been demonstrated in gases [8], atomic vapors [9–12], Rydberg atoms [13], Bose-Einstein condensates [14], trapped ions [15], superconducting qubits [16] and Mossbauer nuclei [17].

Here it is shown - by experiment, simulation, and a simple analytical model - that the linewidth of scattered radiation from a two-dimensional array of nanoantennas is inversely proportional to the lattice constant squared, or directly proportional to the effective number of nanoantennas N_{eff} present within a circle of radius equal to the resonance wavelength of a single antenna. Thus N_{eff} nanoantennas can be said to be radiating collectively, and this can be termed as 'superradiance' pertaining to a scattering system. Although this was predicted many years ago in

simple models [18], and seen in split-ring metamaterial arrays [19], to our knowledge this is the first time that the explicit dependence of linewidth on the number density of scatterers in an array has been shown explicitly and interpreted as 'superradiance'.

Chapters 3 and 4 comprise this first part. Chapter 3 provides extensive background information regarding the phenomenon of superradiance including its quantum-electrodynamical, semi-classical and classical pictures. Comparison is also made with the related phenomenon of superfluorescence [4], which also occurs due to multiple emitters emitting in a correlated fashion, but differs from superradiance on whether the correlation exists at the beginning of the process (superradiance) or builds up as the system evolves (superfluorescence). Chapter 4 details the original work of demonstrating superradiance in an array of plasmonic nanoantennas. This includes a simple analytical model using dipole approximation to calculate the linewidths of the transmission spectrum of arrays of nanoantennas for varying lattice constants, Finite-Difference Time Domain (FDTD) simulations for the same and experimental results.

The second part deals with the study of the scaling laws of Spontaneous Parametric Downconversion or SPDC. SPDC is the spontaneous splitting of a photon into two photons of lower frequency due to parametric interaction with a crystal possessing certain properties [20]. SPDC has become a very useful optical process as it is the source of photons which are entangled in various degrees of freedom such as energy-time, polarization, spatial mode and angular momentum. This property is important in areas of quantum cryptography [21], communication [22] and for carrying out fundamental tests of quantum mechanics such as non-locality and local realism. It can also be used as a bright source of heralded single photons [23]. In this part of the thesis, we examine the effect of variation of optimization parameters such as crystal length, focussing of pump and size of collection modes on the various metrics associates with SPDC sources such as spectral and total bi-photon rate, and total radiance. We also study how detection parameters such as using single or multi-mode fibers or bucket detectors influence the heralding efficiency.

Chapter 5 comprises the third part. We start with a general overview of SPDC and then derive the interaction Hamiltonian and the time-dependent bi-photon state, similar to the treatment in references [24–26]. Then we use Fermi's golden rule [27] to find the spectral and then the total bi-photon generation rate, as discussed in [28]. The effect on this rate, for collinear and non-collinear emission, of crystal length and pump focussing is examined for the cases in which the pump and collection modes are collimated and also for diffracting beams. Subsequently, the effect of crystal length and pump focussing is examined on heralding efficiency using single and multi-mode fibers, calculated by projecting the previously derived SPDC wave-function on Schmidt basis and finding the coupling efficiency of each composite state with the fiber modes. Lastly, the effect of crystal length and pump focussing is examined on radiometric parameters, namely spectral and total radiance, in order to properly characterize the bi-photon source.

Statement of original contribution

Parts two and three of this thesis comprise contributions of original research. My supervisor, Prof. Robert Boyd was the driving force behind both projects with his guidance and making the required resources available for their completion.
In part two, chapter four describes the analytical model, simulation and experiment for demonstration of the superradiance effect in plasmonic nanoantenna arrays. The problem was originally suggested by Prof. Robert Boyd. The design idea as well as the analytical model were conceived by our collaborator Prof. John Sipe, University of Toronto. The nanoantenna and array design were done by me using a commercially available FDTD software. The fabrication of the designed structure was performed by Dr. Sebastian Schulz and Dr. Jeremy Upham who are post-doctoral researchers at Prof. Boyd's group at the University of Ottawa. The transmission spectroscopy to measure the linewidths of the fabricated array was performed by me with help from Dr. Israel de Leon who was a post-doctoral researcher at Prof. Boyd's group at Ottawa at the time. The linewidth calculations from FDTD simulations were also performed by me. The linewidth calculations for the analytical model were performed by Prof. Sipe's graduate student Sylvia Swiecicki. The fourth chapter is a preliminary version of the paper which will be submitted soon for publication and the analytical results were included for completeness.

In the third part, the expression for the total rate calculation from Ling's paper [28] was modified by Filippo Miatto, then a post-doctoral researcher in Prof. Boyd's group at the University of Ottawa. All the calculations were done by me using Mathematica. Marie-Claude Dicaire, a Master's student in Prof. Boyd's group at the University of Ottawa was also a collaborator. The codes used to generate the plots presented in this part are attached in appendix two.

Part I

Nonlinear Optics

Chapter 2

Review of Nonlinear Optics

2.1 Introduction

According to reference [29], nonlinear optics is the study of phenomena that occur due to the modification of material properties in the presence of light of high intensity. The nonlinearity is associated with the fact that material response varies in a nonlinear manner with the applied optical field. To study this effect, we consider the dependence of the dipole moment per unit volume, or polarization $\tilde{P}(t)$ on the applied optical field strength $\tilde{E}(t)$. On application of the optical field, there is displacement of both electrons and the nuclei with respect to the centre of mass of the molecule. Considering dipole approximation, an electric dipole is formed due to charge separation between the negatively charged electron cloud and the positively charged nucleus. At optical frequencies, due to its much larger mass, the oscillations in the nucleus are much weaker than the electronic oscillations. Hence the nuclear contributions are far weaker than the electronic contributions, at least for linear polarizability. The nonlinear susceptibility on the other hand (manifested in terms of Raman scattering), might be comparable or even larger depending on whether we are on or of resonance [30]. But for all practical purposes, we neglect the nuclear contributions for simplicity in our present discussion. The bulk polarization of the entire material is thus a vector sum of the dipole moments of all the molecules [31, 32]. In a linear regime, the induced dipole also oscillates with the same frequency as the driving field and each molecule of the material can be viewed as a harmonic oscillator.

Due to larger mass of the nucleus, these oscillations are very weak and about the mean position of the molecules. The induced polarization in this case can be expressed as:

$$\tilde{P}(t) = \epsilon_0 \chi^{(1)} \tilde{E}(t) \tag{2.1}$$

where ϵ_0 is the permittivity of free space and the $\chi^{(1)}$ is the linear susceptibility. But for larger applied fields (comparable to inter-atomic fields) and proportionately stronger oscillations, this approximation breaks down and the behaviour deviates from that of a harmonic oscillator. In this anharmonic case, nonlinear terms come into play which give rise to different frequency components in the oscillations. These harmonic oscillators then oscillate with different phases depending on the phases of the driving fields and for a particular relative phase, the radiated fields from these oscillators add up. These oscillators then behave

like a phased array of dipole antennas which radiate into a narrow beam in the forward direction. This effect is quite similar in principle to '*superradiance*', which is discussed in the second part of the thesis.

To account for the nonlinear terms, we expand the polarization $\tilde{P}(t)$ as a generalized power series in $\tilde{E}(t)$ and include all the nonlinear contributions as:

$$\begin{aligned} \tilde{P}(t) &= \epsilon_0[\chi^{(1)}\tilde{E}^1(t) + \chi^{(2)}\tilde{E}^2(t) + \chi^{(3)}\tilde{E}^3(t) + ...] \\ \tilde{P}(t) &= \tilde{P}^1(t) + \tilde{P}^2(t) + \tilde{P}^3(t) + ... \end{aligned} \tag{2.2}$$

The constants $\chi^{(2)}$ and $\chi^{(3)}$ are the second- and third-order nonlinear optical susceptibilities, respectively. This is a very simplified notation and does not take into account dispersion or losses because of the instantaneous nature of the response. Under general circumstances when losses and dispersion are present, the susceptibilities depend on frequency. If the vector nature of fields is also taken into account, then $\chi^{(1)}$ is a tensor of rank 2, $\chi^{(2)}$ a tensor of rank 3 and so on. *We later use this tensor representation in chapter 5 where we talk about spontaneous parametric downconversion, a second-order nonlinear optical effect.* $\tilde{P}^1(t)$ is called the linear polarization while $\tilde{P}^2(t)$ and $\tilde{P}^3(t)$ are called the second- and third-order nonlinear polarizations respectively. Thus, the polarization is composed of linear and nonlinear components. A time varying nonlinear polarization is a source of newer electromagnetic field components and hence is key to the description of nonlinear optical phenomena. This is evident in the wave equation for nonlinear media:

$$\bigtriangledown^2 \tilde{E} - \frac{n^2}{c^2}\frac{\partial^2 \tilde{E}}{\partial t^2} = \frac{1}{\epsilon_0 c^2}\frac{\partial^2 \tilde{P}^{NL}}{\partial t^2} \tag{2.3}$$

Here, the nonlinear polarization $\tilde{P}^{NL}$ drives the electric field $\tilde{E}$ and the term $\partial^2\tilde{P}^{NL}/\partial t^2$ represents the acceleration of charges in the medium. This is consistent with Larmor's theorem that accelerating charges generate electromagnetic waves. It should be noted that under certain circumstances such as resonant excitation of atomic systems or under very high applied laser field strength, the power series representation of (2) may not converge. Such cases are dealt with a formalism that includes the possibility of saturation effects.

Susceptibilities may be complex or real depending on whether the nonlinear process involves exchange of energy with the medium or not, respectively. When there is no energy exchange between the interacting waves and the medium and the quantum state of the medium remains unchanged in the end (there may be population transfers between real and virtual levels but they have a very short lifetime), the process is called a 'parametric process'. Examples include SHG, SFG, DFG, OPA, THG, Kerr nonlinearity, SPM, XPM, FWM, etc, using standard notation that will be developed within this chapter. When the quantum state of the medium is changed in the end, the process is called a non-parametric process. Examples include SRS, SBS, multi-photon absorption, saturable absorption, etc. A brief description of all these processes are provided in the sections that follow.

2.2 Second-order nonlinear optical processes

The discovery of second harmonic generation (SHG) in 1961 by Franken et al [2] marked the beginning of the field of nonlinear optics. In 1965, ref. [33] reported the nonlinear light scattering in a quartz crystal generating light with frequency twice that of the incident beam. Difference-frequency generation by a KDP crystal using non-collinear light beams was also reported in 1965 in ref. [34]. Apart from second-harmonic generation, the effects that result from second-order nonlinearity or a non-zero $\chi^{(2)}$ include sum- and difference-frequency generation, optical parametric oscillation and spontaneous parametric downconversion. Material symmetry plays a significant role in determining the second-order response as only non-centrosymmetric materials, or materials lacking inversion symmetry show a second-order response. This will be elaborated later. A brief description of each of the second-order processes mentioned above is as follows.

2.2.1 Second Harmonic Generation (SHG)

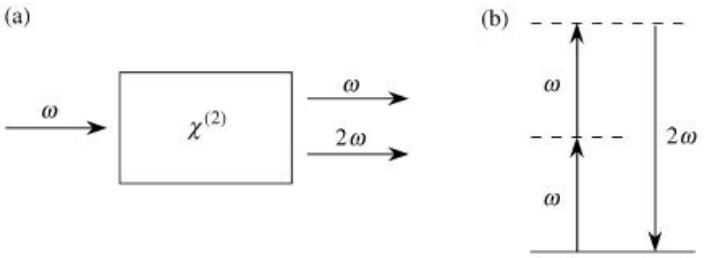

Figure 2.1: (a) Schematic showing SHG process (b) Energy level diagram for SHG process

When a monochromatic laser beam of electric field strength represented by

$$\tilde{E}(t) = Ee^{-i\omega t} + \text{c.c.} \tag{2.4}$$

is incident on a material with non-zero value of $\chi^{(2)}$, it induces a second-order polarization given by

$$\begin{aligned} \tilde{P}^{(2)}(t) &= \epsilon_0\chi^{(2)}(Ee^{-i\omega t} + \text{c.c.})^2 \\ \tilde{P}^{(2)}(t) &= \epsilon_0\chi^{(2)}(2EE^* + E^2e^{-2i\omega t} + E^{*2}e^{2i\omega t}) \\ \tilde{P}^{(2)}(t) &= 2\epsilon_0\chi^{(2)}EE^* + (\epsilon_0\chi^{(2)}E^2e^{-2i\omega t} + \text{c.c.}) \end{aligned} \tag{2.5}$$

The second term oscillates with a frequency 2ω and is the second-harmonic contribution to the polarization, while the constant first term represents a static electric polarization developed in the material (as $\partial^2\tilde{P}^{NL}/\partial t^2$ vanishes) and is called the optical rectification term. So we see that the second harmonic term scales quadratically with the incident electric field. It is to be noted though that $\chi^{(2)}$ has an order of magnitude value of approximately 10^{-12} m/V, and one might thus think that this contribution is not significant. But with proper experimental conditions, very high efficiencies can be obtained such that nearly all the incident power is converted into the second harmonic.

Fig. 2.1b shows an energy level diagram of the SHG process. The solid line indicates the ground state while the dotted lines indicate virtual levels. This diagram illustrates that two photons of frequency ω are annihilated and one photon of frequency 2ω is created.

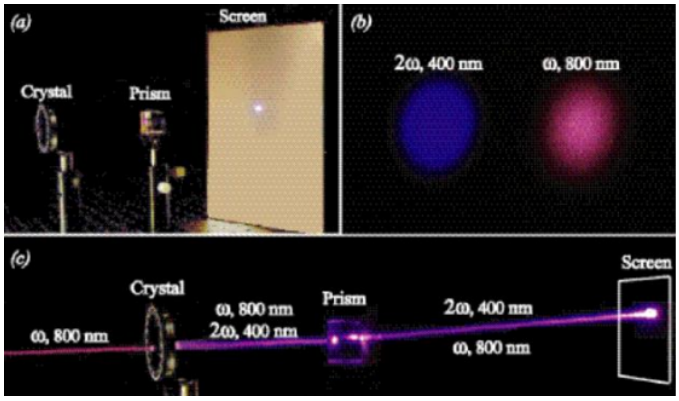

Figure 2.2: SHG from Lithium Niobate crystal (a) Setup, (b) Screen output (c) Trajectories of the pump and the SHG [35]

Mathematical description

The mathematical treatment provided here follows those discussed in refs. [32], [29] and [20]. To develop a mathematical description of SHG, we need to derive the coupled-wave equations for the incident pump field and the generated second-harmonic field within the material. We assume that the medium is lossless at the fundamental frequency ω_1 as well as the second harmonic frequency $\omega_2 = 2\omega_1$ and that the input beams are collimated, monochromatic and continuous-wave. The total electric field within the nonlinear medium is given by

$$\tilde{E}(z,t) = \tilde{E}_1(z,t) + \tilde{E}_2(z,t) \tag{2.6}$$

where

$$\tilde{E}_j(z,t) = E_j(z)e^{-i\omega_j t} + \text{c.c.}, \quad E_j(z) = A_j(z)e^{ik_j z} \tag{2.7}$$

with $k_j = n_j\omega_j/c$ and $n_j = [\epsilon^{(1)}(\omega_j)]^{1/2}$

The amplitude of the second harmonic wave $A_2(z)$ is taken to be a slowly varying function of z when the nonlinear source term is not too large, in the absence of which A_2 is constant (as it should be for a plane wave solution). The nonlinear polarization is:

$$\tilde{P}^{NL}(z,t) = \tilde{P}_1(z,t) + \tilde{P}_2(z,t) \tag{2.8}$$

where

$$\tilde{P}_j(z,t) = P_j(z)e^{-i\omega_j t} + \text{c.c.}, \quad j = 1, 2. \tag{2.9}$$

and

$$P_2(z) = \epsilon_0\chi^{(2)}E_1(z)^2 = \epsilon_0\chi^{(2)}A_1^2e^{2ik_1 z} \tag{2.10}$$

As each frequency component obeys the inhomogeneous wave equation (2.3), we can write the wave equation for the second harmonic as

$$\bigtriangledown^2\,\tilde{E}_2 - \frac{{n_2}^2}{c^2}\frac{\partial^2\tilde{E}_2}{\partial t^2} = \frac{1}{\epsilon_0 c^2}\frac{\partial^2\tilde{P}^2}{\partial t^2} \tag{2.11}$$

On expanding the first term and rewriting the equation, we get

$$\left[\frac{\partial^2 A_2}{\partial z^2} + 2ik_2\frac{\partial A_2}{\partial z} - {k_2}^2 A_2 - \frac{{n_2}^2{\omega_2}^2}{c^2}\frac{\partial^2 A_2}{\partial t^2}\right]e^{i(k_2 z-\omega_2 t)} = \\ = -\frac{{\omega_2}^2}{c^2}\chi^{(2)}{A_1}^2 e^{2ik_1 z-\omega_2 t} \tag{2.12}$$

We take the slowly varying amplitude approximation which allows us to neglect the first term as it is much smaller than the second. Also, using ${k_2}^2 = {n_2}^2{\omega_2}^2/c^2$, we get

$$2ik_2\frac{\partial A_2}{\partial z} = -\frac{\omega_2^2}{c^2}\chi^{(2)}{A_1}^2 e^{i\Delta kz} \tag{2.13}$$

where $\Delta k = 2k_1 - k_2$ is known as the phase or wavevector mismatch factor and is crucial in determining the efficiency of the conversion process. It accounts for the conservation of momentum for the SHG process when we consider the quantum mechanical picture.

For simplicity, we make the undepleted pump approximation which means that $A_1(z)$ is taken to be constant. It is a valid approximation in most cases as at most a negligible fraction of the pump power is transferred to the generated fields. This simplifies the expression even further and we obtain

$$2ik_2\frac{dA_2}{dz} = -\frac{{\omega_2}^2}{c^2}\chi^{(2)}{A_1}^2 e^{i\Delta kz} = -\frac{4{\omega_1}^2}{c^2}\chi^{(2)}{A_1}^2 e^{i\Delta kz} \tag{2.14}$$

On integrating both sides over the length L of the medium, we obtain

$$A_2(L) = \frac{2\omega_1}{n_2 c}\chi^{(2)} \quad \frac{e^{i\Delta kL}-1}{\Delta k}. \tag{2.15}$$

For the case of perfect phase-matching or $\Delta k = 0$, on taking the limit $\Delta k \to 0$ in the above equation, we find

$$A_2(L) = \frac{2i\omega_1}{n_2 c}\chi^{(2)}{A_1}^2 L. \tag{2.16}$$

The intensity is given by $I_2 = 2n_2\epsilon_0 c|A_2(L)|^2$, where

$$|A_2(L)|^2 = \frac{4{\omega_1}^2}{{n_2}^2 c^2}[\chi^{(2)}]^2|A_1|^4 L^2 \tag{2.17}$$

So the SHG intensity scales quadratically with the length of the medium or crystal. For the more general case of a nonzero Δk, we find

$$|A_2(L)|^2 = \frac{4{\omega_1}^2}{{n_2}^2 c^2}(\chi^{(2)})^2|A_1|^4 L^2 \mathrm{sinc}^2(\frac{\Delta kL}{2}). \tag{2.18}$$

In this case, the intensity of the second-harmonic wave varies with the phase mismatch ΔkL as $[\mathrm{sinc}^2(\Delta kL/2)]$ as shown in Fig. 2.3. We see later in chapter 5 that the spectral distribution of an SPDC process also follows the sinc() distribution that we see here and this is because like SHG, SPDC is also a second-order parametric process.

The coherence length, L_{coh}, is defined as the distance at which the output goes out of phase with the pump wave and is given by

$$L_{\mathrm{coh}} = \frac{2}{\Delta k} \tag{2.19}$$

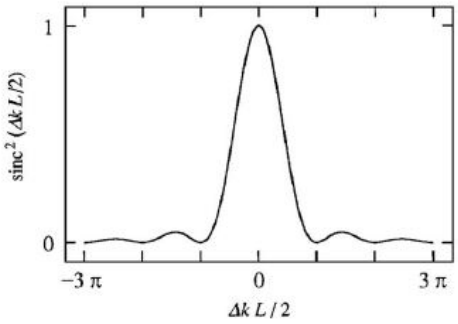

Figure 2.3: Intensity of the second-harmonic wave versus wave-vector mismatch.

2.2.2 Sum Frequency Generation (SFG)

Sum frequency generation is a more general situation than SHG in that the two input pump beams have different frequencies ω_1 and ω_2 , leading to the generation of the sum frequency $\omega_3 = \omega_1 + \omega_2$. The total electric field associated with the input waves is given by

$$\tilde{E}(t) = E_1 e^{-i\omega_1 t} + E_2 e^{-i\omega_2 t} + \text{c.c.} \tag{2.20}$$

The second-order nonlinear polarization in this case is given by

$$\tilde{P}^{(2)}(t) = \epsilon_0 \chi^{(2)} \tilde{E}(t)^2 \tag{2.21}$$

which on substitution of the expression for electric field gives

$$\begin{aligned} \tilde{P}^{(2)}(t) = \epsilon_0 \chi^{(2)} [{E_1}^2 e^{-2i\omega_1 t} + {E_2}^2 e^{-2i\omega_2 t} + 2E_1 E_2 e^{-i(\omega_1+\omega_2)t} + \\ + 2E_1 {E_2}^* e^{-i(\omega_1-\omega_2)t} + c.c.] + 2\epsilon_0 \chi^{(2)} [E_1 {E_1}^* + E_2 {E_2}^*] \end{aligned} \tag{2.22}$$

The polarization $\tilde{P}^{(2)}(t)$ can be expanded in its Fourier series and the corresponding frequency components on both sides are equated to get the complex amplitudes of different frequency components of the nonlinear polarization

$$\begin{aligned} P(2\omega_1) &= \epsilon_0 \chi^{(2)} {E_1}^2; (SHG) \\ P(2\omega_2) &= \epsilon_0 \chi^{(2)} {E_2}^2; (SHG) \\ P(\omega_1 + \omega_2) &= 2\epsilon_0 \chi^{(2)} E_1 E_2; (SFG) \\ P(\omega_1 - \omega_2) &= 2\epsilon_0 \chi^{(2)} E_1 {E_2}^*; (DFG) \\ P(0) &= 2\epsilon_0 \chi^{(2)} [E_1 {E_1}^* + E_2 {E_2}^*]; (OR) \end{aligned} \tag{2.23}$$

As we can see from the above equations, in the most general case of mixing between two pump beams, we get second harmonic (SHG), sum frequency (SFG), difference frequency (DFG) and optical rectification (OR). But all these components are not present at the same time and it is mostly one component that is the dominant one which is determined by the phase-matching condition (to be discussed later).

Mathematical Description

The derivation of the coupled wave equations is similar to that of second-harmonic generation except for the nonlinear source term which in the case of two pump

beams becomes

$$\tilde{P}_3(z,t) = P_3(z)e^{-i\omega_3 t}, \text{ where } P_3(z) = 2\epsilon_0\chi^{(2)}A_1A_2e^{-i(k_1+k_2)z} \tag{2.24}$$

Also,

$$\tilde{E}_3(z,t) = A_3(z)e^{i(k_3z-\omega_3t)} + \text{c.c.}, \quad \omega_3 = \omega_1 + \omega_2 \tag{2.25}$$

where

$$k_3 = \frac{n_3\omega_3}{c}, {n_3}^2 = \epsilon^{(1)}(\omega_3) \tag{2.26}$$

Note that the complex envelope $A_3(z)$ is again a slowly varying function of z in the presence of a small nonlinear source term which would have otherwise been a constant leading to a uniform plane-wave solution. Also, we make the undepleted pump approximation for both A_1 and A_2 and take them as constants in the analysis. As each frequency component of the electric field satisfies the inhomogeneous wave equation, we write the wave equation for the sum frequency term

$$\left[\frac{\partial^2 A_3}{\partial z^2} + 2ik_3\frac{\partial A_3}{\partial z} - {k_3}^2A_3 - \frac{{n_3}^2{\omega_3}^2}{c^2}\frac{\partial^2 A_3}{\partial t^2}\right]e^{i(k_3z-\omega_3t)}$$
$$= -2\frac{{\omega_3}^2}{c^2}\chi^{(2)}A_1A_2e^{i(k_1+k_2)z-\omega_3t} \tag{2.27}$$

Again, making the slowly varying envelope approximation and substituting the value of $k_3 = n_3\omega_3/c$, we obtain

$$\frac{dA_3}{dz} = \frac{i\chi^{(2)}{\omega_3}^2}{k_3c^2}A_1A_2e^{i\Delta kz}, \tag{2.28}$$

where $\Delta k = k_1 + k_2 - k_3$ is the phase or wavevector mismatch factor. Integrating the above equation along the length L of the crystal, we obtain

$$A_3(L) = \frac{i\chi^{(2)}\omega_3A_1A_2}{n_3c} \quad \frac{e^{i\Delta kL}-1}{i\Delta k}. \tag{2.29}$$

The intensity of the sum-frequency wave at the output of the crystal is given by $I_3(L) = 2n_3\epsilon_0c|A_3(L)|^2$ where

$$|A_3(L)|^2 = \frac{2{\chi^{(2)}}^2{\omega_3}^2I_1I_2}{n_1n_2n_3\epsilon_0c^2}L^2\text{sinc}^2\left(\frac{\Delta kL}{2}\right) \tag{2.30}$$

So the sum-frequency intensity also shows a sinc^2 dependence, as was observed for the second-harmonic case. Fig. 2.3 thus also shows the variation of sum-frequency intensity as a function of the phase-mismatch factor.

2.2.3 Difference Frequency Generation (DFG)

In the previous section, we saw that a difference-frequency component was one of the outcomes when two beams interact in a medium with non-zero value of $\chi^{(2)}$. Let us now consider in detail such a situation, which as shown in Fig. 2.4, where two waves ω_3 and ω_1 interact in a lossless optical medium. We use the undepleted pump approximation for the higher-frequency input wave ω_3. The coupled wave

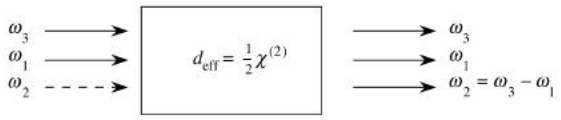

Figure 2.4: Schematic showing the process of difference frequency generation.

equations for the difference-frequency wave ω_2 and the the lower-frequency input wave ω_1 are obtained by a method analogous to that for SFG and are as follows:

$$\frac{dA_1}{dz} = \frac{i{\omega_1}^2\chi^{(2)}}{k_1c^2}A_3{A_2}^*e^{i\Delta kz} \tag{2.31}$$

and

$$\frac{dA_2}{dz} = \frac{i{\omega_2}^2\chi^{(2)}}{k_2c^2}A_3{A_2}^*e^{i\Delta kz} \tag{2.32}$$

where

$$\Delta k = k_3 - k_1 - k_2 \tag{2.33}$$

On solving the above set of differential equations for the case of perfect phase matching, $\Delta k = 0$, we obtain

$$A_1(z) = A_1(0)\cosh\kappa z \tag{2.34}$$

$$A_2(z) = i\left(\frac{n_1\omega_2}{n_2\omega_1}\right)^{1/2}\frac{A_3}{|A_3|}{A_1}^*(0)\sinh\kappa z \tag{2.35}$$

where the coupling constant κ is given by

$$\kappa^2 = \frac{{\chi^{(2)}}^2{\omega_1}^2{\omega_2}^2}{k_1k_2c^4}|A_3|^2. \tag{2.36}$$

Fig. 2.5 shows the spatial evolution of A_1 and A_2 for the case of perfect phase-matching in the undepleted pump approximation. It is observed that both A_1

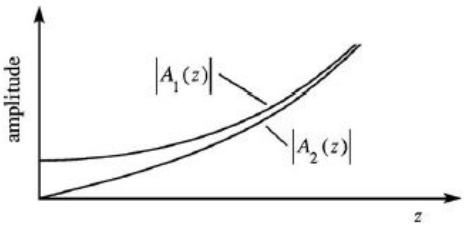

Figure 2.5: Spatial evolution of A_1 and A_2 for the case of perfect phase-matching in the undepleted pump approximation

and A_2 show monotonically increasing growth and that each field asymptotically experiences an exponential growth. The input field A_1 retains its initial phase and the DFG wave A_2 possesses a phase that depends on both that of the pump and of the ω_1 waves. An intuitive explanation for this behavior is that the presence of the ω_2 wave stimulates the generation of the ω_1 wave and vice versa. This process of amplification of the signal wave ω_1 due to nonlinear mixing resulting in the production of an idler is known as 'parametric amplification' as DFG is a parametric process (due to the initial and final quantum mechanical states being identical).

2.2.4 Optical Parametric Oscillation (OPO)

The previous section described the process of parametric amplification by DFG. This gain can be used to produce oscillation when it is supplied with the appropriate positive feedback. This can be done by placing mirrors that are highly reflective at one or both of the signal and idler frequencies on the either side of the nonlinear medium as shown in Fig. 2.6. If the end mirrors are reflecting at both the signal and idler frequencies, the device is called a doubly resonant oscillator, and if it is reflecting at either the signal or the idler frequency, then it is called singly resonant oscillator. The OPO can be used as a source of frequency-tunable radiation for infrared, visible and ultraviolet spectral regions and can produce either continuous wave, nanosecond, picosecond or femtosecond pulsed outputs.

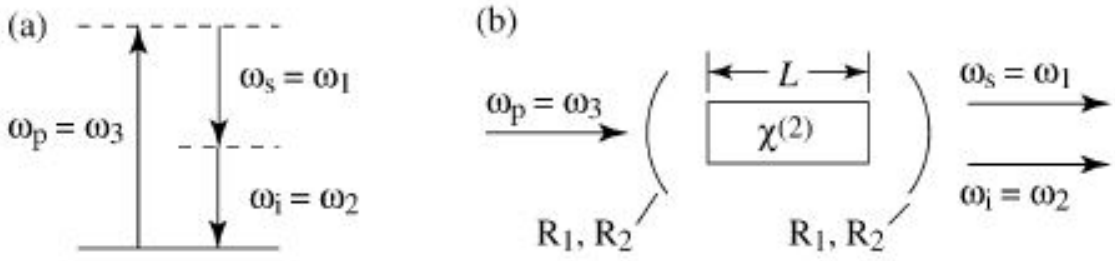

Figure 2.6: (a) Energy-level diagram for a parametric amplification process. (b)Schematic for an OPO.

2.2.5 Parametric Downconversion

The production of simultaneous photon pairs was described as early as 1970 [36]. Also known as parametric fluorescence [37], parametric scattering or SPDC, it is the spontaneous splitting of the pump photon ω_p into signal, ω_s and idler, ω_p photons such that $\omega_p = \omega_s + \omega_i$ (energy conservation) and is stimulated by random vacuum fluctuations. The emitted photons must satisfy the phase-matching conditions due to momentum conservation, or $\vec{k_p} = \vec{k_s} + \vec{k_i}$.

The emitted photon pairs are simultaneously entangled in several sets of complementary degrees of freedom. Specifically, the photon pairs can be entangled in time and energy, in position and momentum, in orbital angular. The fact that the emitted photons display entanglement has enormous implications for quantum information technologies. For example, entanglement allows one to test some of the fundamental properties in quantum mechanics such reality and non-locality. SPDC is also used to build single photon sources. Entanglement between successive pairs does not occur [38]. Fig. 2.7a shows the energy level diagram for this process and 2.7b shows a typical experimental setup.

There are two different configurations for SPDC depending on whether the signal and idler waves have the same or orthogonal polarizations; these are called type I and type II configurations, respectively. For type I, the emission is in the form of concentric cones of signal and idler beams such that each photon of an entangled pair lie opposite to each other on the cones. In type II on the other hand, we get two separate cones for the orthogonal polarizations and each photon of the entangled pair is found opposite to each other on the respective cones. On

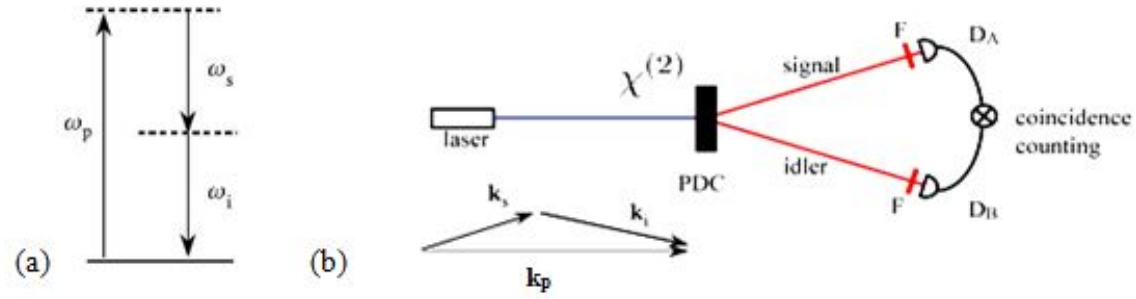

Figure 2.7: (a) Energy-level diagram for a parametric downconversion process (b) Schematic of an experiment to perform coincidence counts for entangled photons

the points of intersection of the two cones, we get photons that are entangled in polarization [39]. Chapter 5 discussed type I SPDC in bulk crystals in considerable detail including many original contributions to the problem.

2.2.6 Phase-matching

In the previous sections, it was explained that the efficiency of all second-order processes depends on the crucial criterion of phase-matching. In vector representation, it is written as

$$\vec{k_1} = \vec{k_1} + \vec{k_3} \tag{2.37}$$

where $|\vec{k_i}| = n_i\omega_i/c$. When we consider collinearly propagating waves in an isotropic medium, this equation reduces to a scalar representation

$$\frac{n_1\omega_1}{c} = \frac{n_2\omega_2}{c} + \frac{n_3\omega_3}{c}. \tag{2.38}$$

From energy conservation, we have $\omega_1 = \omega_2 + \omega_3$. In a non-dispersive medium, we have $n_1 = n_2 = n_3$ and so equation (2.37) is automatically satisfied in a non-dispersive medium due to frequency-matching. But when we have a dispersive medium, the refractive indices are not equal (and increase monotonically with frequency) which means that both frequency and phase-matching conditions are not simultaneously satisfied and all the three waves travel with different velocities in the medium. As a result, we cannot have phase-matching in isotropic, dispersive media.

To compensate for the dispersion, birefringence, which is the dependence of refractive indices on polarization of the waves and the directions with respect to the principal axes of crystal, present in anisotropic media can be used. Hence, by properly adjusting the crystal orientation and the wave polarizations, phase-matching can be achieved. In [40], two ways of achieving phase-matching have been discussed: type I and type II. In type I, both lower frequency waves have ordinary polarization while in type II, one of them has the extraordinary polarization. Fig. 2.9a shows how crystal angle can be tuned to achieve phase-matching in a negative uniaxial crystal. In the case of a uniaxial crystal, we have further two possibilities depending on whether the ordinary refractive index or extraordinary refractive index is larger. Fig. 2.9b shows the dispersion curve for a negative uniaxial crystal. Table 1 shows the phase-matching method for all four cases.

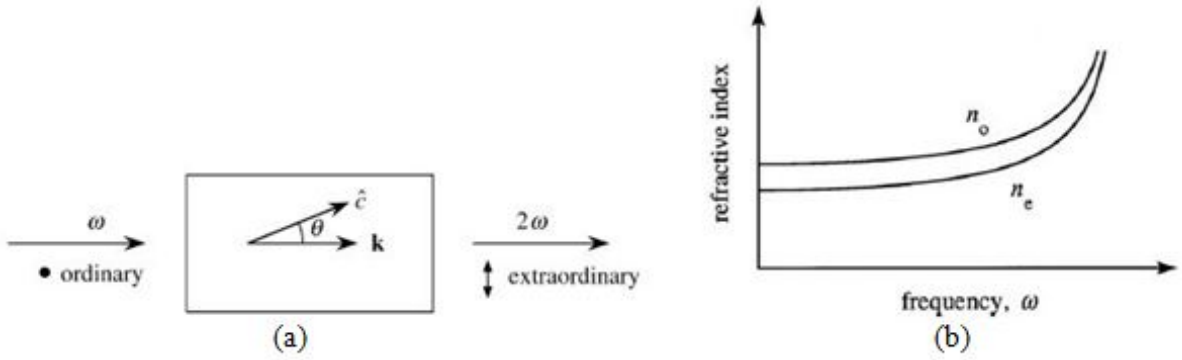

Figure 2.8: (a) Angle tuned phase-matching (b) Dispersion curves for a negative uniaxial crystal

We later use a negative uniaxial crystal for numerical calculations of photon pair generation rates for type I SPDC in chapter 5.

Table 2.1: Phase-matching methods for uniaxial crystal.

	Positive- Uniaxial $(n_e > n_0)$	Negative- Uniaxial $(n_e < n_0)$
Type I	${n_3}^o\omega_3 = {n_1}^e\omega_1 + {n_2}^e\omega_2$	${n_e}^o\omega_3 = {n_1}^o\omega_1 + {n_2}^o\omega_2$
Type II	${n_3}^o\omega_3 = {n_1}^o\omega_1 + {n_2}^e\omega_2$	${n_3}^e\omega_3 = {n_1}^e\omega_1 + {n_2}^o\omega_2$

In cases where there is insufficient or no birefringence to compensate for dispersion, other methods need to be applied to achieve phase-matching. The most important method is called quasi-phase matching where we have a periodically poled nonlinear crystal with the optic axis reversed at a period of less than or equal to twice the coherence length L_{coh} given by equation (2.19). Hence every time the output goes out of phase with the pump causing power to flow back from the output, the sign of $\chi^{(2)}$ flips allowing the output to grow monotonically. Fig. 2.9b shows the quasi-phase matched output in comparison to perfectly phase-matched and phase-mismatched outputs.

2.3 Third-order nonlinear optical processes

The third-order contribution to nonlinear polarization is given by

$$\tilde{P}^{(3)}(t) = \epsilon_0 \chi^{(3)} \tilde{E}(t)^3 \tag{2.39}$$

where $\tilde{E}(t)$ is the total electric field. The polarization then has various frequency components, the simplest being the third harmonic for the case of a monochromatic input.

2.3.1 Third Harmonic Generation (THG)

Let us consider the case of a monochromatic beam incident on the medium with the electric field given by

$$\tilde{E}(t) = Ee^{-i\omega t} + c.c \tag{2.40}$$

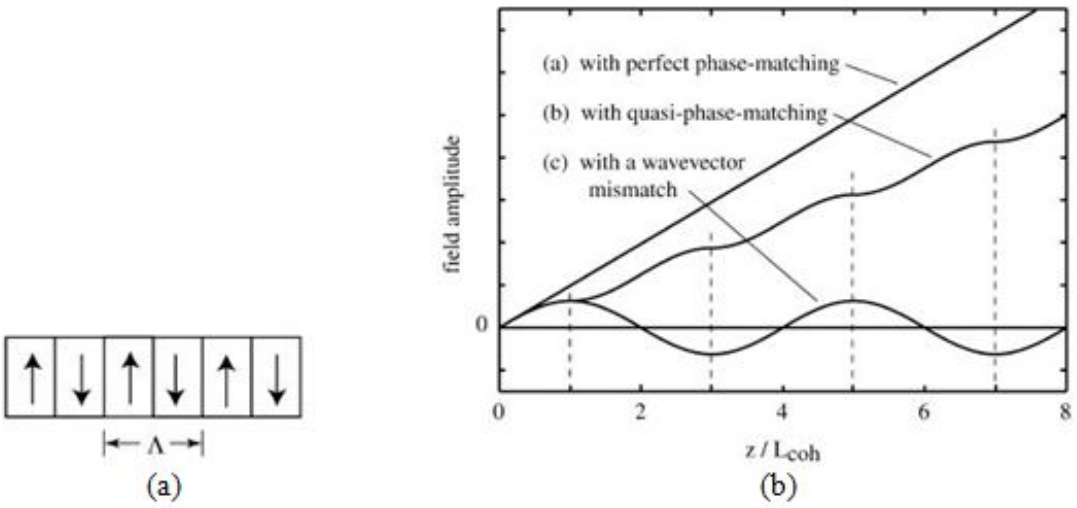

Figure 2.9: (a) A periodically-poled crystal with arrows showing the direction of optic axis (b) Comparison of perfect-phase matching and quasi-phase matching

The nonlinear polarization is then given by

$$\tilde{P}^{(3)}(t) = \epsilon_0 \chi^{(3)}[(E^3 e^{-3i\omega t} + c.c) + 3EE^*(E + E^*)e^{-i\omega t}] \tag{2.41}$$

The first term oscillating at frequency 3ω gives the third harmonic contribution. The energy level diagram for the process is shown in Fig. 2.10.

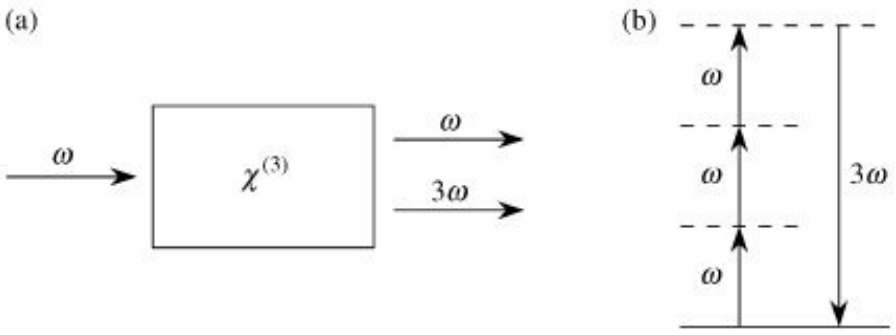

Figure 2.10: (a)Schematic for a THG process (b) Energy level diagram for third harmonic generation

2.3.2 Intensity dependent refractive index

In equation (2.41), the second term oscillating at the frequency of the pump ω has the coefficient which depends on the intensity of the pump. So this contribution leads to a refractive index which depends on the intensity of the pump and is given by

$$n = n_0 + n_2 I \tag{2.42}$$

It is also called the Kerr nonlinearity.

There are two ways in which this nonlinear effect becomes manifest: 1) Self Phase Modulation (SPM): When a strong pump beam modifies its own propagation and 2) Cross Phase Modulation (XPM): When a strong beam modifies the propagation of a weaker probe beam. Due to degeneracy factors associated with the coefficients, the nonlinear refractive index due to two beams, $\bar{n_2}^{\text{cross}}$, is twice that for a single beam, $\bar{n_2}^{\text{self}}$. By using the relation between the refractive index and susceptibility:

$$n_2 = 1 + \chi_{\text{eff}} \tag{2.43}$$

where $\chi_{\text{eff}} = \chi^{(1)} + 3\chi^{(3)}|E|^2$, we find that

$$n_2 = \frac{3}{4{n_0}^2 \epsilon_0 c}\chi^{(3)} \tag{2.44}$$

for the case of SPM.

2.4 Effect of material symmetry

Material symmetry, most importantly the presence of inversion symmetry, plays a very important role in determining the value of susceptibility. All even-order nonlinear responses vanishes identically for centrosymmetric materials, that is, for materials that lack inversion symmetry. Conversely, odd-order nonlinear response is in principle present for all materials. Figs. 2.11a and 2.11b show the potential wells that confine electrons to their parent atom for centrosymmetric and non-centrosymmetric materials. An intuitive explanation for this effect can

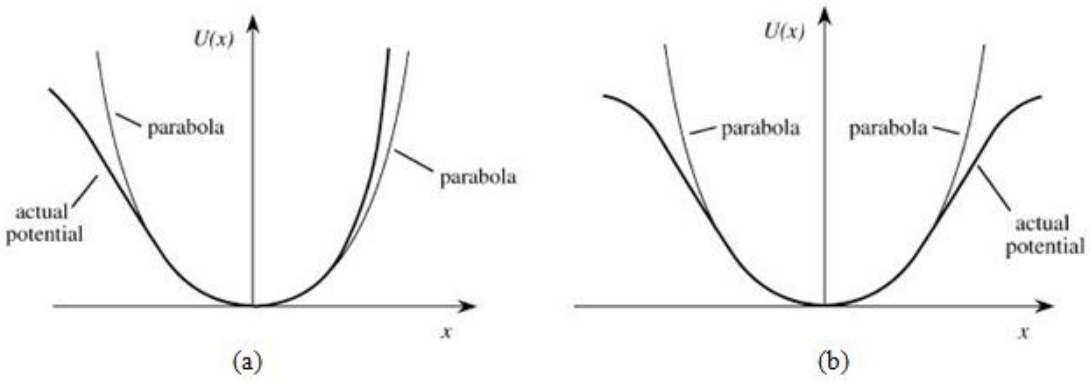

Figure 2.11: (a)Potential well for a non-centrosymmetric medium (b) Potential well for a centrosymmetric medium

be explained by examination of Fig. 2.11, that shows the response for linear, centrosymmetric, and non-centrosymmetric media for a single-frequency applied field. While the response of a linear medium has the same form as the applied field with no distortion, the nonlinear responses for both types of nonlinear media shows significant distortion. For centrosymmetric media with potential well as shown in Fig. 2.11a, only odd-harmonics are present in the response. For non-centrosymmetric media with potential well as shown in Fig. 2.11b, both odd and even harmonics are present. Hence, we get a second-order nonlinear response from only non-centrosymmetric materials.

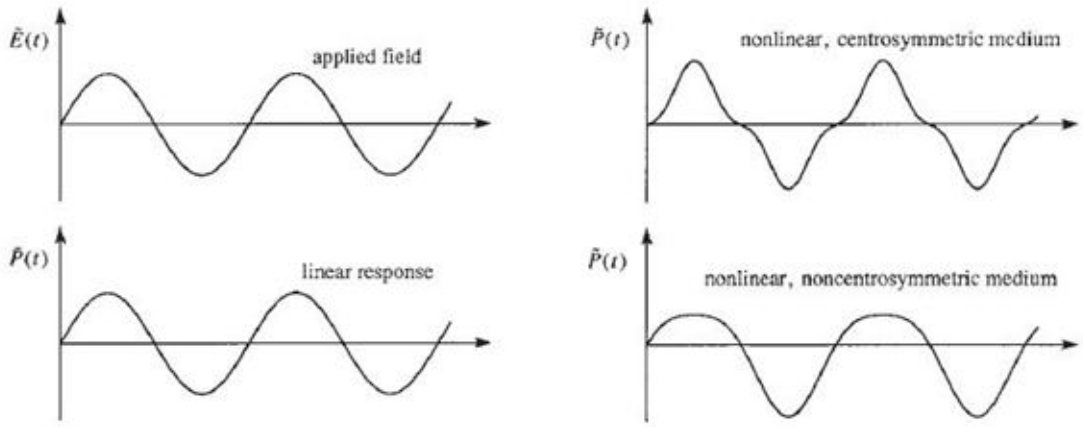

Figure 2.12: Response of centrosymmetric or non-centrosymmetric media to a plane wave excitation

2.5 Nonlinear optics with focussed Gaussian beams

The preceding sections have assumed infinite plane-wave sources for the description on nonlinear effects. But in actual practice, we don't have infinite plane waves. The laser beam typically is a Gaussian, and in this case we need to account for focussing effects including that the effective interaction length is the Rayleigh range of the beam. SHG using focussed Gaussian beams have been discussed in [41], [42] and [43].

For a Gaussian beam with waist diameter w_0, the Rayleigh range is

$$z_R = \frac{\pi {w_0}^2}{\lambda} \tag{2.45}$$

and the peak intensity $P/(\pi {w_0}^2)$ occurs the waist The peak intensity is thus inversely proportional to the length of the interaction region. So for maximum efficiency, the Rayleigh range must be half the length of the medium. But ref. [41] gives a value of $L/2.84$ for the confocal parameter (which is twice the Rayleigh range) for maximum efficiency of SHG. This is because we have an additional phase-mismatch of $\Delta k = 3.2/L$ due to the Guoy phase shift which needs to be compensated. The analysis for this scenario is done in chapter 5 for the case of type-I SPDC for both collinear and non-collinear emission of signal and idler. The results obtained from those calculations are very close to the predictions in ref. [41] for collinear emission. For non-collinear emission, the values are different depending on the emission angle.

2.6 Origin of Third-Order Nonlinear Response

The nonlinear susceptibility is a characteristic of any given medium, and its value depends on the electronic and molecular structure of the material [20]. There are different mechanisms responsible for introducing an intensity-dependent refractive index, and their relative strengths and response times are summarized in Table II.

Table 2.2: Typical values of nonlinear refractive index (for linearly polarized light)

Mechanism	n_2 (cm^2/W)	$\chi^{(3)}(m^2/V^2$	Response Time (sec)
Electronic Polarization	10^{-16}	10^{-22}	10^{-15}
Molecular Orientation	10^{-14}	10^{-20}	10^{-12}
Electrostiction	10^{-14}	10^{-20}	10^{-9}
Saturated atomic absorption	10^{-10}	10^{-16}	10^{-8}
Thermal Effects	10^{-6}	10^{-12}	10^{-3}
Photorefractive effect	(large)	(large)	(intensity-dependent)

Of the effects mentioned, the electronic polarizability is responsible for the generation of optical harmonics and has the fastest response. In liquids, effects due to molecular orientation and electrostriction dominate. Moreover, in solids with no degree of freedom for molecular orientation, electrostriction dominates.

2.6.1 Quantum mechanical explanation of nonlinear optical susceptibility

The parametric nonlinear processes described in previous sections can be interpreted as a form of wave-mixing involving energy exchange among the interacting waves of different frequencies. From a quantum mechanical perspective, they can be viewed as photon interaction processes involving creation of photons of some frequency and annihilation of another. This is represented in the energy-level diagrams illustrated previously. Thus, it involves electron transitions between the different energy levels which may be resonant, if they occur between real energy levels, or non-resonant, if they occur between virtual levels. Resonant transitions leads to a very large value of the susceptibility. The density-matrix formalism is the preferred means to derive expressions for the different orders of the nonlinear susceptibility $\chi^{(n)}$. A perturbation expansion is used to determine the expectation value of the induced dipole moment [20],[29]. Fig. 2.13 shows the expression and Feynman diagrams [44], [29] for the each element of $\chi^{(2)}$, which represents a three photon interaction process.

2.6.2 Non-resonant electronic nonlinearities

Non-resonant nonlinearities arise due to electronic transitions involving virtual levels [29] and are the weakest of all contributions due to their off-resonance nature [29]. But these contributions are important as they are present in all dielectric materials. They are also extremely fast with response times of the order of 10^{-16} s, as the response time in this case is the time required for the atomic cloud to become distorted due to an applied optical field. We can estimate the order of magnitude of $\chi^{(3)}$ in the far-off resonance case by considering the classical, anharmonic model for an oscillator under far-off resonance excitation. The expression obtained is

$$\chi^{(3)} = \frac{N_0 e^4}{\epsilon_0 m^3 {\omega_0}^6 d^2}. \tag{2.46}$$

For the typical values of number density $N_0 = 4 \times 10^{22}\text{cm}^{-3}$, Bohr radius $d = 3 \times 10^{-10}$ m, and resonance frequency $\omega_0 = 7 \times 10^{15}$ rad/s one finds that $\chi^{(3)} \simeq$

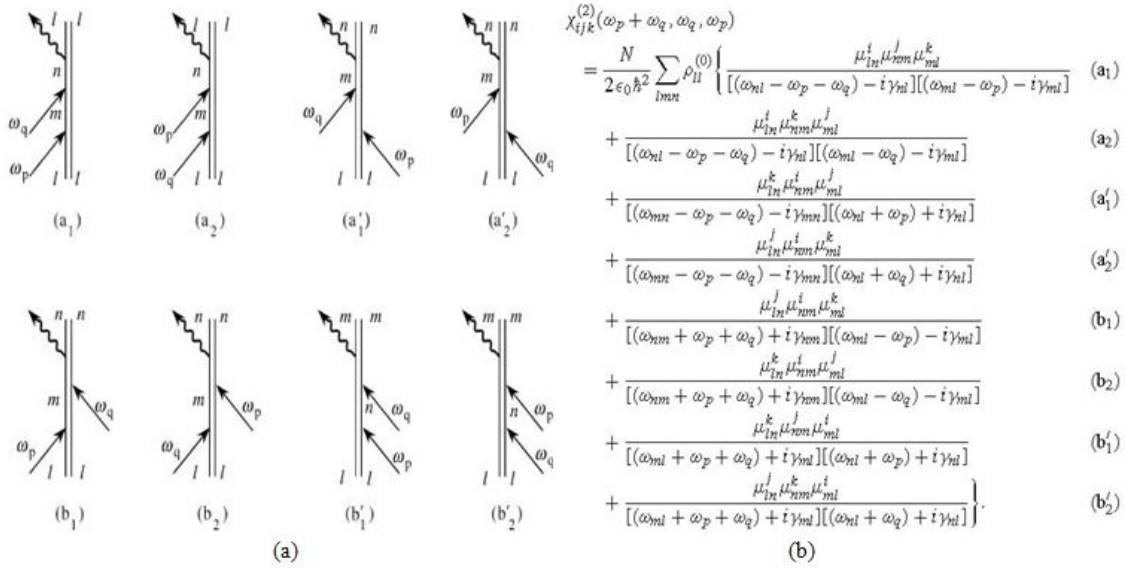

Figure 2.13: (a) Feynman diagrams for the electron transitions involved in a second-order process (b) Expression for $\chi^{(2)}$ in terms of the transition dipole moments of the different transitions involved

$3 \times 10^{-22}\mathrm{m}^2/\mathrm{V}^2$.

2.6.3 Molecular orientation effect

Molecular orientation contribution to the third-order nonlinearity becomes important for anisotropic liquids i.e. liquids which have different polarizability along different axes. When subjected to an optical field, the molecules experience a torque that twists them such that the axis with higher polarizability tends to be aligned along the direction of the applied field. An example of such a liquid is carbon disulfide (CS_2), which is comprised of cigar-shaped (prolate spheroidal) molecule [29]. The polarizability along the molecular axis, α_3, is higher than along

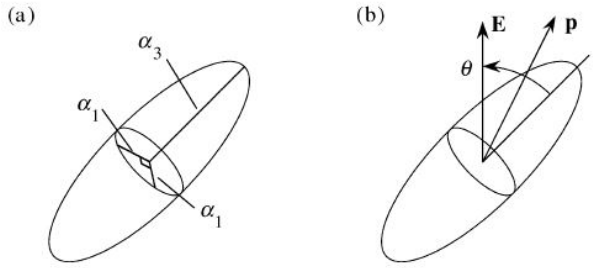

Figure 2.14: (a) The CS_2 molecule (b) Dipole moments that develop within the molecule upon application of an electric field

the transverse axis, α_1. Due to this, the induced dipole moment has a much larger component along the molecular axis than along the transverse axis and is not parallel to the applied field as shown in the figure. A net torque then acts on the molecule given by $\vec{\tau} = \vec{p} \times \vec{E}$ which tends to align the molecule with the applied

electric field. But thermal agitation introduces a randomness in the molecular orientation. For a number density N_0, temperature T, and neglecting the local field effects, the first- and third-order susceptibilities for the given polarizabilities are given by

$$\chi^{(1)} = N_0\Big(\frac{1}{3}\alpha_3 + \frac{2}{3}\alpha_1\Big) \tag{2.47}$$

$$\chi^{(1)} = \frac{2N_0}{45}\frac{(\alpha_3 - \alpha_1)^2}{kT} \tag{2.48}$$

where k is the Boltzmann constant. The response for this effect is slower as it takes some time for the molecules to align with the applied field, and the response time is of the order of picoseconds.

2.6.4 Thermal effects

Thermal contributions to the nonlinearity occur when the incident laser power when passing through them medium is absorbed causing an increase in temperature and a change in the refractive index of the material with temperature. This change is negative for gases but may be either positive or negative for condensed matter depending on the internal structure of the material [29]. It is a non-local optical phenomenon as the refractive index change at some point depends on the laser intensity nearby. The response time is of the order of nanoseconds and is very slow as the time taken to change the temperature of the material can be long. Mathematically, this change in refractive index with temperature can be expressed by the following relation

$$\tilde{n} = n_0 + \Big(\frac{dn}{dT}\Big)\tilde{T_1} \tag{2.49}$$

where (dn/dT) describes the temperature dependence of refractive index while $\tilde{T_1}$ accounts for the change in temperature due to incident laser field and obeys the heat transport equation

$$(\rho_0 C)\ \frac{\partial \tilde{T_1}}{\partial t} - \kappa \bigtriangledown^2 \tilde{T_1} = \alpha_l \tilde{I}(r) \tag{2.50}$$

where $\rho_0 C$ denotes the heat capacity per unit volume, κ denotes the thermal conductivity and α_l the linear absorption coefficient of the material.

There are a number of effects that can occur due to thermal contributions to the nonlinearity such as the formation of thermally induced optical grating, pattern formation etc., which have been discussed in [45]-[46].

2.7 Measurement of optical nonlinearity: Z-scan

Z-scan, first reported in [47], is a single beam technique to measure both real and imaginary components of the nonlinear refractive index coefficient. To measure the real (refraction) coefficient, a tightly focussed Gaussian beam is made incident on the sample and the transmission through the nonlinear medium (assumed to be thinner than the diffraction length of the medium) is measured at the far-field

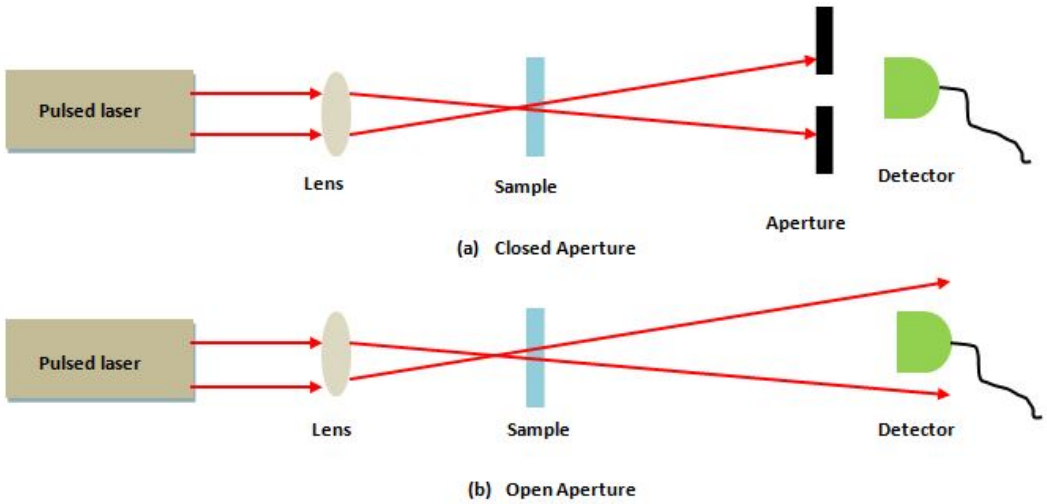

Figure 2.15: (a) Closed aperture scan schematic to measure real part of $\chi^{(3)}$ (b) Open aperture scan schematic to measure imaginary part of $\chi^{(3)}$

through an aperture. The setup is shown in Fig. 2.15. To examine the effect of translation of the sample along the beam path, we consider a material with a negative value of n_2. We are ignoring the losses for the moment. When the sample is far away from the focus, due to low intensity of the optical field on the sample, there is no effect on the transmitted beam as the nonlinear contribution to the refractive index $n_2 I$ is very low. As the sample is moved from a negative z towards the focus, a negative lensing effect on the beam takes place prior to focus and the beam divergence at the aperture is reduced leading to increased transmission through the aperture. When the sample is moved beyond the focal plane towards positive z, the negative lensing effect causes defocussing at the aperture causing a decrease in transmission. This suggests that there is a null at the focus. The transmittance as a function of sample position for CS_2 is shown in Fig. 2.16a. The peak-valley positions are reversed if the sample has a positive value of n_2.

When there are absorptive nonlinearities present, the transmittance curve shows asymmetrical peak and valley distribution. The presence of multi-photon absorption results in a larger valley while saturable absorption results in a larger peak. It is to be noted that the nonlinear refraction effect is probed by the aperture. When the aperture is removed from the far-field, the transmittance depends on absorption nonlinearities and there is no effect of nonlinear refraction. The transmittance obtained for an open aperture case is symmetrical with respect to the focus where the maxima (for saturable absorption) or the minima (for multi-photon absorption) occurs. Hence, the Z-scan measurement can not only be used to calculate the sign of nonlinear refraction, but the absorption mechanism within the sample as well. Compared to the other methods of measuring nonlinearity such as nonlinear interferometry [49], degenerate four wave mixing [50], nearly degenerate three wave mixing [51], ellipse rotation [52] and beam distortion [53], Z-scan is a much simpler and sensitive process.

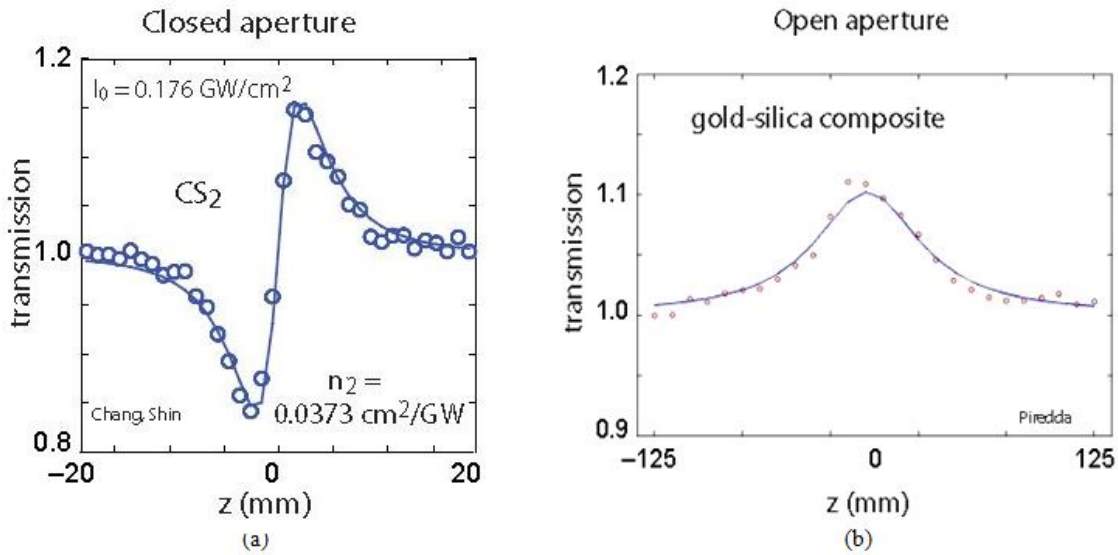

Figure 2.16: (a) Closed aperture scan result for CS_2 from Bahae et al [47] (b) Open aperture scan result for gold-silica composite [48]

2.8 Self Action Effects

Self-action effects are the effects in which a light beam modifies its own propagation by means of the nonlinear response of the medium. Common self-action effects are discussed briefly below.

2.8.1 Self Focussing

When an intense beam of light modifies the optical properties of the medium such that it is caused to come to a focus within the medium, the phenomenon is called self-focussing of light, or catastrophic collapse [29], [54]. For a positive value of n_2, a beam with a varying transverse intensity profile induces refractive index variation with a maximum index at the centre of the beam that is larger than that at the periphery, creating a positive lens such that the beam comes to focus within the material. This situation results when the self-focussing effect is not compensated by diffraction or other nonlinearities (like quintic nonlinearity due to $\chi^{(5)}$). Also, the beam power P must be greater than the critical power for self-trapping, called P_{cr}, so that the self-focussing is larger than diffraction and other defocussing effects.

Chiao et al. [55] give the following expression for P_{cr} assuming a circular beam of uniform intensity and radius w_0

$$P_{cr} = \frac{\pi(0.61)^2{\lambda_0}^2}{8n_0n_2} \tag{2.51}$$

where λ_0 is the vacuum wavelength of the applied optical field. The value of P_{cr} depends not only on the input beam profile, but is also different for bulk media and waveguides [56]. The distance at which the intensity becomes anomalously large is called the self-focussing length, z_{sf} or collapse length, L_{col} [54]. The expression

for the self-focussing length $z_{\rm sf}$ given by Kelley is [54]

$$z_{\rm sf} = \frac{2n_0{w_0}^2}{\lambda_0}\frac{1}{\sqrt{P/P_{cr}-1}}. \tag{2.52}$$

Note that $z_{\rm sf}$ scales with power as approximately $1/P^{1/2}$. For sufficiently high powers though, this collapse distance scales with $1/P$ as was demonstrated for cw beams propagating in CS_2 [57],[58]. In the previous cases, it was assumed that the input beams have no noise. But when noise is present, there is a second collapse threshold much greater than $P_{\rm cr}$, called $P_{\rm MF}$, where the input beam breaks up into multiple filaments for powers higher than $P_{\rm MF}$ as discussed by Fibich et al in [59].

2.8.2 Optical Solitons

An optical soliton is any optical field that does not change its shape (spatially or temporally) during propagation due to exact cancellation of nonlinear and linear focussing and defocussing effects within the medium. We can have two kinds of solitons depending on which profile, spatial or temporal, is preserved during propagation. A spatial soliton is formed due to exact cancellation of self-focussing and diffraction, while a temporal soliton is formed when there is cancellation of self-phase modulation and dispersion within the medium. We may also have a spatio-temporal soliton when all these effects balance simultaneously. We describe the spatial and temporal solitons in the following sections.

Self trapping and spatial solitons

When there is an exact balance between self-focussing and diffraction, the beam of light propagates with a constant diameter and the phenomenon is called self-trapping of light [55]. The power carried by the beam is exactly equal to the P_{cr}, the critical power for self-trapping. Under these conditions, the beam forms its own waveguide and propagates without spreading. The nonlinear pulse propagation for this case is given by [29]

$$\bigtriangledown_T{}^2 A + 2ik\frac{\partial A}{\partial z} = -\frac{2k^2 n_2}{n_0}|A|^2 A \tag{2.53}$$

which is also called the nonlinear Schrödinger equation (NLSE). The first term on the left accounts for diffraction while the term on the right accounts for self-focussing. When A(x,y,z) varies along only one transverse dimension, say x, (or the case of a slab-shaped beam) the solution is called a spatial soliton and is given by

$$A(x,z) = A_0\ \mathrm{sech}(x/x_0)e^{i\gamma z} \tag{2.54}$$

where x_0 is the width of the field distribution of the soliton. For a cylindrical beam, where the transverse field variation has both x and y components, there is no analytic solution to the NLSE. The NLSE in cylindrical coordinates is written as

$$\frac{d^2A(r)}{dr^2} + \frac{1}{r}\frac{dA(r)}{dr} - A(r) + A^3(r) = 0 \tag{2.55}$$

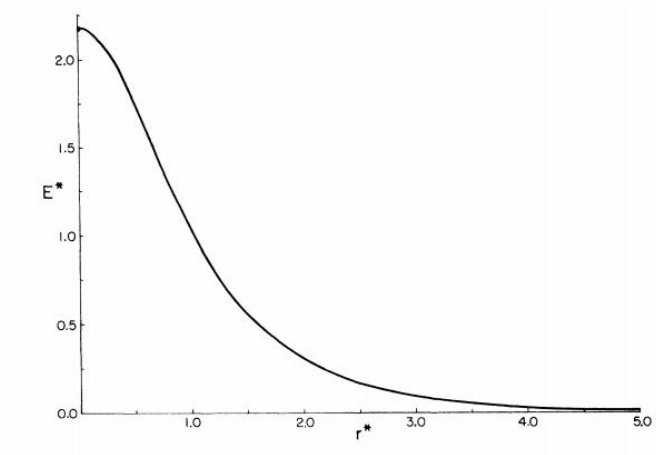

Figure 2.17: Radial profile of the self-focussed beam, also called the Townes profile [55]

and the numerical solution, shown in fig. 2.17, is called the Townes profile [55].

In the absence of any saturation effects or plasma defocussing, this solution is not stable [60] and is susceptible to perturbations which might cause the beam either to diffract or self-focus [61]. However, when a beam self-focusses, the on-axis component evolves into the circularly symmetric Townes profile irrespective of the initial beam profile as discussed in [62] and [63] and the collapsed on axis portion carried exactly P_{cr} power. But for super-gaussian beams, the beam self focusses into a ring profile as reported in [64].

Spatial solitons can also be viewed as stationary wave-packets that are localized in space. As such, they have the unique property that their energy and momentum is conserved even when they interact with each other leading to a number of interesting effects like soliton fusion, fission and annihilation [60]. The first spatial soliton was observed in a sodium vapor cell by Ashkin and Bjorkholm in 1974 [65]. Later on, spatial solitons were also observed in CS_2 in 1985 [66], in AlGaAs waveguides [67], and in nematic liquid crystals [68].

Temporal Solitons

When short optical pulses propagate within a non-dispersive, nonlinear medium, it experiences a nonlinear phase shift due to the medium's Kerr response [29]. If we assume that response of the medium is instantaneous, then the nonlinear phase shift experienced by an optical pulse of instantaneous pulse intensity $I(t)$ travelling through a medium of length L and central frequency ω_0 is

$$\phi_{\mathrm{NL}}(t) = -n_2 I(t)\omega_0 L/c \tag{2.56}$$

This is known as self-phase modulation as a propagating optical pulse modifies its own phase due to the medium's nonlinearity as it propagates. This leads to spectral broadening. But in most instances, we also need to take into account the dispersion within a medium. For a pulse

$$\tilde{E}(t) = \tilde{A}(z,t)e^{i(k_0 z - \omega_0 t)} + c.c. \tag{2.57}$$

the pulse propagation equation for a dispersive and nonlinear medium is given by [29]

$$\frac{\partial \tilde{A}_s}{\partial z} + \frac{1}{2} i k_2 \frac{\partial^2 \tilde{A}_s}{\partial \tau^2} = i\gamma |\tilde{A}_s|^2 \tilde{A}_s \tag{2.58}$$

where

$$\tilde{A}_s(z,\tau) = \tilde{A}(z,t), \quad \tau = t - \frac{z}{v_g}, \tag{2.59}$$

with v_g being the group velocity. The second term on the left hand side of equation (5.58) takes account of group velocity dispersion while the term on the right hand side takes account of self-phase modulation. Under proper circumstances, there can be an exact cancellation of the pulse spreading due to the two effects and the pulse shape is preserved as it propagates. These pulses are called temporal optical solitons. The fundamental solution for equation (2.58) is given by

$$\tilde{A}_s(z,\tau) = A_s^0 \,\mathrm{sech}(\tau/\tau_0) e^{i\kappa z} \tag{2.60}$$

Higher order solutions to equation (2.58) have been discussed in [69] and [70]. Existence of temporal solitons in optical fibre was proposed in 1973 by Hasegawa and Tappert in [71]. Since then, many demonstrations of temporal solitons propagating over long distances have been demonstrated in [72, 73].

2.8.3 Small-scale filamentation

Small-scale filamentation, also known as beam breakup, is the breakup of an intense laser beam (with powers much higher than the P_{cr}) into multiple filaments, due to amplification of modulational instabilities and noise present in the optical wavefront by four-wave mixing [74]. The transverse intensity produced as a result may have a random distribution and reduced spatial coherence or may have highly regular pattern as shown in Fig. 2.18 [75]. Each of the filaments produced are al-

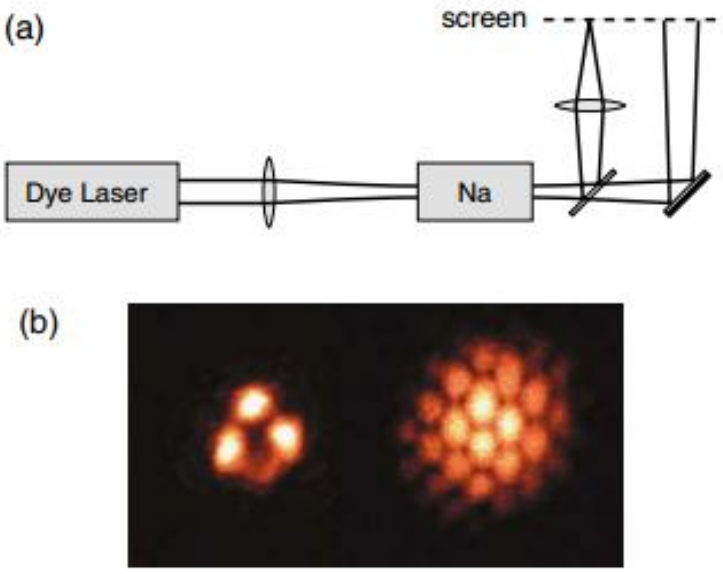

Figure 2.18: (a) Schematic of the experimental setup used in [75] (b) Honey-comb pattern obtained in far-field

most ideal solitons, have the cylindrically symmetric Townes profile and carry the power P_{cr} [76]. Fig. 2.19 illustrates the amplification process of wavefront perturbations. The field within the medium is composed of a strong on-axis component

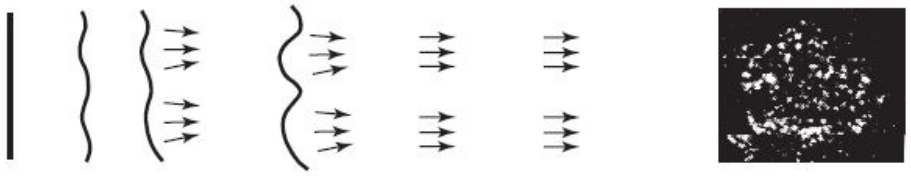

Figure 2.19: Amplification of wavefront perturbations to give multiple filaments

and weak, side-modes with non-collinear but symmetric k-vectors. The variation of gain coefficient of these side-modes with the magnitude of their wave-vectors is shown in fig. 2.20. The peak value of the gain-coefficient occurs when the four-wave mixing process is phase-matched. Beam breakup into multiple filaments have

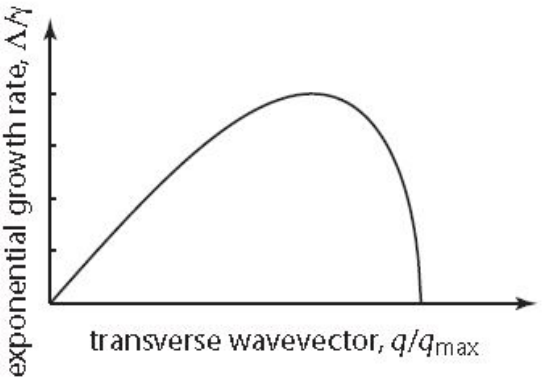

Figure 2.20: Gain coefficient of side-modes vs wavevectors

been reported by many groups in [77–83]. A possible application reported in [84] suggests that loss of spatial coherence can be used as a power limiter by reducing intensity at the focus.

2.9 Local field effects

The treatment described above for calculating susceptibilities was based on macroscopic Maxwell equations which considers the spatial average of microscopic electric fields. But the actual atomic transitions within the material are dependent on the local field which acts on the transition dipole moments associated with the material. For condensed matter, with atomic densities of the order of 10^{15}atoms/cm^3, the difference between the local-field and the macroscopic field becomes significant and local-field needs to be considered [85]. There are different models for performing local-field corrections depending on the optical medium under consideration. For a homogeneous medium, for example, we multiply the local field correction factor L to the macroscopic field to calculate the local field. Different models applied to calculate L are: (1) the Lorentz local-field model, (2) the Onsager model, and (3) the real-cavity model. The Lorentz model and the Onsager model are

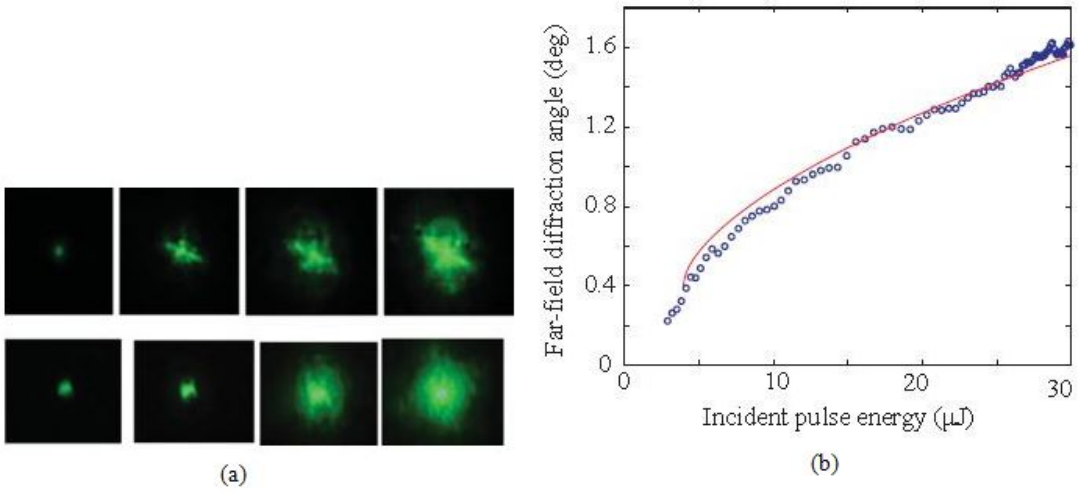

Figure 2.21: (a) Small scale filamentation in CS_2. Top: Near-field intensity distributions, Bottom: Far-field intensity distributions with increasing pulse energy from left to right (b) Farfield diffraction angle vs incident pulse energy showing a square root variation of the angle

applicable for homogeneous media, with Lorentz model used specifically for solids while Onsager model is used for polar liquids. The real-cavity model is used to describe composite materials [85]. The Lorentz model is the most commonly used model and is described in the following subsection.

2.9.1 Lorentz local field

The Lorentz-Lorenz law gives the following expression for the linear susceptibility [29]

$$\chi^{(1)} = \frac{N_0\alpha}{1-\frac{4\pi}{3}N_0\alpha} \quad \text{or} \quad \frac{\epsilon^{(1)}-1}{\epsilon^{(2)}+2} = \frac{4\pi}{3}N_0\alpha, \tag{2.61}$$

where N_0 is the number density of dipoles within the medium (assumed to be a rectangular lattice) and α is the polarizability for a single dipole. The local field is expressed as the sum of local field contributions for dipoles within the assumed cavity (with radius greater than dipole separation but less than optical wavelength), and the average macroscopic polarization for dipoles outside the cavity. Hence, the local field $\tilde{E}_{\text{loc}}$ is given (in gaussian units) by

$$\tilde{E}_{\text{loc}} = \tilde{E} + \frac{4\pi}{3}\tilde{P} \tag{2.62}$$

Since $\tilde{P} = \chi^{(1)}\tilde{E}$, the expression for local field is given by

$$\tilde{E}_{\text{loc}} = \frac{\epsilon^{(1)}+2}{3}\tilde{E}. \tag{2.63}$$

2.9.2 Nano-composite materials for nonlinear optics

Local-field effects can substantially boost the nonlinear response. For example, it was shown in [86] that the expression for the third-order susceptibility with

local-field effects taken into account is

$$\chi^{(3)}(\omega_k = \omega_l + \omega_m + \omega_n, \omega_l, \omega_m, \omega_n) = N_0 \gamma^{(3)}(\omega_k) L(\omega_k) L(\omega_l) L(\omega_m) L(\omega_n) \quad (2.64)$$

where N_0 is the number density of dipoles, $\gamma^{(3)}$ is the hyperpolarizability leading to the generation of the sum-frequency ω_k and the local field correction factor is given by $L(\omega_i) = [\epsilon^{(1)}(\omega_1) + 2]/3$.

Composite materials are made of two or more constituents with different susceptibilities, and they can alter the local field substantially depending on the choice of materials and the configuration. We can tailor these composites to exhibit the desired optical properties. In fact, the composite material can possess an enhanced nonlinearity that can even exceed those of individual materials. Especially important are nano-composite materials; these are nanoscale mixtures of different materials in which the individual particles are much smaller than the optical wavelength, but nonetheless are large enough so that they can be characterized by their own dielectric constants. Optical properties such as n_2 and $\chi^{(3)}$ of such materials are characterized by their effective or volume-averaged values. Some of the different geometries for these nano-composites are illustrated in Fig. 2.22. Some of these geometries are described in the following subsections.

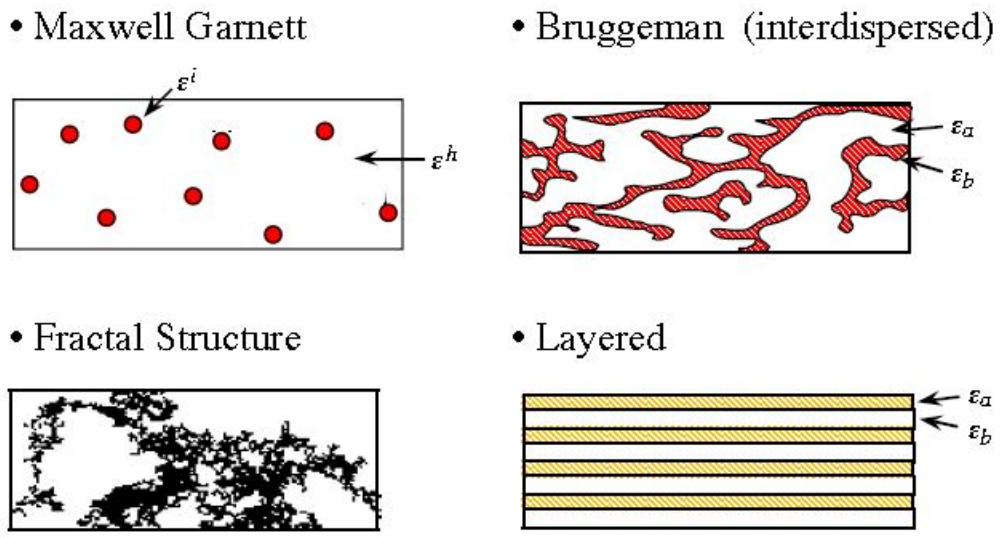

Figure 2.22: Examples of nanocomposite geometries that have been used to construct materials with enhanced nonlinear optical response [85]

Layered composite materials

An example of a material with a layered geometry is shown in Fig. 2.22. It is composed of alternating layers of materials, say a and b, that have different optical properties and different thicknesses, which are assumed to be much smaller than the optical wavelength. The structural properties of each constituent are assumed to be essentially the same as for a bulk sample of such a material. The optical properties of the composite structure are dependent on the volume average of each constituent. For example, to enhance the contribution of material a to the nonlinear optical response of the composite, material b, must have a larger

refractive index than material a. The enhancement of the $\chi^{(3)}$ response occurs as a result of the non-uniform distribution of the incident electric field between constituents a and b [87]. It was shown theoretically [88] that to have such an enhancement, the more nonlinear material, for instance material a, must have the smaller linear refractive index.

For p-polarized light incident on the layered composite, the effective permittivity ϵ_{eff} is given in terms of the volume fractions f_a and f_b and the permittivities of individual materials by [88]

$$\frac{1}{\epsilon_{\text{eff}}} = \frac{f_a}{\epsilon_a} + \frac{f_b}{\epsilon_b}. \tag{2.65}$$

Moreover, for the limiting case in which component b has a vanishingly small nonlinear response, the effective nonlinear response of the material becomes [88]

$$\chi^{(3)}_{\text{eff}} = \left|\frac{\epsilon_{\text{eff}}}{\epsilon_a}\right|^2 \left(\frac{\epsilon_{\text{eff}}}{\epsilon_a}\right)^2 f_a {\chi_a}^{(3)}. \tag{2.66}$$

For s-polarized light, the effective permittivities are

$$\epsilon_{\text{eff}} = f_a\epsilon_a + f_b\epsilon_b \quad \text{and} \quad \chi^{(3)}_{\text{eff}} = f_a\chi^{(3)}_a. \tag{2.67}$$

In [87], a layered geometry with alternating layers of titanium dioxide (material b) and the nonlinear optical polymer PBZT (material a) was investigated and a maximum enhancement of 35% of the third-order susceptibility was obtained which was experimentally measured in terms of the acquired nonlinear phase-shift by a propagating laser beam. In [89], the third-order susceptibility representing the electro-optic response of a layered composite material made of alternating layers of barium titanate and doped polycarbonate was investigated for different volume fill fractions. The predicted enhancement curve vs fill fraction of the polycarbonate is shown in Fig. 2.23b. One sees that an enhancement of the electrooptic response by a factor as large as 3.2 can be obtained.

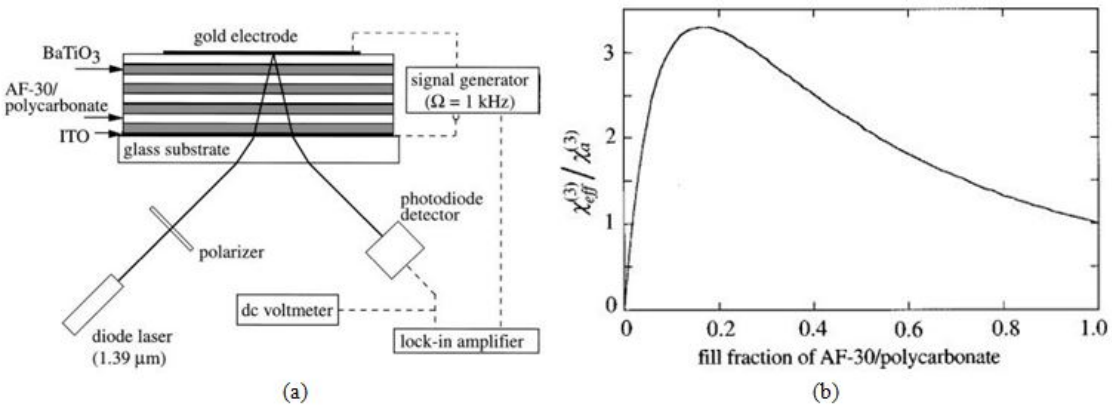

Figure 2.23: (a) Layered geometry and experimental setup used in [89], (b) Predicted susceptibility enhancement curve

Metal-Dielectric Photonic Crystals

Metals possess a very large and fast intrinsic nonlinear response. For example, the $\chi^{(3)}$ value of noble metals is 10^6 times higher than fused silica and has a sub-picosecond response [90]. However, it has proven difficult to access this nonlinearity due to high attenuation associated with metals. Due to this high attenuation, metals structures with a thickness larger than tens of nm are non-transmitting. Attempts to circumvent this high loss using local-field effects have been made by using colloidal metal nanoparticles [91], granular metal films [92], glasses doped with nanoparticles [90] and metal-dielectric composites in Maxwell-Garnett [93] and Bruggeman geometries [94], [95].

It has been shown [96] that a metal-dielctric photonic crystal (MDPC) can be highly transmissive within a certain controllable spectral range for metal thicknesses even larger than the skin depth. Such a MDPC was proposed [97] and demonstrated [48] as a nonlinear photonic material. It was argued [96] [97], that, since the large attenuation of light in metals is more due to re-radiation than absorption, a method akin to Bragg reflection can be employed to redirect the light in the forward direction. Figs. 2.24a and 2.24b compare the electric field distribution within a bulk Cu sample of thickness 40 nm and a MDPC with alternating layers of gold and silica of thicknesses 16 nm and 98 nm respectively, having resonance at 650 nm. Due to the resonance nature of the structure, the nonlinearity was measured in terms of the fractional change in nonlinear transmission and reflection and the comparison with bulk metal values are shown in Figs. 2.24c and 2.24d.

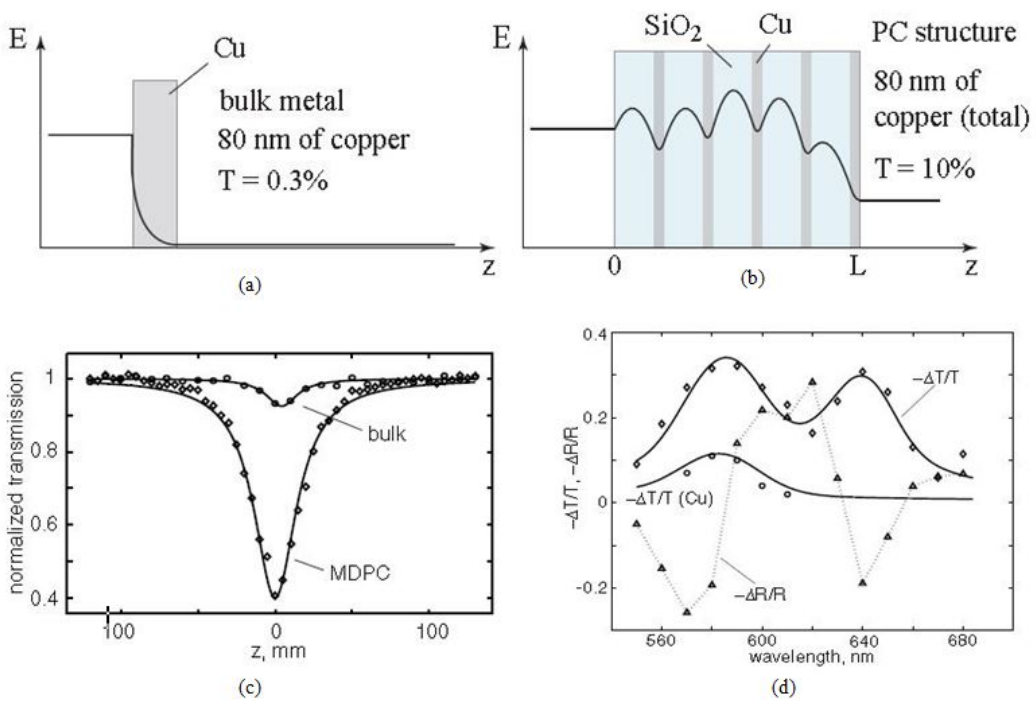

Figure 2.24: (a) Electric field distribution within bulk copper, (b) electric field distribution within the MDPC, (c) normalized transmission measured for bulk copper and the MDPC using the z-scan method, and (d) measured fractional nonlinear change in reflection and transmission for bulk copper and for the MDPC.

2.9.3 Counter-intuitive consequence of local-field effects

In ref. [98], it was demonstrated that local-field effects can be used for sign reversal of the nonlinear absorption process. A colloid of metal nanoparticles in a glassy matrix showed saturable absorption, due to local-field correction even though the metal and glass themselves showed induced absorption. For a composite material consisting of a host material h (with permittivity ϵ_h) and inclusions i (with permittivity ϵ_i) the effective permittivity of the medium as a whole can be written in terms of the fill-fraction f of the inclusions

$$\epsilon = \epsilon_h \frac{1+2\eta f}{1-\eta f} \tag{2.68}$$

where

$$\eta = \frac{\epsilon_i - \epsilon_h}{\epsilon_i + 2\epsilon_h} \tag{2.69}$$

The third-order susceptibility can be written as

$$\chi^{(3)} = f {q_i}^2 |q_i|^2 {\chi_i}^{(3)} + {q_h}^2 |q_h|^2 \left[(1-f) + xf\right] {\chi_h}^{(3)} \tag{2.70}$$

where

$$x = \frac{8}{5}\eta^2|\eta|^2 + \frac{6}{5}\eta|\eta|^2 + \frac{8}{5}\eta^3 + \frac{18}{5}(\eta^2 + |\eta|^2) \tag{2.71}$$

q_i and q_h are the local-field factors for the host and inclusions respectively and are given by

$$q_i = \frac{\epsilon + 2\epsilon_h}{\epsilon_i + 2\epsilon_h} \tag{2.72}$$

$$q_h = \frac{\epsilon + 2\epsilon_h}{3\epsilon_h} \tag{2.73}$$

For small fill-fractions, $\epsilon \simeq \epsilon_h$ and $q_h \simeq 1$. So the effective $\chi^{(3)}$ becomes

$$\chi^{(3)} = f {q_i}^2 |q_i|^2 \chi_i^{(3)} + \chi_h^{(3)} \tag{2.74}$$

Even though the sign of both contributions to $\chi^{(3)}$ is the same, we can have cancellation of the two at surface-plasmon resonance due to the condition

$$\mathrm{Re}[\epsilon_i(\omega_s)] = -2\mathrm{Re}[\epsilon_h] \tag{2.75}$$

where ω_s is the surface plasmon resonance frequency. The local-field factor for the inclusions, q_i, then becomes purely imaginary since $q_i \approx 3\mathrm{Re}[\epsilon_h]/i\mathrm{Im}[\epsilon]$. Thus, at the surface plasmon resonance, ${q_i}^2 < 0$. If $\chi_i^{(3)}$ and $\chi_h^{(3)}$ have the same sign, for a particular fill-fraction f we have sign reversal of $\chi^{(3)}$.

Physically, we have a phase-difference between the field within inclusion and the externally applied field which is essentially given by the phase of q_i. This phase-difference becomes $\pi/2$ at surface plasmon resonance making q_i imaginary. This phase-shift occurs due to coupling of the p-polarized component of incident light with arbitrary polarization into surface-plasmons at resonance. If $\chi_i^{(3)}$ and $\chi_h^{(3)}$ have the same sign, the sign-reversal occurs at two fill-fractions f, as can be seen from equation (2.74). But only the lower fill-fraction is feasible as higher values of f lead to higher nonlinear absorption. In [98], a colloid of

gold in $1,1',3,3,3',3'$-hexamethylindotricarbocyanine iodide (HITCI) (a reverse-saturable absorber), methanol and water showed this sign-reversal in Im$[\chi^{(3)}]$ which can be seen in Fig. 2.25 showing open-aperture Z-scan traces. Curves 1-5 have a valley indicating reverse-saturable absorption, whereas 6-9 have a peak, showing saturable absorption.

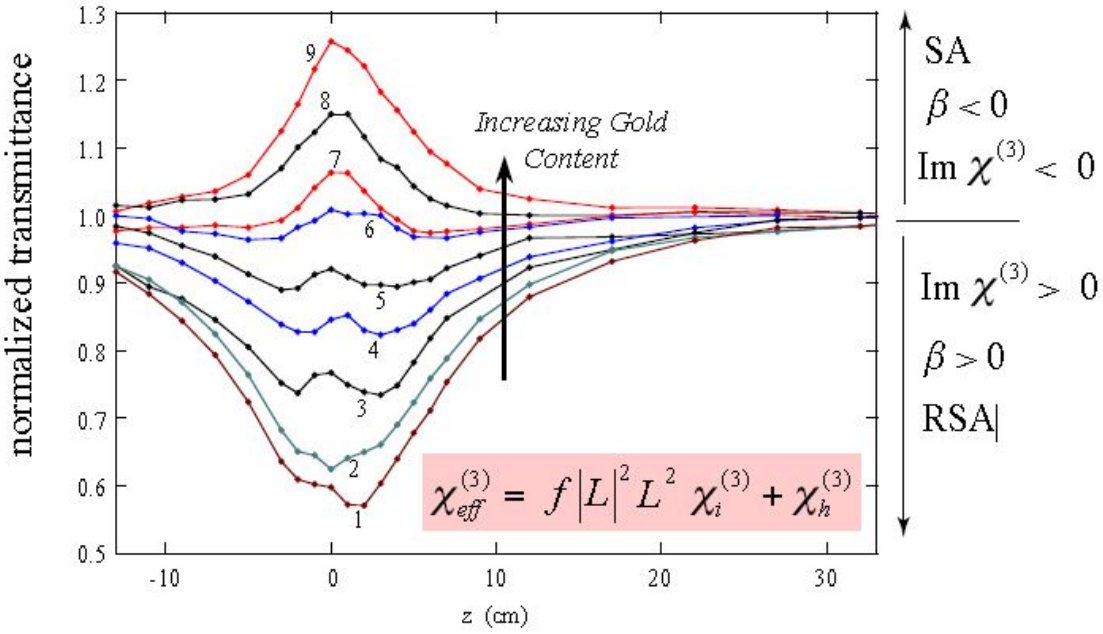

Figure 2.25: Normalized transmission curves obtained from Z-scan measurements showing reversal of the sign of Im$[\chi^{(3)}$.

2.10 Nonlinear Plasmonics

Reasons for using plasmonic response in the context of nonlinear optics and photonics include the following:
(1) Strong local-field enhancement: Surface plasmon polaritons (SPP) and localized surface plasmons (LSP) can provide very strong local field enhancements [99].
(2) Ultrafast response: Plasmonic excitations can respond on the scale of femtoseconds, making ultrafast signal processing possible [100].
(3) Plasmon resonances are very sensitive to the dielectric constant of surrounding media [101]. This fact allows for the tailoring of the plasmonic response.
(4) Sub-wavelength dimensions: At the nanoscale, plasmonic structures have very sub-wavelength dimensions and phase-matching is not important. Thus the nonlinear optical signal is emitted in all directions, irrespective of the propagation direction of the incident field and is incoherent [102].

Limiting factors to plasmonic responses are ohmic and radiative losses, which not only reduce the propagation length of SPP but also the local-field enhancement. SHG using plasmonic structures has been achieved using different configurations. The very first example employed SHG from surface enhancement using roughened silver surfaces [103] where there was considerable enhancement of the SHG signal compared to a flat surface. Other methods employing surface en-

hancement have been reported in [104, 105]. Third-harmonic generation due to surface enhancement has also been reported in [106]. SHG from individual nanoparticles such as gold nano-spheres [107], nano-cones [108], nano-apertures [109] and nano-cups [110] have also been reported. Structured plasmonic surfaces which are non-centrosymmetric like arrays of split ring resonators (SRR) [111], arrays of L-shaped nano-antennas [112] have also been reported to have enhanced SHG.

The intrinsic nonlinear response of SPPs has been explored [113] for gold films. These results showed a strong wavelength dependence of the nonlinear refraction as well as increase in the nonlinear absorption with larger pulse durations. This increase in nonlinear absorption was attributed to the 'hot-electron' effect or 'Fermi-smearing' mechanism, which is a kind of thermal effect with a sub-picosecond response.

2.11 Slow and fast light

The group velocity of light is the velocity of propagation of the envelope of a light pulse. It can be represented mathematically as $v_g = c/n_g$ where we have introduced the group index [114]

$$n_g = n + \omega \frac{dn}{d\omega}, \tag{2.76}$$

where n is the refractive index and ω is the frequency of light. The phase velocity is the velocity with which points of constant phase of an optical field propagate within the medium and is equal to c/n. When light propagates in a medium for which the group velocity v_g is much smaller than the speed of light in vacuum, that is, for $v_g \ll c$, the phenomenon is called slow light. Fast light occurs when the group velocity becomes larger than c, which is also called superluminal propagation, or when v_g is negative, which is also known as backward propagation. From the expressions for the group index and group velocity, it is clear that a higher group index results in a lower group velocity, which is possible if the value of $dn/d\omega$ is large and positive, which is possible in the case of normal dispersion. For fast light, $dn/d\omega$ must be large and negative, which is possible for anomalous dispersion [115] [116]. Thus, resonant systems having an absorption (gain) resonance can be used to achieve slow (fast) light. To examine this argument more fully, let us consider the plots of the absorption, gain α and refractive index n vs ω as shown in Fig. 2.26. The motivation is distortion-free propagation of pulses through media with different group indices. At the resonance, the absorption (gain) has a maxima and due to Kramers-Kronig relations, the refractive index makes a transition from maxima (minima) to minima (maxima). This steep transition results in a large value of $dn/d\omega$ and consequently in a lower or higher group velocity depending on the sign of $dn/d\omega$. For resonances in an atomic vapor, this group index can become as large as 10^4. But close to resonance the absorption also becomes large, and the slow (fast) is no longer easily measurable. The first experimental observation of slow light and fast light in resonant systems with negligible pulse distortion was by Carruthers and Bieber in 1969 [117]. But these results were limited by the presence of strong resonant absorption. To counteract the effect of large absorption, many schemes have been employed such as electromagnetically induced transparency (EIT) [118], coherent population oscillation

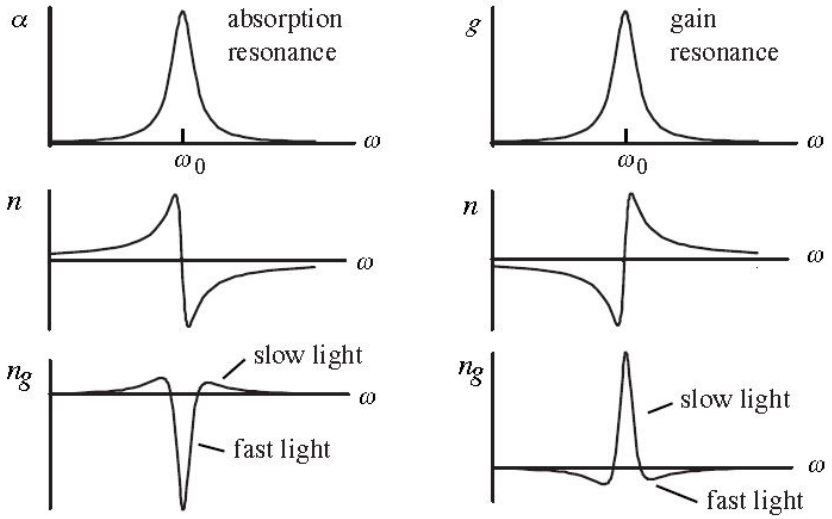

Figure 2.26: Dispersion curves for absorption and gain resonances

(CPO) [119, 120], stimulated Brillouin scattering (SBS) [121–123], stimulated Raman scattering (SRS) [124] and couple resonator optical waveguides (CROWs) [125]. A very important experiment using Bose-Einstein condensates achieved slow light with group velocity of 17m/s using EIT [118]. EIT was first described theoretically by Harris et al. [126] and is a technique in which, under the influence of a large saturating optical field, the material is rendered transparent to resonant laser light. In the experiment of Hau et al. [118], the nanokelvin temperatures of the sample caused reduced Doppler broadening making the dispersion curve very steep leading to such a low group velocity. EIT was also used later by Budker et al. in a Rb vapor cell to achieve group velocities as low as 8m/s [127]. Smilar technique was used later to achieve "stopped-light" [128].

Similarly, electromagnetically induced absorption has been used to achieve superluminal propagation, or fast light in [129] with group velocity of $-c/23\,000$. Since slow light has possible applications for tunable optical delays, optical memories, and data storage, a slow light source at room temperature is desirable. Some techniques to achieve slow-light at room temperatures are described in the following subsections.

2.11.1 Slow light using SBS

Slow light using SBS in single-mode optical fibres at telecommunication wavelengths has been demonstrated [121, 123]. In this case, we have counter-propagating signal waves (ω) and pump waves (ω_p) within the fiber, and the maximum delay is produced when the signal frequency corresponds to Brillouin resonance frequency, i.e. $\omega = \omega_p - \Omega_B$, where Ω_B is the Brillouin frequency. Due to a lowered group velocity, one observes a delay in the pulse propagation time, which can be adjusted by varying the intensity I_p of the pump beam. The SBS process is a gain process in which the generated Stokes wave undergoes amplification by means of its coupling with the pump wave and an acoustic through an acoustic wave [29], [70]. Mathematically, the signal intensity variation with pump and signal is expressed

as

$$\frac{dI_s}{dz} = -gI_sI_p \quad \text{where} \quad g = g_0\frac{(\Gamma_B)}{\Gamma_B + 2i(\omega - \omega_p)}. \tag{2.77}$$

Here g is the complex gain factor associated with the SBS process. The nonlinear refractive index n_2 thus depends on the imaginary part of g from which the propagation vector, k_s, and subsequently the group velocity can be calculated as $v_g = (dk_s/d\omega)^{-1}$. The transit time difference for a medium of length L can be subsequently calculated, as discussed in ref [115]. Fig. 2.27 shows the temporal evolution of Stokes pulses for a given gain value and different pulse lengths. There are several limiting processes that limit the observed delay, such as higher-order dispersion effects for very short pulse lengths, gain saturation for very high input Stokes pulse intensities, and spontaneous Brillouin scattering for very high gain values.

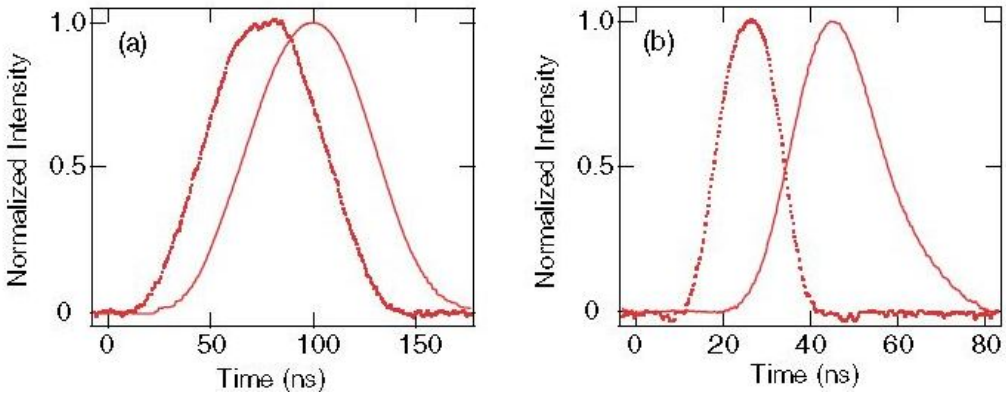

Figure 2.27: Temporal evolution of Stokes pulses for (a) 63 ns duration pulse, (b) 15 ns duration pulse

2.11.2 Slow light by coherent population oscillations

Coherent population oscillations are a quantum effect that lead to the creation of a spectral hole in the absorption profile of a probe beam passing through an appropriate medium. These population oscillations are a periodic modulation of the ground state populations at the beat frequency δ between the pump and probe waves. For $\delta \leq (1/T_1)$, with T_1 being the population relaxation time, these population oscillations have a significant magnitude. This method of introducing a spectral hole in a homogeneously broadened absorption spectrum was first predicted by Schwartz and Tan in [130] and was demonstrated by Hillman et al. for the case of a ruby crystal pumped by an Ar ion laser [131]. Slow light using this method of introducing a spectral hole was demonstrated in a ruby crystal where group velocities as low as 57.5 $\pm$ 0.5 m/s was observed in [120]. Here, a laser input at 514.5 nm from an Ar ion laser with pulse duration of the order of 1 ms was amplitude modulated to create frequency shifted pump beams which were then focussed tightly within the crystal. A vary narrow spectral hole of linewidth (HWHM) 35.8 Hz was observed which broadens with increased power. It is this narrow dip in the absorption profile that leads to very large values of $dn/d\omega$ and

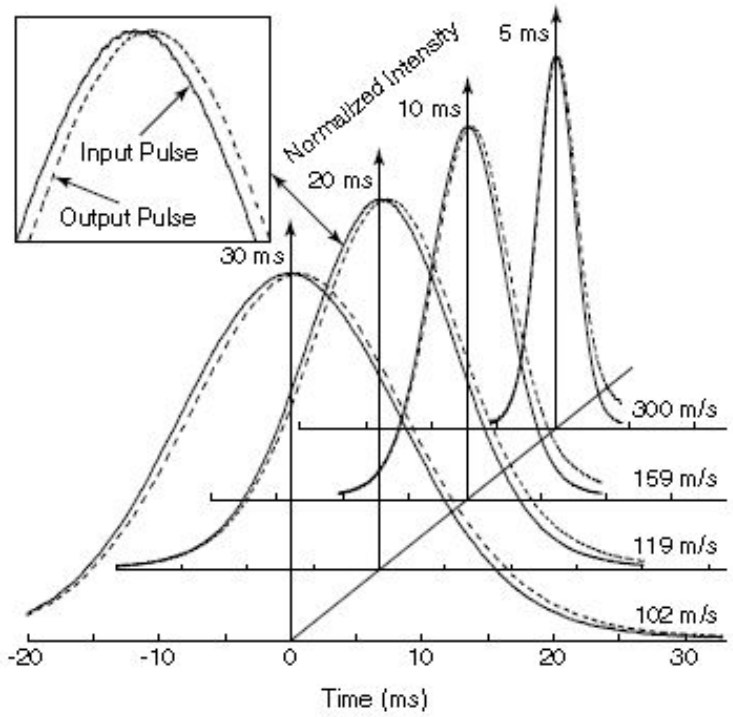

Figure 2.28: Normalized input and output pulse intensities for different pulse durations

hence very low group velocities. Fig. 2.28 shows the different pulse delays with increased pulse durations.

Coherent population oscillations have also been used to achieve superluminal propagation in alexandrite due to formation on an anti-hole (increased absorption in a narrow spectral region) [119]. The superluminal response obtained in laboratory is shown in Fig. 2.29.

2.11.3 Slow and fast light in Erbium-Doped Fibre Amplifiers (EDFAs)

Slow and fast light has been successfully demonstrated [122] using the nonlinear optical response of EDFAs. The mechanism is that of coherent population oscillations (CPOs) involving the erbium ground-state population. Because of the widespread use of EDFAs in telecommunications, a slow light source using EDFA has many potential important applications. Also, the use of fibre allows longer interaction lengths causing even larger delays. The width of the spectral hole is determined by the frequency of the population oscillations. Fig. 2.30 shows the dependence of the fractional pulse advancement on both modulation frequency and on laser power.

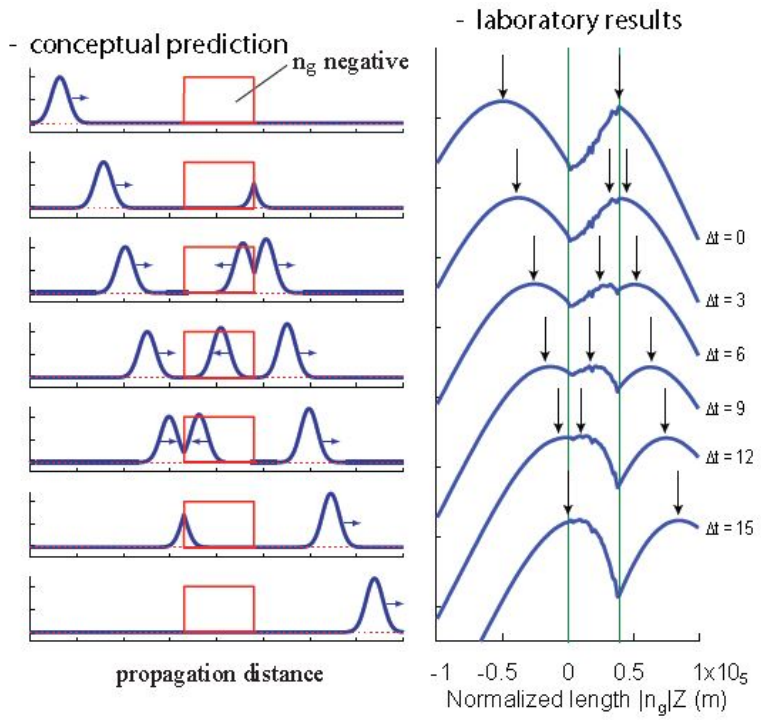

Figure 2.29: Left: Conceptual prediction of superluminal propagation; Right: Laboratory results of Bigelow et al. (2003). [119].

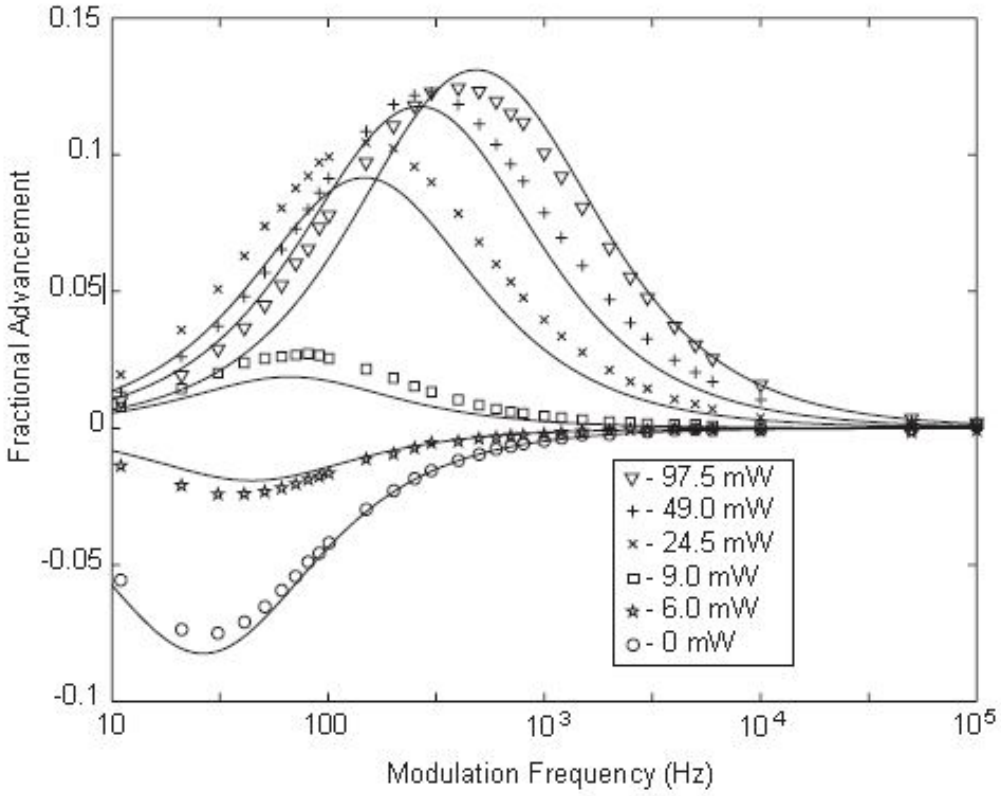

Figure 2.30: Dependence of fractional pulse delay after propagation through EDFA on the pump frequency and power

2.12 Spontaneous and stimulated light scattering

Until now, we have dealt with parametric processes which involve light-by-light scattering. We will now discuss inelastic scattering of light by various material media. Light scattering occurs due to fluctuations and inhomogeneities in optical properties of the medium. A completely homogeneous medium cannot scatter light into directions other than the exact forward direction, as a consequence of complete destructive interference that occurs in other directions [132]. Scattering into the forward direction is fully coherent and is the origin of the index of refraction [133]. Fig. 2.31 illustrates this concept where we see that if the density of the material is

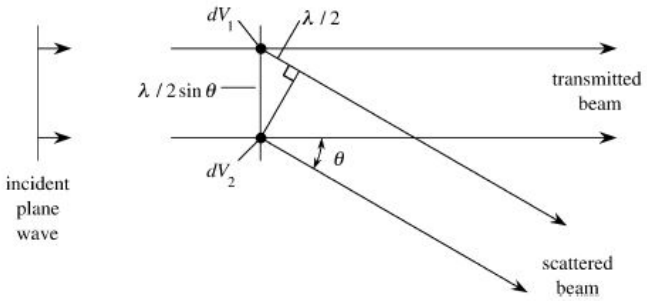

Figure 2.31: Light scattering in a material medium.

uniform, the contribution due to molecules in volume dV_1 exactly cancels that due to molecules in dV_2 in all other directions except forward, while for a non-uniform material density, these contributions do no exactly cancel out. Light scattering can be classified as stimulated or spontaneous depending on whether or not the fluctuations responsible for the scattering are induced by the incident laser field. Let us next consider the most general case of a light scattering experiment as

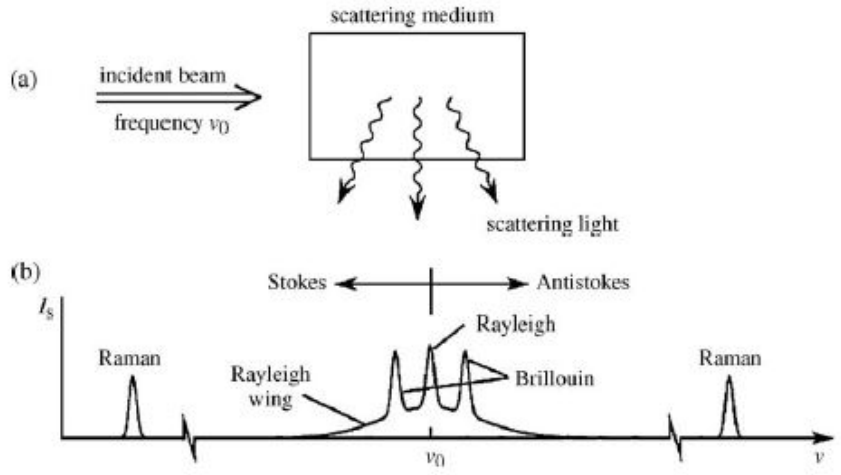

Figure 2.32: (a) A general light scattering experiment, (b) Spectrum of the scattered light showing source of various frequency components

shown in Fig. 2.32a. When we examine the spectrum of the scattered light, as shown in Fig. 2.32b, we find contributions from different scattering mechanisms

such as Rayleigh, Raman, Brillouin and the distant wing of the Rayleigh line. The frequency components of scattered light which are lower (higher) than that of the incident field are called Stokes (anti-Stokes) [29]. Raman scattering occurs due to interaction of light with the vibrational modes of molecules of the medium and is equivalent to scattering from optical phonons. Brillouin scattering occurs due to scattering of light from propagating density waves or sound waves and is equivalent to scattering from acoustic phonons. Rayleigh scattering on the other hand occurs due to static or non-propagating density fluctuations and is quasi-elastic in nature as it induces no frequency-shift. Rayleigh-wing scattering occurs in anisotropic molecules due to fluctuations in molecular orientation and due to a very rapid reorientation of molecules, has a very broad spectrum. The table shown below states the typical linewidth, frequency-shifts, relaxation times and gain for the different light scattering processes.

Table 2.3: Typical values of parameters for different light scattering processes

Process	Shift (cm^{-1})	Linewidth (cm^{-1})	Relaxation Time (sec)	Gain (m/MW)
Raman	1000	5	10^{-12}	$5X10^{-5}$
Brillouin	0.1	$5X10^{-3}$	10^{-9}	10^{-4}
Rayleigh	0	$5X10^{-4}$	10^{-8}	10^{-6}
Rayleigh-wing	0	5	10^{-12}	10^{-5}

2.12.1 Stimulated light scattering

Spontaneous light scattering is a weak process and the efficiency is quite low even for condensed matter. Stimulated processes on the other hand can be highly efficient. Also, the emission from spontaneous scattering is in the form of a dipole, while that for a stimulated light scattering is in the form of a narrow cone in the forward or the backward direction [29]. Conceptually, there are two separate configurations for studying stimulated light scattering [29]:

(1) The generator configuration: In this case, only the pump beam is applied externally to the scattering medium, and the Stokes signal wave and phonon wave are created from noise within the medium. This process is shown in Fig. 2.33a. For stimulated Brillouin scattering (SBS), the Stokes wave is amplified in all directions except in the exact forward direction, although it is usually observed only in the backward direction due to maximum spatial overlap with the pump in this case. Conversely, for stimulated Raman scattering (SRS), the Stokes signal is emitted in both the forward and backward directions.

(2) The amplifier configuration: In this configuration, as shown in Fig. 2.33b, both the pump and a weak Stokes seed signal are applied externally to the medium, and both the Stokes signal and the phonon waves are amplified. A strong coupling between the Stokes beam and pump occurs only when the frequency of the seed is close to the Stokes frequency of the generator case. Hellwarth in [134] has explained the fundamental relation between spontaneous and stimulated light scattering in terms of the photon occupation numbers in different field modes. He argues that the probability per unit time P_S for a photon to be emitted into Stokes mode S is given by

$$P_S = Dm_L(m_S + 1), \tag{2.78}$$

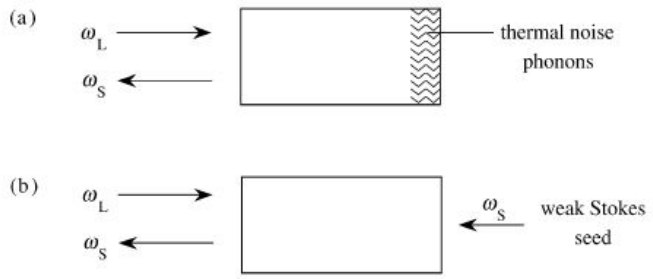

Figure 2.33: (a) Generator configuration for SBS; (b) amplifier configuration for SBS.

where m_L is the mean number of photons per mode in the incident laser field, m_S is the number of photons in the Stokes mode and D is the proportionality constant that depends on the physical properties of the medium. From this assumption, one can deduce that the rate of change of the number of photons in a given Stokes mode for a wave traveling in the positive z direction with velocity c/n is given by

$$\frac{dm_S}{dz} = \frac{1}{c/n} D m_L (m_S + 1) \tag{2.79}$$

For the case of spontaneous emission, the occupation number in Stokes mode can be assume to be much smaller than unity and the solution of Eq. (2.79) becomes

$$m_S(z) = m_S(0) + \frac{1}{c/n} D m_L z \tag{2.80}$$

Hence, the Stokes intensity increases linearly with the length of the Raman medium. For the case of stimulated scattering, the number of photons contained in the Stokes mode can be assumed to be much larger than unity, which leads to the prediction

$$m_S(z) = m_S(0) e^{Gz} \quad \text{where} \quad G = \frac{D m_L}{c/n} \tag{2.81}$$

where G is the Raman gain coefficient. Thus, the Stokes intensity for a stimulated scattering case increases exponentially with z. The significance of this result is that Hellwarth was able to obtain an equation that relates the gain coefficient G of the stimulate process to the quantity D that quantifies the efficiency of the spontaneous process. For this reason, Hellwarth's result is sometimes said to show that for any spontaneous light scattering process there is a stimulated analog.

Stimulated Brillouin scattering (SBS)

Spontaneous Brillouin scattering was first predicted theoretically in 1918 by Mandelstam [135] and then later independently by Brillouin [136] in 1922. Gross [137] provided the first experimental evidence of Brillouin scattering in crystals and liquids. Fig. 2.34 shows the scattering of an incident laser beam of frequency ω_L with a travelling pressure (or density wave) i.e. a sound wave of frequency Ω. Due to the acoustic wavefronts travelling away from the incident laser wave, the scattered light is shifted downward in frequency leading to a Stokes wave with frequency $\omega_S = \omega_L - \Omega$. The interference of this pump wave and the Stokes wave

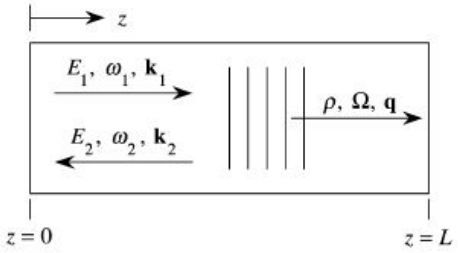

Figure 2.34: Scattering of an incident laser beam with sound wave

leads to a wave of frequency $\omega_L - \omega_S$ which is of course equal to Ω and thus the acoustic wave is reinforced. This acoustic wave further beats with the incident laser field leading to Stokes wave and so on. This situation leads to a kind of positive feedback system which under proper circumstances leads to amplification of both the Stokes wave and the acoustic wave exponentially [29]. There are two different mechanisms for Stokes wave amplification due to the acoustic wave and the laser field:
1) Electrostriction: In the presence of a high optical intensity, materials have the tendency to become more compressed, leading to increased density. Here, the interference between the Stokes wave and the laser field leads to fringes of high and low light intensity which show density variation due to electrostriction and hence lead to a propagating density wave or acoustic wave.
2) Optical Absorption: In regions of high optical intensity, heat generation can cause material expansion leading to decreased density on those regions. This process also leads to the generation of an acoustic wave.

Let us consider the case of an SBS generator as shown in the Fig. 2.33a. From the phonon dispersion relation $\Omega_B = |q_B|v$ and momentum conservation, we get the expression for Brillouin frequency as

$$\Omega_B = \frac{\frac{2v}{c/n}\omega_1}{1 + \frac{v}{c/n}} \tag{2.82}$$

Since nv/c is very small for most cases, we can approximate the Brillouin frequency as

$$\Omega_B = \frac{2v}{c/n}\omega_1 \tag{2.83}$$

For the case of an SBS amplifier, the Stokes frequency ω_2 is determined by the laboratory settings and the acoustic wave frequency is given by $\Omega = \omega_1 - \omega_2$. In a sense the Stokes frequency ω_2 is arbitrary, but the acoustic wave is efficiently excited only when the Stokes seed frequency is chosen such that Ω lies within the Brillouin linewidth Γ_B. If we consider the coupled-amplitude equations for the SBS amplifier case, we see that there is no phase-mismatch term, indicating that SBS is a pure gain process and is automatically phase-matched. Hence, we can write the coupled-intensity equations as

$$\frac{dI_1}{dz} = -gI_1I_2 \tag{2.84}$$

$$\frac{dI_2}{dz} = -gI_1I_2 \tag{2.85}$$

where g is the SBS gain factor given by

$$g = g_0 \frac{(\Gamma_B/2)^2}{(\Omega_B - \Omega)^2 + (\Gamma_B/2)^2}, \qquad g_0 = \frac{\gamma_e^2 \omega_2}{nvc^3 \rho_0 \Gamma_B}. \tag{2.86}$$

For a constant pump intensity, the output intensity for a medium of length L is given by

$$I_2(z) = I_2(L) e^{gI_1(L-z)} \tag{2.87}$$

Stimulated Raman scattering (SRS)

C.V. Raman discovered the spontaneous Raman scattering in 1930 [138]. Stimulated Raman scattering occurs when the incident optical field within a medium interacts with the vibrational modes of molecules. Let us consider the simplest, classical explanation of SRS as discussed in [139], where each vibrational mode is described by a simple harmonic oscillator with time-varying internuclear distance as $\tilde{q}(t)$, resonance frequency ω_v, damping constant γ and equilibrium inter-nuclear separation as q_0. The equation of motion can be written as

$$\frac{d^2\tilde{q}}{dt^2} + 2\gamma \frac{d\tilde{q}}{dt} + {\omega_v}^2 \tilde{q} = \frac{\tilde{F}(t)}{m} \tag{2.88}$$

with $\tilde{F}(t)$ being the restoring force and m the reduced nuclear mass. It is assumed that the optical polarizability depends on the inter-nuclear separation $\tilde{q}(t)$ according to

$$\tilde{\alpha}(t) = \alpha_0 + \left(\frac{\partial \alpha}{\partial q}\right)_0 \tilde{q}(t) \tag{2.89}$$

where α_0 is the equilibrium polarizability. Oscillations in the molecular coordinate $\tilde{q}(t)$ lead to periodic modulations in the polarizability with time which in turn leads to variation in the refractive index with time as

$$\tilde{n}(t) = \sqrt{\tilde{\epsilon}(t)} = [1 + N\tilde{\alpha}(t)]^{1/2} \tag{2.90}$$

This modulation in refractive index with time forms frequency sidebands on the transmitted light with frequency $\pm\omega_v$. These frequency sidebands then beat with the incident laser field to generate a Stokes wave with frequency $\omega_S = \omega_L - \omega_v$ and modulate the intensity at the same frequency. This modulated intensity in turn coherently excites the molecule to oscillate at ω_v. From the expression for the polarizability α in equation (2.89), we can derive the expression for Raman susceptibility which is given by

$$\chi_R(\omega_S) = \frac{\epsilon_0 (N/6m) (\partial\alpha/\partial q)_0^{\,2}}{{\omega_v}^2 - (\omega_L - \omega_S)^2 + 2i(\omega_L - \omega_S)\gamma} \tag{2.91}$$

The real and imaginary parts of Raman susceptibility are shown in Fig. 2.35. The valley of the imaginary part of susceptibility denotes the Raman resonance.

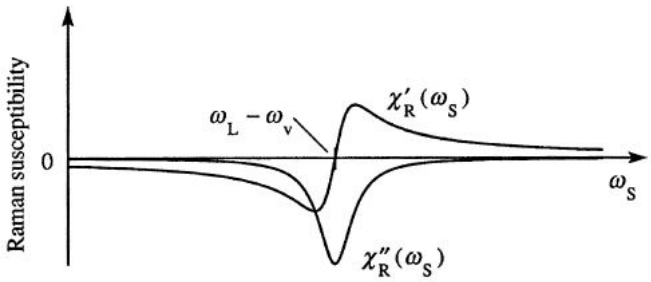

Figure 2.35: Real and imaginary parts of Raman susceptibility

2.13 Summary

This chapter is supposed to provide a brief pedagogical overview of the basic principles of nonlinear optics and highlight some of the recent advances in the area. We started off with the general expression for polarization including the nonlinear components. Then we discussed parametric processed due to second-order and third-order nonlinearities. We developed coupled mode equations for second-order effects like SHG and discussed the importance of phase-matching and the different ways to achieve it. Then we briefly discussed the various third-order nonlinear effects like THG and the intensity dependent refractive index. We subsequently discussed self-action effects arising due to the intensity dependent refractive index. A brief review of spatial and temporal solitons was provided later along with results from some of the current research in the field.

We also discussed the origins of optical nonlinearities like molecular orientation and thermal effects and ways to measure them using Z-scan techniques. Local field corrections were also discussed along with some recent research to enhance nonlinear response using composite materials due to these local-field effects. Later, getting slow light and fast light using nonlinear properties like SBS were discussed. Last but not the least, non-parametric nonlinear effects such as stimulated and spontaneous Raman scattering and Brillouin scattering were discussed.

Part II

Superradiance and its plasmonic counterpart

Chapter 3

Superradiance

3.1 Introduction

Superradiance is a co-operative many-body effect in a collection of N emitters which results in the emission of radiation in the form of a pulse with intensity proportional to N^2 and a lifetime which is proportional to $1/N$. It is coherent resonant emission from multiple emitters and was first discussed by Bloembergen and Pound in the context of nuclear magnetic resonance [86]. It was Robert Dicke who first described this concept with a more general approach in his seminal paper published in 1954 [3]. According to him, *when a collection of resonant emitters (molecules, atoms or quantum dots) radiates spontaneously such that the total energy is emitted as a very short pulse, whose decay time is much shorter than for the case of independently emitting radiators, and whose peak power is much larger than that of the independently emitting radiators, the system is called superradiant.* The emission occurs in a well defined direction depending on the geometry of the system and the emitters become spontaneously phase-locked after excitation with a coherent pulse. In the dipole approximation, this phase-locking would imply the existence of a macroscopic dipole moment which is a sum of the individual dipole moments of the emitters.

Bonifacio and Luigiato in [4] distinguish between superradiance and the similar collective process of 'superfluorescence' on the basis of whether this correlation exists at the beginning of the process (at time $t = 0$) or not. If the emitters are completely uncorrelated at the beginning, and the correlation builds up as the system evolves and a macroscopic dipole moment emerges, the process is termed *superfluorescence*. This gradual emergence of correlations, due to interactions of the emitters with the field, makes the process inherently quantum in nature and no completely classical description is possible. Superradiance, on the other hand, is the case where a macroscopic dipole moment already exists at the beginning and the system evolves with the gradual radiative decay of these emitters. This

process can be described by a completely classical model. It is simply N dipoles oscillating in phase. But both these terms have been used somewhat interchangeably, particularly when talking about collective effects in systems such as atomic vapor. In our work, although we are only concerned with the classical picture, a brief description of the quantum picture is important in order to introduce Dicke's original formalism.

3.2 Mathematical models

The problem of mathematically modelling superradiance has been treated with quantum electrodynamics, semi-classical and classical approaches in [3, 5–7]. Although a realistic superradiance experiment is affected by a number of spurious effects such as collision and inhomogeneous broadening, dipole-dipole dephasing and nonlinear propagation effects [5], these simple theoretical models provide a lot of insight into the actual process and hence will be summarized in the proceeding sections. There are two distinct regimes in which we can discuss superradiance depending on the volume V in which the emitters are confined:
(a) $V < {\lambda_0}^3$, where λ_0 is the resonance wavelength of a single emitter, or the case where each emitter is within a resonance wavelength away from each other, and
(b) $V > {\lambda_0}^3$.
The analysis of case (b) follows directly from (a) by including propagation terms $e^{i\mathbf{k}.\mathbf{r}}$ with the operators. Hence we deal with case (a) first.

3.2.1 Quantum electrodynamic model for N emitters confined within a volume $V < {\lambda_0}^3$

We make the following assumptions in order to simplify the analysis without compromising on the essential features of the process:
(1) *All molecules/atoms/emitters are identical.*
(2) *The electric field is assumed to be spatially non-varying along the dimensions of the molecule/atom/emitter, which is also the dipole approximation.*
(3) *Dipole-dipole interaction will be ignored.* (This exclusion becomes important later on when we discuss superradiance in plasmonic systems.)
(4) *The wave-functions of the system of N atoms is symmetric with respect to permutations of emitters or the interchange of emitters.* It was shown in [140] using group theory that the wave function of the combined superradiative state is completely symmetric with respect to the interchange of particles. If the wave-function were to be anti-symmetric, it would correspond to a state which does not decay at all.

(5) *We consider that the atoms/emitters interact with all the modes of the radiation field.* Only two energy levels in the emitter/atom that interact with the cavity field are considered: (i) the ground state $|g\rangle$ and (ii) the excited state $|e\rangle$. The energy difference between the two levels is $\hbar\omega_0$.

Spontaneous emission from a single atom within a cavity of volume V

The Jaynes-Cummings model describes spontaneous emission from a single two-level atom confined within a cavity of volume V (also the quantization volume for the electric field) [141]. The total electric-field within this cavity is a vector sum of the single-mode cavity fields for different modes $(\vec{k}, \Lambda)$ (here Λ stands for polarization of the field and is also the polarization of the $|e\rangle \rightarrow |g\rangle$ transition) is

$$\hat{\mathbf{E}}(\mathbf{r}, t) = \sum_{\mathbf{k},\Lambda} \mathbf{e}_\Lambda \Big(\frac{\hbar\omega_k}{\epsilon_0 V}\Big)^{1/2} (\hat{a}_k(t) e^{i\mathbf{k}.\mathbf{r}} + \hat{a}_k^\dagger(t) e^{-i\mathbf{k}.\mathbf{r}}). \tag{3.1}$$

Here $\mathbf{e}_\Lambda$ is the polarization vector, $\hat{a}_k$ and $\hat{a}_k^\dagger$ are the annihilation and creation operators respectively, and $\omega_k = k/c$ is the angular frequency of the k-th plane-wave component. The time-evolution of the operators $\hat{a}_k$ and $\hat{a}_k^\dagger$ are given by

$$\hat{a}_k(t) = \hat{a}_k(0) e^{-i\omega_k t};\ \hat{a}_k^\dagger(t) = \hat{a}_k^\dagger(0) e^{i\omega_k t}.$$

In the dipole approximation, the interaction Hamiltonian is given by

$$\hat{H}_I = -\hat{\mathbf{p}}.\hat{\mathbf{E}}, \tag{3.2}$$

where $\hat{\mathbf{p}} = -e\hat{\mathbf{r}}$ with $\hat{\mathbf{r}}$ being the position operator and $-e$ being the electron charge. Atomic transition operators are projection operators $|f\rangle \langle i|$ from an initial state $|i\rangle$ to a final state $|f\rangle$, where $(i, f) = (g, e)$ for photon absorption and $(i, f) = (e, g)$ for photon emission

$$\hat{\sigma}_+ = |e\rangle \langle g| , \tag{3.3}$$

$$\hat{\sigma}_- = |g\rangle \langle e| . \tag{3.4}$$

The time-evolution of these transition operators is given by

$$\hat{\sigma}_\pm(t) = \hat{\sigma}_\pm(0) e^{\pm i\omega_0 t}.$$

The atomic inversion operator, whose eigen-values are the population difference between the ground state and the excited state, is

$$\hat{\sigma}_3 = |e\rangle\langle e| - |g\rangle\langle g|. \tag{3.5}$$

These operators obey the Pauli spin algebra, that is

$$[\hat{\sigma}_+, \hat{\sigma}_-] = \hat{\sigma}_3, \tag{3.6}$$

$$[\hat{\sigma}_3, \hat{\sigma}_\pm] = \pm 2\hat{\sigma}_\pm. \tag{3.7}$$

Only the off-diagonal elements of the dipole operator $\hat{p}_\Lambda$ are non-zero, or $\langle e|\hat{p}_\Lambda|e\rangle = \langle g|\hat{p}_\Lambda|g\rangle = 0$, as the transition occurs only for states with the opposite parity, which also implies no radiative transition occurs for the same state [141, 142]. The zero-level of energy is assumed to be halfway between the two states. The dipole moment operator is given by

$$\hat{p}_\Lambda = p_\Lambda|g\rangle\langle e| + p^*_\Lambda|g\rangle\langle e| = p_\Lambda\hat{\sigma}_- + p^*_\Lambda\hat{\sigma}_+ = p_\Lambda(\hat{\sigma}_- + \hat{\sigma}_+), \tag{3.8}$$

where $\langle e|\hat{p}_\Lambda|g\rangle = p_\Lambda$ and is the transition dipole moment from state $|e\rangle$ to state $|g\rangle$ and is assumed to be real. The interaction Hamiltonian is

$$\hat{H}_I = -\hat{\mathbf{p}}.\hat{\mathbf{E}} = \sum_{\mathbf{k},\Lambda} \hbar g_{k,\Lambda}(\hat{a}_k e^{i\mathbf{k}.\mathbf{r}} + \hat{a}^\dagger_k e^{-i\mathbf{k}.\mathbf{r}})(\hat{\sigma}_- + \hat{\sigma}_+), \tag{3.9}$$

where $g_{k,\Lambda} = -p_\Lambda(\frac{\omega_k}{\hbar\epsilon_0 V})^{1/2}$. The free-atomic Hamiltonian is given by

$$\hat{H}_A = \frac{1}{2}(Ee - Eg)\hat{\sigma}_3 = \frac{1}{2}\hbar\omega_0\hat{\sigma}_3, \tag{3.10}$$

where E_e is the energy of the excited state, E_g is the energy of the ground state, and $\hbar\omega_0$ is the energy difference between the two states. The free-field Hamiltonian after dropping zero-point energy term which does not contribute to the dynamics of transition between the atomic states is

$$\hat{H}_F = \sum_{\mathbf{k}} \hbar\omega_k \hat{a}^\dagger_k \hat{a}_k. \tag{3.11}$$

The total Hamiltonian can then be written as

$$\begin{aligned}\hat{H} &= \hat{H}_A + \hat{H}_F + \hat{H}_I \\ &= \frac{1}{2}\hbar\omega_0\hat{\sigma}_3 + \sum_{\mathbf{k}} \hbar\omega_k \hat{a}^\dagger_k \hat{a}_k + \sum_{\mathbf{k},\Lambda} \hbar g_{k,\Lambda}(\hat{\sigma}_- + \hat{\sigma}_+)(\hat{a}_k e^{i\mathbf{k}.\mathbf{r}} + \hat{a}^\dagger_k e^{-i\mathbf{k}.\mathbf{r}}).\end{aligned} \tag{3.12}$$

From the time dependence of the operators we get the following terms for within the summation for the last term

$$\begin{aligned}
\hat{\sigma}_+\hat{a}_k &\sim e^{i(\omega_0-\omega_k)t},\\
\hat{\sigma}_-\hat{a}_k^\dagger &\sim e^{-i(\omega_0-\omega_k)t}\\
\hat{\sigma}_-\hat{a}_k &\sim e^{-i(\omega_0+\omega_k)t},\\
\hat{\sigma}_+\hat{a}_k^\dagger &\sim e^{i(\omega_0+\omega_k)t}.
\end{aligned}$$

Now we make the rotating wave-approximation, that is for $\omega_k \approx \omega_0$ we neglect the last two terms in the summation which are rapidly oscillating. So the total Hamiltonian becomes

$$\hat{H} = \frac{1}{2}\hbar\omega_0\hat{\sigma}_3 + \sum_{\mathbf{k}} \hbar\omega\hat{a}_k^\dagger\hat{a}_k + \sum_{\mathbf{k},\Lambda} \hbar g_{k,\Lambda}(\hat{\sigma}_-\hat{a}_k^\dagger e^{-i\mathbf{k}.\mathbf{r}} + \hat{\sigma}_+\hat{a}_k e^{i\mathbf{k}.\mathbf{r}}), \tag{3.13}$$

where the first term corresponds to stimulated emission and the second term corresponds to absorption.

Spontaneous emission from an ensemble of N two-level atoms in a cavity of volume $V < {\lambda_0}^3$

The Jaynes-Cummings model of spontaneous emission from a single two-level atom can be extended to the relevant problem of collective spontaneous emission from an ensemble of N two-level atoms. The summarized version of the derivation presented here follows Dicke's original derivation as well as the ones provided by [5–7]. Any other sources of linewidth broadening, such as collision, inhomogeneous and Doppler broadening are neglected. Each atom can exist only in two energy eigenstates: the excited state $|e\rangle$, which will be denoted by $|+\rangle$ in this section so as to be consistent with Dicke's formalism, and the ground state $|g\rangle$, which will be denoted by $|-\rangle$. The zero-level of energy is assumed to be halfway between the two states. The energy eigen-states of the N atoms is a tensor product of the eigenstate of each atom. A typical wave-function of the system of N atoms will be

$$|\Psi_m\rangle = U_g(\mathbf{r}_1, \mathbf{r}_2, ..., \mathbf{r}_i..., \mathbf{r}_N)\,|+ + ... - ...+\rangle\,. \tag{3.14}$$

Here, $|+ + ... - ...+\rangle$ is one of the many eigen-states in which the system can exist depending on the different permutations of the atoms being in the excited state and the ground state. The index m_N signifies population inversion and is equal to

$$m_N = \frac{1}{2}(n_+ - n_-), \tag{3.15}$$

where n_+ is the number of atoms in the excited state, n_- is the number of atoms in the ground state and $n_+ + n_- = N$, N being the number of particles.

The emission (absorption) of a single photon involves one of the n_+ (n_-) atoms in the excited (ground) state decaying (being excited) radiatively to the ground (excited) state by emitting (absorbing) a single photon of frequency ω_0. We now define the *collective versions* of the Pauli spinors $\hat{\sigma}_1$, $\hat{\sigma}_2$ and $\hat{\sigma}_3$ signifying the atomic transitions and inversion for the j-th atom as

$$\hat{R}_1^{(j)}(... \pm ...) = \frac{1}{2}(... \mp ...), \tag{3.16a}$$

$$\hat{R}_2^{(j)}(... \pm ...) = \pm\frac{1}{2}i(... \mp ...), \tag{3.16b}$$

$$\hat{R}_3^{(j)}(... \pm ...) = \pm\frac{1}{2}(... \pm ...), \tag{3.16c}$$

$$\hat{R}_\pm^{(j)} = \hat{R}_1^{(j)} \pm i\hat{R}_2^{(j)}. \tag{3.16d}$$

In the above equations, j is the position of $\pm$ for the j-th atom, that is the j-th atom can be in a ground state or an excited state. Now we sum over the N atoms to get the collective versions of the transition operators for the whole system as

$$\hat{R}_{1,2,3} = \sum_{j=1}^{N} \hat{R}_{1,2,3}^{(j)}, \tag{3.17a}$$

$$\hat{R}_\pm = \sum_{j=1}^{N} \hat{R}_\pm^{(j)}. \tag{3.17b}$$

For a collection of N atoms, propagation effects are accounted for by the pterm $e^{\pm i\mathbf{k}.\mathbf{r}_j}$ in the operator definition. Propagation did not come into play in the previous case when we had a single atom. But for the system where the cavity volume $V < \lambda_0^3$, we can exclude these terms. These terms will come into play later on when we deal with the case of extended systems. For the sake of completeness, here we write the operator representations including the propagation terms

$$\hat{R}_{\mathbf{k}\pm} = \sum_{j=1}^{N} \hat{\sigma}_\pm^{(j)} e^{\pm i\mathbf{k}.\mathbf{r}_j}, \tag{3.18a}$$

$$\hat{R}_{\mathbf{k}3} = \sum_{j=1}^{N} \hat{\sigma}_3^{(j)} e^{i\mathbf{k}.\mathbf{r}_j}. \tag{3.18b}$$

These operators obey the commutation relations [7]

$$[\hat{R}_{\mathbf{k}+}, \hat{R}_{\mathbf{k}'-}] = \hat{R}_{(\mathbf{k}-\mathbf{k}'),3}, \tag{3.19a}$$

$$[\hat{R}_3, \hat{R}_{\mathbf{k}\pm}] = \pm 2\hat{R}_{\mathbf{k}\pm}. \tag{3.19b}$$

Similar to equation (3.8), the dipole moment operator associated with the $|e\rangle$ to $|g\rangle$ transition of the j-th atom, which is also polarized along the same direction Λ, is given by

$$\hat{\mathbf{p}}^{(j)}.\hat{\mathbf{e}}_\Lambda = \hat{p}_\Lambda^{(j)} = p_\Lambda^{(j)}(\hat{R}_{k,+}^{(j)} + \hat{R}_{k,-}^{(j)}), \tag{3.20}$$

where $p_\Lambda^{(j)} = \langle ... + ... | \, \hat{p}_\Lambda \, | ... - ... \rangle$, for transition of the j-th atom, and is assumed to be real. The collective dipole moment p_Λ is the sum of dipole moments of individual atomic transitions or

$$p_\Lambda = \sum_{j=1}^{N} p_\Lambda^{(j)}. \tag{3.21}$$

Similar to equation (3.13), we write the Hamiltonian for the new system of N atoms by replacing the individual atom transition operators with their collective versions and making the rotating wave approximation

$$\hat{H} = \frac{\hbar\omega_0}{2}\hat{R}_{k,3} + \sum_k \hbar\omega_k \hat{a_k}^\dagger \hat{a_k} + \sum_k g_{k,\Lambda}(\hat{R}_{k,+}\hat{a}_k + \hat{R}_{k,-}\hat{a}_k^\dagger), \tag{3.22}$$

or $\hat{H} = \hat{H}_0 + \sum_k \hat{H}_k$, where $\hat{H}_k$ is the interaction Hamiltonian between the cavity field and the atoms and $\hat{H}_0$ is the combined free-field and the free-atomic Hamiltonian. The coefficient $g_{k,\Lambda} = \sqrt{\frac{2\pi\hbar}{V\omega_k}} p_\Lambda$.

For the case where $V \ll \lambda_0^3$, we can approximate $\mathbf{k}.\mathbf{r}_i \ll 1$, and drop the propagation term $e^{i\mathbf{k}.\mathbf{r}_i}$ from the Hamiltonian expression and substitute $\omega_k = \omega$ giving

$$\hat{H} = \frac{\hbar\omega_0}{2}\hat{R}_3 + \hbar\omega\hat{a}^\dagger\hat{a} + g(\hat{R}_+\hat{a} + \hat{R}_-\hat{a}^\dagger). \tag{3.23}$$

From the expression for the collective inversion operator,

$$\hat{R}_3 \, |\Psi_m\rangle = m_N \, |\Psi_m\rangle \, , \tag{3.24}$$

where m_N, given by equation (3.15), equals half the population inversion. We define operator $\hat{R}^2$ such that

$$\hat{R}^2 = \hat{R}_1^2 + \hat{R}_2^2 + \hat{R}_3^2 = \frac{1}{2}(\hat{R}_+\hat{R}_- + \hat{R}_-\hat{R}_+) + \hat{R}_3^2. \tag{3.25}$$

Comparing with angular momentum operators, the operator $\hat{R}^2$ is analogous to $\hat{L}^2$ and $\hat{R}_3$ is analogous to $\hat{L}_z$. $\hat{R}_3$ and $\hat{R}^2$ commute and we choose a set of stationary states to be the eigen-states of both $\hat{R}_3$ and $\hat{R}^2$. The operator $\hat{R}^2$ has an eigen-value $r(r+1)$, similar to $\hat{L}^2$ which has eigen-values of $l(l+1)\hbar$. 'r', termed as the 'co-operation number', is always positive, and can have integer or half-integer

values which satisfy the following relation

$$|m_N| \leq r \leq \frac{1}{2}N. \tag{3.26}$$

The new eigen-states with the suffices m_N and r satisfy the following equations

$$\hat{R}_3 \left|\Psi_{m_N,r}\right\rangle = m_N \left|\Psi_{m_N,r}\right\rangle, \tag{3.27a}$$

$$\hat{R}^2 \left|\Psi_{m_N,r}\right\rangle = r(r+1) \left|\Psi_{m_N,r}\right\rangle. \tag{3.27b}$$

Also

$$\hat{R}_\pm \left|\Psi_{m_N,r}\right\rangle = N_\pm \left|\Psi_{m_N\mp1,r}\right\rangle, \tag{3.28}$$

where $N_\pm$ is the normalization factor. The term $\hat{R}_- \left|\Psi_{m_N,r}\right\rangle$ corresponds to the case of radiative decay of a single atom in the excited state $|+\rangle$ to the ground state $|-\rangle$ while emitting a photon of energy $\hbar\omega_0$. The term $\hat{R}_+ \left|\Psi_{m_N,r}\right\rangle$ corresponds to the inverse process of absorption of a photon of energy $\hbar\omega_0$ and transition of the atom from ground state $|-\rangle$ to the excited state$|+\rangle$. To find the normalization factor, we have

$$\begin{aligned}
|N_\pm|^2 &= \langle\Psi_{m_N,r}| \hat{R}_\mp \hat{R}_\pm \left|\Psi_{m_N,r}\right\rangle \\
&= \langle\Psi_{m_N,r}| \hat{R}^2 - \hat{R}_3^2 \mp \hat{R}_3 \left|\Psi_{m_N,r}\right\rangle \\
&= (r \pm m_N)(r \mp m_N + 1),
\end{aligned}$$

where r and m_N also satisfy the following relations

$$\langle\Psi_{r,m_N}| \sum_i \hat{R}_+^{(i)} \hat{R}_-^{(i)} \left|\Psi_{r,m_N}\right\rangle = r + m_N, \tag{3.29a}$$

$$\langle\Psi_{r,m_N}| \sum_i \hat{R}_-^{(i)} \hat{R}_+^{(i)} \left|\Psi_{r,m_N}\right\rangle = r - m_N, \tag{3.29b}$$

where $r + m_N$ is the number of atoms in the excited state and $r - m_N$ is the number of atoms in ground state. The degeneracy d_{r,m_N} of each stationary state is given by [3]

$$d_{r,m_N} = \frac{N\,!\,(2r+1)}{(\frac{N}{2}-r)\,!\,(\frac{N}{2}+r+1)}. \tag{3.30}$$

Thus the state with the largest value of 'm_N' and 'r', which is $r = m_N = \frac{N}{2}$, is completely non-degenerate (or has a degeneracy of $d_{\frac{N}{2},\frac{N}{2}} = 1$). The degeneracy increases as we move to lower co-operation numbers.

For radiative transitions, there should be no change in 'r' and due to selection rules (due to which there is a transition dipole moment associated only with states of the opposite parity), there should be a unity change in 'm_N' ($(m_N - 1)$ for

emission and $(m_N + 1)$ for absorption of a single photon). If we start with the maximum value of 'm_N' (which for a state in a given co-operation number, 'r', is equal to 'r') there should be $(r - m_N)$ photon emissions to get to a given state 'm_N'. This means that to get to the state Ψ_{r,m_N} from $\Psi_{r,r}$, we must apply the $\hat{R}_-$ operator $(r - m_N)$ times on $\Psi_{r,r}$ as follows

$$|\Psi_{m_N,r}\rangle = [(\hat{R}^2 - \hat{R}_3^2 - \hat{R}_3)^{-\frac{1}{2}}\hat{R}^-]^{r-m_N}\,|\Psi_{r,r}\rangle\,, \tag{3.31}$$

where the $(\hat{R}^2 - \hat{R}_3^2 - \hat{R}_3)^{-\frac{1}{2}}$ operator takes care of the normalization of the wave function. With this definition the wave-function of the $|\Psi_{m_N,r}\rangle$ state (also written as $|m_N, r\rangle$), the transition dipole moment associated with its transition to the $|\Psi_{m_N\pm1,r}\rangle$ (similarly written as $|m_N \pm 1, r\rangle$) is given by

$$\langle m_N, r|\,(\hat{R}_+ + \hat{R}_-)\,|m_N \mp 1, r\rangle = |N_\pm| = [(r \pm m_N)(r \mp m_N + 1)]^{\frac{1}{2}}. \tag{3.32}$$

From Fermi's Golden Rule [27, 143], the intensity of emitted spontaneous radiation due to a transition from $|m_N, r\rangle$ to $|m_N - 1, r\rangle$ is proportional to the probability of the transition or the square of the transition dipole moment giving

$$I = I_{sp}(r + m_N)(r - m_N + 1), \tag{3.33}$$

where I_{sp} is the intensity of spontaneous radiation emitted from a single atom.

If there is complete population inversion, or

$$r = m_N = \frac{N}{2},\ \text{then}\ I = NI_{sp}.$$

This is the case where each atom decays independently of the other and the total emitted power is the sum of powers emitted by individual atom, as it would be for the incoherent case. If, on the other hand, co-operation number 'r' is large and 'm_N' is small, for example when,

$$r = \frac{N}{2}\,\text{and}\,m_N = 0\,\text{then}\,I = I_{sp}\frac{N}{2}\Big(\frac{N}{2} + 1\Big),$$

or the field due to each emitter is summed up resulting in power which is proportional to the square of the number of atoms present in the system. This happens when all the emitters are emitting coherently, resulting in an emission rate which is much larger than the previous incoherent case. This state of the system is termed by Dicke as "superradiant" [3]. For the case where all the atoms are in the ground state,

$$r = \frac{N}{2}\,\text{and}\,m_N = -\frac{N}{2}\text{then}\,I = 0,$$

which means that the emission stops completely.

If we start with a completely inverted system (or at time $t = 0$, $r = m_N = N/2$) and let it evolve with time, we would observe that at first the atoms decay independently of each other with a radiation rate proportional to the number of atoms present. Emission of each photon would lower the value of 'm_N' by unity, but would result in no change in 'r'. Hence the system will cascade down a ladder of states, each separated by the same energy, $\hbar\omega_0$, until all the atoms have decayed to the ground state. This lowering of 'm_N' would in turn increase the radiation rate until it peaks at the half-way point where there are half the number of atoms each in the excited state and in the ground state. With further emission of radiation, the rate will decrease until it becomes 0 for the case where all the atoms end up in the ground state. Thus, this system of N atoms evolves as a cascaded emission down a ladder of equidistant states, much like how an atom with angular momentum R and emitting spontaneously, evolves. Fig 3.1 shows the energy-level diagram of the collective energy eigen-states along with the cascaded emission down the ladder. We again emphasize here that the atomic system is completely symmetric with respect to permutation, which means that it does not matter which atom is in the excited state and which atom is in the ground state as long as the number of atoms in the excited state is $(r + m_N)$ and the number of atoms in the ground state is $(r - m_N)$. This is a consequence of the assumption that all the atoms are confined within a volume $V < \lambda_0^3$.

The states with lower values of 'r', or co-operation number have higher

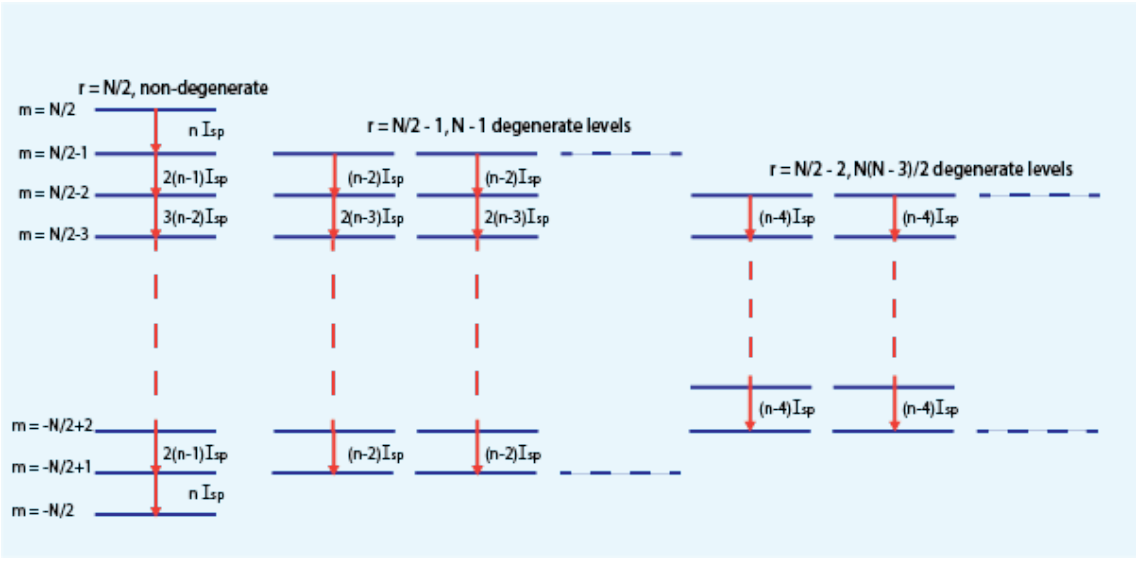

Figure 3.1: Energy-level diagram showing cascaded emission down the ladder of equidistant states

degeneracy and lower radiation rates. Also, the transitions between the degenerate states are non-radiative. But in most practical cases, there will be a uniform

field already present in order to excite the atoms, which breaks this degeneracy condition. If the exciting field is strong enough, such as an intense pulse, we can assume that all the atoms would be driven to the excited state. So for all practical purposes, we can refrain from talking about these lower 'r' degenerate states.

Let us examine the evolution of a system with all atoms initially in the excited state, or $r = m_N = N/2$ at time $t = 0$, qualitatively. As mentioned previously, the atoms at first start to decay independently of each other with the incoherent spontaneous emission rate of NI_{sp} and as the system moves down the ladder to lower values of m_N, the radiation rate (or the probability of emission of a photon) increases until there are exactly half the number of atoms in the excited state and half in the ground state. With further decrease in m_N, the radiation rate lowers until it becomes zero when all the atoms have decayed to the ground state. We can hypothesize that this increase in radiation rate is a direct consequence of the emergence of correlations between the atoms and it is instructive to look into the dipole-dipole correlations for confirmation of this hypothesis [5].

For a single atom [27]

$$I = I_{sp}\langle\hat{\sigma}_+\hat{\sigma}_-\rangle.$$

We can generalize this for N atoms as [5]

$$I = I_{sp}\langle\hat{R}_+\hat{R}_-\rangle = I_{sp}(r + m_N)(r - m_N + 1), \tag{3.34}$$

where the last equality comes from equation (3.33). The second term can be written as a summation

$$\langle\hat{R}_+\hat{R}_-\rangle = \langle\sum_i \hat{R}_+^{(i)} \sum_j \hat{R}_-^{(j)}\rangle = (r + m_N)(r - m_N + 1). \tag{3.35}$$

which can be expanded as

$$\langle\sum_i \hat{R}_+^{(i)} \sum_j \hat{R}_-^{(j)}\rangle = \sum_i \langle\hat{R}_+^{(i)}\hat{R}_-^{(i)}\rangle + \sum_i \sum_j \langle\hat{R}_+^{(i)}\hat{R}_-^{(j)}\rangle.$$

The last term is the cross-correlation between different atoms. For our symmetrical state, this cross-correlation is the same for all the different combinations i and j. There are $N(N-1)$ combinations for the cross-correlation between any two dipoles in the system of N atoms. Hence we can simplify the equation as

$$\langle\sum_i \hat{R}_+^{(i)} \sum_j \hat{R}_-^{(j)}\rangle = \sum_i \langle\hat{R}_+^{(i)}\hat{R}_-^{(i)}\rangle + N(N-1)\langle\hat{R}_+^{(i)}\hat{R}_-^{(j)}\rangle,$$

where $\langle \hat{R}_+^{(i)} \hat{R}_-^{(j)} \rangle$ is the cross-correlation between the i-th and j-th atoms. We can then write

$$\langle \hat{R}_+^{(i)} \hat{R}_-^{(j)} \rangle = \frac{r^2 - m_N^2}{N(N-1)}. \tag{3.36}$$

If we start with the case where $r = m_N = N/2$, we see that the correlation between atoms is zero and that the atoms radiate independently. This is consistent with the previous observation that the total intensity is the sum of individual intensities, as would be for a collection of atoms radiating independently and incoherently. For a constant value of $r = N/2$, we see that the correlation keeps increasing until $m_N = 0$. The correlation is maximized when the difference between r and m_N is the largest, which happens when $r = N/2$ and $m_N = 0$. This is also the point where we get the maximum intensity of emitted radiation and we are in the superradiant state. For lower values of m, the correlation decreases further until it becomes zero again for $r = N/2, m_N = -N/2$, or when all the atoms are in the ground state. This proves that the increase in radiation rate or intensity is accompanied by an increase in correlation between the atoms. At the point of maximum radiation rate, these correlations lead to the appearance of a macroscopic dipole moment which is equal to the sum of the individual dipole moments, as seen in equation (3.21). For very large values of N, we can simply say that the intensity scales with N^2, making the lifetime of emission $1/N$ times shorter than that of the individual atom for energy conservation. This behaviour directly results from the symmetry of the system and indistinguishability of the atoms.

Bonifacio and Luigiato have distinguished the case just discussed, where the macroscopic dipole moment emerges from a totally uncorrelated state, as 'superfluorescence' [4]. This effect can only be observed in quantum systems and no classical analog is possible due to the inherent quantum nature of fluorescence of each atom which starts the process. Superradiance then, in their more stricter definition, is the case where we start out with the maximum correlated case and let the system evolve, or $r = N/2$; $m_N = 0$ at time $t = 0$. In the context of correlation between emitters, we can observe superradiance in classical systems but not superfluorescence. This is the case that we are actually interested in. But first we must discuss the case of N atoms confined within a volume $V > \lambda_0^3$.

Time evolution of N-atom superradiant system

Let the time constant associated with the radiative lifetime of a single isolated atom be τ_0. The intensity of emission $I_k(t)$ into a solid angle along the direction

k satisfies the following relation [7]

$$\frac{d}{dt}\langle \hat{a}_k^\dagger \hat{a}_k \rangle = I_k(t) = \frac{1}{4\pi\tau_0}\langle \hat{R}_{k,+}(t)\hat{R}_{k,-}(t)\rangle, \tag{3.37}$$

where τ_0 is the radiative decay time associated with a single isolated atom. Generalizing equation (3.25) for a mode k, we can write

$$\hat{R}_k^2 = \frac{1}{2}(\hat{R}_{k,+}\hat{R}_{k,-} + \hat{R}_{k,-}\hat{R}_{k,+}) + \hat{R}_{k,3}^2. \tag{3.38}$$

Also, from the conservation of Bloch vector length [7]

$$\langle \hat{R}_k^2 \rangle = \frac{1}{2}\langle (\hat{R}_{k,+}\hat{R}_{k,-} + \hat{R}_{k,-}\hat{R}_{k,+})\rangle + \langle \hat{R}_{k,3}^2 \rangle = r(r+1). \tag{3.39}$$

Using the commutation relations in equation (3.19) and some algebraic manipulation, we write

$$\langle \hat{R}_{k,+}\hat{R}_{k,-}\rangle = \langle \hat{R}_k^2\rangle + \frac{1}{2}\langle \hat{R}_{k,3}\rangle - \langle \hat{R}_{k,3}^2\rangle = r(r+1) + \frac{1}{2}\langle \hat{R}_{k,3}\rangle - \langle \hat{R}_{k,3}^2\rangle. \tag{3.40}$$

We assume r to be maximum ($= N/2$) and rewrite equation (3.40) as

$$\langle \hat{R}_{k,+}\hat{R}_{k,-}\rangle = \frac{N}{2}\Big(\frac{N}{2}+1\Big) + \frac{1}{2}\langle \hat{R}_{k,3}\rangle - \langle \hat{R}_{k,3}^2\rangle. \tag{3.41}$$

When an atom in the excited state decays and a photon is emitted, m_N which is half the population inversion is reduced by 1/2 while the number of photons in all the k mode combined increases by one. Hence 1/2 the rate of decrease in the expectation value of $\hat{R}_3$ must be equal to the rate of increase in the photon number in all the modes, which is the expectation value of $\hat{a}_k^\dagger \hat{a}_k$ summed over k. So we write

$$\frac{d}{dt}\Big\langle \frac{1}{2}\hat{R}_3 + \sum_k \hat{a}_k^\dagger \hat{a}_k \Big\rangle = 0. \tag{3.42}$$

From (3.37) and (3.42) we get

$$4\pi I_k(t) = -\frac{1}{2}\frac{d}{dt}\langle \hat{R}_3\rangle. \tag{3.43}$$

Summing both sides of the equation (3.41) for all k and using equations (3.37) and (3.43) we get

$$\frac{d}{dt}\langle \hat{R}_3\rangle = -\frac{2}{\tau_0}\Big[\frac{N}{2}\Big(\frac{N}{2}+1\Big) + \frac{1}{2}\langle \hat{R}_3\rangle - \langle \hat{R}_3^2\rangle\Big]. \tag{3.44}$$

Depending on the initial condition, or the value of $\langle \hat{R}_3 \rangle(t=0)$, we get the two separate solutions of superfluorescence and superradiance. If the initial condition is $\langle \hat{R}_3 \rangle(t=0) = N/2$, we start with complete population inversion and a completely uncorrelated state and the solution of the differential equation is

$$\langle \hat{R}_3 \rangle(t) = -(N+1)\tanh\Big(\frac{t-t_0}{2\tau_c}\Big), \tag{3.45}$$

where

$$\tau_c = \frac{\tau_0}{N+1}, \tag{3.46a}$$

$$t_0 = \frac{\tau_0 \ln N}{N+1}. \tag{3.46b}$$

The intensity of emitted radiation in direction k is then calculated using equations (3.43) and (3.45) as [6], [7]

$$I_k(t) = \frac{(N+1)^2}{16\pi\tau_0}\operatorname{sech}^2\Big(\frac{t-t_0}{2\tau_c}\Big). \tag{3.47}$$

'τ_c' is the characteristic decay time of the ensemble of N atoms and for very large value of N, the decay time is shortened by a factor of $1/N$. 't_0' is the time delay required to reach the peak intensity, which is proportional to $(N+1)^2$ or N^2 for very large values of N. The initial intensity (at time $t=0$) is $(N+1)^2\operatorname{sech}^2(-\ln N/2)$ which is proportional to N for very large values of N. This is the superfluorescence case, according to [4], as the initial intensity is the same as the incoherent case (proportional to N) and the peak intensity is reached after a certain time delay t_0 during which the correlations are built up.

Fig 3.2 shows the plot of superfluorescent radiation intensity normalized to the maximum incoherent intensity $N/(4\pi\tau_0)$ vs time for different number of atoms confined within a fixed volume. As shown in fig 3.2, the superfluorescent intensity is the same as the incoherent intensity at time $t=0$, then reaches a maximum after a certain time delay which decreases with increase in the number of atoms, following which the intensity decays at a rate approximately N times faster than the incoherent case. Fig 3.3 shows the comparison of the time evolution of a system of two atoms, one radiating superfluorescently and the other radiating incoherently (both atoms emitting independently).

If the initial condition is $\langle \hat{R}_3 \rangle(t=0) = 0$, or half the number of atoms are in the ground state and half are in the excited state, the intensity of emitted radiation in direction k is

$$I_k(t) = \frac{(N+1)^2}{16\pi\tau_0}e^{-\left(\frac{t}{\tau_c}\right)}. \tag{3.48}$$

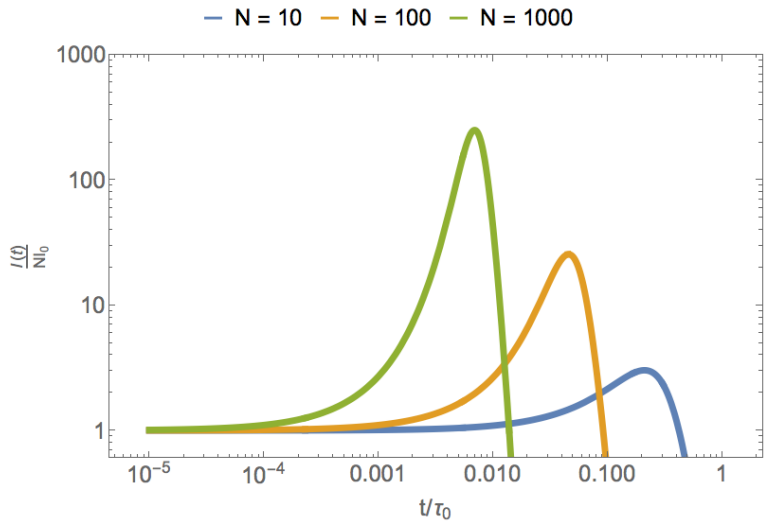

Figure 3.2: Superfluorescent radiation intensity normalized to the maximum incoherent intensity ($NI_0 = \frac{N}{4\pi\tau_0}$) as a function of time normalized to the decay time τ_0

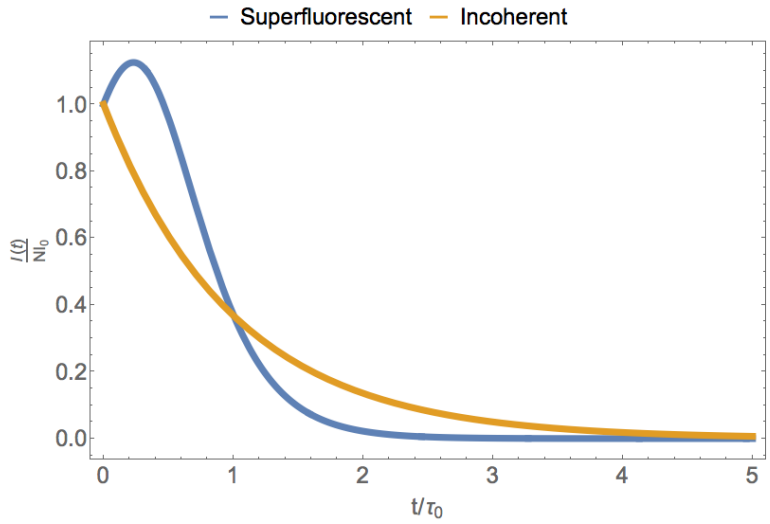

Figure 3.3: Radiation intensity normalized to the maximum incoherent intensity ($NI_0 = \frac{N}{4\pi\tau_0}$) as a function of time normalized to the decay time τ_0 for superfluorescent case (blue) and incoherent case (orange)

The initial radiation intensity is the maximum which then decays with a characteristic decay time τ_c which is, again, shorter by a factor of $1/N$. This is the superradiance case as, according to [4], the initial intensity is maximum due to the initial state being maximally correlated. Fig 3.4 shows the comparison of the time evolution of a system of two atoms, one radiating superradiantly and the other radiating incoherently (both atoms emitting independently). As shown in fig 2.4, there is no delay time associated with the build up of correlation and the radiation intensity decays approximately N times faster than the incoherent case.

The spectral width of emitted intensity for both cases can be found from

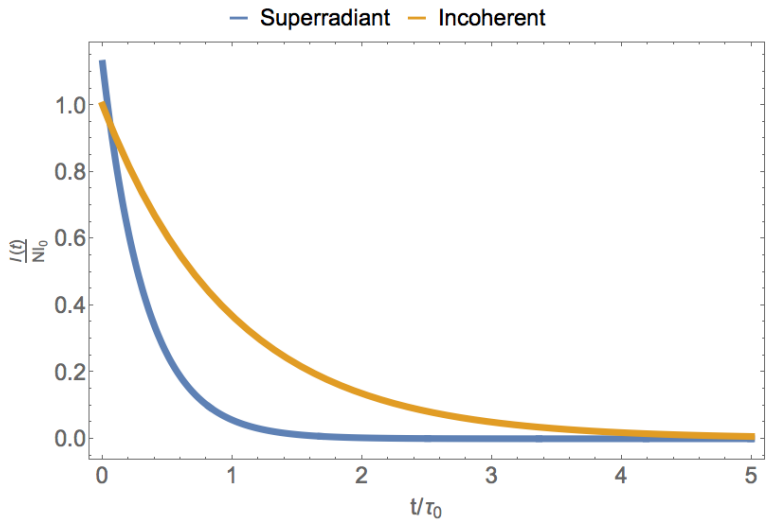

Figure 3.4: Radiation intensity normalized to the maximum incoherent intensity ($NI_0 = \frac{N}{4\pi\tau_0}$) as a function of time normalized to the decay time τ_0 for superradiant case (blue) and incoherent case (orange)

the electric field intensity, $E(t)$, which is the product of the square root of $I_k(t)$, the slowly varying amplitude of the emitted radiation, and the rapidly varying component $e^{-i\omega_0 t}$, ω_0 being the angular frequency of the transition: $\Delta m = -1$.

$$E(t) = \begin{cases} (I(t))^{1/2} e^{-i\omega_0 t}, & t \geq 0 \\ 0, & t < 0 \end{cases}$$

The spectral distribution of intensity, $|E(\omega)|^2$, is then obtained by taking the squared modulus of the Fourier transform of $E(t)$. The spectral linewidth, $\Delta\omega$, is then the variance of the intensity distribution. For both the superfluorescent and the superradiant case, this comes out to be [6, 7]

$$\Delta\omega = 0.427 \frac{N}{\tau_0} = N\gamma_0, \tag{3.49}$$

where γ_0 is the spectral linewidth for a single isolated atom. Thus the linewidth for a coherently radiating ensemble of N emitters becomes N times the linewidth of independently radiating emitters.

3.2.2 Quantum electrodynamic model for N emitters confined within a volume $V > {\lambda_0}^3$

In the previous case, the precise arrangement of emitters was not included as its effect was negligible for a system with $V < {\lambda_0}^3$. But when we consider extended systems, the retardation effects become important and propagation terms must be included in the definition of operators. Superradiance in extended systems has

been discussed previously in [6] which is summarized in this section.

When we sum up the transition operators for each atom to get their collective versions, this time we include the propagation term $e^{i\mathbf{k}.\mathbf{r}_j}$ for each operator. The total emitted intensity is then calculated by integrating the product of the intensity in a given direction $\hat{k}$ and the average of square modulus (for intensity) retardation factor over all atoms. The averaging of retardation factors is what makes the intensity dependant on the arrangement of atoms within the confining volume. Also, the intensity is not isotropic and is emitted into a solid angle. This behaviour is characterized by a parameter 'μ' called the shape-factor. μ depends on the shape and size of the containing volume V for the emitters [6]. The parameter N in equations (3.45)- (3.48) is then replaced by $N\mu$ to get the expression for radiation rate in direction k for an extended system [6]

$$I_k(t) = \frac{(N\mu+1)^2}{16\pi\tau_0}\,\mathrm{sech}^2\left(\frac{t-t_0}{2\tau_c}\right), \tag{3.50a}$$

$$I_k(t) = \frac{(N\mu+1)^2}{16\pi\tau_0} e^{-\left(\frac{t}{\tau_c}\right)}, \tag{3.50b}$$

where

$$\tau_c = \frac{\tau_0}{N\mu+1} \tag{3.51a}$$

$$t_0 = \frac{\tau_0 \ln N\mu}{N\mu+1} \tag{3.51b}$$

The shape-factor μ is very small, in general, making the parameter $N\mu$ smaller than N. This reduces the co-operative effect a lot.

The angular distribution of emitted radiation is of interest here as in contrast to the previous case, in which all the field modes were equivalent and the radiation was isotropic (hence $I(t) = 4\pi I_k(t)$), the shape of the confining volume may favour particular modes. Hence there is preferential emission of radiation in a particular direction governed by diffraction [6, 7]. For example, in a cylindrical volume, the modes with wave-vectors parallel to the axis of the cylinder are dominant.

Although it was mentioned above that the shape-factor greatly reduces the magnitude of the overall superradiant/superfluorescent effect, when the angular distribution of emitted radiation is taken into account, the superradiant/superfluorescent behaviour can be said to be exhibited in a particular direction. Most of the radiation is actually emitted in a small cone along the direction of excitation, especially when it is parallel to the major axis of the contaning volume [6]. For input excitation at an angle to the major axis, the radiation is emitted in symmetrical cones parallel to the incoming radiation about the direction of the major axis. The solid angle subtended by the cone is inversely proportional to the

confining volume. This phenomenon is also referred to as '*coherence brightening*' [144], [145].

If one also considers the time evolution of an extended system along with the angular spread, one finds that as mentioned in [6], at time $t = 0$, if there is complete population inversion, the emitted radiation is isotropic and the intensity is proportional to $N\mu$, similar to the incoherent case. After the time delay t_0, the correlation is maximum and the system emits with an intensity proportional to $(N\mu)^2$ in the cone along the direction of excitation. This is the superfluorescent case. For the superradiant case, the system starts emitting in the cone along the direction of excitation with an intensity proportional to $(N\mu)^2$ from the very beginning. Rehler and Eberly have plotted the angular distribution of radiation for different shapes of the containing volume and different atomic densities [6].

It is important to note that for an extended system, dephasing mechanisms such as van-der Waals interaction significantly reduce the superradiance effect. One way of getting around this problem is to resonantly couple a smaller sized sample to a cavity. The resonant enhancement due to the cavity compensates for these dephasing factors and helps in observing superradiance effects at a much lower density of particles than in the uncoupled state [5].

3.2.3 Classical Model

The properties of superradiance can also be described by a classical model. In this case, N oscillators oscillate in phase from the beginning of the process. This implies that in the dipole approximation, a macroscopic dipole moment exists at the beginning of the process which is the sum of the dipole moments of individual oscillators. The classical model is derived in this section and is similar to the one given in [6].

We consider N identical electric dipoles oscillating with frequency ω and dipole moment $\mathbf{p}(t)$ confined within a volume V which may be of any arbitrary size. We make the quasi-electrostatic approximation in which the decay-time of the dipole is assumed to be much larger than the oscillation time period of the dipole. No dipole-dipole interaction is considered at this point. All the dipoles are excited at time $t = 0$ and then undergo radiative decay. The dipoles are not necessarily in phase and oscillate with angular frequency ω, which is equal to the angular frequency of the initial excitation. The time-dependence of the envelope of dipole moment of each dipole $\mathbf{p}(t)$ is thus

$$\mathbf{p}(t) = \mathbf{p}_0 e^{-\gamma_0 t/2}, \tag{3.52}$$

where γ_0 is the decay constant of a single isolated dipole and $\mathbf{p}_0$ is the initial value. The total vector potential with the retardation included is

$$\mathbf{A}(\mathbf{r},t) = -\frac{i\mu_0\omega}{4\pi}\sum_{i=1}^{N}\mathbf{p}(t)\frac{e^{i\mathbf{k}.(\mathbf{r}-\mathbf{r}_i)}}{|\mathbf{r}-\mathbf{r}_i|}\cos\left(\omega t-\phi_i\right) \tag{3.53}$$

From the vector potential, the electric field $\mathbf{E}$ and the magnetic field $\mathbf{H}$ can be calculated, from which the time-averaged Poynting vector is calculated in order to get rid of the fast varying component at twice the oscillating frequency. The power emitted per unit solid angle in the direction $\mathbf{n}$ is then calculated from the time averaged Poynting vector as

$$\frac{dP}{d\Omega} = \frac{1}{2}\,\mathrm{Re}\big\{[r^2\mathbf{n}.(\mathbf{E}\times\mathbf{H})]\big\} = \left(\frac{dP}{d\Omega}\right)_0 N^2\Big|\frac{1}{N}\sum_{i=1}^{N}e^{i(\mathbf{k}.(\mathbf{r}-\mathbf{r}_i)-\phi_i)}\Big|^2, \tag{3.54}$$

where $\left(\frac{dP}{d\Omega}\right)_0$ is the power per unit solid angle emitted by a single isolated dipole and is equal to [146]

$$\left(\frac{dP}{d\Omega}\right)_0 = \frac{c^2Z_0}{32\pi^2}k^4|\mathbf{p}(t)|^2\sin^2\theta_p. \tag{3.55}$$

Here Z_0 is the characteristic impedance of free space, θ_p is the angle between $\mathbf{p}$ and $\mathbf{n}$, and c is the speed of light in vacuum.

In the quasi-electrostatic approximation, the average potential energy $W(t)$ of N electric dipoles with dipole moment $\mathbf{p}$, charge Q and mass M is given by [146], [147]

$$W(t) = \frac{NM\omega^2}{2}\left(\frac{|\mathbf{p}(t)|}{Q}\right)^2 \tag{3.56}$$

The total power emitted by the dipoles is hence

$$P = \frac{dW(t)}{dt} = N^2\int\left(\frac{dP}{d\Omega}\right)_0\Big|\frac{1}{N}\sum_{i=1}^{N}e^{i(\mathbf{k}.(\mathbf{r}-\mathbf{r}_i)-\phi_i)}\Big|^2 d\Omega \tag{3.57}$$

Solving equations (3.56) and (3.57) for $W(t)$ we get

$$W(t) = W(0)e^{-\frac{t}{\tau_c}}, \tag{3.58}$$

where τ_c is the characteristic decay time which is related to the decay time of a

single isolated oscillator τ_0 by the following relations

$$\tau_c = \frac{\tau_0}{N\mu} \tag{3.59a}$$

$$\tau_0 = \gamma_0^{-1} = \left[\frac{1}{M\omega^2}\left(\frac{Q}{|\mathbf{p}(0)|}\right)^2 \int \frac{c^2 Z_0}{32\pi^2} k^4 |\mathbf{p}(t)|^2 \sin^2\theta d\Omega\right]^{-1} \tag{3.59b}$$

$$\mu = \frac{\tau_0}{M\omega^2}\left(\frac{Q}{|\mathbf{p}(0)|}\right)^2 \int \left(\frac{dP}{d\Omega}\right)_0 \left|\frac{1}{N}\sum_{i=1}^{N} e^{i(\mathbf{k}.(\mathbf{r}-\mathbf{r}_i)-\phi_i)}\right|^2 d\Omega \tag{3.59c}$$

So the decay time is shortened by a factor of $1/N$ due to co-operative effects while the maximum power is increased by N^2. From simple Fourier analysis, we can easily see that the spectral linewidth is broadened by a factor N, as shown in equation (3.49). Again, due to the inclusion of the propagation term $e^{-i\mathbf{k}.\mathbf{r}}$, we get the $N\mu$ instead of the simpler N dependence. All these conclusions are consistent with the predictions made by the quantum-electrodynamical model thus confirming that superradiance can be observed in classical systems as well.

3.3 Experimental demonstrations

Skribanowitz et al [8] were the first to demonstrate Dicke superradiance, or more specifically in their case superfluorescence, in the IR regime by optically pumping HF gas in 1973. They showed that when HF gas at pressure higher than 10 mTorr was pumped with a HF laser, the relaxation energy between two rotational sub-levels of the first vibrational state was emitted after a considerable time delay ($\approx 2\,\mu s$) as a very short pulse. The time delay increased with decreasing pressure while the intensity decreased and eventually oscillations were observed in the emitted intensity due to absorption and re-emission of the emitted radiation, similar to the Rabi oscillations. Later on, many experiments showed Dicke superradiance in atomic vapors such as Cesium ([9], [10] and [148]), Rubidium [149], Barium [11], Thallium [12] and Sodium [150]. Reference [9] showed that the degeneracy of atomic levels is very important in determining emission properties and they showed the presence of quantum beats due to different hyperfine structures present in the energy levels of Cesium. Reference [150] showed Doppler beats in the emitted radiation depending on the direction of excitation and many-atom beats due to presence of different isotopes in the mixture. Gross et al [13] showed superradiance in the microwave region using Rydberg atoms. The trigger for superradiant effect in their case was blackbody radiation and not spontaneous emission, unlike the other cases.

Superradiant and subradiant emission was demonstrated in a system of trapped

ions for the first time in reference [15]. They demonstrated the variation of radiative linewidth with distance between the trapped ions in the form of a sinc(kR) function for both superradiant (transition dipoles in phase) and the subradiant (transition dipoles out of phase) cases. A similar experiment was reported for a pair of gold nanospheres by Dahmen et al [151] where the spectral linewidth of the scattered light oscillated between superradiance and subradiance. Recently, Inouye et al [14] demonstrated off-resonant superradiant scattering from an elongated specimen of Bose-Einstein condensate. On excitation of the condensate with a laser beam polarized perpendicular to the major axis of the condensate, highly directional emission in the forward direction was observed along with recoil scattering of atoms at 45° with respect to the axis. The radiative decay lifetime was also substantially reduced unlike the incoherent Rayleigh scattering case. Reference [152] showed long range interaction and collective radiative effects in a system of quantum dots which behaved as an ensemble, an evidence of superradiance.

Superradiant (bright mode with a faster decay rate) and subradiant (dark mode with slower decay rate) modes were observed in a system of two superconducting qubits coupled to a microwave cavity by references [153], [154] and [16] for strong coupling, one-dimensional coupling and a weak coupling with the cavity respectively. Single-photon superradiance and the associated collective Lamb shift (shift in resonance of emitted radiation due to absorption and emission of virtual photons) was demonstrated in a collection of Mossbauer ^{57}Fe nuclei in reference [155].

Chapter 4

Superradiance in two-dimensional arrays of nano-antennas

4.1 Introduction

Particle plasmon resonances (PPRs) are resonant oscillations of the electron cloud of nanoparticles on being excited with an incoming optical field [156]. They increase the scattering and absorption cross-section of the nanoparticle. It has been shown, that these PPRs (resonance wavelength as well as the linewidth) depend on the shape of the nanoparticle and the permittivities of the material comprising the nanostructure and that of the substrate or the medium in which it is embedded [157], [158].

The resonances of coupled plasmonic nanoparticles and their optical scattering properties have been studied extensively in recent years [159–164]. In such systems, the term superradiance is often used to describe coupled modes that exhibit a linewidth that is broader than that of the individual particles constituting the system. These so-called 'superradiant modes' possess an enhanced overall dipole moment resulting from the alignment of the dipole moments of the individual particles, which in turn lead to an enhanced scattering rate [160]. However, this phenomenon is different from Dicke's superradiance, as the 'superradiant modes' result from near-field coupling between the nanoparticles, while Dicke's superradiance relies only on radiative coupling [3].

The broadening of the resonance linewidth has also been observed in two-dimensional periodic arrays of plasmonic nanoparticles [19, 165–169]. In these systems, the effect has also been explained by an enhanced scattering rate resulting from a near-field dipole-dipole coupling [19, 169], as well as by a retarded long-range interaction between the nanoparticles [167]. The far-field coupling in a periodic three-dimensional arrangement of plasmonic nanowires was also stud-

ied [170]. In this case, the observed broadening of the transmittance linewidth and complete destructive (constructive) interference in forward (backward) direction at the Bragg condition was described as phenomenon similar to Dicke's superradiance.

More recently, Iida [171] showed numerically that the scattering cross-section linewidth of a linear arrangement of gold nanospheres is proportional to the number of nanospheres illuminated. The finding was also referred to as Dicke-like superradiance, but the analysis did not provide a physical insight into the phenomenon. In a follow up investigation, Tokonami and co-workers [172] considered a dielectric bead covered by gold nanospheres and observed experimentally a broadening of the scattering cross-section linewidth of ~ 100 meV when the distance between the nanospheres was reduced by ~ 1 nm. However, their experiment suffered from a large variation in the average particle size and a not-well-defined separation between the nanospheres, which could have led to inhomogeneous broadening and hence obscured the contribution of the claimed superradiance effect.

Although the linewidth broadening for arrays of nanostructures has been called, in some cases, Dicke-like superradiance, no study yet has provided a physical insight into the phenomenon, and in particular into the exact dependence of the linewidth on the number density of plasmonic nanoparticles. In this work, we consider a scattering problem for an array of nanoparticles with varying lattice constants. Through a series of transmission-spectroscopy experiments and numerical simulations, we show that the resonance linewidth of a two-dimensional array of dipole nanoantennas is directly proportional to the effective number of nanoantennas contained within a circle of radius equal to the optical wavelength. Furthermore, using a simple analytical model we provide physical insights indicating that the cooperative scattering effect observed in the collection of dipole nanoantennas can indeed be described as a classical manifestation of superradiance.

4.2 Simple Analytical Model

Spectral linewidth is the most convenient parameter to measure for plasmonic systems because the plasmon lifetime is of the order of 3-5 fs, making it very difficult to measure the dynamics of radiative decay. Hence our indicator of Dicke superradiance is the N-dependence of spectral linewidth of transmitted light from a square array of rectangular nanorods. In our analytical model, for ease of calculation, we model the nanoantennas as ellipsoids and only consider their dipole moment contribution. An infinite square array of these ellipsoids with lattice constants $a_x = a_y = a$, which are smaller than the resonance wavelength, are

embedded within a homogeneous medium made of BK7 glass with permittivity ϵ_2. Scattering from a planar array of resonant scatterers with lattice constants smaller than the resonance wavelength takes place in the form of a plane wave and there are no diffraction lobes present [173], [174]. Considering a planar array of these nanoantennas instead of a small number of scatterers also gives a larger signal that becomes important considering the very small scattering cross-sections of individual nanoantennas. Also it removes the dependence of the effect on the precise arrangement of these antennas within the circle of radius λ_0 due to uniform excitation of each antenna (uniform excitation and regular arrangement is an important criteria for observation of superradiance [175], [5]).

The plane containing the array of nanoantennas is taken to be the xy-plane,

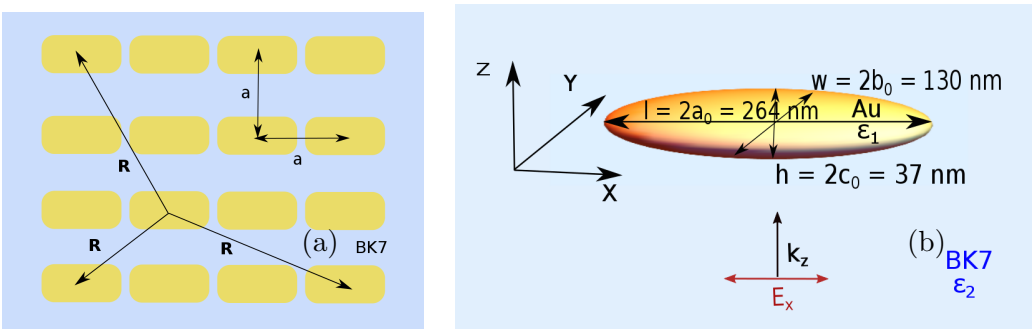

Figure 4.1: (a) Planar square array of gold nanorods embedded within BK7 glass, (b) Ellipsoid dimensions and excitation geometry used for the analytical model

or $z = 0$, as shown in Fig. 4.1b. The exciting field is normally incident and polarized along the length of the nanoantenna or equivalently along the major axis of the ellipsoid, which is assumed to be parallel to the x-axis, as shown in Fig. 4.1b. Johnson and Christy parameters [176] are used for the permittivity ϵ_1 of gold. The static polarizabilities for the nanorod and the ellipsoid will be slightly different due to the difference in shape, but we are interested in a phenomenological explanation for the effect and essentially any nanoparticle shape will do as long as it has a larger scattering cross-section than the absorption cross-section. This is important so that any change in linewidth is due to radiative interaction.

The static polarizability tensor $\overleftrightarrow{\alpha}$ for the ellipsoid is expressed in the principal axis coordinates as a diagonal matrix with the following elements [177]

$$\begin{aligned}
\alpha_{xx} &= \frac{\epsilon_0(\epsilon_1-\epsilon_2)V}{1+\frac{1}{2}(\frac{\epsilon_1}{\epsilon_2}-1)A_{a_0}}, \\
\alpha_{yy} &= \frac{\epsilon_0(\epsilon_1-\epsilon_2)V}{1+\frac{1}{2}(\frac{\epsilon_1}{\epsilon_2}-1)A_{b_0}}, \\
\alpha_{zz} &= \frac{\epsilon_0(\epsilon_1-\epsilon_2)V}{1+\frac{1}{2}(\frac{\epsilon_1}{\epsilon_2}-1)A_{c_0}},
\end{aligned} \tag{4.1}$$

where $V = \frac{4\pi}{3} a_0 b_0 c_0$ is the volume of the ellipsoid and $A_{i,\, i=a_0,b_0,c_0}$ are the shape factors given by [177]

$$A_i = a_0 b_0 c_0 \int_0^\infty \frac{ds}{(s+i)^2 \sqrt{(s+a_0)^2 (s+b_0)^2 (s+c_0)^2}};\; i = a_0, b_0, c_0, \tag{4.2}$$

The total electric field $\mathbf{E}_{\text{tot}}$ at a particular dipole, of dipole moment $\mathbf{p}$, is the vector sum of the incident field at the dipole $\mathbf{E}_{\text{inc}}$, its own radiation-reaction field and the retarded fields from all the other dipoles,

$$\mathbf{E}_{\text{tot}} = \mathbf{E}_{\text{inc}} + \frac{1}{4\pi\epsilon_0} \frac{2}{3c^3} in\omega^3 \mathbf{p} + \sum_{\mathbf{R}\neq 0} \overleftrightarrow{\mathbf{G}}\,(-\mathbf{R}).\mathbf{p}, \tag{4.3}$$

where n is the refractive index of gold, c is the speed of light, ϵ_0 is the vacuum permittivity, $\mathbf{R}$ is the lattice vector as shown in Fig. 4.1a, $\overleftrightarrow{\boldsymbol{G}}\,(\mathbf{r})$ is the Green's tensor for the dipole, and $\mathbf{E}_{\text{inc}}$ is the incident plane wave at the position of the dipole. The second term on the right hand side of equation (4.3) is the radiation-reaction term of the dipole while the last term is the sum of the retarded fields from all the other dipoles. The last term is also represented by $\overleftrightarrow{\boldsymbol{\beta}}$, called the dynamic interaction constant. For normal incidence, the dipole moment is identical for each dipole and is given by

$$\mathbf{p} = \overleftrightarrow{\alpha}\; \mathbf{E}_{\text{tot}} = \overleftrightarrow{\alpha} \left[\mathbf{E}_{\text{inc}}(\mathbf{r}) + \frac{1}{4\pi\epsilon_0} \frac{2}{3c^3} in\omega^3 \mathbf{p} + \overleftrightarrow{\boldsymbol{\beta}}\; .\mathbf{p} \right], \tag{4.4}$$

For the xy-plane containing the dipoles, $G_{xz}(-\mathbf{R}) = G_{yz}(-\mathbf{R}) = 0$. Also, since we have a square lattice and normally incident light $\sum_{\mathbf{R}\neq 0} G_{xy}(-\mathbf{R}) = \sum_{\mathbf{R}\neq 0} G_{zz}(-\mathbf{R}) = 0$. The only non-zero components of the tensor $\overleftrightarrow{\boldsymbol{\beta}}$ are the xx and the yy terms, which happen to be equal for the square array. We refer to these non-zero terms as β *(or $\beta_{xx} = \beta_{yy} = \beta$)*. Local-field approach for a 2-D structure, similar to the Lorentz-Lorenz model for a bulk crystal, can be used to calculate $\overleftrightarrow{\boldsymbol{\beta}}$. There are various approaches of performing this calculation. Reference [174] calculates the surface current density followed by energy conservation relations to find the imaginary part of β, and also shows that it depends on the nearest neighbours of the dipole. Reference [173] uses the Poisson summation formula followed by singularity cancellation to get the exact analytic expression for the imaginary part of β [178]. A brief summary of the derivation given in reference [174] follows.

4.2.1 Derivation of the dynamic interaction constant

To find the total field at a particular dipole, a circle of radius R with origin at the dipole is introduced around the dipole. The total interaction field $\sum_{\mathbf{R}\neq 0} \overleftrightarrow{\mathbf{G}}(-\mathbf{R}).\mathbf{p}$ at the dipole is the vector sum of the field due to dipoles lying outside the circle (referred to as hole from now onwards) called $\mathbf{E}_{\text{sheet}}$, and due to the dipoles enclosed within the hole excluding the reference dipole in question called $\mathbf{E}_{\text{hole}}$, that is

$$\mathbf{E}_{\text{int}} = \beta\mathbf{p} = \mathbf{E}_{\text{sheet}} + \mathbf{E}_{\text{hole}}. \tag{4.5}$$

$\mathbf{E}_{\text{sheet}}$ can be calculated analytically as it becomes a continuous sum for a large enough R. This is justified as the effect of dipoles far enough from the reference dipole in question is that of an averaged polarization. $\mathbf{E}_{\text{hole}}$ on the other hand is a discrete sum of a finite number of dipoles enclosed within the hole. The field due to a dipole of moment $\mathbf{p}$ at a distance r is given by

$$\mathbf{E}_p = \frac{1}{4\pi\epsilon}\left(k^2(\hat{\mathbf{n}}\times\mathbf{p})\times\hat{\mathbf{n}}\frac{e^{ikr}}{r} + (3\mathbf{n}(\mathbf{n}.\mathbf{p}) - \mathbf{p})\Big(\frac{1}{r^3} - \frac{ik}{r^2}\Big)e^{ikr}\right), \tag{4.6}$$

with $\hat{\mathbf{n}}$ being the unit vector directed along the position vector $\mathbf{r}$ and $k = \omega\sqrt{\mu\epsilon}$ is the wave-number within the medium. The discrete dipoles are replaced by a homogenous polarized sheet with a surface density of dipole moments given by

$$\mathbf{p}_s = \frac{\mathbf{p}}{a^2}, \tag{4.7}$$

a^2 being the area of the unit cell of the square-lattice with lattice constant a. In our case, the dipole moment of each dipole is directed in-plane along the x-axis. $\mathbf{E}_{\text{sheet}}$ is then given by

$$\mathbf{E}_{\text{sheet}} = \int \mathbf{E}_{ps}\, ds, \tag{4.8}$$

where

$$\mathbf{E}_{ps} = \frac{1}{4\pi\epsilon}\left(k^2(\mathbf{n}\times\mathbf{p}_s)\times\mathbf{n}\frac{e^{ikr}}{r} + (3\mathbf{n}(\mathbf{n}.\mathbf{p}_s) - \mathbf{p}_s)\Big(\frac{1}{r^3} - \frac{ik}{r^2}\Big)e^{ikr}\right), \tag{4.9}$$

and the surface integral is taken over the entire plane for $r > R$. Rewriting the integral in polar coordinates

$$\mathbf{E}_{\text{sheet}} = \frac{\mathbf{p}_s}{4\pi\epsilon}\int_0^{2\pi}\int_R^{\infty}\left(k^2\sin^2\phi + (3\cos^2\phi - 1)\frac{1-ikr}{r^2}\right)\frac{e^{ikr}}{r} r\, dr\, d\phi. \tag{4.10}$$

On integrating we get

$$\mathbf{E}_{\text{sheet}} = \frac{i\omega \mathbf{p}_s \eta_0}{4n}\Big(1 + \frac{1}{ikR}\Big)e^{ikR}, \tag{4.11}$$

where η_0 is the characteristic impedance of the free space.

Now we introduce the averaged surface current density $\mathbf{J}$ written as

$$\mathbf{J} = -i\omega \mathbf{p}_s. \tag{4.12}$$

We expand exponential in equation (4.11) using Taylor's series and substitute for $\mathbf{J}$ to get

$$\mathbf{E}_{\text{sheet}} = -\frac{\eta_0}{4nikr}\mathbf{J} - \frac{\eta_0}{2n}\mathbf{J} + O(kR). \tag{4.13}$$

The term $\mathbf{J}\eta_0/2n$ is the plane wave radiated by the complete sheet including the hole. Regarding the field contribution of the dipoles located within the hole, it has been shown in reference [174] that it is out of phase with the field contributions due to the sheet. Also, for a large enough value of R, both $\mathbf{E}_{\text{sheet}}$ and $\mathbf{E}_{\text{hole}}$ are oscillatory as the dipole fields fall of with $1/R$ while the number of dipoles within the hole increase proportional to R. The local field is thus shown to converge to a finite value for a large enough R. This means that the local-field depends on the nearest neighbours in an infinite array. Hence, the predictions made by this simple analytical model for an infinite periodic array will also be valid for a finite sized array.

Next, to find the total field, we take the limiting value of R, termed R_0, such that there is only one dipole enclosed within the hole. This makes $\mathbf{E}_{\text{hole}} = 0$. The total field is then given by

$$\mathbf{E}_{\text{tot}} = \mathbf{E}_{\text{inc}} + \mathbf{E}_{\text{int}} = \mathbf{E}_{\text{inc}} + \beta \mathbf{p}, \tag{4.14}$$

where $\beta_{xx} = \beta_{yy} = \beta$, the only non-zero terms of the dynamic interaction tensor for our case. From equation (4.11) we can write for β

$$\beta = \frac{i\omega\eta_0}{2na^2}\Big(1 + \frac{1}{ikR_0}\Big)e^{ikR_0}. \tag{4.15}$$

The value of R_0 is given as $R_0 = a/1.438$ in reference [174]. For $R < R_0$, we are in the static limit and $\mathbf{E}_{\text{int}}$ blows up.

For a single dipole, the dipole moment is related to the incident electric field as

$$\mathbf{p} = \overleftrightarrow{\alpha}\ \mathbf{E} \tag{4.16}$$

Since the dipole moment to be aligned parallel to the incident electric field, we get rid of the tensor notation and write the inverse polarizability as

$$\frac{1}{\alpha} = \xi - i\xi^{'} - \frac{i}{4\pi\epsilon_0}\frac{2n\omega^3}{3c^3}, \tag{4.17}$$

with n being the refractive index of the surrounding medium. The last term in the above equation is the radiative-reaction term and it determines the resonance linewidth. The $\xi^{'}$ and ξ terms depend on the shape, size and material of the scatterer as well as the frequency. The $\xi = 0$ case corresponds to resonance condition while $\xi^{'} > 0$ corresponds to passive particle with a non-zero absorption. In order to compare the radiative behaviour of a single dipole to that of a planar array of these dipoles, we define $\tilde{\alpha}$, the effective polarizability which characterizes the dipole response to only the incident field as

$$\mathbf{p} = \tilde{\alpha}\mathbf{E}_{\text{inc}} = \alpha\mathbf{E}_{\text{tot}}. \tag{4.18}$$

Equation (4.17) can then be written as a scalar equation

$$\frac{p_i}{\alpha_{ii}} = \frac{p_i}{\tilde{\alpha}_{ii}} + \beta p_i;\ i = x, y. \tag{4.19}$$

Note that our incident field is only polarized along the x-direction. So we can drop the indices in equation (4.19) and only consider the x-polarized response.

The power lost in each dipole due to absorption and radiation is

$$P_{ext} = -\frac{\omega}{2}\,\text{Im}\,\tilde{\alpha}|E_{\text{inc}}|^2, \tag{4.20}$$

where $\tilde{\alpha} = \tilde{\alpha}_{xx}$. We can write the radiated power by each particle (in both forward and backward directions) within the array as

$$P_{rad} = 2 \times \text{cell area} \times |\mathbf{S}| = 2a^2.\frac{1}{2}\,\text{Re}\,EH^*, \tag{4.21}$$

where $\mathbf{S}$ is the time-averaged Poynting vector and $E = -\eta_0 J/2n$ and $H = -J/2$ are the electric field (along x-axis here) and magnetic field (along y-axis here) respectively for the plane dipoles aligned along x-axis. The current density J can be written from equations (4.7), (4.12) and (4.18) as

$$J = -\frac{i\omega\tilde{\alpha}}{a^2}E_{\text{inc}}. \tag{4.22}$$

Substituting J from equation (4.22) in (4.21) we get

$$P_{\text{rad}} = \frac{a^2\eta_0|J|^2}{4n} = \frac{\eta_0\omega^2}{4na^2}|\tilde{\alpha}|^2|E_{\text{inc}}|^2. \tag{4.23}$$

For no absorption, $P_{\text{ext}} = P_{\text{rad}}$. Thus, equations (4.20) and (4.23) give

$$\text{Im}\,\frac{1}{\tilde{\alpha}} = -\frac{\eta_0\omega}{2na^2}. \tag{4.24}$$

Substituting the above result in equation (4.17) and assuming $\xi^{'} = 0$ for the lossless case, we get

$$\text{Im}\,\beta = -\frac{k^3}{6\pi\epsilon_0} + \frac{\eta_0\omega}{2na^2} = -\frac{k^3}{6\pi\epsilon_0} + \frac{k}{2\epsilon_0 a^2}. \tag{4.25}$$

Although we assumed that the particles are lossless, the above expression for interaction constant is an exact one for lattice constants much smaller than wavelength, as the interaction between the particles is due to radiation fields. Re-writing the expression for effective polarizability of the dipole in an array, we get

$$\frac{1}{\tilde{\alpha}} = \text{Re}\left(\frac{1}{\alpha} - \beta\right) + i\,\text{Im}\,\frac{1}{\alpha} - \frac{1}{4\pi\epsilon_0}\frac{2}{3c^3}in\omega^3 N_{\text{eff}}, \tag{4.26}$$

where $N_{\text{eff}} = 3\lambda_0^2/4\pi n^2 a^2$ is the effective number of dipoles enclosed within a circle of radius equal to the resonance wavelength, λ_0. The $\text{Im}\,1/\alpha$ term is responsible for losses due to absorption. The $\text{Re}(\beta)$ term causes a shift in the resonance wavelength depending on the lattice constant. The last term on the right hand side is the similar to the radiation-reaction term in equation in (4.17) for a single dipole. But there is a an enhancement factor, N_{eff} in the term. From the Sipe-Kranendonk condition [18], this term is proportional to the radiative damping, or the linewidth of resonance. Thus the radiative damping of a dipole is enhanced by a factor of N_{eff} (or $1/a^2$) in a planar square array due to co-operative effects. Effectively, this broadening of linewidth is proportional to the number of dipoles enclosed within a circle of radius λ_0 is quite similar to Dicke superradiance in which the broadening in radiative linewidth is proportional to the number of emitters within a volume smaller than λ_0^3. Hence we expect to see the radiative linewidth with $1/a^2$ as a manifestation of co-operative effect of the array, or 'superradiance'.

For experimental verification of this effect, we perform transmission measurements on the array of nanoantennas. The transmission and reflection spectrum can be analytically calculated using a transmission line model or an effective index method. The transmission line model is described below.

4.2.2 Transmission and reflection from the planar array

The reflectivity and transmissivity can be obtained using the equivalent transmission line formulation formulation as discussed in [174]. In this case, the entire array is modelled as a shunt load of imepedance Z_a to a transmission line of characteristic impedance η, which is the intrinsic impedance of the surrounding medium as shown in Fig. 4.2. We still use the scalar approximation as the surface

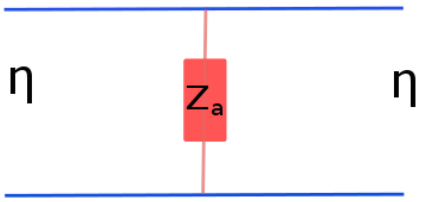

Figure 4.2: Transmission line model of the planar array of dipoles

current density is assumed to be directed along the incident field. The scattered field, E_{ref}, from a current sheet of surface current density J is $-(\eta/2)J$. Assuming normal incidence, we can write the total field as

$$E_{\text{tot}} = E_{\text{inc}} + E_{\text{ref}} = E_{\text{inc}} - \frac{\eta}{2}J = Z_a J. \tag{4.27}$$

Using the result of equation (4.22) in (4.27), we can write

$$E_{\text{tot}} = \left(i\frac{a^2}{\omega\tilde{\alpha}} - \frac{\eta}{2}\right)J = Z_a J. \tag{4.28}$$

Hence, the reflection and transmission coefficients are

$$\tilde{r} \;\; = \tfrac{E_{\text{ref}}}{E_{\text{inc}}} \;\; = \frac{-\frac{\eta}{2}}{Z_a + \frac{\eta}{2}}, \tag{4.29}$$

$$\tilde{t} \;\; = 1 + \tilde{r} \;\; = \frac{Z_a}{Z_a + \frac{\eta}{2}}. \tag{4.30}$$

Hence the transmittance $\tilde{T}$, or the ratio of transmitted power to incident power and the reflectance $\tilde{R}$, or the ratio of reflected power to the incident power are

$$\tilde{R} = |\tilde{r}|^2 = \frac{\eta^2\omega^2|\tilde{\alpha}|^2}{4a^4} = \left(\frac{\pi}{n}\right)^2\left(\frac{\lambda}{a}\right)^4\left(\frac{\tilde{\alpha}}{\epsilon_0\lambda^3}\right)\left(\frac{\tilde{\alpha}^*}{\epsilon_0\lambda^3}\right), \tag{4.31}$$

$$\tilde{T} = |\tilde{t}|^2 = 1 - \frac{\pi}{n}\left(\frac{\lambda}{a}\right)^2 2\,\text{Im}\left\{\left(\frac{\tilde{\alpha}}{\epsilon_0\lambda^3}\right)\right\} + \left(\frac{\pi}{n}\right)^2\left(\frac{\lambda}{a}\right)^4\left(\frac{\tilde{\alpha}}{\epsilon_0\lambda^3}\right)\left(\frac{\tilde{\alpha}^*}{\epsilon_0\lambda^3}\right). \tag{4.32}$$

4.3 Results

For experimental demonstration of these predictions, linear transmission measurements were performed on a set of 6 samples with varying lattice constant, a, from 250 nm to 500 nm in steps of 50 nm. The experimental setup along with the SEM image of a fabricated sample are shown in Fig. 4.3.

The fabrication was performed using electron beam lithography in a Raith Pio-

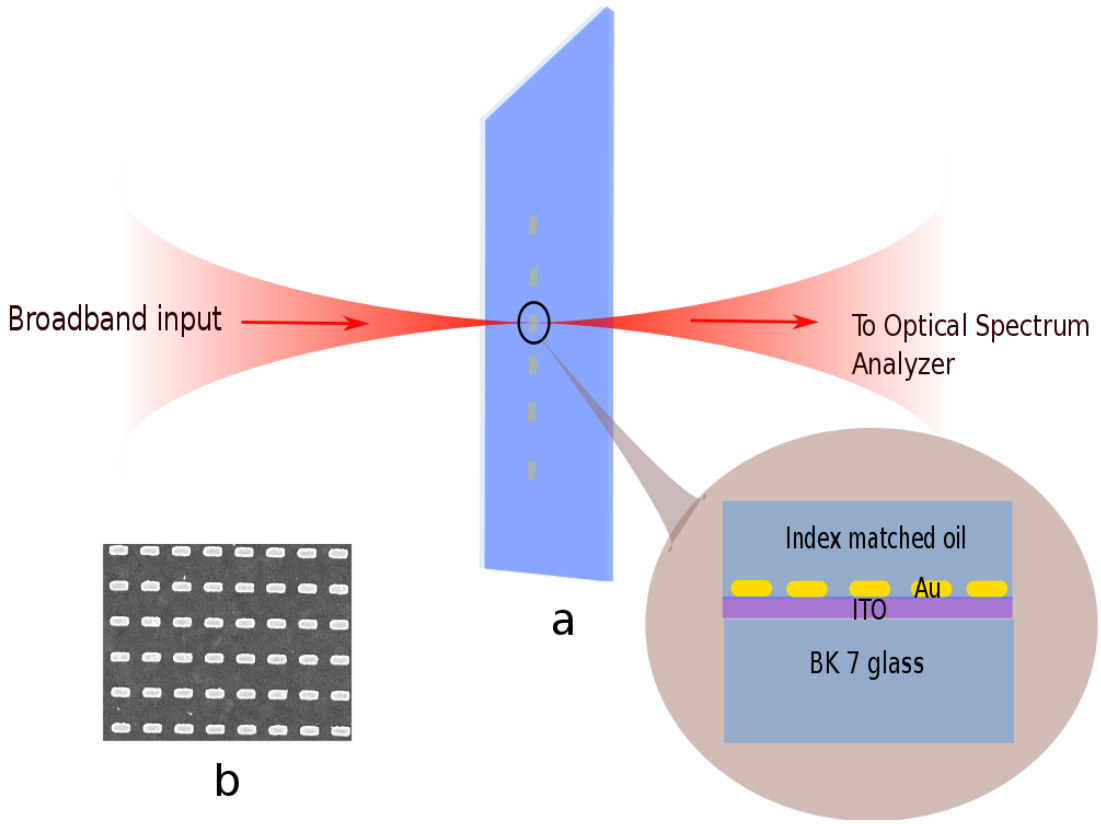

Figure 4.3: (a) Schematic showing the setup of the experiment. Inset shows the sketch of each sample. (b) SEM image of a sample

neer 30 kV e-beam system to form a patterned resist on a 1 mm thick fused silica substrate. A 23-nm-thick layer of ITO (indium tin oxide) was deposited on the substrate for efficient charge dissipation (this 23-nm-thick ITO layer was included in the simulations) followed by inverse-patterning with a photoresist. Then a gold film of thickness 30 nm was deposited and the resist was removed by the process of lift-off leaving behind the patterned gold on the substrate. Each of the 6 fabricated samples was 100 μm $\times$ 100 μm in size. The fabricated nanorods had an average length of 212.5 nm, width of 105 nm and thickness of 30 nm. To make the background medium symmetric, the sample was coated with index-matched oil, and a cover-slip was placed on top.

The broadband source was a white-light halogen lamp that was focussed on the required sample using a 0.4 NA objective. The spot size was small enough to

be entirely contained within the area of the sample to avoid artefacts in our measurements. The transmitted light was collected using a 0.1 NA objective which collects light only within a cone of half angle 5.74°, or near normal incidence. This light was then fiber-coupled to a Yokogawa AQ6370C optical spectrum analyzer, and the spectrum was measured. The spectrum recorded for transmission through the array was normalized to the transmission spectrum of the glass + ITO + oil assembly to get the normalized spectrum. These normalized spectra were then fitted to Lorentzians from which the linewidth was extracted (code attached in Appendix 1). The measured and fitted extinction spectra are shown in Fig. 4.4.

In order to compare these experimental results with the predictions from

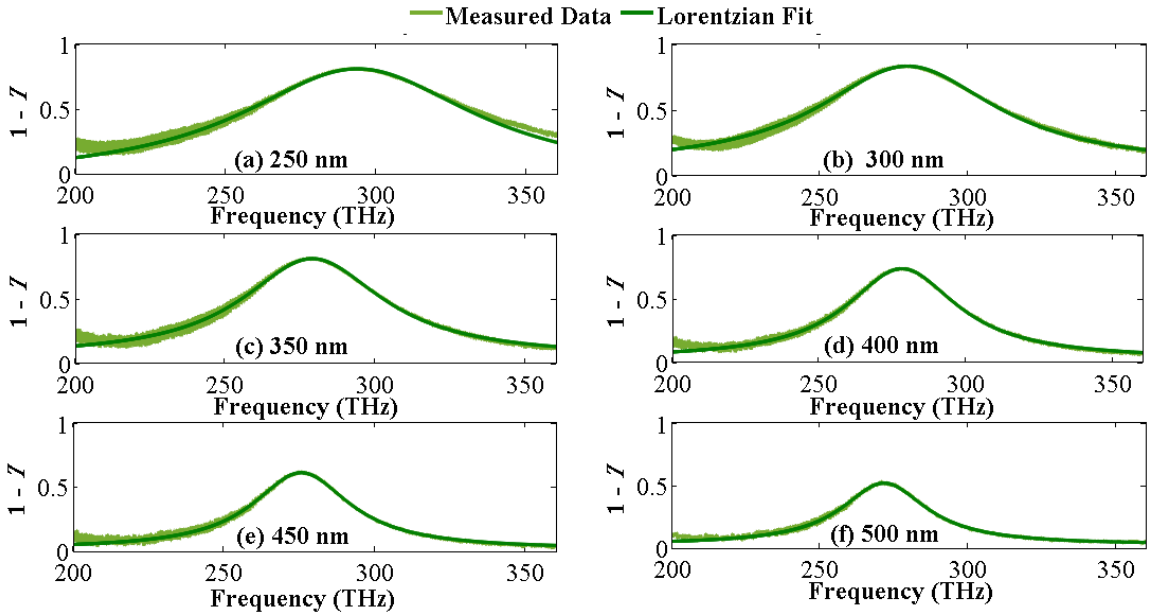

Figure 4.4: Measured extinction spectra (dark green) along with the corresponding Lorentzian fits (light green) for different lattice constants

the analytical model, we performed numerical simulations for square arrays of nanorods with varying lattice constants under periodic boundary conditions using a commercial Maxwell equations solver based on the finite diffidence time domain (FDTD) method. These numerical simulations provide results for ideal experimental conditions and should be closer to the analytical predictions. Gold nanorods with a rectangular cross-section and dimensions same as the average dimensions of the fabricated sample were arranged in a square lattice on a BK7 substrate with a layer of BK7 on top and a 23-nm-thick layer of ITO sandwiched in between. Broadband light polarized along the length of the nanorod was normally incident on the array. For verification of the analytical model, the dimensions of the ellipsoid were chosen to have the same volume as the nanorod (see Fig. 4.1b) with similar scattering and absorption cross-sections.

The spectrum of the scattering, absorption, and extinction cross sections ob-

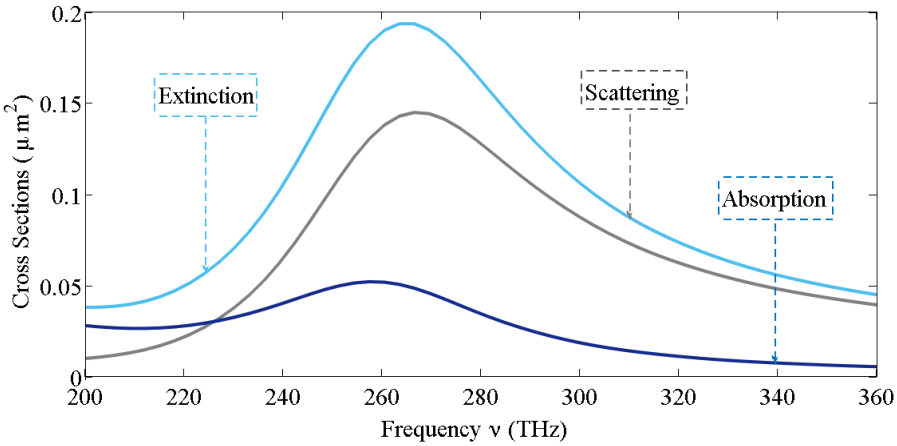

Figure 4.5: Scattering, absorption and extinction cross-sections of a single isolated nanorod

tained from FDTD simulations are plotted in Fig. 4.5. The scattering resonance of an isolated nanorod for excitation along its length was found to be at wavelength 1125 nm (frequency 266.5 THz). We see that the scattering cross-section at resonance is more than twice the absorption cross-section. The designed nanoantennas are hence very good scatterers and well-suited for studying co-operative radiative effects. The spectrum of the polarizability tensor components α_{xx} and α_{yy} for an isolated nanorod calculated by summing the current density for excitations along its length and width respectively, as obtained from FDTD, over the volume of the nanorod are shown in Fig. 4.6 and Fig. 4.7 respectively.

The lattice constant of this array was varied from 250 nm to 500 nm in steps

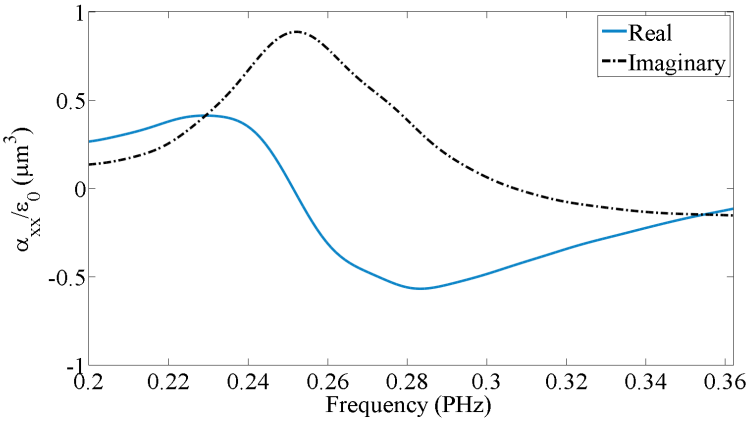

Figure 4.6: Polarizability tensor component α_{xx}

of 50 nm and the spectrum of the transmitted light was recorded. The full-width at half-maximum (FWHM) linewidth was calculated by fitting a Lorentzian to the extinction spectra.

Fig. 4.8 shows the plot of the analytically calculated, simulated and exper-

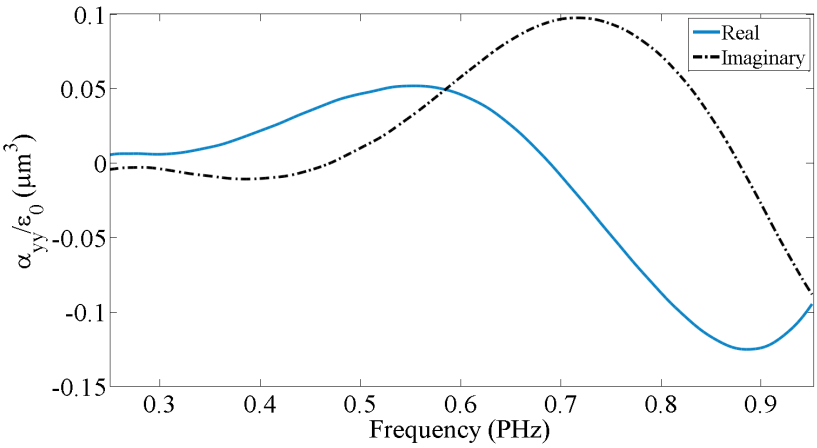

Figure 4.7: Polarizability tensor component α_{yy}

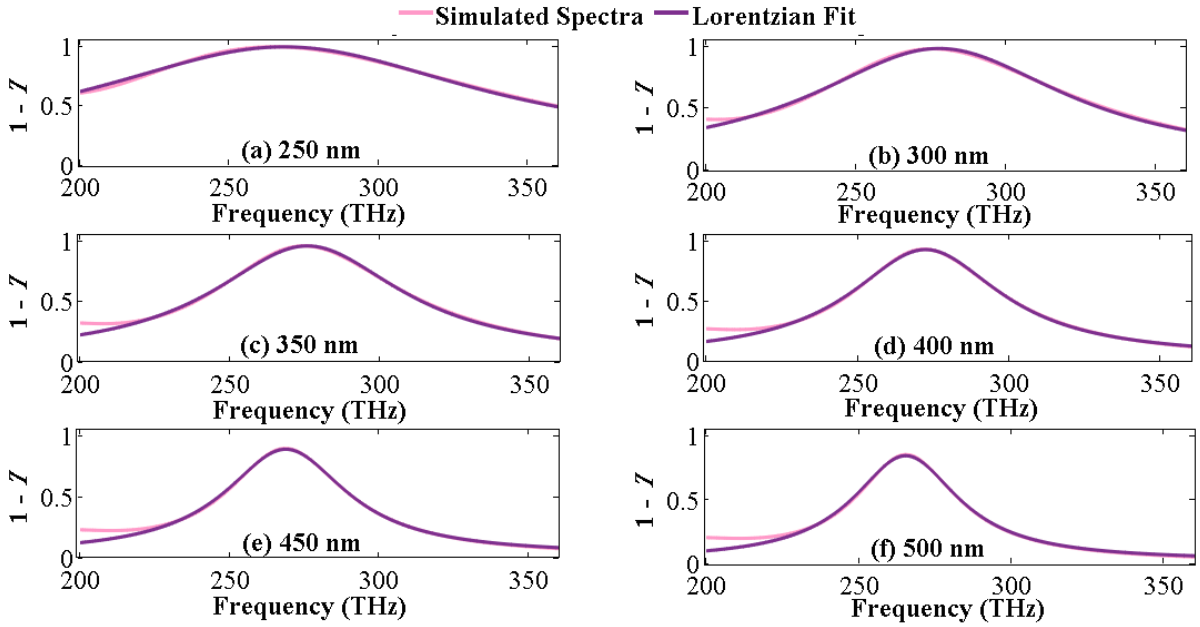

Figure 4.8: Simulated extinction spectra (magenta) along with the corresponding Lorentzian fits (purple) for different lattice constants

imentally measured FWHM linewidths vs lattice constant a and a power curve a^{-x} fitted to each dataset. We compare these values of x with the theoretically predicted value of -2. The exponent x was found to be -2.024 from simulations, -1.82 from the experiment and -2 from the analytical model, each with a 5% goodness-of-fit. The analytically calculated and the simulated value of exponent are almost equal to the predicted value of -2 while the measured value from the experiment lies within 10% of the predicted value of -2. We attribute the discrepancies between experimental and analytical results to deviations from the ideal dimensions and shape of the nanorods caused by inaccuracies in the fabrication process. Even so, the value of the exponent obtained from the analytical model, simulation and the experiment are almost equal to the predicted value,

from which we conclude that this is indeed a demonstration of superradiance in plasmonic systems.

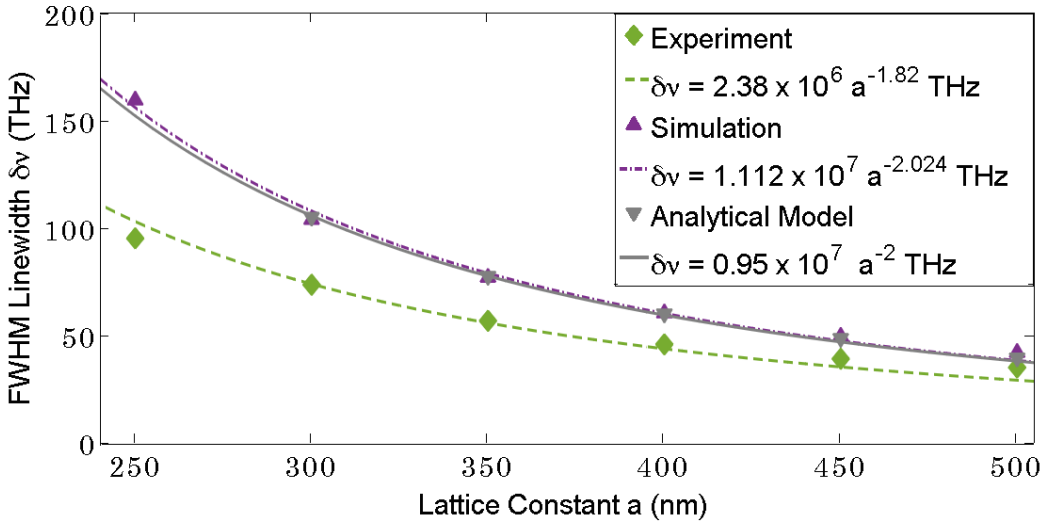

Figure 4.9: FWHM linewidths obtained from the analytical model (grey), experiment (green) and simulations (purple) vs. lattice constant a. The exponents of a in all three cases are within within 10% of the predicted value of -2

4.4 Conclusions

We have demonstrated superradiance in plasmonic structures by showing the dependence of spectral linewidth on the effective number of nanoantennas through a simple analytical model, FDTD simulations, and experiment. The experimental values are in reasonable agreement with the numerical and analytical results. Although we refer this linewidth broadening as superradiance, apart from the scaling of linewidth, no other parameter follows the scaling of Dicke's particular case. The reason is that we are working with scatterers and not emitters. Individual scatterers themselves can be treated as a two-level system with an excited state and a ground state. But there is no formation of the ladder of states like in the case of emitters. Hence we never fulfil the condition $r = N/2$ and $m = 0$, or half the emitters being excited and half being in ground state, which Dicke refers to as superradiant. Regardless, the dependence of linewidth on the number density of nanoantennas shows that this is still a co-operative effect and follows the scaling as suggested by Dicke.

4.5 Future Work

We have investigated the properties of the nanoantenna array under normal incidence. A possible next step would be to investigate the properties of the array for oblique incidence of light polarized along both s and p-polarizations. This would provide an intuition of the effect of the in-plane wave-vector on the radiative properties of the array. Further, this problem can be extended to 3-D by including a second layer of nanoantennas separated by varying distances from the original layer and investigate the effect of changing layer separations on the spectrum.

Part III

Spontaneous Parametric Downconversion (SPDC)

Chapter 5

The scaling laws of Spontaneous Parametric Downconversion

5.1 Introduction

Spontaneous Parametric Downconversion or SPDC is a parametric scattering process in which a pump photon of frequency ω_p and wave-vector $\mathbf{k}_p$, travelling within a crystal possessing a second-order nonlinearity, spontaneously splits into two photons of lower energy called the signal, of frequency ω_s and wave-vector $\mathbf{k}_s$, and idler, of frequency ω_i and wave-vector $\mathbf{k}_i$. The emitted photons obey energy conservation as $\omega_p = \omega_s + \omega_i$ as well as momentum conservation, $\mathbf{k}_p = \mathbf{k}_s + \mathbf{k}_i$, which manifests as phase-matching conditions that must be met by the three photons. Generally, birefringence of the material is used to achieve phase-matching [29].

SPDC has become a very important process in quantum communication [179], cryptography [21] and performing fundamental tests of quantum mechanics such as non-locality and local realism [180]. This is because the signal and idler photons are quantum-mechanically entangled in various degrees of freedom such as energy-time, spatial mode and polarization [181]. Moreover, SPDC can be used as a source for heralded single photons [23]. So designing a bright SPDC source is of considerable advantage. This simply means that the bi-photon rate should be maximized in order to have the highest brightness.

Another parameter that must be maximized is the heralding efficiency, or the conditional probability of detecting a signal photon given that an idler photon is detected. When we deal with heralded single-photon sources, a high heralding efficiency is very important. Experiments, such as tests of Bell's inequality violations impose a threshold on heralding efficiency ($> 66\%$) [182] and a high heralding efficiency also guarantees a lower quantum bit error rate. Hence the two important metrics that need to be maximized are: (1) bi-photon generation rate

and (2) heralding efficiency.

The SPDC process may be classified as type-I or type-II depending on whether the polarizations of the signal and idler are same or are orthogonal, respectively. In type-I, the pump is orthogonally polarized to both signal and idler and the emission of the photons occurs in the form of concentric cones with opening angle depending on the angle between the crystal axis and the pump, as shown in Fig. 5.1. In type-II, the signal and idler photons are orthogonally polarized to each other and the emission occurs in the form of two cones, as shown in Fig. 5.1. A type-0 configuration is also used where the crystal is periodically-poled to have quasi-phase matching and the signal, idler and pump have the same polarization [22]. The down-converted photons are emitted into an infinite continuum

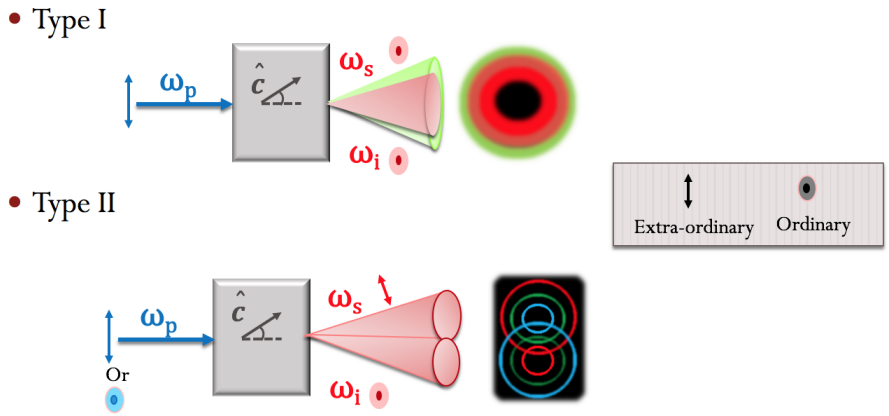

Figure 5.1: Schematic showing type-I and type-II SPDC configurations

of modes. In most experiments, these photons are collected in single-mode fibers that are coupled to coincidence detectors. Using single-mode fibers ensures that the photons are in a well-defined spatial mode, a Gaussian, and also optimizes the collection efficiency [183]. Prior investigations into designing a bright SPDC source has focussed on optimizing adjustable parameters such as crystal length, focussing of the pump beam and collection mode size [25, 26, 28, 184, 185].

Ling et al [28] have analyzed type-I SPDC in a non-collinear emission geometry with collimated Gaussian beams as the target modes. They provide an expression for the joint spectral emission rate and total bi-photon generation rate. The problem with their expression is that it diverges for degenerate type-I SPDC. Also, due to their assumption that pump, signal and idler are collimated beams, the expression is only valid in the thin crystal limit. To analyze the thick-crystal regime, diffraction effects in the three beams must be considered. Bennink [26] does include the effects of diffraction in his analysis, but it is limited to the case of collinear emission. Although collinear emission is an important case to consider with regards to the understanding of the basic physics of the process, it is not a

practical one as the signal and idler beams cannot be separated. One can in principle use a beam-splitter to split the beams, but the maximum possible heralding efficiency is reduced to 50% [185]. In this work, we attempt to extend the results of Ling at al [28] and Bennink [26] by analyzing the effects of crystal length and focussing of pump, signal and idler beams on the joint spectral rate and total rate of generation of bi-photons as well as spectral and total radiance of the SPDC source for Gaussian target modes. We also investigate the heralding efficiency for different collection optics such as single-mode fiber (SMF), multi-mode fiber (MMF) and bucket detectors.

5.2 Interaction Hamiltonian and bi-photon rate

The derivation of interaction Hamiltonian and the SPDC state is similar to the one given by references [24–26]. The derivation of spectral and total emission rates is similar to that provided by Ling et al [28].

The macroscopic polarization $\mathbf{P}$ induced by incident electric field $\mathbf{E}$ within a nonlinear medium can be written as [29]

$$\mathbf{P} = \epsilon_0 \chi^{(1)} \cdot \mathbf{E} + \epsilon_0 \chi^{(2)} : \mathbf{EE} + \epsilon_0 \chi^{(3)} \vdots \mathbf{EEE} + \dots \tag{5.1}$$

where $\chi^{(1)}$ is the linear susceptibility and $\chi^{(2)}$ and $\chi^{(3)}$ are the second- and third-order susceptibility respectively. The $\chi^{(2)}$ term is responsible for second-order parametric interaction and is the lowest-order nonlinear term. For an incident field E_i, the second-order polarization is

$$P_i = \sum_{j,k} \epsilon_0 \chi^{(2)}_{ijk} E_j E_k, \tag{5.2}$$

where (j, k) represent the cartesian components of the fields. The associated interaction energy of the the three beams is

$$H_I = \frac{1}{2} \int_V d^3r P_i(\mathbf{r}, t) E_i(\mathbf{r}, t) dV = \frac{1}{2} \int_V d^3r \sum_{j,k} \epsilon_0 \chi^{(2)}_{ijk}(\mathbf{r}) E_i(\mathbf{r}, t) E_j(\mathbf{r}, t) E_k(\mathbf{r}, t) \tag{5.3}$$

where the integration is performed over the volume of the nonlinear medium. The interaction Hamiltonian operator $\hat{H}_I$ is similarly given by [20]

$$\hat{H}_I = \int_V d^3r \, \epsilon_0 (\chi^{(2)}(\mathbf{r}) : \hat{\mathbf{E}}_p^+(\mathbf{r}, t) \hat{\mathbf{E}}_s^-(\mathbf{r}, t) \hat{\mathbf{E}}_i^-(\mathbf{r}, t) + \text{H.c.}) \tag{5.4}$$

where the suffices (p, s, i) stand for pump, signal and idler respectively and $\hat{\mathbf{E}}(\mathbf{r}, t)$ are the quantized electric-field operators. We make the un-depleted pump approximation [29] and treat it classically. The pump is assumed to be a monochromatic, continuous wave and is given by

$$\mathbf{E}_p(\mathbf{r}, t) = \frac{1}{2}(\hat{\mathbf{E}}_p^+(\mathbf{r}, t) + \hat{\mathbf{E}}_p^-(\mathbf{r}, t)) = \frac{1}{2}(E_{p0}U_p(x, y, z)e^{i\mathbf{k}_p\cdot\mathbf{r}-i\omega_p t}\mathbf{e}_p + c.c) \tag{5.5}$$

where E_{p0} is the electric-field amplitude of the pump, $\mathbf{e}_p$ is the polarization vector, ω_p is the pump angular frequency and $\mathbf{k}_p$ is the wave-vector. $U_p(x, y, z)$ is the spatial mode of the pump which is assumed to be a Gaussian beam of the form

$$U_p(x, y, z) = \sqrt{\frac{2}{\pi}}\frac{W_p}{q_p}\exp\left(-\frac{x^2 + y^2}{q_p}\right) \tag{5.6}$$

with $q_p = W_p^2 + 2iz/k_p$ and W_p is the waist size of the pump. The signal and idler fields are quantized and represented in plane-wave mode expansion as

$$\hat{\mathbf{E}}_{s,i}(\mathbf{r}, t) = i\sum_{k_{s,i}}\sqrt{\frac{\hbar\omega_{s,i}}{2\epsilon_0 n_{s,i}^2 V}}e^{i\mathbf{k}_{s,i}\cdot\mathbf{r}-i\omega_{s,i}t}\mathbf{e}_{s,i}\hat{a}_{k_{s,i}} + \text{H.c.} \tag{5.7}$$

where V is the quantization volume, $\mathbf{e}_{s,i}$ and $\mathbf{k}_{s,i}$ are the polarization and the wave-vectors respectively and $n_{s,i}$ are the refractive indices of the signal and idler respectively. Note that the i preceding the summation and in the exponent stands for the square root of -1 and is not to be confused with the suffix i for idler.

The initial state is a two-mode vacuum $|0, 0\rangle$. $\hat{H}_I$ operates on $|0, 0\rangle$ to give the state $|\Psi\rangle$. In the interaction picture, the state $|\Psi\rangle$ evolves in time according to

$$|\Psi\rangle = \exp\left(\frac{1}{i\hbar}\int_0^t dt_1\hat{H}_I(t_1)\right)|0, 0\rangle \approx \left(1 + \frac{1}{i\hbar}\int_0^t dt_1\hat{H}_I(t_1)\right)|0, 0\rangle \tag{5.8}$$

The second term in the above expression corresponds to the first order perturbation and is the SPDC state, $|\Psi_{SPDC}\rangle$ which is written as

$$|\Psi_{SPDC}\rangle = \frac{1}{i\hbar}\int_0^t dt_1\int_{-\infty}^{\infty} d^3r d_{\text{eff}}E_{p0}U_p(\mathbf{r})\sum_{k_s,k_i}\frac{\hbar\sqrt{\omega_s\omega_i}}{2\epsilon_0 n_s n_i V}e^{i\Delta\mathbf{k}\cdot\mathbf{r}}e^{-i\Delta\omega t}\hat{a}_{k_s}^\dagger\hat{a}_{k_i}^\dagger|0, 0\rangle\,, \tag{5.9}$$

where

$$2d_{\text{eff}} = \mathbf{e}_p\chi^{(2)} : \mathbf{e}_s\mathbf{e}_i,$$

$\Delta\mathbf{k}(= \mathbf{k}_p - \mathbf{k}_s - \mathbf{k}_i)$ is the wave-vector mismatch and $\Delta\omega = (\omega_p - \omega_s - \omega_i)$ is the frequency mismatch. Integrating with respect to time, we get

$$|\Psi_{SPDC}\rangle = \pi i \int_{-\infty}^{\infty} d^3r d_{\text{eff}} E_{p0} U_p(\mathbf{r}) \sum_{k_s,k_i} \frac{\sqrt{\omega_s\omega_i}}{V n_s n_i} e^{i\Delta\mathbf{k}\cdot\mathbf{r}} \delta(\omega_s + \omega_i - \omega_p) \hat{a}^\dagger_{k_s} \hat{a}^\dagger_{k_i} |0,0\rangle \,. \tag{5.10}$$

The Dirac delta function in frequency guarantees energy conservation by requiring $\omega_p = \omega_s + \omega_i$. The $e^{i\Delta\mathbf{k}\cdot\mathbf{r}}$ accounts for phase-matching or momentum conservation. Due to the summation over k-vectors (whose values are determined by phase-matching) the state is not separable and hence the signal and idler photons are entangled.

5.2.1 Projection of signal and idler into Gaussian spatial modes

The SPDC emission occurs in an infinite number of spatial modes. Equation (5.10) has been derived for the case where the signal and idler are treated as plane-waves emitted in a range of propagation directions, $\hat{k}_s$ and $\hat{k}_i$ respectively, whose values are determined by momentum conservation. We can include the spatial degree of freedom in our mode-decomposition by projecting the bi-photon state to either the Hermite-Gaussian (HG) or Laguerre-Gaussian (LG) basis as follows

$$|\Psi_{SPDC}\rangle = \sum_{l_s,p_s;l_i,p_i} \left\langle LG^{l_s}_{p_s}, LG^{l_i}_{p_i} \middle| \Psi_{SPDC} \right\rangle \left| LG^{l_s}_{p_s}, LG^{l_i}_{p_i} \right\rangle ; \tag{5.11a}$$

$$|\Psi_{SPDC}\rangle = \sum_{l_s,m_s;l_i,m_i} \langle HG_{l_s,m_s}, HG_{l_i,m_i} | \Psi_{SPDC} \rangle \, | HG_{l_s,m_s}, HG_{l_i,m_i} \rangle ; \tag{5.11b}$$

For the first part of our analysis, we study the variation of bi-photon generation rate into single-mode fibers (SMFs) coupled to coincidence detectors with various parameters such as crystal length, pump beam focussing and collection mode size. So we post-select $|\Psi_{SPDC}\rangle$ on only the fundamental fiber mode by projecting it on the fundamental mode of the fiber, approximated as a Gaussian for convenience. We assume that $U_{s,i}(x,y,z)$ is a Gaussian beam given by

$$U_{s,i}(x,y,z) = \sqrt{\frac{2}{\pi}} \frac{W_{s,i}}{q_{s,i}} \exp\left(-\frac{x^2+y^2}{q_{s,i}} \right). \tag{5.12}$$

Hence the projected bi-photon state on a pair of Gaussian signal and idler modes, $|\psi\rangle = \langle g_{k_s}, g_{k_i}|\Psi_{SPDC}\rangle\,|g_{k_s,k_i}\rangle$, is

$$|\psi\rangle = \pi i \int d^3r d_{\text{eff}} E_{p0} U_p(r) \sum_{k_s,k_i} \frac{\sqrt{\omega_s\omega_i}}{V n_s n_i} U_s^*(r) U_i^*(r) e^{\Delta\mathbf{k}\cdot\mathbf{r}} \delta(\omega_s + \omega_i - \omega_p) \hat{a}_{k_s}^\dagger \hat{a}_{k_i}^\dagger \,|0,0\rangle\,. \tag{5.13}$$

In practice, the collection optics such as fibers and detectors are located at the focal plane of a lens which limits the range of transverse k-vectors that are collected. Another limiting factor on k-vectors of the collection modes is phase-matching. The volume integral in the above equation will be called the overlap integral, $\Phi(\Delta k)$, from now onwards and is evaluated in Cartesian coordinates over the volume of the non-linear crystal. Here we make the assumption that the transverse extent of the crystal is much larger than the pump waist and for convenience we take the limits along x and y to be the entire real axis. We assume the origin to be located at the centre of the crystal. The limits of integration over z are taken from $-L/2$ to $L/2$, L being the length of the crystal. We rewrite the overlap integral as

$$\Phi(\Delta k) = \int_{-l/2}^{l/2} dz \int_{-\infty}^{\infty} dx dy \frac{e^{i\Delta\mathbf{k}\cdot\mathbf{r}}}{\sqrt{q_s q_i}} U_p(\mathbf{r}) U_s^*(\mathbf{r}) U_i^*(\mathbf{r}). \tag{5.14}$$

The overlap integral includes the scaling parameters of the SPDC process as well as the phase-mismatch term $e^{i\Delta\mathbf{k}\cdot\mathbf{r}}$.

5.2.2 Bi-photon generation rate

To obtain the transition rate, $R(k_s)$, from the initial state $|0,0\rangle$ to the final state $|1_{k_s}, 1_{k_i}\rangle$ (or one signal and idler photon emitted with wave-vectors $\mathbf{k}_s$ and $\mathbf{k}_i$ respectively) for a fixed signal state, we use Fermi's golden rule [27], as is also done in [28]. First the density of idler states per unit energy, $\rho_i(\Delta E)$, is found where ΔE is given by

$$\Delta E = \hbar\Delta\omega = \hbar\big(\omega_p - k_p\frac{c}{n_s} - k_i\frac{c}{n_i}\big). \tag{5.15}$$

$\rho_i(\Delta E)$ is hence given by

$$\rho_i(\Delta E) = \frac{\partial N}{\partial(\Delta E)} = \frac{\partial N}{\partial k_i}\frac{\partial k_i}{\partial(\Delta E)}. \tag{5.16}$$

Substituting equation (5.15) in equation (5.16), we get

$$\frac{\partial k_i}{\partial(\Delta E)} = \frac{n_i}{\hbar c}. \tag{5.17}$$

For freely propagating modes within the cubical quantization volume $V(= L^3)$, the separation between each mode in the k-space is $(2\pi/L)$ along each k_x, k_y and k_z. Hence the number of modes per unit idler wave-vector is

$$\frac{\partial N}{\partial k_i} = \Big(\frac{L}{2\pi}\Big)^3 = \frac{V}{8\pi^3}, \tag{5.18}$$

making the energy density of idler states as

$$\rho_i(\Delta E) = \frac{V}{8\pi^3}\frac{n_i}{\hbar c} \tag{5.19}$$

From Fermi's golden rule, the transition rate $R(k_s)$ is given by

$$R(k_s) = \frac{2\pi}{\hbar}|\left\langle f\right|\hat{H}_I\left|i\right\rangle|^2\rho_i(\Delta E), \tag{5.20}$$

where $|\left\langle f\right|\hat{H}_I\left|i\right\rangle|$ is the transition matrix element given by

$$|\left\langle f\right|\hat{H}_I\left|i\right\rangle| = \left\langle 1_{k_s}, 1_{k_i}\right|\pi\Phi(\Delta k)d_{\text{eff}}E_{p0}\frac{\hbar\sqrt{\omega_s\omega_i}}{Vn_sn_i}e^{-i(\omega_s+\omega_i-\omega_p)t}\hat{a}^\dagger_{k_s}\hat{a}^\dagger_{k_i}\left|0,0\right\rangle. \tag{5.21}$$

Equation (5.20) is then given by

$$R(k_s) = |d_{\text{eff}}E_{p0}\Phi(\Delta k)|^2\frac{\omega_s\omega_i}{4\pi^2n_s^2n_icV}. \tag{5.22}$$

To obtain the joint spectral rate or bi-photon generation rate per unit signal frequency ω_s, we take the product of $R(k_s)$ and the number signal modes per unit frequency $\rho_s(\omega_s)$. We follow the same argument used to calculate $\rho_i(\Delta E)$, we get the expression for $\rho_s(\omega_s)$ as

$$\rho_s(\omega_s) = \frac{V}{8\pi^3}\frac{n_s}{c}. \tag{5.23}$$

Hence the joint spectral rate $\frac{dR(\omega_s)}{d\omega_s}$ is

$$\frac{dR(\omega_s)}{d\omega_s} = |d_{\text{eff}}E_{p0}\Phi(\Delta k)|^2\frac{\omega_s\omega_i}{32\pi^5n_sn_ic^2}. \tag{5.24}$$

The power P_0 of the pump beam is written as

$$P_0 = \frac{1}{2}\frac{\epsilon_0n_pc}{\alpha_p^2}|E_{p0}|^2, \tag{5.25}$$

where $\alpha_p^2 = 2/\pi W_p^2$. Using equations (5.24) and (5.25) we get the spectral rate in terms of pump power P as

$$\frac{dR(\omega_s)}{d\omega_s} = |d_{\text{eff}}\alpha_p\Phi(\Delta k)|^2 \frac{P_0\omega_s\omega_i}{16\pi^5\epsilon_0 n_p n_s n_i c^3}. \tag{5.26}$$

The total bi-photon generation rate is calculated from the spectral rate by integrating the spectral rate over all signal frequencies ω_s. We assume narrowband spectral filtering (centered at $\omega_p/2$ with a bandwidth of 2Δ) of the signal and idler at the output, which limits out integration limits for ω_s from $\frac{1}{2}\omega_p + \Delta$ to $\frac{1}{2}\omega_p - \Delta$. We assume an ideal square filter for a simpler qualitative analysis. Hence the total bi-photon generation rate is

$$R_T = |d_{\text{eff}}\alpha_p\Phi(\Delta k)|^2 \frac{P_0}{16\pi^5 n(\omega_p)\epsilon_0 c^3} \int_{-\Delta}^{\Delta} d\delta \frac{(\frac{\omega_p}{2}+\delta)(\frac{\omega_p}{2}-\delta)}{n(\frac{\omega_p}{2}+\delta)n(\frac{\omega_p}{2}-\delta)} |\Phi(\Delta k)|^2, \tag{5.27}$$

where P_0 is the power of the pump beam from equation (5.25). We have accounted for dispersion by including the frequency dependence of the refractive index of the crystal n within the integral. For our calculations, we use the Sellemeier relations for refractive index. **All the results presented here are obtained for the case of a BBO crystal pumped at 355 nm and for the degenerate case (both signal and idler have wavelengths 710 nm) with type-I phase-matching**. The Sellemeier equations for a BBO crystal are

$${n_o}^2(\lambda) = 2.7405 + \frac{0.0184}{\lambda^2 - 0.0179} - 0.0155\lambda^2, \tag{5.28a}$$

$${n_e}^2(\lambda) = 2.3730 + \frac{0.0128}{\lambda^2 - 0.0156} - 0.0044\lambda^2, \tag{5.28b}$$

where λ is in microns and subscripts 'e' and 'o' stand for extra-ordinary and ordinary polarizations respectively. Fig. 5.2 shows the variation of refractive indices with wavelength. For the case of type-I phase-matching for a negative-uniaxial crystal as considered here, the pump has extraordinary polarization while the signal has ordinary polarization.

In the following sections we analyze the different SPDC geometries and compare the spectral and total bi-photon rates. These geometries are: (1) collinear emission and (2) non-collinear emission with collimated beams; (3) collinear emission and (4) non-collinear emission with a diffracting pump; (5) collinear emission and (6) non-collinear emission with diffracting pump, signal and idler beams.

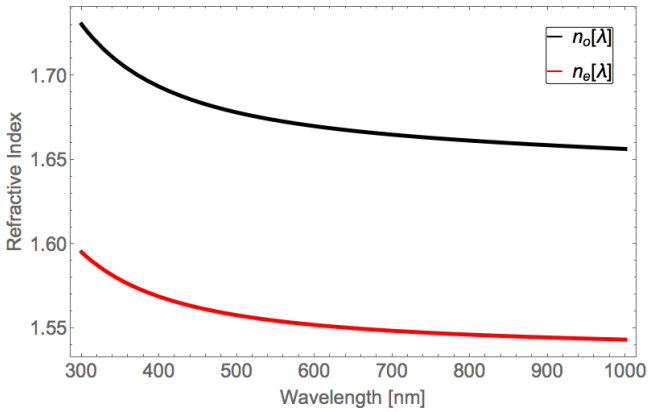

Figure 5.2: Refractive index of BBO vs wavelength for ordinary and extra-ordinary polarizations

5.3 Collimated beams

For this particular case, both the pump beam and the target signal and idler beams are treated as paraxial Gaussian beams with negligible variation of their waist size along the direction of propagation, which is a valid assumption in the thin crystal limit. The transverse mode-function (including the phase) is given by

$$g_m(x_m, y_m, z_m) = \sqrt{\frac{2}{\pi {W_m}^2}} e^{ik_m z_m} U_m(x_m, y_m) = e^{ik_m z_m} e^{-\frac{(x_m^2 + y_m^2)}{{W_m}^2}}, \tag{5.29}$$

where $k_m = \frac{2\pi}{\lambda_m}, m = i, s, p$ is the wave number of the corresponding signal, idler and pump beams, W_m is the waist size of the pump and (x_m, y_m, z_m) correspond to the local coordinate systems of each of the beams. Note that we use a slightly different convention for mode functions in this analysis than the one used for deriving the bi-photon state to be consistent with Ling's convention [28].

5.3.1 Collinear emission

For collinear emission, the coordinate systems for signal, idler and pump are the same. The expression for overlap function is

$$\Phi(\Delta k) = \frac{8}{\pi^3 W_p W_s {W_i}^2} \int_{-l/2}^{l/2} dz \int_{-\infty}^{\infty} dy \int_{-\infty}^{\infty} dx \, \exp\big(-A(x^2 + y^2) + i(k_p - k_s - k_i)z\big), \tag{5.30a}$$

$$A = \frac{1}{{W_p}^2} + \frac{1}{{W_s}^2} + \frac{1}{{W_i}^2}. \tag{5.30b}$$

Upon integration with respect to x and y, we get

$$\Phi(\Delta k) = \frac{8}{\pi W_p W_s {W_i}^2 A} \int_{-l/2}^{l/2} dz \, \exp(i(k_p - k_s - k_i)z). \tag{5.31}$$

Upon further integration with respect to z, we obtain the familiar sinc function for the overlap

$$\Phi(\Delta k) = \frac{8l}{\pi W_p W_s {W_i}^2 A} \mathrm{sinc}(\Delta k l). \tag{5.32}$$

On substituting this expression for $\Phi(\Delta k)$ in equation (4.15), we get the joint spectral rate.

For degenerate downconversion, the signal and idler wavelength is 710 nm and the states are identical in their spatial modes. For our calculations here, we assume a W_p of 35.35 μm, and W_s and W_i of 50 μm. A pair of lenses can be used to couple the signal and idler beams to single mode fibers, which typically have core diameters around 10 μm at 710 nm. The variation of spectral rate with signal wavelength while keeping the pump wavelength constant at 355 nm is shown in Fig. 5.3a. We see that the spectrum has the expected sinc-function dependence and is fairly narrowband with a FWHM bandwidth of 10 nm. Also, the highest spectral rate is obtained for the degenerate case, that is λ_s =710 nm. The bandwidth does not change even with a change in waist sizes of the beams. Narrowband filters can further increase the spectral purity of these states.

Spatial walk-off between the three collimated beams is not relevant due to collinearity. Further, for perfect phase-matching, the spectral emission rate should increase quadratically with crystal length, as shown in Fig. 5.3b. There is however an optimum waist size of the signal and idler collection modes for every pump waist and as shown in Fig. 5.3c, W_p must be $1/\sqrt{2}$ times the signal/idler waist. The crystal length was taken as 2 mm. The reason is that the overlap increases on increasing W_p until this value. For pump waists larger than this value, due to the normalization of the transverse modes (or finite amount of power carried by the pump), we get lesser pump amplitude within the overlap region thereby decreasing the value of the spectral rate. This scaling is independent of crystal length. A similar effect is also seen for the non-collinear case and has already been reported by Ling et al [28]. Fig. 5.3d shows the total rate vs crystal length, calculated by integrating over the range of frequencies within the spectral filter centred at $\omega_p/2$. The total rate increases almost quadratically until a crystal length of 1 mm and almost linearly beyond. This should be because the phase mismatch Δkl is quite small within the narrow band of frequencies for smaller crystal lengths making the sinc factor approximately 1. For larger crystal lengths, this becomes proportional to $1/\Delta kl$ which causes the smaller increase in total rate obtained by integrating

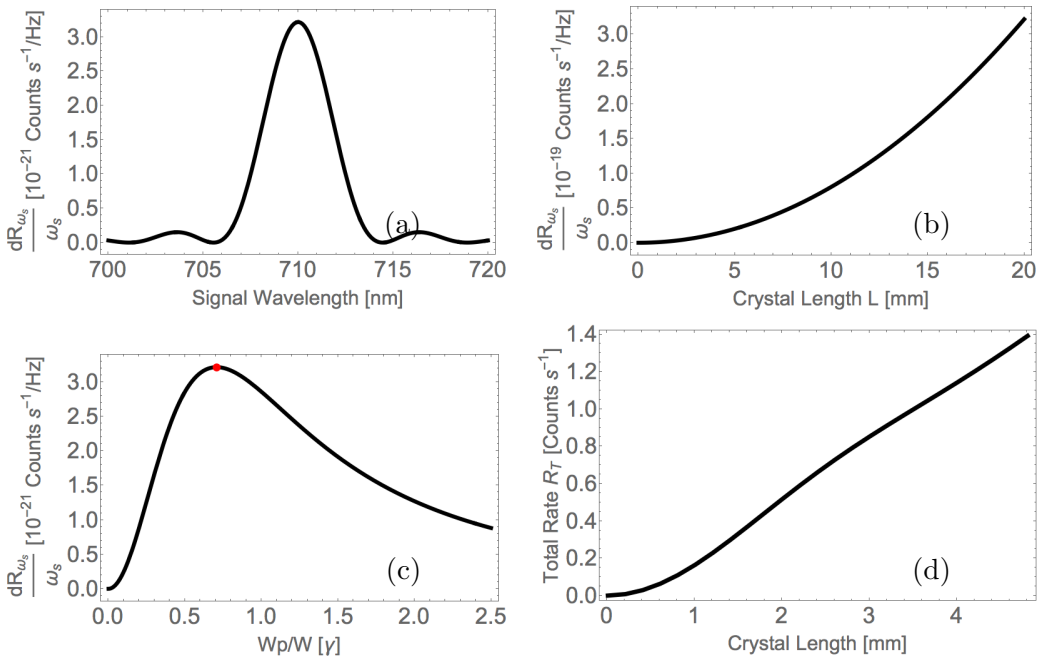

Figure 5.3: (a) Spectrum of generated signal photons is the familiar sinc() function we know for second-order nonlinear processes, (b) plot of joint spectral rate vs crystal length. The spectral rate increases quadratically with crystal length, (c) joint spectral rate vs W_p/W. The maxima occurs when $W_p/W = 1/\sqrt{2}$ and (d) total biphoton rate vs crystal length. Total rate also increases with crystal length and the trend is dependent on the bandwidth of the spectral filter used at the collection modes.

the spectral rates over the range of frequencies that are passed by the band-pass filter. If the bandwidth of the filter is made even narrower than the 5 nm taken here, the variation in total rate resembles the spectral rate very closely.

5.3.2 Non-collinear emission

Fig. 5.4. shows the setup for the case of a thin crystal pumped with a collimated Gaussian pump beam of waist size W_p and collimated Gaussian collection modes of the same waist size W propagating at an angle $\theta_s = \theta_i = \theta$ with the pump. The pump, signal and idler mode functions are

$$g_m(x_m, y_m, z_m) = \sqrt{\frac{2}{\pi {W_m}^2}} e^{ik_m z_m} U_m(x_m, y_m) = e^{ik_m z_m} e^{-\left(\frac{x_m^2 + y_m^2}{{W_m}^2}\right)} \tag{5.33}$$

where (x_m, y_m, z_m) correspond to the local coordinates of the pump, signal and idler beams. For the pump beam, the coordinate system is the same as the global coordinate system while for the signal and idler beams, they are rotated by angles

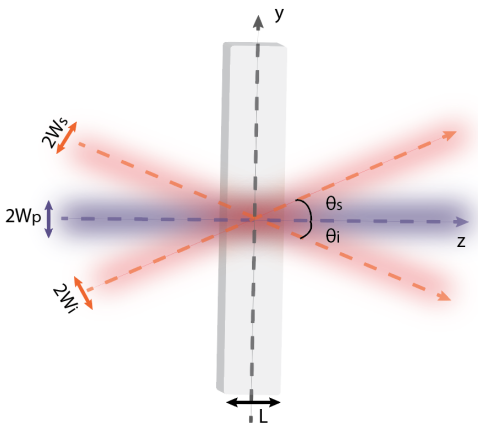

Figure 5.4: Schematic showing setup for non-collinear emission into collimated Gaussian modes

θ_s and θ_i respectively such that

$$x_s = x;\ y_s = y\cos\theta_s + z\sin\theta_s;\ z_s = -y\sin\theta_s + z\cos\theta_s, \tag{5.34a}$$

$$x_i = x;\ y_i = y\cos\theta_i - z\sin\theta_i;\ z_i = y\sin\theta_i + z\cos\theta_i. \tag{5.34b}$$

Substituting equations (5.22) and (5.23) in the equation (5.10) and upon integrating with respect to x and y, we get the following expression for the overlap integral.

$$\Phi(\Delta\mathbf{k}) = \frac{\pi}{\sqrt{AC}} e^{-{\Delta k_y}^2/4C} \int dz e^{-Hz^2+izK}, \tag{5.35}$$

where

$$
\begin{aligned}
A &= \frac{1}{W_p^2} + \frac{1}{W_s^2} + \frac{1}{W_i^2}, \\
C &= \frac{1}{W_p^2} + \frac{\cos^2\theta_s}{W_s^2} + \frac{\cos^2\theta_i}{W_i^2}, \\
D &= \frac{\sin 2\theta_s}{W_s^2} - \frac{\sin 2\theta_i}{W_i^2}, \\
F &= \frac{\sin^2\theta_s}{W_s^2} + \frac{\sin^2\theta_i}{W_i^2}, \\
H &= F - \frac{D^2}{4C}, \\
K &= \Delta k_y \frac{D}{2C} + \Delta k_z, \\
\Delta k_y &= \frac{n_o(\omega_s)\omega_s}{c}\sin\theta_s - \frac{n_o(\omega_i)\omega_i}{c}\sin\theta_i, \\
\Delta k_z &= \frac{n_{e\phi}(\omega_p)\omega_p}{c} - \frac{n_o(\omega_s)\omega_s}{c}\cos\theta_s - \frac{n_o(\omega_i)\omega_i}{c}\cos\theta_i, \\
n_{e\phi} &= \frac{1}{\sqrt{\left(\frac{\sin\phi}{n_e(\omega_p)}\right)^2 + \left(\frac{\cos\phi}{n_o(\omega_p)}\right)^2}}.
\end{aligned}
$$

Upon integration with respect to z, we get

$$
\Phi(\Delta\mathbf{k}) = \frac{\pi^{3/2}}{2\sqrt{ACH}} e^{-(\Delta {k_y}^2/4C - K^2/4H)} \left[\mathrm{Erf}\left(\frac{iK+HL}{2\sqrt{H}}\right) - i\mathrm{Erfi}\left(\frac{iK+HL}{2\sqrt{H}}\right)\right]. \tag{5.36}
$$

For our calculations, we again assume type-I phase-matching under degenerate conditions with the same mode waist W for both signal and idler beams propagating at an angle $\theta = 0.01$ rad with the pump axis within the crystal. This leads to the half-angle of the emission cone measured outside the crystal of 0.0166 rad (0.953°) from Snell's law. The pump is again taken to be at 355 nm making the degenerate signal/idler wavelength 710 nm. Fig. 5.5a shows a plot of the half-angle of the emission cone after refraction from the face of the crystal for both collinear emission and the present case. The phase-matching angle for a half-angle of 0.0166 rad is 32.954° and in the plot of Fig. 5.5a, $\theta_s = 0.953°$, shown as the horizontal dotted black line, is tangent to the graph at $\lambda_s = 710$ nm. For larger emission angles, the horizontal line intersects the curve at two different wavelengths representing two different wavelengths for the signal and idler (non-degenerate case). Fig. 5.5b shows the variation of the spectrum of $R_{\omega_s}(\omega_s)$ with W_p while maintaining W_s at 50 μm and a crystal length of 2 mm. We see that again the maxima is obtained for the degenerate case and that the spectrum becomes quite wide with tighter focussing of the pump along with an increase in the peak. This is due to

the $\sqrt{C}$ scaling of the width of the overlap function, which in turn scales inversely with W_p making the spectrum broader for a smaller pump waist. The spectral rate is also maximized when W_p is 0.707 times the W_s, similar to the collinear case. Higher bandwidth for smaller waist sizes also means a lower coherence time of the field at the detector. This indicates a lower temporal correlation between the signal and idler photons [24].

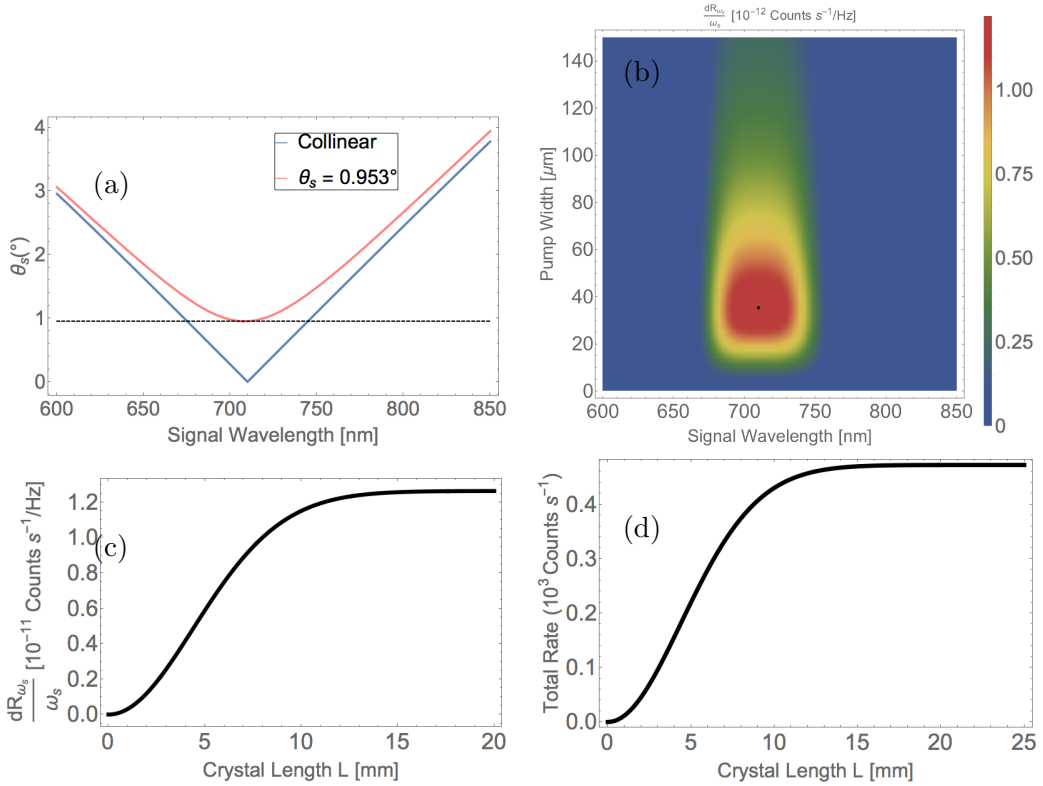

Figure 5.5: (a) Emission cone half-angle for collinear and non-collinear emission at an emission angle of 0.953 °, (b) Joint spectral rate vs signal wavelength and pump waist. The black dot is the maximum spectral rate at which $\lambda_s = 710$ nm and $W_p = 0.707 W_s$. (c) Joint spectral rate vs crystal length shows saturation of the spectral rate with crystal length as a result of walk-off due to noncollinear propagation and (d) Total biphoton rate vs crystal length also shows saturation due to walk-off

Figs. 5.5c and 5.5d show the variation of joint spectral rate and the total rate with crystal length for a W_p of 35.35 μm and W_s of 50 μm. Here we see that both rates saturate at crystal length around 20 mm. This is because of spatial walk-off due to non-collinear propagation of the three beams. For thinner crystals, the overlap continues to increase with crystal length until a certain length after which the overlap region remains the same and increasing crystal length has no effect on this. Hence there is saturation of the spectral and total rates after a certain crystal length. This saturation occurs for lower crystal lengths if we assume a wider bandwidth for the filters due to the dependence of phase-mismatch ΔkL

on the crystal length. We also note that the emission rates are higher for non-collinear emission than for collinear emission for the same crystal parameters and focussing. This is also due to the $1/\sqrt{C}$ scaling of the overlap integral, where the C parameter varies with $\cos(\theta)$. However, to get higher emission rates, we can simply make the crystal longer for collinear emission, which is not an option for non-collinear emission due to spatial walk-off.

5.4 Diffracting pump with collimated collection modes

The previous section dealt with the calculation of bi-photon generation rate into collimated Gaussian spatial modes when the crystal is also pumped with a collimated Gaussian pump beam. This is a very simplistic scenario which does hold true for thin crystals. We can however introduce more complexity to the analysis by considering the pump to be a diffracting Gaussian beam while the collection modes are taken to be collimated Gaussian spatial modes. Still, it might not be enough to completely do away with the thin crystal limit as in thicker crystals, we also need to consider diffraction in the collection modes. In the subsequent sections, we discuss how the spectral rate varies with the focussing parameter of the pump beam as well as the waist size of the collection modes for both collinear and non-collinear emission.

5.4.1 Collinear geometry

The mode function for the pump is now given by

$$g_p(\mathbf{r}) = \sqrt{\frac{2}{\pi}}\frac{W_p}{q_p}\exp\Big(-\frac{x^2+y^2}{q_p}+ik_pz\Big),\ q_p = W_p^2+2iz/k_p. \tag{5.37}$$

Here W_p is the waist size of the pump beam. The signal/idler modes on the other hand are given by

$$g_{s,i}(\mathbf{r}) = \sqrt{\frac{2}{\pi {W_{s,i}}^2}}e^{ik_{s,i}z}U_{s,i}(x,y) = e^{ik_{s,i}z_{s,i}}e^{-\frac{(x^2+y^2)}{{W_{s,i}}^2}}. \tag{5.38}$$

Substituting these expressions in equation (5.14) and integrating with respect to x and y , we get

$$\Phi(\Delta k) = \frac{2}{W_pW_sW_i}\int_{-L/2}^{L/2}dz\,\frac{1}{1+\frac{iz}{z_{\rm rp}}}\frac{1}{\frac{2}{W^2}+\frac{1}{1+\frac{iz}{z_{\rm rp}}}}\exp(i(k_p-k_s-k_i)z), \tag{5.39}$$

where z_{rp} is the Rayleigh range of the pump beam given by $z_{\mathrm{rp}} = \frac{\pi {W_p}^2}{\lambda_p}$. The integration in equation (5.39) cannot be performed analytically must be numerically calculated.

As we do not end up with a closed-form expression for the spectral rate in this case, we examine the variation in overlap integral with parameters such as crystal length, focussing parameter of the pump ($\xi = \frac{L\lambda_p}{2\pi {W_p}^2}$) and waist sizes of the collection modes. The expression for overlap integral can be re-written in terms of the focussing parameter ξ as

$$\Phi(\xi, \phi) = \int_{-1}^{1} (\frac{\xi}{A_\xi L \lambda_p})^{0.5} \frac{4 e^{i\phi u/2}}{W^2(1 + iu\xi)}, \tag{5.40}$$

where

$$A_\xi = \frac{2\pi\xi}{L} \frac{1}{\lambda_p(1 + iu\xi)} + \frac{2}{W^2},$$

and the variable $u = 2z/L$. ϕ is the phase-mismatch angle and equals $\Delta k L$, with L being the crystal length and W the collection mode waist. Since we are working in the collinear geometry, there will be no spatial walk-off with increasing the length of the crystal, similar to the case of collinear and collimated beams. Hence the overlap integral and the joint and total rates should keep increasing with crystal length.

Fig. 5.6a shows how the spatial overlap varies with W_s and the relative size

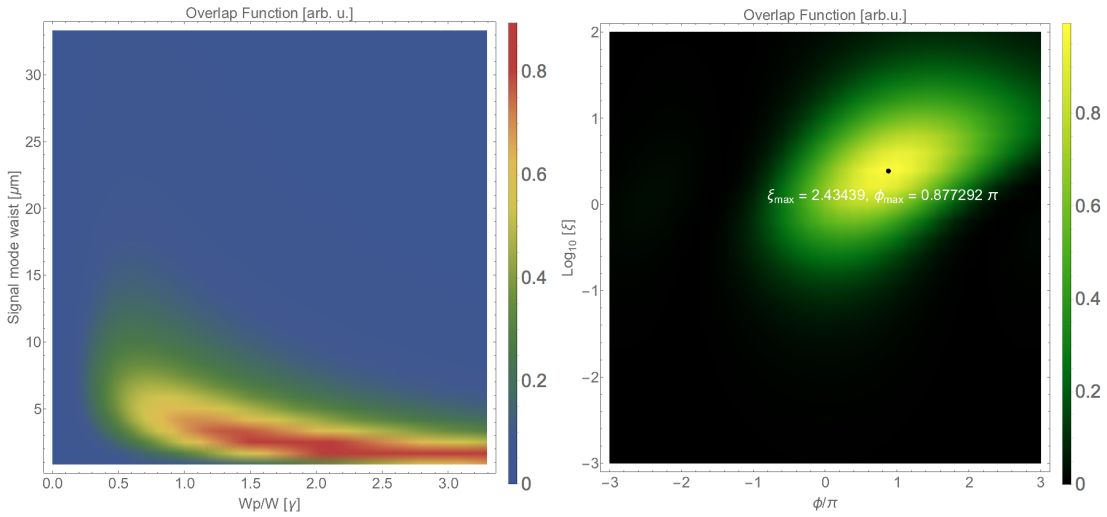

(a) (b)

Figure 5.6: (a) Overlap function vs Ratio of pump waist to signal waist 'W_p/W' vs signal mode waist W_s for a crystal length of 1 mm and (b) Variation of spatial overlap with focussing parameter, ξ, and phase-mismatch, ϕ

of the pump waist with respect to the collection mode for a fixed crystal length of 1 mm. In this case, we see that for collection mode sizes larger than 15 μm, W_p

follows the same scaling of 0.707 times the W_s. This is because the pump waist required for larger collection mode waists is also larger, which increases the overlap as we have even looser focussing conditions and we tend towards the limiting case of all three beams being collimated. The effect of diffraction becomes significant when the waist sizes of the collection modes are much smaller so that the pump needs to be more tightly focussed. To maximize the overlap, the Rayleigh range of the pump must be increased which means that W_p must be increased. This effect of diffraction is evident from Fig. 4.6b which plots the overlap integral vs the phase-mismatch ϕ and the focussing parameter ξ for a W_s of 3 μm and a crystal length of 1 mm. The maxima of the overlap occurs when $\xi = 2.434$ and $\phi = 0.877\pi$. Kleinman and Boyd in [41] have established the optimum beam parameters for sum frequency generation and parametric amplification using focussed Gaussian beams which are: $\xi = 2.84$ and $\phi = -1.01\pi$. The value of ξ in our case is close to that provided by Kleinman, but it starts deviating strongly from this value if the waist size of the collection modes is taken to be larger than 5 μm. Also, the phase mismatch is different from that calculated by Kleinman and Boyd as in our case, we only need to compensate for the Guoy phase-shift of the pump beam and not the signal and idler beams. This is not a very precise model if we are to take beam diffraction into account and talk about regimes other than the thin crystal regime where the collimated Gaussian beams assumption is valid.

5.4.2 Non-collinear Geometry

The formulation for calculation of spatial overlap is similar to the case of non-collinear emission with collimated Gaussian beams except that the pump is now given by equation (5.37). After integrating with respect to x and y, we get the following expression for overlap

$$\Phi(\Delta\mathbf{k}) = \int \frac{\pi}{\sqrt{AC}} e^{-\Delta {k_y}^2/4C} dz e^{-Hz^2+izK}, \tag{5.41}$$

where

$$
\begin{aligned}
A &= \frac{1}{W_p^2(1+\frac{iz}{z_{\mathrm{rp}}})} + \frac{1}{W_s^2} + \frac{1}{W_i^2}, \\
C &= \frac{1}{W_p^2(1+\frac{iz}{z_{\mathrm{rp}}})} + \frac{\cos^2\theta_s}{W_s^2} + \frac{\cos^2\theta_i}{W_i^2}, \\
D &= \frac{\sin 2\theta_s}{W_s^2} - \frac{\sin 2\theta_i}{W_i^2}, \\
F &= \frac{\sin^2\theta_s}{W_s^2} + \frac{\sin^2\theta_i}{W_i^2}, \\
H &= F - \frac{D^2}{4C}, \\
K &= \Delta k_y \frac{D}{2C} + \Delta k_z, \\
\Delta k_y &= \frac{n_o(\omega_s)\omega_s}{c}\sin\theta_s - \frac{n_o(\omega_i)\omega_i}{c}\sin\theta_i, \\
\Delta k_z &= \frac{n_{e\phi}(\omega_p)\omega_p}{c} - \frac{n_o(\omega_s)\omega_s}{c}\cos\theta_s - \frac{n_o(\omega_i)\omega_i}{c}\cos\theta_i, \\
n_{e\phi} &= \frac{1}{\sqrt{\left(\frac{\sin\phi}{n_e(\omega_p)}\right)^2 + \left(\frac{\cos\phi}{n_o(\omega_p)}\right)^2}},
\end{aligned}
$$

where $z_{\mathrm{rp}} = \frac{\pi {W_p}^2}{\lambda_p}$ is the Rayleigh range of the pump. The integration with respect to z over the length of the crystal has to be calculated numerically.

Fig. 5.7a shows the variation of the joint spectral rate with respect to crystal

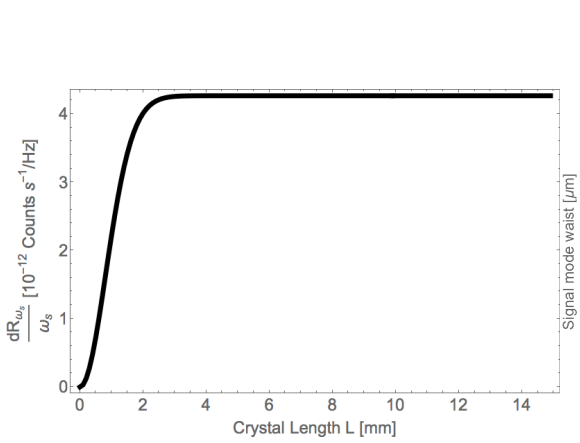

(a)

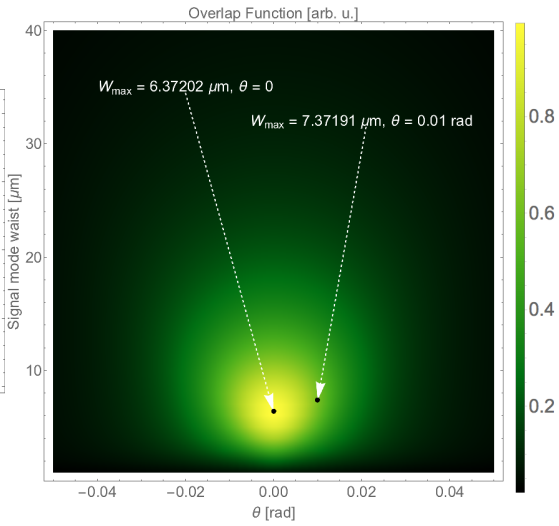

(b)

Figure 5.7: (a) Joint spectral rate vs crystal length again shows saturation with crystal length due to non-collinear propagation walk-off and (b) Variation of spatial overlap with W_s and θ. The highest overlap occurs for collinear and non-collinear propagation

length for non-collinear emission at an angle of 0.01 rad with W_s of 50 μm and W_p 0.707 times the W_s (loose focussing of the pump). In contrast to the collimated beams case, here we see that the saturation of spectral rate occurs at a much lower crystal length of 5 mm. This is due to diffraction of the pump. Fig. 5.7b. shows the variation of spatial overlap with emission angle θ for different collection mode widths while maintaining the pump width to be 0.707 times the collection mode width. The crystal length in both cases was taken to be 1 mm. We see that the maximum overlap occurs for collinear emission for a particular range of signal mode waist and the emission cone has a half angle of about 0.15 rad. The optimum W_s for collinear emission is 6.372 μm which corresponds to a focussing parameter of $\xi = 2.78393$ for the pump which is very close to the value predicted by Kleinman and Boyd [41]. For a non-collinear emission at 0.01 rad, the optimum collection mode size is 7.372 μm which corresponds to a focussing parameter of $\xi = 2.079$ for the pump. For larger emission angles, the pump needs to be focussed more loosely to increase the overlap.

5.5 Diffracting pump, signal and idler

This is the most general scenario to find the emission rates into single transverse Gaussian modes, as we can do away with the thin crystal approximation by including diffraction in all three beams. Both collinear and non-collinear emission have been examined in the subsequent sections. The waists of all the beams are assumed to be located at the centre of the crystal because from symmetry we can see that the overlap is highest when the beams have their centres co-incident [26].

5.5.1 Collinear Geometry

We calculate of the overlap integral for the degenerate case and show that the focussing parameters are the same for all three beams, that is $\xi_p = \xi_s = \xi_i$. The mode functions for all three beams are given by

$$g_m(\mathbf{r}) = \frac{W_m}{q_m} \exp\Big(-\frac{x^2+y^2}{q_m} + ik_m z_m\Big),\ q_m = W_m^2 + 2iz_m/k_m,\ m = (s,i,p). \quad (5.42)$$

Substituting these expressions for mode functions in equation (5.14) and integrating with respect to x and y we obtain

$$\Phi(\Delta k) = \frac{2\sqrt{2}}{\pi W_p W_s W_i} \int_{-L/2}^{L/2} dz \frac{1}{(1+\frac{iz}{z_{rp}})} \frac{1}{(1-\frac{iz}{z_{rs}})} \frac{1}{(1-\frac{iz}{z_{ri}})} \frac{1}{A} e^{i(k_p-k_s-k_i)z}, \quad (5.43a)$$

$$A = \frac{1}{{W_p}^2(1+\frac{iz}{z_{rp}})} + \frac{1}{{W_s}^2(1-\frac{iz}{z_{rs}})} + \frac{1}{{W_i}^2(1-\frac{iz}{z_{ri}})}, \quad (5.43b)$$

where $z_{rp} = \frac{\pi {W_p}^2}{\lambda_p}$ and $z_{rs,ri} = \frac{\pi {W_{s,i}}^2}{\lambda_s}$.

The integration with respect to z has to be carried out numerically. It is more convenient to discuss the properties of the three beams if we write the overlap integral in terms of the focussing parameters of the beams by making the substitutions $z = \frac{Lu}{2}$, $\xi_p = \frac{L\lambda_p}{2\pi {W_p}^2}$ and $\xi_{s,i} = \frac{L\lambda_{s,i}}{2\pi {W_{s,i}}^2}$ and integrating u from -1 to 1. Rewriting equation (5.43) after making these substitutions, we get

$$\Phi(\xi_p, \xi_s, \xi_i, \phi, L) = \frac{L}{\lambda_p \lambda_s \lambda_i} \int_{-1}^{1} du \frac{\sqrt{\xi_p \xi_s \xi_i} e^{(i\phi u/2)}}{A(1+iu\xi_p)(1-iu\xi_s)(1-iu\xi_i)}, \quad (5.44a)$$

$$A = \frac{2\pi}{L}\left(\frac{\xi_p}{(1+iu\xi_p)} + \frac{\xi_s}{(1-iu\xi_s)} + \frac{\xi_i}{(1+iu\xi_i)}\right), \quad (5.44b)$$

$$\phi = \Delta k L = (k_p - k_s - k_i)L. \quad (5.44c)$$

The focussing parameters of both signal and idler should be the same i.e. $\xi_s = \xi_i$ as the spatial modes of the signal and idler should be similar for degenerate SPDC.

Fig. 5.8a shows the plot of the overlap integral for the focussing parameter

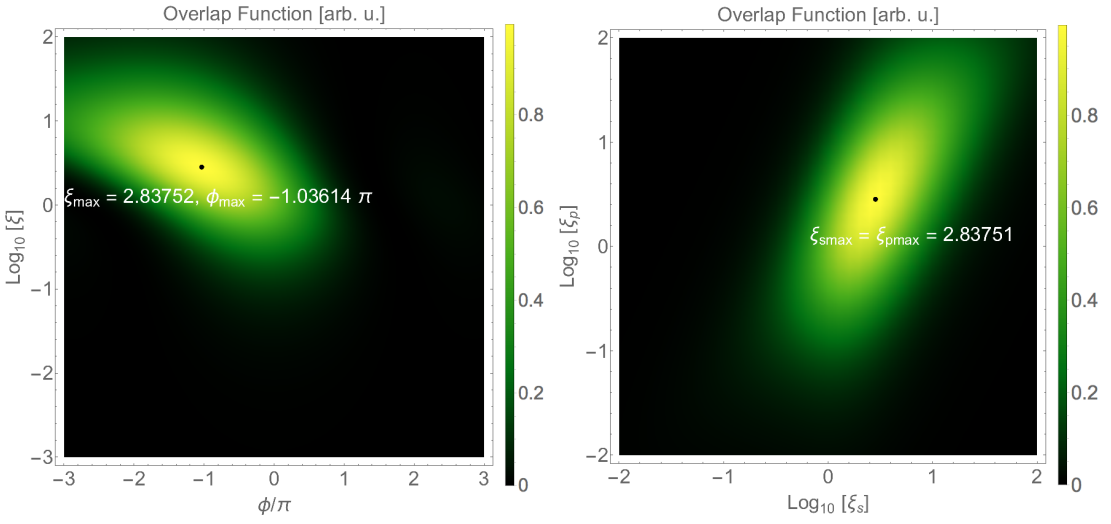

(a) (b)

Figure 5.8: (a) Overlap function vs focussing parameter $\xi = \xi_s = \xi_i = \xi_p$ vs phase-mismatch ϕ and (b) Overlap function vs ξ_s vs ξ_p. The maxima (black dot) of overlap occurs when $\xi_s = \xi_i = \xi_p \approx 2.84$ and $\phi \approx -1.04\pi$.

(taken to be the same for the pump, signal and idler) and the phase-mismatch ϕ and we see that the maximum overlap occurs when $\xi \simeq 2.8376$ and $\phi \simeq -1.036\pi$. Fig. 5.8b shows the plot spatial overlap for varying pump focussing and signal focussing parameters while maintaining the phase-mismatch at -1.036π. The crystal length for both cases was taken to be 1 mm. We see that the peak occurs when the pump focussing equals signal focussing and approximately 2.84. This confirms the assumption made previously for taking the focussing parameters of the pump, signal and idler to be the same. This also gives back the previous result where W_p is 0.707 or $1/\sqrt{2}$ times W_s. These results agree with that established by Kleinman and Boyd regarding sum-frequency generation and parametric interaction with focussed Gaussian beams [41]. Hence we conclude that the efficiency of an inherently quantum process like SPDC is maximized by the parameters that also maximize classical second-order nonlinear processes like sum- and difference-frequency generation if we consider emission into a single spatial mode.

The expression for spatial overlap derived by Bennink in [26] and shown in equation (5.45) is different from the one we derive later. Fig. 5.9 shows a plot for spatial overlap vs focussing parameter and phase-mismatch as derived by Bennink. The maxima occurs at $\xi = 2.7708$ and $\phi = -1.02\pi$ which is very close to the established values by Kleinman and Boyd [41].

$$\Phi(\xi, \phi) = \int_{-1}^{1} du \frac{\sqrt{\xi} e^{i\phi u/2}}{1 - i\xi u}. \tag{5.45}$$

5.5.2 Non-collinear Geometry

This is most general scenario for analyzing parametric downconversion rates into single transverse Gaussian modes in that we consider non-collinear emission and do away with the thin crystal approximation by considering diffraction in all the beams. Fig. 5.10 shows the schematic for this case. The pump, signal and idler field distributions are given by the following expression

$$g_m(\mathbf{r}) = \frac{W_m}{q_m} \exp\Big(- \frac{x_m^2 + y_m^2}{q_m} + ik_m z_m \Big),\ q_m = W_m^2 + 2iz_m/k_m. \tag{5.46}$$

Here W_m is the waist radius of the beam 'm' and k_m is the wave-number. Here, the subscripts m represent the local coordinate system for each beam. The local coordinate systems are obtained by rotating the global coordinates by the desired emission angle θ_s or θ_i for the signal and idler beams respectively. The expressions

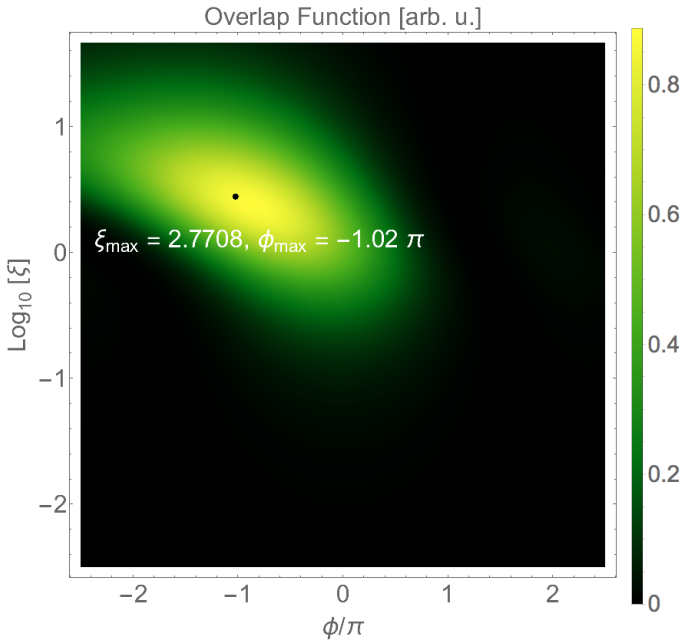

Figure 5.9: Variation of spatial overlap with focussing parameter $\xi_s = \xi_i = \xi_p$ and phase-mismatch ϕ for the model given in [26]. The maxima (black dot) occurs for values of ξ and ϕ (white text) very close to the values given by [41]

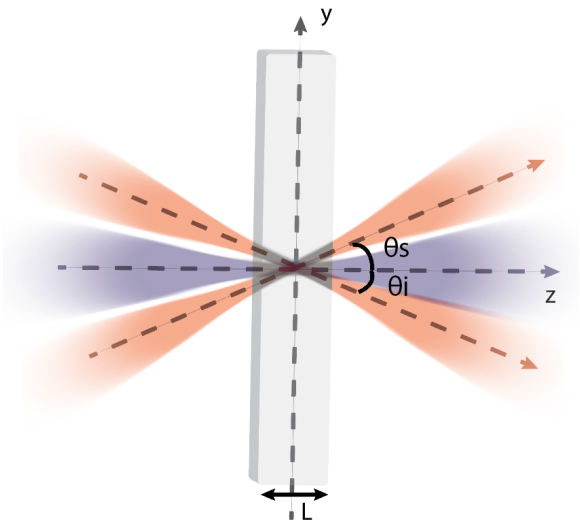

Figure 5.10: Schematic showing setup for non-collinear emission into Gaussian modes

for the rotated coordinate systems are restated for clarity.

$$x_s = x;\ y_s = y\cos\theta_s + z\sin\theta_s;\ z_s = -y\sin\theta_s + z\cos\theta_s, \tag{5.47a}$$

$$x_i = x;\ y_i = y\cos\theta_i - z\sin\theta_i;\ z_i = y\sin\theta_i + z\cos\theta_i. \tag{5.47b}$$

We get the following expression for the overlap function after substituting the mode-functions in equation (5.14)

$$\Phi(\Delta k) = \int_{-L/2}^{L/2} dz \int_{-\infty}^{\infty} dy\, dx \frac{e^{(-Ax^2-By^2-Cz^2-Dyz+iK)}}{W_s(1-i\frac{z\cos\theta_s - y\sin\theta_s}{z_{rs}})W_i(1-i\frac{(z\cos\theta_i+y\sin\theta_i}{z_{ri}})W_p(1-i\frac{z}{z_{rp}})}, \tag{5.48}$$

where

$$\begin{aligned}
A &= \frac{1}{W_p^2(1-i\frac{z}{z_{rp}})} + \frac{1}{W_s^2(1-i\frac{z\cos\theta_s - y\sin\theta_s}{z_{rs}})} + \frac{1}{W_i^2(1-i\frac{z\cos\theta_i+y\sin\theta_i}{z_{ri}})}, \\
B &= \frac{1}{W_p^2(1-i\frac{z}{z_{rp}})} + \frac{\cos^2\theta}{W_s^2(1-i\frac{z\cos\theta_s - y\sin\theta_s}{z_{rs}})} + \frac{\cos^2\theta}{W_i^2(1-i\frac{z\cos\theta_i+y\sin\theta_i}{z_{ri}})}, \\
C &= \frac{\sin^2\theta_s}{W_s^2(1-i\frac{z\cos\theta - y\sin\theta}{z_{rs}})} + \frac{\sin^2\theta_i}{W_i^2(1-i\frac{z\cos\theta+y\sin\theta}{z_{ri}})}, \\
D &= \frac{\sin 2\theta_s}{W_s^2(1-i\frac{z\cos\theta - y\sin\theta}{z_{rs}})} - \frac{\sin 2\theta_i}{W_i^2(1-i\frac{z\cos\theta+y\sin\theta}{z_{ri}})}, \\
K &= (k_i\sin\theta_i - k_s\sin\theta_s)y + (k_i\cos\theta_i + k_s\cos\theta_s - k_p)z = \Delta k_y y + \Delta k_z z.
\end{aligned}$$

The integration in x is a Gaussian integrated over the entire real axis which gives

$$\int_{-L/2}^{L/2} dz \int_{-\infty}^{\infty} dy\, \frac{\sqrt{\pi}e^{(-By^2-Cz^2-Dyz+iK)}}{\sqrt{A}W_s(1-i\frac{z\cos\theta_s - y\sin\theta_s}{z_{rs}})W_i(1-i\frac{(z\cos\theta_i+y\sin\theta_i}{z_{ri}})W_p(1-i\frac{z}{z_{rp}})}. \tag{5.49}$$

The above equation cannot be put in a form in which the y and z terms are separable, which is why the integration has to be performed numerically, which makes the calculation cumbersome.

Fig. 5.11a shows the variation of spectral rate (proportional to the overlap function) with crystal length for the degenerate case with an emission angle of $\theta_s = \theta_i = \theta = 0.01$ rad with a W_s of 50 μm and $W_p = 0.707W_s$. Fig. 5.11b shows the variation of the overlap function with crystal length for $W_s = 10\mu$m and $W_p = 0.707W_s$, or a tighter focussing of all three beams. We see that for a looser focussing, the spectral rate ultimately saturates for larger crystal lengths. For a tighter focussing, on the other hand, the spectral rate peaks at around 7 mm crystal length and then saturates. This is an effect of spatial walk-off due to both diffraction of the beams as well as the non-collinear propagation. Fig. 5.11c shows the variation of spectral rate with W_s while maintaining the W_p at 0.707 times the signal waist and a crystal length of 1 mm. The maxima occurs at a signal waist of around 8 μm which makes the focussing parameter, ξ, equal to 1.766. Fig. 5.11d shows variation of the overlap function with a focussing parameter of all three beams at a crystal length of 5 mm. Here the peak is

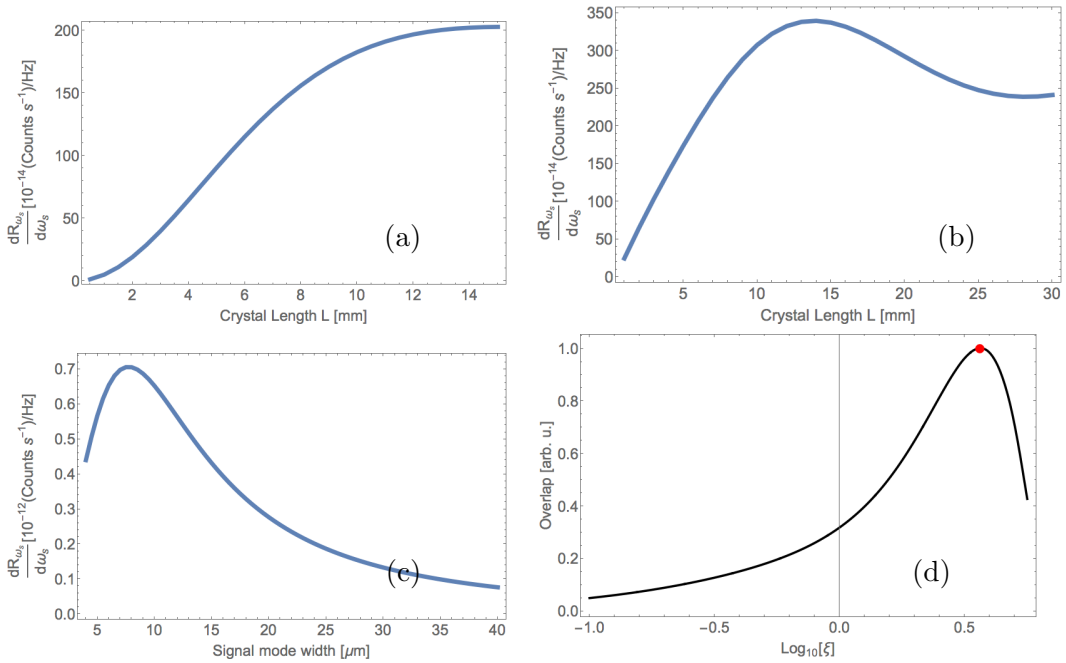

Figure 5.11: (a) Joint spectral rate vs crystal length for $W_s = W_i = 50\mu$m. For looser focussing, the behaviour is similar to collimated Gaussian beams and there is saturation of spectral rate with crystal length due to non-collinear propagation walk-off, (b) Spatial overlap vs crystal length for $W_s = W_i = 10\mu$m. For tighter focussing, the walk-off due to diffraction also contributes, (c) Joint spectral rate vs W_s for a crystal length of 1 mm. The maxima again occurs when $W_P/W_s = 1/\sqrt{2}$ and (d) Spatial overlap vs focussing parameter ξ for a crystal length of 5 mm. Red dot indicates the maxima which occurs for $\xi = 3.63$

observed at $\xi = 10^{0.56} = 3.63$. Perfect phase-matching is assumed for all cases. These values of optimum focussing parameters imply that the optimum focussing will be different for different emission angles due to non-collinear propagation. In the limit of collinear propagation, we should get the original result by Kleinman and Boyd [41].

5.6 Heralding Efficiency

Heralding efficiency is the conditional probability of detecting a photon given that its partner has already been detected. Or in other words, it is the probability that once a photon is detected, the other will be detected as well. If we define '$C_{s,i}$' as the event that the signal (idler) detector clicks and detects the photon then the heralding efficiency is

$$P(C_s|C_i) = \frac{P(C_s, C_i)}{P(C_i)}, \tag{5.50}$$

where $P(C_s|C_i)$ is the conditional probability of detecting a signal photon given that the idler has been detected, $P(C_s, C_i)$ is the joint probability of detecting

both signal and idler photons and $P(C_i)$ is the probability of detecting the idler photon. If we talk in terms of rates, then under perfect experimental conditions in which the detectors are perfectly aligned, have a unit quantum efficiency, and the collection modes couple perfectly to the modes of the detecting system, the heralding efficiency will be equal to 1 and the rate of detection of a single photon or singles will be the same as the rate of detection of both photons or coincidences. However, this is hardly ever the case in practical experiments and we are always limited by the limited quantum efficiency of detectors, the alignment of coupling fibers and noise.

5.6.1 Schmidt Decomposition

Schmidt decomposition is a method of decomposing a pure state $|\Psi\rangle$ in a bi-partite composite system AB in the following way

$$|\Psi\rangle = \sum_i \sqrt{p_i}\,|i_A, i_B\rangle\,, \tag{5.51}$$

where $|i_A\rangle$ and $|i_B\rangle$ are orthonormal states in system A and B respectively and $\sum_i p_i = 1$ [141]. The requirement is that the number of basis states used for decomposition be minimal. The higher the number of states used for decomposition, the more entangled the system is. If a single joint state can represent the state $|\Psi\rangle$, then the system is separable. We can use the dimensionality of the Schmidt decomposition of our bi-photon state to understand the entanglement of our system.

The SPDC state studied so far is entangled in two degrees of freedom, namely energy and wave-vector. This can be seen in the plane-wave mode expansion of the bi-photon state in equation (5.9) where the radial frequencies must satisfy the relation $\omega_p = \omega_s + \omega_i$. Also, the wave-vectors must be related as $\mathbf{k}_p = \mathbf{k}_s + \mathbf{k}_i$ in order to maximize the spatial overlap and hence the generation rate. In this way, if we perform a measurement of either the energy or propagation direction of the signal photon, we know for sure the energy and propagation direction of the idler photon.

The plane wave expansion of the state does not however take into account free space propagation of the signal and idler outside the crystal prior to measurement. Following [186], we express the bi-photon state in the wave-vector space as

$$|\psi_{SPDC}\rangle = \int\int d\mathbf{k}_s d\mathbf{k}_i A(\mathbf{k}_s, \mathbf{k}_i)\hat{a_s}^\dagger(\mathbf{k}_s)\hat{a_i}^\dagger(\mathbf{k}_i)\,|0,0\rangle\,, \tag{5.52}$$

where $A(\mathbf{k}_s, \mathbf{k}_i)$ is a function which describes the mode function of the pump as well as the phase-matching condition.

To get this representation, we start with equation (5.9) which is re-written with the electric field components of the pump, signal and idler written as Fourier transforms of their counterparts in the wave-vector space which are

$$E_p(\mathbf{r}, t) = \int d^3k_p \tilde{E}_p(\mathbf{k}_p) e^{i(\mathbf{k}_p \cdot \mathbf{r} - \omega_p t)}, \tag{5.53a}$$

$$E^{\dagger}_{s,i}(\mathbf{r}, t) = \int d^3k_{s,i} \tilde{E}_{s,i}(\mathbf{k}_{s,i}) e^{i(\mathbf{k}_{s,i} \cdot \mathbf{r} - \omega_{s,i} t)} a^{\dagger}_{k_s,k_i}. \tag{5.53b}$$

Substituting the above expressions in equation (5.9) we get

$$|\Psi_{SPDC}\rangle = \frac{d_{\text{eff}}}{i\hbar} \int_0^t dt_1 \int d^3r \int d^3k_p \int d^3k_s \int d^3k_i \tilde{E}_p \tilde{E}_{s,i} e^{i(\Delta\mathbf{k}\cdot\mathbf{r} - \Delta\omega t_1)} a^{\dagger}_{k_s} a^{\dagger}_{k_i} |0, 0\rangle , \tag{5.54}$$

where $\Delta\mathbf{k}(= \mathbf{k}_p - \mathbf{k}_s - \mathbf{k}_i)$ is the wave-vector mismatch and $\Delta\omega = (\omega_p - \omega_s - \omega_i)$ is the frequency mismatch. Integrating with respect to space and time we get

$$|\Psi_{SPDC}\rangle = \frac{d_{\text{eff}}}{i\hbar} \int d^3k_p \int d^3k_s \int d^3k_i \tilde{E}_p \tilde{E}_{s,i} \delta(\omega_p - \omega_s - \omega_i) \xi(\mathbf{k}_p - \mathbf{k}_s - \mathbf{k}_i) a^{\dagger}_{k_s} a^{\dagger}_{k_i} |0, 0\rangle , \tag{5.55}$$

where

$$\xi(\mathbf{k}_p - \mathbf{k}_s - \mathbf{k}_i)) = \int_{\infty}^{\infty} dx \int_{\infty}^{\infty} dy \int_{-L/2}^{L/2} dz \, e^{i(\mathbf{k}_p - \mathbf{k}_s - \mathbf{k}_i)\cdot\mathbf{r}}. \tag{5.56}$$

For transverse dimensions of the crystal much larger than its thickness, the integral along x and y axes give a Dirac delta function while that along z gives a sinc function. Equation (5.56) then becomes

$$\xi(\mathbf{k}_p - \mathbf{k}_s - \mathbf{k}_i)) = \delta(\mathbf{q}_p - \mathbf{q}_s - \mathbf{q}_i)) \sqrt{\frac{L}{\pi k_p}} \text{sinc}\left(\frac{L\Delta k_z}{2}\right) \exp\left(-i\frac{L\Delta k_s}{2}\right), \tag{5.57}$$

where $\mathbf{q}_{p,s,i}$ are transverse wave-vectors of the three beams. Now we assume that the emission angle of the signal and idler is very small so that we can make the following approximation

$$\Delta k = \frac{|\mathbf{q}_i - \mathbf{q}_s|^2}{2k_p}. \tag{5.58}$$

The steps that follow and the subsequent results are based on the analysis given in [187]. Integrating equation (5.55) with respect to k_p and assuming a collimated Gaussian pump beam of waist W_p we get

$$A(\mathbf{q}_s, \mathbf{q}_i) = \frac{W_p}{\sqrt{2\pi}} e^{-\frac{{W_p}^2}{4}|\mathbf{q}_s + \mathbf{q}_i|^2} \sqrt{\frac{2L}{\pi^2 k_p}} \text{sinc}\left(\frac{L}{4k_p}|\mathbf{q}_s - \mathbf{q}_i|^2\right) e^{-i\frac{L}{4k_p}|\mathbf{q}_s - \mathbf{q}_i|^2}, \tag{5.59}$$

where $\mathbf{q}_{s,i}$ are the transverse wave-vectors of the signal and idler respectively which can be written in cylindrical coordinates as

$$\mathbf{q}_{s,i} = \begin{pmatrix} \rho_{s,i}\cos\phi_{s,i} \\ \rho_{s,i}\sin\phi_{s,i} \\ 0 \end{pmatrix}. \tag{5.60}$$

The expression for $A(\mathbf{q}_s, \mathbf{q}_i)$ after performing the above substitution is

$$A(\rho_i, \rho_s, \phi_i, \phi_s) = \frac{W_p}{\sqrt{2\pi}} e^{-\frac{W_p^2}{4}(\rho_i^2+\rho_s^2+2\rho_i\rho_s\cos(\phi_i-\phi_s))} \sqrt{\frac{2L}{\pi^2 k_p}} \mathrm{sinc}\left(L\frac{\rho_s^2+\rho_i^2-2\rho_s\rho_i}{}\right). \tag{5.61}$$

Now we must decompose our SPDC state in a particular basis and find the probability amplitudes for the occurrence of each mode in the SPDC state. For this, the SPDC wavefunction must be projected on a set of modes in the joint basis of signal and idler. We perform the projection onto Laguerre-Gaussian basis for both signal and idler as they are circularly-symmetric solutions of the paraxial wave equation and it is easier to deal with the problem of finding overlaps for fiber modes in a cylindrical coordinate system. Since the incoming pump beam carries no angular momentum, the signal and idler must carry equal and opposite orbital angular momentum (OAM) for momentum conservation (a result that follows later). We follow the method given in reference [187] to perform the projection.

The projection amplitudes of the SPDC state onto a pair of LG modes in cylindrical coordinates $C_{p_s,p_i}^{l_s,l_i}$ are

$$C_{p_s,p_i}^{l_s,l_i} \propto \int_0^\infty \int_0^\infty \int_0^{2\pi} \int_0^{2\pi} A(\rho_i, \rho_s, \phi_i, \phi_s)[{LG_{p_s}}^{l_s}(\rho_s, \phi_s)]^*[{LG_{p_i}}^{l_i}(\rho_i, \phi_i)]^* \rho_i\rho_s d\phi_i d\phi_s d\rho_i d\rho_s, \tag{5.62}$$

where ${LG_p}^l(\rho, \phi)$ is the normalized Laguerre-Gauss mode given by

$${LG_p}^l(\rho, \phi) = (-1)^p \sqrt{\frac{W^2 p!}{2\pi(p+|l|)!}} \left(\frac{\rho W}{\sqrt{2}}\right)^{|l|} \exp\left(-\frac{\rho^2 W^2}{4}\right) {L_p}^{|l|}(\frac{\rho^2 W^2}{2}) \exp\left(i(l\phi+\frac{\pi}{2})\right). \tag{5.63}$$

W is the beam waist and is assumed to be at $z = 0$ and hence at the centre of the crystal. ${L_p}^{|l|}(.)$ is the associated Laguerre polynomial. The $\exp(il\phi)$ term accounts for helical phase of the LG mode and the beam carries an orbital angular momentum of $\pm\hbar l$. The phase-front of the beam makes l complete 2π rotations within a wavelength of propagation which causes the modes to have a zero intensity and a phase-singularity at their centre except for the cases where the azimuthal index, l, is 0. The transverse intensity pattern of the beams for $l > 0$ is shaped like a ring with the zero intensity region increasing in size as the magnitude of

l is increased. The $l = 0$ has a high intensity at the centre and its lowest order radial mode is a Gaussian. The radial index accounts for the number of bright rings present in the intensity pattern.

$A(\rho_i, \rho_s, \phi_i, \phi_s)$ in equation (5.61) can be expanded as a superposition of plane waves, each with a phase of $\exp(il(\phi_i - \phi_s))$, as follows

$$A(\rho_i, \rho_s, \phi_i - \phi_s) = \sum_{-\infty}^{\infty} f_l(\rho_i, \rho_s) e^{il(\phi_i - \phi_s)}, \tag{5.64}$$

On substituting this expression in equation (5.63) and performing the angular integration, we get

$$A(\rho_i, \rho_s, \phi_i - \phi_s) = \sum_{-\infty}^{\infty} f_l(\rho_i, \rho_s) \int_0^{2\pi} \int_0^{2\pi} e^{il_s\phi_s} e^{il_i\phi_i} e^{il(\phi_i - \phi_s)} \propto \delta_{l,-l_i}\delta_{l,l_s}. \tag{5.65}$$

This implies conservation of angular momentum, $l_s = -l_i = l$. There is no such explicit relation between the radial indices.

The sinc function can be written as the inverse Fourier transform of a step function to get

$$\mathrm{sinc}\left(\frac{|\mathbf{q}_i - \mathbf{q}_s|^2 L}{4k_p}\right) = \frac{1}{L}\int_{-L/2}^{L/2} dt \exp\left(-i\frac{|\mathbf{q}_i - \mathbf{q}_s|^2 t}{2k_p}\right). \tag{5.66}$$

The result of integration, $C_{p_s,p_i}^{l_s,l_i}$, as calculated in [187] is as follows

$$C_{p_s,p_i}^{l_s,l_i} \propto K_{p_i,p_s}^{|l|} \int_{-L/2}^{L/2} dt \frac{B^{|l|}(1-\frac{4I}{T})^{p_s}(1-\frac{4S}{T})^{p_i}}{T^{|l|+1}} \, {}_2F_1\left[\begin{matrix} -p_i, -p_s, \\ -p_i - p_s - |l| \end{matrix} \quad \frac{T(T-4I-4S+4)}{(T-4S)(T-4I)}\right], \tag{5.67}$$

where

$$K_{p_i,p_s}^{|l|} = \frac{(p_i + p_s + |l|)!}{\sqrt{p_i! p_s! (p_s + |l|)! (p_i + |l|)!}}, \tag{5.68a}$$

$$B = -\left(\frac{2t}{W_i W_s k_p} + \frac{L}{W_i W_s k_p} + \frac{iW_p^2}{W_i W_s}\right), \tag{5.68b}$$

$$I = \frac{W_p^2}{2W_i^2} + \frac{1}{2} + \frac{it}{W_i^2 k_p} + \frac{iL}{2W_i^2 k_p}, \tag{5.68c}$$

$$S = \frac{W_p^2}{2W_s^2} + \frac{1}{2} + \frac{it}{W_s^2 k_p} + \frac{iL}{2W_s^2 k_p}, \tag{5.68d}$$

$$T = 4IS + B^2. \tag{5.68e}$$

Here ${}_2F_1$ is the Gauss hypergeometric function. This integral is evaluated numerically for different values of the pump, signal and idler beam waists to get the probability amplitude, $C^{l_s,l_i}_{p_s,p_i}$, and then the probability $P^{l_s,l_i}_{p_s,p_i} = |C^{l_s,l_i}_{p_s,p_i}|^2$.

Fig. 5.12 shows the probability distributions calculated for various crystal lengths and focussing parameters. Fig. 5.12a shows $P^{0,0}_{p_s,p_i}$ vs signal and idler radial indices for $W_s = W_i = W_p = 25\mu$m, L =1 mm. We see that there are cross-correlations between the signal and idler radial indices as also discussed in [187]. Fig. 5.12b shows $P^{2,-2}_{p_s,p_i}$ for the same parameters but for a higher azimuthal index. We see an overall lower values of probabilities but a similar distribution. Fig. 5.12c shows $P^{l,-l}_{p,p}$ vs azimuthal index l and the common radial index for signal and idler p for the same parameters. For $|l| \geq 4$, the probability is quite low and we can assume that the probabilities beyond this l value are effectively zero. Fig. 5.12d shows $P^{0,0}_{p_s,p_i}$ vs signal and idler radial indices for a looser focussing of all three beams. There are much lower cross-correlations between the signal and idler radial indices in this case. As we see in a later plot, this also means a wider probability distribution in azimuthal indices. Fig. 5.12e shows $P^{0,0}_{p_s,p_i}$ vs radial indices for a longer crystal length. The overall distribution has a similar trend, except for there being a larger cross-correlation between the radial indices for particular values than others. Fig. 5.12f shows $P^{0,0}_{p_s,p_i}$ vs radial indices for the parameters as in Fig. 5.12a except for a much looser pump focussing. Although there is lowering of the values of the probabilities, we see a slightly more reduced cross-correlation between the different radial indices of signal and idler than the case of a looser focussing overall for all three beams. This also corresponds to, as we see later, a wider azimuthal probability distribution. We can say that a looser focussing of the pump has a larger effect on probability distribution than the focussing of the collection modes.

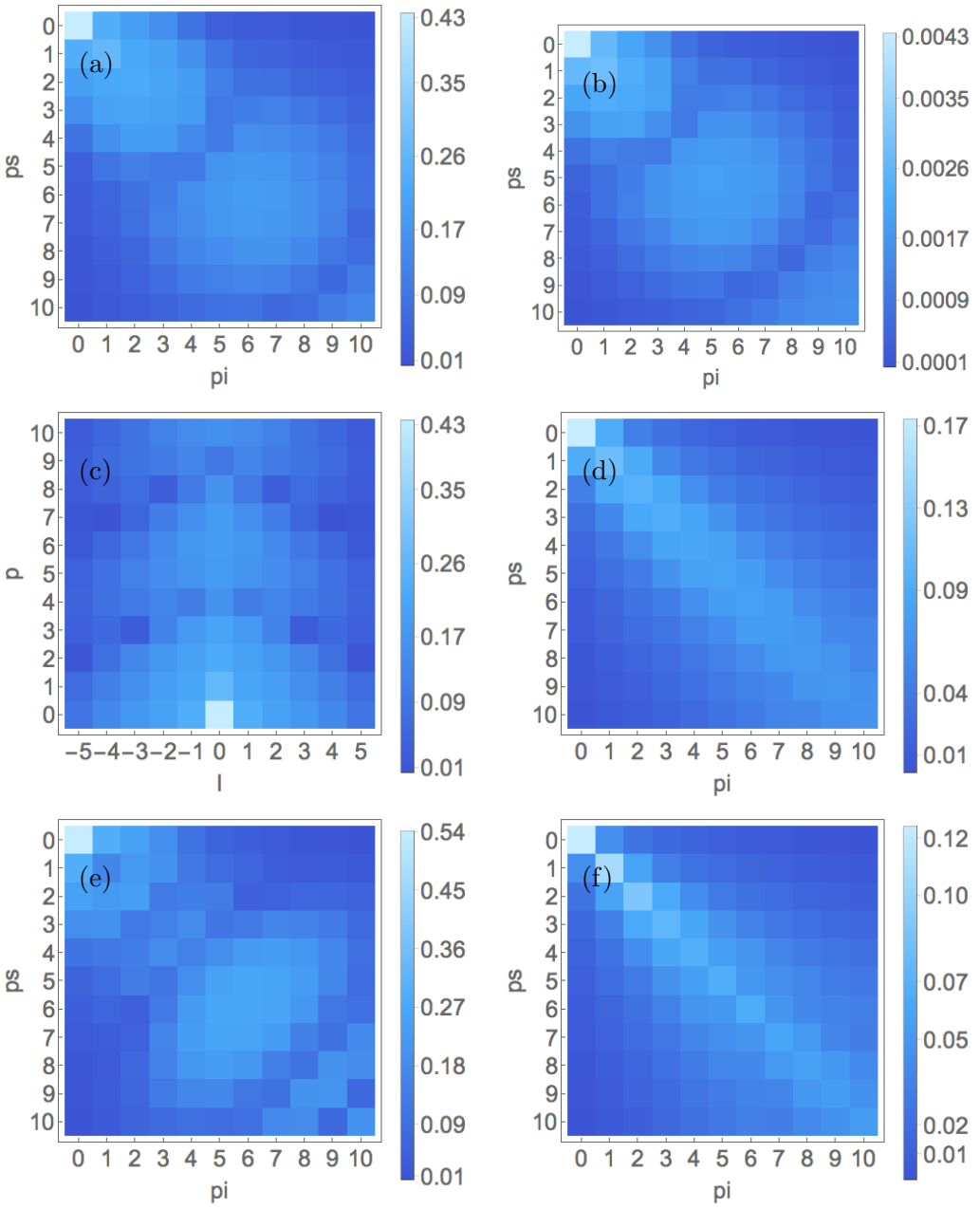

Figure 5.12: $P^{l_s,l_i}_{p_s,p_i}$ for (a) $W_s = W_i = W_p = 25\mu$m, L =1 mm and $l = 0$, (b) $W_s = W_i = W_p = 25\mu$m, L =1 mm and $l = 4$. The probability distribution with respect to radial indices for the signal and idler are similar for different azimuthal indices ($l = 0$ in (a) and $l = 4$ in (b)) except for the values of probabilities which are significantly lower for higher azimuthal indices. Also, the distribution is not orthogonal in the radial indices of signal and idler. (c) $W_s = W_i = W_p = 25\mu$m, L =1 mm and $ps = pi = p$, or probability distribution for the same radial indices for both signal and idler and different azimuthal indices. The probability decreases uniformly for higher absolute azimuthal indices. (d) $W_s = W_i = W_p = 100\mu$m, L =1 mm and $l = 0$, or looser focussing and same crystal length (e) $W_s = W_i = 25\mu$m, $W_p = 250\mu$m, L =5 mm, $l = 0$, or looser focussing but larger crystal length and (f) $W_s = W_i = W_p = 25\mu$m and L =5 mm and $l = 0$, or larger crystal length and tighter focussing

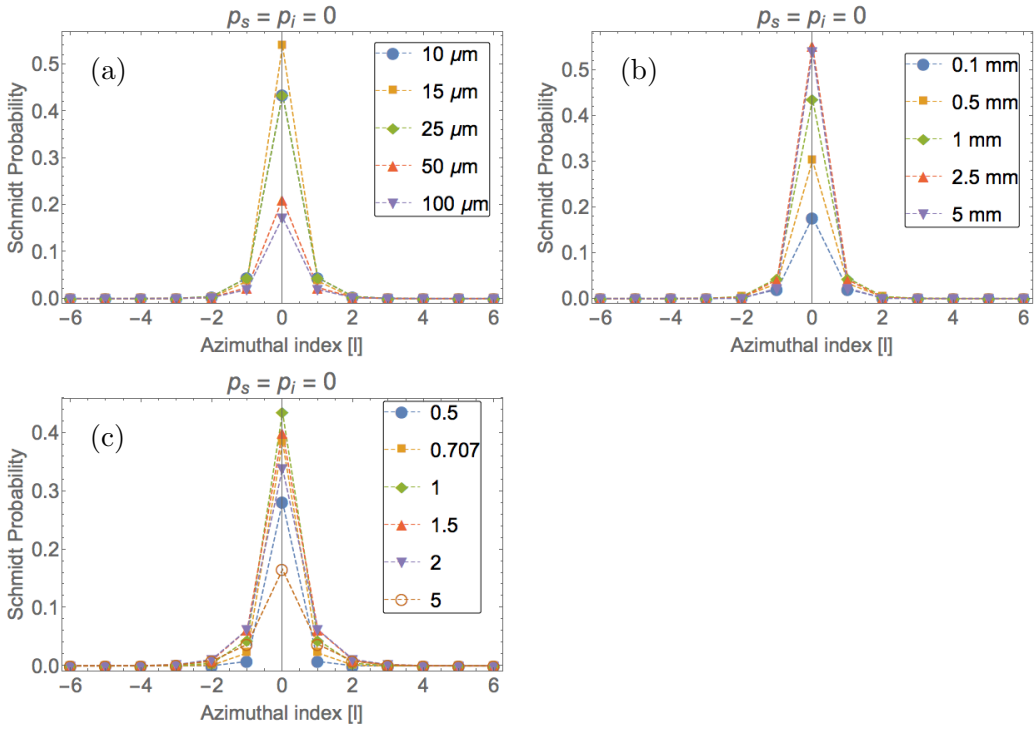

Figure 5.13: $P^{l,-l}_{0,0}$ vs l for (a) different W with $W_s = W_i = W_p$ for L =1 mm, (b) different crystal lengths for $W_s = W_i = W_p = 25\mu$m, (c) different γs where $\gamma = W_p/W$, $W_s = W_i = W$ and $L = 1$mm

Fig. 5.13a shows the joint probability distribution of Schmidt modes of the SPDC state with the azimuthal index l for a crystal of length 1 mm for different collection mode waists. Fig. 5.13b shows the joint probability distribution vs azimuthal index l for $W_s = W_i = W_p = 25$ μm and different crystal lengths. We see that the beam waist of 15 μm shows the narrowest distribution. The distribution becomes slightly wider for a lower waist of 10 μm and becomes much wider for larger waists. Also, smaller crystal lengths produce a wider probability distribution and hence give a higher degree of entanglement. Thus we can say that a looser focussing of the pump produces higher degree of entanglement. Fig. 5.13c shows the joint probability distribution vs azimuthal index l for $W_s = W_i =$ 25 μm and different degrees of pump focussing $\gamma(= W_p/W)$. It is interesting to note that the distribution is the most narrow for the same pump waist size as the collection modes and becomes wider for both tighter and looser pump focussing.

We compare these results qualitatively with the Schmidt number, K, which is the effective number of modes required for decomposition, for both tight focussing and loose focussing cases while assuming a Gaussian approximation to the phase-matching term instead of a sinc. The Schmidt number is given by [187]

$$K = \frac{1}{4}\left(\sqrt{\xi_p} + \frac{1}{\sqrt{\xi_p}}\right)^2, \tag{5.69}$$

where $\xi_p = \frac{L\lambda_p}{2\pi {W_p}^2}$ is the focussing parameter of the pump beam with wavelength λ_p, waist size W_p and crystal length L. Note that we have not included the refractive index of the crystal for our Schmidt decomposition. For a 355 nm pump beam of waist size 25 μm and crystal length 1 mm has $K = 3.28 \simeq 3$, while for a beam waist of 37.5 μm, $K = 6.723 \simeq 7$ and $K = 1.283 \simeq 1$ for $W_p = 3.75\mu$m . So we have much larger number of Schmidt modes for a looser focus. There are also larger number Schmidt modes for a very tight focus, but not as much. Also, a lower Schmidt number leads to most power being concentrated in the lowest order mode LG_0^0 as can be seen from Fig. 5.12.

5.6.2 Heralding Efficiency Calculation

The density operator of $|\Psi_{SPDC}\rangle$ can be written from equation (5.51) as

$$\hat{\rho} = \sum_{m,n} \sqrt{p_m p_n}\, |h_m, g_m\rangle \langle h_n, g_n| \,. \tag{5.70}$$

The reduced density operator of the signal state $|\Psi_s\rangle = \sum_m \sqrt{p_m}\, |g_m\rangle$ is

$$\hat{\rho}_s = \sum_m p_m\, |g_m\rangle \langle g_m| \,. \tag{5.71}$$

Detection of the signal and idler photons can be described by defining probability operator measures (POMs) [188]. The probability of a positive detection is limited by the coupling efficiency of the mode to the fiber and the quantum efficiency of the detector. The POM operator for a positive detection is $\hat{C}$, and for a negative detection is $1 - \hat{C}$ for each detector. We have a detector for each signal and idler to make coincidence measurements. The POM for each detector is given by

$$\hat{C}_s = \eta_s \sum_l q_l^s \hat{h_l}, \tag{5.72a}$$

$$\hat{C}_i = \eta_i \sum_l q_l^i \hat{g_l}, \tag{5.72b}$$

where $\eta_{s,i}$ is the quantum efficiency of the detectors and $q_{s,i}^l$ is the coupling probability of the l-th mode. The heralding efficiency is then found using the conditional probability relation of equation (5.50) as

$$\text{HE} = P(C_i|C_s) = \frac{P(C_I, C_s)}{P(C_s)} = \frac{Tr(\hat{\Psi}(\hat{C_i} \otimes \hat{C_s}))}{Tr(\hat{\Psi}_s \hat{C_s})}. \tag{5.73}$$

Substituting equations (5.71) and (5.72) in the above equation and simplifying we get the relation

$$\mathrm{HE} = \eta_i \frac{\sum_l p_l q_l^s q_l^i}{\sum_l q_l^s}. \tag{5.74}$$

5.6.3 Single mode fiber (SMF)

So far we have talked only about parametric downconversion into single transverse Gaussian modes which is relevant when we have single mode fibers coupled to photon counters to collect the signal and idler photons. The heralding efficiency for the case of a SMF, assuming a unit quantum efficiency of the coupled detector, is the probability of coupling of the signal-mode to the fiber mode given that the idler mode is already detected. This is simply the coupling efficiency of the signal mode to the fiber and will be proved mathematically later. For our calculation of heralding efficiency when we have a SMF coupled to a detector at the output port, we assume Gaussian transverse modes for both the fiber and the signal which are given by

$$U_m(x,y) = \sqrt{\frac{2}{\pi {W_m}^2}} e^{-\frac{(x^2+y^2)}{{W_m}^2}}, \tag{5.75}$$

where $m = s, f$ stand for the signal and fiber modes respectively. In equation (5.75), instead of the summation, we now only have a single element. The heralding efficiency for a SMF coupled to a detector of quantum efficiency η is then given by

$$\mathrm{HE} = \eta_i q_0^i = \eta \frac{|\int_{-\infty}^{\infty} dx\, dy\, U_s(x,y) U_f(x,y)|^2}{\int_{-\infty}^{\infty} dx\, dy\, |U_s(x,y)|^2 \int_{-\infty}^{\infty} dx\, dy\, |U_f(x,y)|^2}. \tag{5.76}$$

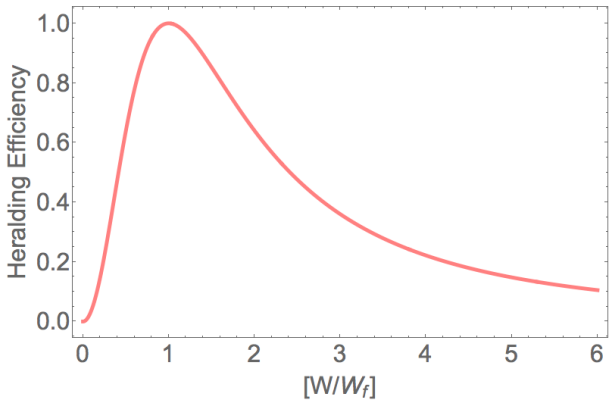

Figure 5.14: Variation of heralding efficiency HE with the ratio of fiber mode waist to the signal waist for a SMF coupled to a detector ($\eta = 1$)

Fig. 5.14 shows a plot of heralding efficiency vs the ratio of fiber-mode waist to the signal waist. Note that the efficiency is maximum when the ratio is equal to unity that is, when there is perfect mode-matching. A lens can be used to focus the signal beam and achieve perfect mode-matching. For detectors with responsivity higher than 0.5 A/W for 710 nm signal wavelength, quantum efficiencies

close to 0.9 can be achieved. Here, the quantum efficiency is taken to be perfect that is, $\eta = 1$, for ease of comparison. Thus, for a well-aligned and perfectly mode-matched fiber, we can achieve maximum HE only limited by the detector's quantum efficiency.

5.6.4 Multi-mode fiber (MMF)

The SPDC state is generated over a range of frequencies and in all spatial modes for each frequency. We post-select over a very narrow band of the frequency spectrum using band-pass filters. Using fibers to couple the SPDC modes to detectors also performs a post-selection of the spatial modes on the basis of the fiber modes. The coupling efficiencies of each signal/idler mode will be different. For a SMF, only the lowest order spatial mode, or the Gaussian, couples to the fiber and the coupling efficiencies of all other modes are very close to 0. For a MMF, we need to consider all the SPDC modes for calculation of heralding efficiency.

Coupling to multi-mode fiber

To find the heralding efficiency for the case of a MMF, we need to project each of these Laguerre-Gaussian signal/idler modes on each mode of the fiber and find their coupling efficiency. We consider a fiber with core diameter $d_0 = 50\mu$m and numerical aperture of NA= 0.1. The V-number for the fiber at 710 nm, which is the signal/idler wavelength for degenerate case) is given by

$$V = \frac{\pi d_0 \mathrm{NA}}{2\lambda_s} = 22.1239. \tag{5.77}$$

The approximate number of modes is thus $N \simeq V^2/2 = 244.733 \simeq 244$. The fiber is thus highly multimodal at this wavelength. Next we calculate the coupling efficiencies of the signal modes with fiber. We assume a signal mode waist size of 25 μm for this calculation. The fiber modes are given by [189]

$$E_{l,m}(\rho, \phi) = \frac{J_{|l|}(\frac{U_m \rho}{a})}{J_{|l|}(U_m)} e^{il\phi}, \tag{5.78}$$

where U_m is obtained by solving the following equations for each l

$$V\sqrt{1-b}\frac{J_1(V\sqrt{1-b})}{J_0(V\sqrt{1-b})} = V\sqrt{b}\frac{K_1(V\sqrt{b})}{K_0(V\sqrt{b})}, \text{for } l = 0, \tag{5.79a}$$

$$V\sqrt{1-b}\frac{J_{l-1}(V\sqrt{1-b})}{J_l(V\sqrt{1-b})} = -V\sqrt{b}\frac{K_{l-1}(V\sqrt{b})}{K_l(V\sqrt{b})}, \text{for } l \geq 0. \tag{5.79b}$$

The Laguerre-Gauss modes for radial index p and azimuthal index l in the coordinate space are given by

$$LG_p{}^l(\rho,\phi) = \sqrt{\frac{p!W^2}{2\pi(p+|l|)!}}\left(\frac{\rho\sqrt{2}}{W}\right)^{|l|}\exp\left(-\frac{\rho^2}{W^2}\right)L_p^{|l|}(\frac{2\rho^2}{W^2})\exp\left(i(l\phi)\right). \quad (5.80)$$

The coupling efficiency of each $LG_p{}^l$ mode to each (l',m) mode is found using the following expression [190]

$$q_l^p = \sum_{l',m}\frac{|\int_0^\infty\int_0^{2\pi}\rho d\rho\, d\phi\, E_{l',m}(\rho,\phi)[LG_p^l(\rho,\phi)]^*|^2}{(\int_0^\infty\int_0^{2\pi}\rho d\rho\, d\phi\,|E_{l',m}|^2\int_0^\infty)(\int_0^{2\pi}\rho d\rho\, d\phi\,|LG_p{}^l(\rho,\phi)|^2)}. \quad (5.81)$$

We assume perfect alignment of the fiber for simplicity.

Figs. 5.15 shows the coupling probabilities of the LG_p^l modes vs radial and

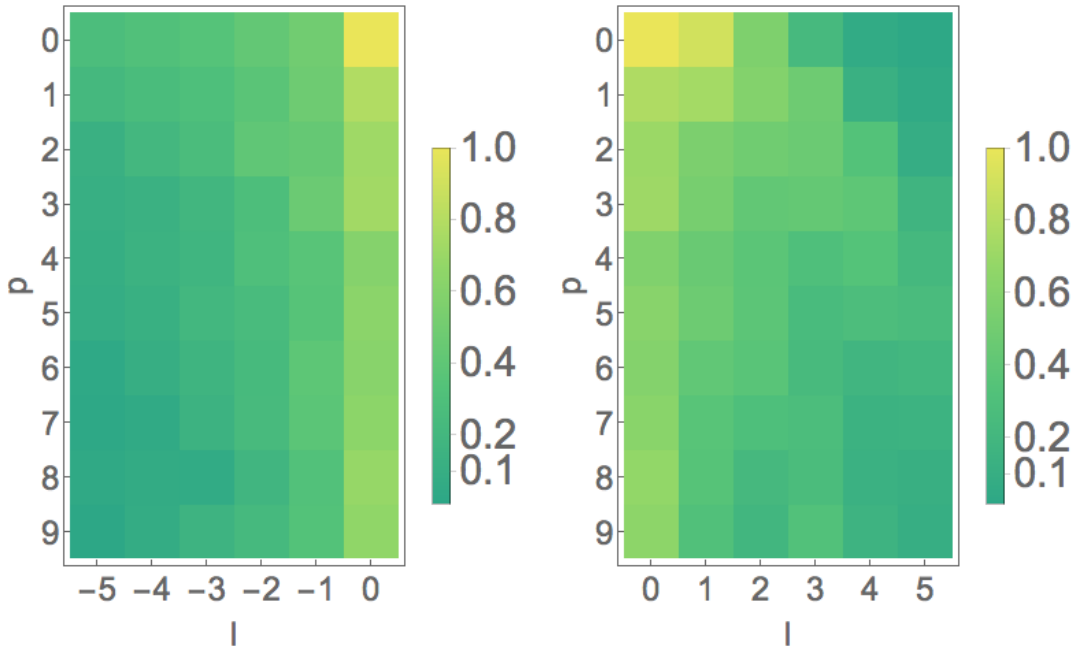

(a) (b)

Figure 5.15: Coupling probabilities of $LG_p^{|l|}$ modes vs l and p for l varying from (a) -5 to 0 and (b) 0 to 5 respectively

azimuthal indices to the given MMF of core diameter 50 μm with the emission mode waist matched to the fiber, that is $W_s = 25\mu$m. We see that the fundamental mode $l = p = 0$ always has the maximum coupling probability. The Schmidt probabilities for signal modes of different sizes as well as their coupling efficiencies with a MMF of core diameter of 25 μm were calculated using the method described in (5.6.1). The quantum efficiency, η_i, is taken as 1. The coupling efficiencies and the Schmidt probabilities so calculated are substituted in equation (5.74) to obtain

the heralding efficiency.

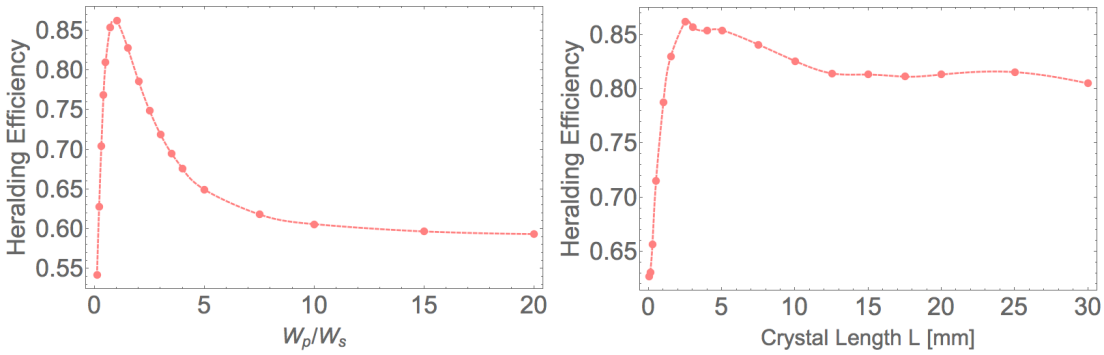

(a) (b)

Figure 5.16: Variation of heralding efficiency with (a) $\gamma(= W_p/W_s)$ and (b) crystal length L

Fig. 5.16a shows the variation of the numerically calculated heralding efficiency, HE, with the ratio of pump waist, W_p, to the signal waist, W_s for a crystal length of L =1 mm and $W_s = 25\mu$m. The maximum heralding efficiency occurs for $W_p = W_s$ and decreases for both higher and lower pump waists. Note that the optimum pump waist calculated previously for maximum bi-photon generation rate was 0.707. This is due to the different form of the phase-matching function used in both analyses. Regardless of the form used, a pump waist much closer to the collection mode waist should maximize both bi-photon rate and the heralding efficiency. But it clearly results in a lower heralding efficiency, though not by much. We also assumed perfect quantum efficiency for our detectors. A lower quantum efficiency would further reduce the difference in the expected values of HE between the two pump waists. So there is a slight trade-off, between maximizing the pair generation rate and heralding efficiency by changing the pump focussing. Also, because we are now post-selecting over a larger number of modes, there is averaging of the spatial projections which results in a lower maximum value of heralding efficiency for a multi-mode fiber than for the case of a single mode fiber ($HE_{\max} = 1$) which projects over a single mode and performs no such averaging.

Fig. 5.16b shows the variation of heralding efficiency with crystal length for $W_p = W_s = 25\mu$m. HE increases with increasing crystal length until the maxima which occurs for $L = 1$ mm and then shows a slight decrease for higher lengths and ultimately saturates at 0.805 after some variations. The reason for an increase in HE with length should be due to a decrease in the Schmidt number and a narrower probability distribution leading to the fundamental mode having the maximum emission probability and hence lower averaging. The subsequent vari-

ations for $L > 1$ mm should be due to the different spatial overlaps within the crystal which is taken as a $\mathrm{sinc}(\Delta kL)$ in our case.

5.6.5 Bucket Detectors

Bucket detectors are single-pixel detectors and provide no information other than whether a photon is incident on it or not. They do not perform any spatial filtering and each mode couples with an efficiency which depends on the overlap between that mode and the detector [191]. A Silicon transimpedence amplified photodetector with a large active area can be used as a bucket detector for our wavelength of interest (710 nm). The quantum efficiency η is related to spectral responsivity R_i of the detector by the following relation [192]

$$R_i = \eta \frac{e\lambda}{hc} \approx \eta \frac{\lambda(\mu\mathrm{m})}{1.24(\mu\mathrm{m\ W/A})}, \tag{5.82}$$

where e is the electron charge, h is the Planck's constant and c is the velocity of light. For responsivites larger than 0.46 A/W, quantum efficiency as high as 0.8 can be obtained at a wavelength of 710 nm.

Equation (5.74) can be again used for calculation of heralding efficiency. The Schmidt probabilities for the different LG_p^l modes can be obtained as before. But here the coupling efficiency of each LG_p^l mode q_l^p is calculated by finding the overlap of each mode with a circular aperture of radius 'a' equal to that of the detector's active area. Hence the equation (5.81) in our case becomes

$$q_l^p = \frac{|\int_0^a \int_0^{2\pi} \rho d\rho\, d\phi\, [LG_p^l(\rho,\phi)]|^2}{\int_0^\infty \int_0^{2\pi} \rho d\rho\, d\phi\, |LG_p{}^l(\rho,\phi)|^2}. \tag{5.83}$$

Note that in this case, for a given value of p, both $+l$ and $-l$ have the same coupling efficiency.

The coupling efficiency of modes can be varied by changing the waist size of collection modes at the detector, W_D, by one of the two ways: (1) using lenses of different focal lengths and placing the centre of the crystal (which coincides with the waist of collection and pump modes) at their foci, or (2) using a Galilean or Keplerian beam expander (a 4-f system) after the crystal. Intuitively, the heralding efficiency must be largest when the detector is underfilled as larger number of modes (higher radial and azimuthal indices) will be collected with high efficiency. As we start increasing W_D by changing the parameters of the beam expander, we start to overfill the detector and modes with higher radial and azimuthal indices have very low overlap with the detector. This lowers the summation over the radial and azimuthal indices in equation (5.74) thereby lowering the heralding efficiency.

For our analysis, we assume a signal/idler waist size of 25 μm and a detector active area radius of 0.5 mm. The crystal length is taken to be 1 mm. The quantum efficiency is also assumed to be unity for easy comparison. Fig. 5.17a shows the variation of heralding efficiency with the ratio of the collection mode waist after the beam expander to the radius of the active area a. As predicted before, the heralding efficiency increases with higher underfilling of the detector. Fig. 5.17b shows the variation of heralding efficiency with the ratio of pump waist to signal waist. The detector waist W_D is kept fixed at 50 μm, signal waist W_s as 25 μm and the crystal length as 1 mm. The coupling efficiencies of each LG_p^l mode remains the same but the Schmidt distribution varies with the pump waist. For these values of the signal and detector waists, the coupling efficiencies of modes with $p \leq 10$ and for l values within the spiral bandwidth, are very close to unity. We see a similar trend as seen for the case of the multi-mode fiber and the heralding efficiency maximizes when $W_p/W_s \simeq 1$.

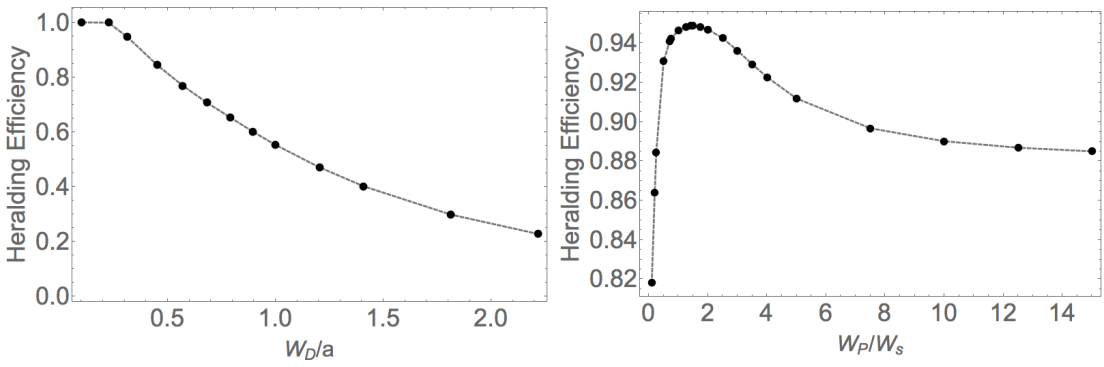

(a) (b)

Figure 5.17: Variation of heralding efficiency with (a) $\gamma(= W_D/a)$ and (b) W_p/W_s

5.6.6 Limitations of the calculation

Due to the initial assumption of nearly collinear emission, we cannot obtain a picture of what would happen for non-collinear emission in general. The optimum focussing parameters should be different in that case due to spatial walk-off associated with non-collinear propagation which is not accounted for in this method. We have also ignored diffraction effects within the crystal for the collection modes which should also change the optimum parameters. But the general result here should hold true for thin crystals and very small emission angles.

5.7 Spectral and total Radiance of the SPDC source

At this point it is useful to think in terms of the radiometric parameters of our SPDC source. The radiance, Ł$_{rad}$, of a source is the amount of power radiated by the source per unit projected area per unit solid angle [193]. Spectral radiance is the power per unit frequency radiated by the source per unit projected area per unit solid angle. Since radiance remains conserved in a lossless system, it is the most fundamental radiometric quantity and can be used to calculate all the other radiometric quantities such as irradiance, E_{rad}, radiant intensity, I_{rad}, etc.

We have calculated the spectral and total pair generation rates for our SPDC source for both non-collinear and collinear emission geometries into single transverse Gaussian modes. To keep the analysis simple, we neglect any diffraction effects within the crystal and assume non-collinear emission of signal/idler photons. The pair generation rate is also the signal/idler photon flux. Thus, the radiant power, P_{rad} is the pair generation rate R_{ω_s} times the photon energy, $\hbar\omega_s$. The spectral radiance is therefore

$$L_{\mathrm{rad}}(\omega_s) = \frac{\hbar\omega_s R_{\omega_s}(\omega_s)}{A_{proj.}\Omega_s}. \tag{5.84}$$

In order to calculate the product $A_{proj.}\Omega$, we can make use of the Friis Radiometric formula [194], which accounts for the diffractive spreading of the beams outside the crystal. According to the formula,

$$A_{proj.}\Omega = \lambda^2. \tag{5.85}$$

This is exactly valid if we consider our source to be a square aperture. In our case, the cross-section of the collection modes is circular. From the Abbe diffraction condition, the radius of cross-section 'r' of the signal beam at a distance 'R' from the crystal is given by

$$r = \frac{1.22\lambda_s R}{W_s}. \tag{5.86}$$

Thus the solid-angle subtended on the source is

$$\Omega_s = \frac{\pi r^2}{R^2} = \frac{\pi(1.22\lambda_s)^2}{W_s^2}. \tag{5.87}$$

The projected area of the source is πW_s^2. So we can write

$$A_{proj.}\Omega_s = (1.22\pi)^2\lambda^2. \tag{5.88}$$

Rewriting equation (5.85) we get

$$\mathrm{L}_{\mathrm{rad}}(\omega_s) = \frac{\hbar\omega_s R_{\omega_s}(\omega_s)}{(1.22\pi\lambda_s)^2} \tag{5.89}$$

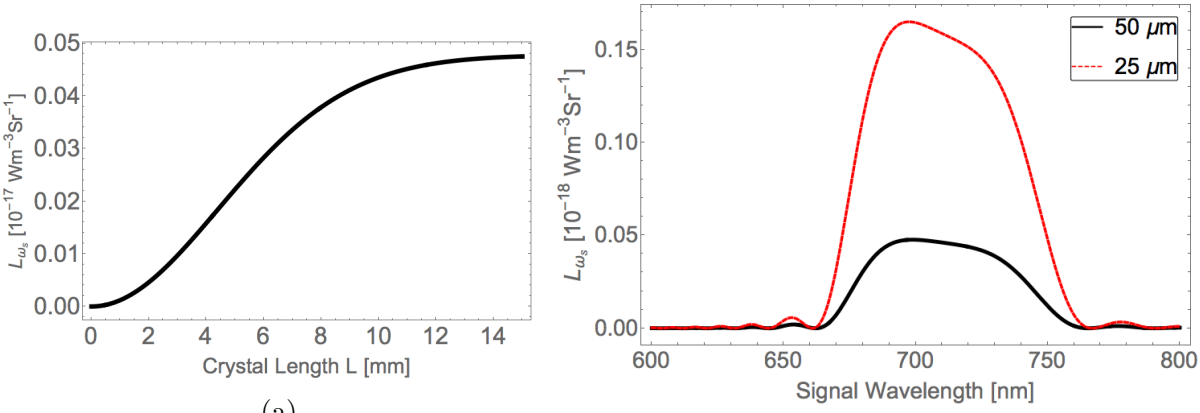

(a) (b)

Figure 5.18: Spectral radiance vs (a) crystal length and (b) signal wavelength for non-collinear emission

Fig. 5.18a shows the plot of spectral radiance or brightness vs crystal length for a collection mode waist size of $W_{s,i} = 25$ μm while using the relation obtained earlier for optimum pump waist or $W_p = 0.707W_s$. The emission angle within the crystal is taken to be $\theta_s = \theta_i = 0.01$ rad, which makes the emission cone half-angle to be 0.1667 rad. The pump wavelength is 355 nm under degenerate conditions. The spectral radiance also saturates around crystal length of 9 mm, similar to the spectral pair generation rate as seen earlier. Fig. 5.18b shows the spectrum of radiance for two different collection mode sizes: 25 μm and 50 μm and the lower collection mode waist leads to higher spectral radiance, an obvious result. The spectrum is quite broad, almost 100 nm for both cases, similar to the spectrum of the biphoton rate. There is also asymmetry in the spectrum which might be due to the $1/{\lambda_s}^2$ scaling.

To calculate the total radiance of the source, the spectral radiance must be integrated over the range of frequencies determined by the narrowband filters, with a bandwidth of 5 nm centered around the degenerate wavelength of 710 nm. Fig. 5.19 shows the scaling of the total radiance with crystal length, with the same parameters as those used for the calculation of spectral radiance, and we see that it also saturates with crystal length around 7 mm.

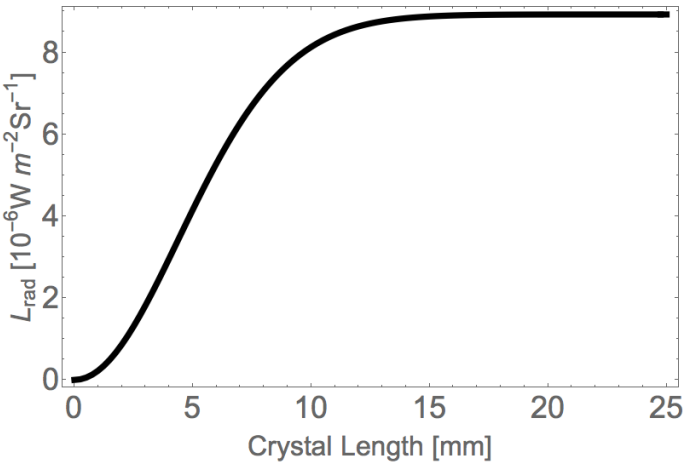

Figure 5.19: Total Radiance vs crystal length 'L' for non-collinear emission

5.8 Conclusions

We have examined the dependence of spectral and total pair generation rate of a degenerate SPDC process, which is type-I phase-matched, into a pair of single transverse Gaussian modes in collinear and non-collinear emission geometries. We observed that both spectral and total pair generation saturate with crystal length for non-collinear emission due to the effect of spatial walk-off. For collinear emission, there is no saturation and the total rate keeps increasing almost linearly with crystal length as the overlap region also keeps increasing as the crystal is made longer. For non-collinear emission, there is spatial walk-off between the three beams due to non-collinear propagation. So we see that both spectral and total rates ultimately saturate for large enough crystal lengths. Also, the optimum pump beam waist size for both cases comes out to be $1/\sqrt{2}$ of the collection mode waist size.

We also included the effect of beam diffraction in the formulation and we see that when we include diffraction in all three beams for collinear emission, we get the same results for the beam parameters as that obtained by Kleinman and Boyd in [41]. There is slight difference in the beam parameters for non-collinear emission and it may be attributed to the spatial walk-off due to non-collinearity of the beams. We have also calculated the spectral and total radiance of our SPDC source for non-collinear emission case with collimated Gaussian beams for the pump, signal and idler and we see the same trend as we saw for the spectral and total pair generation rates respectively.

Further, we have calculated the heralding efficiency (HE) for the case when we use single mode fibers for coupling the photons to the detector and we get the very obvious result that HE is maximized when the collection mode and the fundamental mode of the fiber match. We extended this analysis for multi-mode

fibers by performing Schmidt decomposition of the multi-modal SPDC state and then individually calculating the coupling efficiency of each mode to the fiber annd the heralding efficiency. We found that the optimum pump waist in this case turns out to be the same as the collection mode waist and not $1/\sqrt{2}$ times as required for maximizing the pair generation rate. Although there is not a significant difference in the heralding efficiency for the two pump waists, there is still some trade-off. This analysis was also performed for bucket detectors and we found that as predicted, focussing the collection mode waist such that the active area of the detector is underfilled maximizes the heralding efficiency. The only limiting factor in such a situation is the quantum efficiency of the detector itself. The relative scaling of pump waist and signal waist is similar to what we found for the multi-mode fiber.

5.9 Future Work

The present analysis is limited to degenerate, type-I SPDC. Also, the analysis for heralding efficiency was done for a collinear or nearly collinear geometry. A possible future work may include extension into non-degenerate SPDC with type-I as well as type-II phase-matching. Non-collinear geometry in the analysis of heralding efficiency may also be included. The theoretical results presented here may also be verified experimentally.

Chapter 6

Conclusions and future work

Here I summarize the results obtained from the original research part of this thesis (parts two and three). Although each part has its own separate concluding statements, a cohesive summary of all the relevant results presented here is presented for clarity.

The problem statement for part two was to observe superradiance in plasmonic nanoantenna arrays. Square planar arrays of gold nanorods with varying lattice constants were designed and fabricated. A simple analytical model using dipole approximation, and FDTD simulations were used to calculate the linewidths of the transmission spectrum of these arrays. The results from theoretical model and simulations were then verified using an experiment to measure the linear transmission spectrum of these arrays. The experimental values were in reasonable agreement with the numerical and analytical results. We observed a $1/a^2$ decrease in linewidth with increasing lattice constant a. This implies that the linewidth is proportional to N_{eff}, the effective number of nanoantennas within a square resonance wavelength λ_0. We consider this to be a demonstration of superradiance due to the explicit scaling of linewidth with the number of nanoantennas within an area $A < \lambda_0^2$.

The present work involved examining the radiative properties of the nanoantenna array under normal incidence. An interesting problem for future work would be to investigate the properties of the array for oblique incidence of light polarized along both s and p-polarizations. This would provide an intuition for the effect of the in-plane wave-vector on the radiative properties of the array. Further, this problem can be extended to 3-D by including a second layer of nanoantennas separated by varying distances from the original layer and investigate the effect of changing layer separations on the spectrum. This should also give an incite into how the Bloch modes within each array couple to each other depending on the separation between the two arrays.

In the third part of this thesis, we developed the scaling laws of spontaneous

parametric downconversion (SPDC) where we examined the dependence of spectral and total pair generation rate of a degenerate SPDC process, which is type-I phase-matched, into a pair of single transverse Gaussian modes in collinear and non-collinear emission geometries. We observed that both spectral and total pair generation saturate with crystal length for non-collinear emission due to the effect of spatial walk-off. For collinear emission, there is no saturation and the total rate keeps increasing almost linearly with crystal length as the overlap region also keeps increasing as the crystal is made longer. For non-collinear emission, there is spatial walk-off between the three beams due to non-collinear propagation which causes the spectral and total rates ultimately saturate for large enough crystal lengths. The optimum pump beam waist size for both cases was found to be $1/\sqrt{2}$ of the collection mode waist size.

The effect of beam diffraction was also included in the formulation and we see that when we include diffraction in all three beams for collinear emission, we get the same results for the beam parameters as that obtained by Kleinman and Boyd in [41]. There is slight difference in the beam parameters for non-collinear emission and it may be attributed to the spatial walk-off due to non-collinearity of the beams. We have also calculated the spectral and total radiance of our SPDC source for non-collinear emission case with collimated Gaussian beams for the pump, signal and idler and we see the same trend as we saw for the spectral and total pair generation rates respectively. For non-collinear emission, both spectral and total radiances saturate due to the aforementioned reasons.

We also calculated the heralding efficiency (HE) for the case when we use single mode fibers for coupling the photons to the detector and we get the very obvious result that HE is maximized when the collection mode and the fundamental mode of the fiber match. We extended this analysis for multi-mode fibers by performing Schmidt decomposition of the multi-modal SPDC state and then individually calculating the coupling efficiency of each mode to the fiber annd the heralding efficiency. We found that the optimum pump waist in this case turns out to be the same as the collection mode waist and not 0.707 times as required for maximizing the pair generation rate. Although there is not a significant difference in the heralding efficiency for the two pump waists, there is still some trade-off. This analysis was also performed for bucket detectors and we found that as predicted, focussing the collection mode waist such that the active area of the detector is underfilled maximizes the heralding efficiency. The only limiting factor in such a situation is the quantum efficiency of the detector itself. The relative scaling of pump waist and signal waist is similar to what we found for the multi-mode fiber.

The analysis presented here is limited to degenerate, type-I SPDC. This analysis can be extended to the case of non-degenerate SPDC with type-I as well

as type-II phase-matching. Non-collinear geometry in the analysis of heralding efficiency may also be included. For type-II phase-matching, the scaling laws governing the degree of polarization entanglement can be derived using a similar approach. Experimental verification of the results presented here may also be done.

Appendices

Appendix A

Matlab code for calculation of linewidths from spectrum data

```
clear all; clc;
%% Experimental results
% Declaring parameters
period = 250:50:500; % Array of lattice constants in nm
c=3e8;
linewidthexp_lam=zeros(1,length(period));
% Array for measured linewidth values
linewidthexp_freq=zeros(1,length(period));
Te1=zeros(1751,length(period));
% Measured extinction spectra for all lattice constants
Te2=Te1; % Lorentzian fitted spectra vs wavelengths
Te3 = Te1; % Lorentzian fitted spectrum for frequency
%% Finding linewidths
for k=1:length(period)
   % Loading data files
     filename=['lattice_' num2str(period(k)) '.mat'];
    load(filename);
    T2=Nanorods./ITO;
    % Normalizing response of nanorods w.r.t. ITO response
    T1=1-T2(300:length(lambda)-600); % Finding extinction for curve-fitting
    freq=(1e-12*c)./(lambda.*1e-9); % Declaring frequency array in THz
    lambda2=lambda(300:length(lambda)-600);
    % Truncated wavelength array for proper curve fitting

    [Tf param resnorm residual] = lorentzfit(lambda2,T1,[],[],'3c');
    % Lorentzian fit for wavelength spectra
    % Lorentzian fit for frequency spectra
    [Tf2 param2 resnorm2 residual2] = lorentzfit(freq(300:length(freq)...
        -600),1-T2(300:length(freq)-600),[],[],'3c');
```

```
    % Storing actual extinction spectra for each lattice constant
    Te1(1:length(lambda),k)=1-abs(T2);
    % Fitted Lorentzian spectra vs wavelengths
    Te2(1:length(lambda),k)=(param(1)*param(3))./((lambda-param(2)).^2+...
        (param(3)/2)^2) + param(4);
    % Fitted Lorentzian spectra vs frequency
    Te3(1:length(freq),k)=(param2(1)*param2(3))./((freq-param2(2)).^2+...
        (param2(3)/2)^2) + param2(4);
    %% Storing calculated \gamma values of the two Lorentzians
    linewidthexp_lam(k)=param(3); % Wavelength
    linewidthexp_freq(k)=param2(3); % Frequency

end

%figure; plot(1e9.*period,linewidthexp_lam,'-or','linesmoothing','on');
%figure; plot(1e9.*period, linewidthexp_freq,'-ob','linesmoothing','on');
%figure;
ind = 6;
%figure; plot(lambda,Te1(:,ind),'g',lambda,Te2(:,ind),'b')
%figure; plot(freq,Te1(:,ind),'g',freq,Te3(:,ind),'b')
%figure; subplot(3,2,1); plot(freq,Te1(:,1),'k',freq,Te3(:,1),'r');
%subplot(3,2,2); plot(freq,Te1(:,2),'k',freq,Te3(:,2),'r')
%subplot(3,2,3); plot(freq,Te1(:,3),'k',freq,Te3(:,3),'r')
%subplot(3,2,4); plot(freq,Te1(:,4),'k',freq,Te3(:,4),'r')
%subplot(3,2,5); plot(freq,Te1(:,5),'k',freq,Te3(:,5),'r')
%subplot(3,2,6); plot(freq,Te1(:,6),'k',freq,Te3(:,6),'r')

%% Simulation results
clear lambda;
% Declaring parameters
linewidthsim_lam=zeros(1,length(period));
% Array for measured linewidth values
linewidthsim_freq=zeros(1,length(period));
Ts1=zeros(150,length(period));
% Measured extinction spectra for all lattice constants
Ts2=Ts1; % Lorentzian fitted spectra vs wavelengths
Ts3 = Ts1; % Lorentzian fitted spectrum for frequency
%% Finding linewidths
for k=1:length(period)
   % Loading data files
     filename=['sim_2_1100_Au_ito_' num2str(period(k)) '.mat'];
    load(filename);
    T1s=1-T; % Finding extinction for curve-fitting
    lam = lambda.*1e9;
    freqs = f.*1e-12;
    [Tsf params resnorms residuals] = lorentzfit(lam(30:115),...
        T1s(30:115),[],[],'3c'); % Lorentzian fit for wavelength spectra
```

```
    % Lorentzian fit for frequency spectra
    [Tsf2 params2 resnorms2 residuals2] = lorentzfit(freqs(30:130),...
        T1s(30:130),[],[],'3c');
    % Storing actual extinction spectra for each lattice constant
    Ts1(1:length(lambda),k)= T1s;
    % Fitted Lorentzian spectra vs wavelengths
    Ts2(1:length(lambda),k)=(params(1)*params(3))./((lam-params(2)).^2+...
        (params(3)/2)^2) + params(4);
    % Fitted Lorentzian spectra vs frequency
    Ts3(1:length(freqs),k)=(params2(1)*params2(3))./((freqs-...
        params2(2)).^2+(params2(3)/2)^2) + params2(4);
    %% Storing calculated \gamma values of the two Lorentzians
    linewidthsim_lam(k)=params(3); % Wavelength
    linewidthsim_freq(k)=params2(3); % Frequency

end
periodi = 240:5:505;
lfit_ana = 0.95e7.*(periodi.^(-2));
lfit_exp = 2.38e6.*(periodi.^(-1.82));
lfit_sim = 1.112e7.*(periodi.^(-2.024));
period2 = 300:50:500;
% linewidthana_freq = [183.044 120.452 84.201 60.765 45.640 32.963];
linewidthana_freq = [104.784 77.342 59.851 48.465 39.384];
figure; plot(period, linewidthexp_freq,'ob',periodi, lfit_exp,'-b',...
    'linesmoothing','on');
hold on; plot(period, linewidthsim_freq,'or',periodi, lfit_sim,'-r',...
    'linesmoothing','on');
hold on; plot(period2, linewidthana_freq,'ok',periodi, lfit_ana,'-k',...
    'linesmoothing','on');

 %% lorentzfit() function
 function [yprime params resnorm residual] = lorentzfit(x,y,p0,bounds,nparams)
% LORENTZFIT fits a single- or multi-parameter Lorentzian function to data
%
%   LORENTZFIT(X,Y) returns YPRIME(X), a Lorentzian fit to the data
%   found using LSQCURVEFIT. The function Y(X) is fit by the model:
%       YPRIME(X) = P1./((X - P2).^2 + P3) + C.
%
%   [YPRIME PARAMS RESNORM RESIDUAL] = LORENTZFIT(X,Y) returns YPRIME(X)
%   values in addition to fit-parameters PARAMS = [P1 P2 P3 C]. The RESNORM
%   and RESIDUAL outputs from LSQCURVEFIT are also returned.
%
%   [...] = LORENTZFIT(X,Y,P0) can be used to provide starting
%   values (P0 = [P01 P02 P03 C0]) for the parameters in PARAMS.
%
%   [...] = LORENTZFIT(X,Y,P0,BOUNDS) may be used to define lower
%   and upper bounds for the possbile values for each parameter in PARAMS.
```

```
%       BOUNDS = [LB1 LB2 LB3 LB4;
%                 UB1 UB2 UB3 UB4].
%   If the user does not wish to manually define values for P0, it may be
%   enetered as an empty matrix P0 = []. In this case, default values will
%   be used. The default bounds for all parameters are (-Inf,Inf).
%
%   [...] = LORENTZFIT(X,Y,P0,BOUNDS,NPARAMS) may be used to specify the
%   number of parameters used in the Lorentzian fitting function. The
%   number of parameters defined in P0 and BOUNDS must match the function
%   specified by NPARAMS. If the user does not wish to manually define
%   values for P0 or BOUNDS, both may be enetered as empty matricies:
%   P0 = []; BOUNDS = [].
%
%   -NPARAMS options
%
%           '1'     - Single parameter Lorentzian (no constant term)
%                     L1(X) = 1./(P1(X.^2 + 1))
%
%           '1c'    - Single parameter Lorentzian (with constant term)
%                     L1C(X) = 1./(P1(X.^2 + 1)) + C
%
%           '2'     - Two parameter Lorentzian (no constant term)
%                     L2(X) = P1./(X.^2 + P2)
%
%           '2c'    - Two parameter Lorentzian (with constant term)
%                     L2C(X) = P1./(X.^2 + P2) + C
%
%           '3'     - Three parameter Lorentzian (no constant term)
%                     L3(X) = P1./((X - P2).^2 + P3)
%
% [DEFAULT] '3c'    - Three parameter Lorentzian (with constant term)
%                     L3C(X) = P1./((X - P2).^2 + P3) + C
%
%   X and Y must be the same size, numeric, and non-complex. P0 and BOUNDS
%   must also be numeric and non-complex. NPARAMS is a character array.
%
%   Examples:
%       x = -16:0.1:35;
%       y = 19.4./((x - 7).^2 + 15.8) + randn(size(x))./10;
%       [yprime1 params1 resnorm1 residual1] = lorentzfit(x,y,[20 10 15 0]);
%       figure; plot(x,y,'b.','LineWidth',2)
%       hold on; plot(x,yprime1,'r-','LineWidth',2)
%
%       [yprime2 params2 resnorm2 residual2] = lorentzfit(x,y,[],[],'3');
%       figure; plot(x,y,'b.','LineWidth',2)
%       hold on; plot(x,yprime2,'r-','LineWidth',2)
%
```

```
%   See also: lsqcurvefit.

% Jered R Wells
% 11/15/11
% jered [dot] wells [at] duke [dot] edu
%
% v1.1 (03/09/12)
%
% REF: http://www.home.uos.de/kbetzler/notes/fitp.pdf
%

% Check inputs

p3 = ((max(x(:))-min(x(:)))./10).^2;
p2 = (max(x(:))+min(x(:)))./2;
p1 = max(y(:)).*p3;
c = min(y(:));

lb = [-Inf,-Inf,-Inf,-Inf];
ub = [Inf,Inf,Inf,Inf];

if ~all(size(x)==size(y)); error 'X and Y must be the same size'; end
if ~isnumeric(x)||~isreal(x); error 'X must be numeric and real'; end
if ~isnumeric(y)||~isreal(y); error 'Y must be numeric and real'; end
if nargin==2;
    p0 = [p1 p2 p3 c];
elseif nargin==3
    if ~isnumeric(p0)||~isreal(p0);error 'P0 must be numeric and real';end
    if isempty(p0);
        p0 = [p1 p2 p3 c];
    elseif numel(p0)~=4
        error 'P0 must be empty or it must contain four parameter values';
    end
elseif nargin==4
    if ~isnumeric(p0)||~isreal(p0);error 'P0 must be numeric and real';end
    if isempty(p0);
        p0 = [p1 p2 p3 c];
    elseif numel(p0)~=4
        error 'P0 must be empty or it must contain four parameter values';
    end
    if ~isnumeric(bounds)||~isreal(bounds)
        error 'BOUNDS must be numeric and real';
    end
    if isempty(bounds)
    elseif ~all(size(bounds)==[2 4])
        error 'BOUNDS must be empty or it must be a 2x4 matrix';
    else
```

```
        lb = bounds(1,:);
        ub = bounds(2,:);
    end
    if any(lb>=ub)
        error 'Lower bounds must be less than upper bounds';
    end

elseif nargin==5
    if ~isnumeric(p0)||~isreal(p0);error 'P0 must be numeric and real';end
    if ~isnumeric(bounds)||~isreal(bounds)
        error 'BOUNDS must be numeric and real';
    end

    switch lower(nparams)
        case '1'
            % Define P0, LB, UB
            if isempty(p0);
                p1 = max(y(:)); p0 = p1;
            elseif numel(p0)~=1
                error 'P0 must be empty or have one element for ...
                NPARAMS = ''1''';
            end

            if isempty(bounds)
                lb = -Inf; ub = Inf;
            elseif ~all(size(bounds)==[2 1])
                error 'BOUNDS must be empty or it must be a 2x1 matrix for...
                 NPARAMS = ''1''';
            else
                lb = bounds(1,:); ub = bounds(2,:);
            end

            if any(lb>=ub)
                error 'Lower bounds must be less than upper bounds';
            end

            [params resnorm residual] = lsqcurvefit(@lfun1,p0,x,y,lb,ub);
            yprime = lfun1(params,x);

        case '1c'
            % Define P0, LB, UB
            if isempty(p0);
                p1 = max(y(:)); p0 = [p1 c];
            elseif numel(p0)~=2
                error 'P0 must be empty or have two elements for ...
                NPARAMS = ''1c''';
            end
```

```
        if isempty(bounds)
            lb = [-Inf,-Inf]; ub = [Inf,Inf];
        elseif ~all(size(bounds)==[2 2])
            error 'BOUNDS must be empty or it must be a 2x2 matrix for ...
            NPARAMS = ''1c''';
        else
            lb = bounds(1,:); ub = bounds(2,:);
        end

        if any(lb>=ub)
            error 'Lower bounds must be less than upper bounds';
        end

        [params resnorm residual] = lsqcurvefit(@lfun1c,p0,x,y,lb,ub);
        yprime = lfun1c(params,x);
    case '2'
        % Define P0, LB, UB
        if isempty(p0);
            p2 = ((max(x(:))-min(x(:)))./10).^2;
            p1 = max(y(:)).*p2;
            p0 = [p1 p2];
        elseif numel(p0)~=2
            error 'P0 must be empty or have two elements for...
             NPARAMS = ''2''';
        end

        if isempty(bounds)
            lb = [-Inf,-Inf]; ub = [Inf,Inf];
        elseif ~all(size(bounds)==[2 2])
            error 'BOUNDS must be empty or it must be a 2x2 matrix for ...
            NPARAMS = ''2''';
        else
            lb = bounds(1,:); ub = bounds(2,:);
        end

        if any(lb>=ub)
            error 'Lower bounds must be less than upper bounds';
        end

        [params resnorm residual] = lsqcurvefit(@lfun2,p0,x,y,lb,ub);
        yprime = lfun2(params,x);
    case '2c'
        % Define P0, LB, UB
        if isempty(p0);
            p2 = ((max(x(:))-min(x(:)))./10).^2;
            p1 = max(y(:)).*p2;
```

```
            p0 = [p1 p2 c];
        elseif numel(p0)~=3
            error 'P0 must be empty or have three elements for ...
            NPARAMS = ''2c''';
        end

        if isempty(bounds)
            lb = [-Inf,-Inf,-Inf]; ub = [Inf,Inf,Inf];
        elseif ~all(size(bounds)==[2 3])
            error 'BOUNDS must be empty or it must be a 2x3 matrix for...
             NPARAMS = ''2c''';
        else
            lb = bounds(1,:); ub = bounds(2,:);
        end

        if any(lb>=ub)
            error 'Lower bounds must be less than upper bounds';
        end

        [params resnorm residual] = lsqcurvefit(@lfun2c,p0,x,y,lb,ub);
        yprime = lfun2c(params,x);
    case '3'
        % Define P0, LB, UB
        if isempty(p0);
            p0 = [p1 p2 p3];
        elseif numel(p0)~=3
            error 'P0 must be empty or have three elements for ...
            NPARAMS = ''3''';
        end

        if isempty(bounds)
            lb = [-Inf,-Inf,-Inf]; ub = [Inf,Inf,Inf];
        elseif ~all(size(bounds)==[2 3])
            error 'BOUNDS must be empty or it must be a 2x3 matrix for ...
            NPARAMS = ''3''';
        else
            lb = bounds(1,:); ub = bounds(2,:);
        end

        if any(lb>=ub)
            error 'Lower bounds must be less than upper bounds';
        end

        [params resnorm residual] = lsqcurvefit(@lfun3,p0,x,y,lb,ub);
        yprime = lfun3(params,x);
    case '3c'
        % Define P0, LB, UB
```

```
            if isempty(p0);
                p0 = [p1 p2 p3 c];
            elseif numel(p0)~=4
                error 'P0 must be empty or have four elements for ...
                NPARAMS = ''3c''';
            end

            if isempty(bounds)
            elseif ~all(size(bounds)==[2 4])
                error 'BOUNDS must be empty or it must be a 2x4 matrix for ...
                NPARAMS = ''3c''';
            else
                lb = bounds(1,:); ub = bounds(2,:);
            end

            if any(lb>=ub)
                error 'Lower bounds must be less than upper bounds';
            end

            [params resnorm residual] = lsqcurvefit(@lfun3c,p0,x,y,lb,ub);
            yprime = lfun3c(params,x);
        otherwise
            error 'Invalid entry for NPARAMS'
    end
    return
else
    error 'Invalid number of input arguments specified';
end

[params resnorm residual] = lsqcurvefit(@lfun3c,p0,x,y,lb,ub);
yprime = lfun3c(params,x);

end % MAIN

function F = lfun1(p,x)
F = 1./(p.*(x.^2 + 1));
end % LFUN1

function F = lfun1c(p,x)
F = 1./(p(1).*(x.^2 + 1)) + p(2);
end % LFUN1C

function F = lfun2(p,x)
F = p(1)./(x.^2 + p(2));
end % LFUN2

function F = lfun2c(p,x)
```

```
F = p(1)./(x.^2 + p(2)) + p(3);
end % LFUN2C

function F = lfun3(p,x)
F = (p(1)*p(3))./((x-p(2)).^2+(p(3)/2)^2);
end % LFUN3

function F = lfun3c(p,x)
F = (p(1)*p(3))./((x-p(2)).^2+(p(3)/2)^2) + p(4);
end % LFUN3C
```

Appendix B

Mathematica code for SPDC calculations

Collinear emission case with collimated beams

(SI units used)

```
Clear["Global`*"]
$Assumptions = {n0 > 0, ωp ∈ Reals, m > 0, 0 < u < 1, 0 < v < 1, L > 0, k ∈ Reals, Δ > 0, W > 0, Wp > 0};
(*Lengths in m, susceptibility in m/V, angles in rad*)
```

L = Crystal length,
W = Signal/Idler SMF mode diameter
Wp = Pump diameter
$\theta s = \theta i = \theta$ = Angles of the overlapping signal and idler fiber modes used in calculation of overlap integral
λp = Pump Wavelength
λs = Signal Wavelength
$\lambda i = \frac{1}{\frac{1}{\lambda s} - \frac{1}{\lambda p}}$ = Idler Wavelength
z = Distance from crystal along propagation direction (= 1m here)
ϕ = Overlap Integral
Rωs = Joint Spectral Emission Rate
Φrad = Spectral Radiant Flux
Erad = Spectral Irradiance (at the detector/fiber) (Can also calculate it for the source by replacing the differential area with that of the source)
Irad = Spectral Radiometric Intensity
Lrad = Spectral Brightness or Spectral Radiance

Degenerate SPDC With Type-I Phase-Matching

```
c =  3 × 10^8; d = 2.4 × 10^-12;
ϵ0 = 8.85 × 10^-12; hbar = 1.054 × 10^-34;
ω[λ_] := (2 Pi c) / λ ;
no[λ_] := Sqrt[2.7405 + 0.0184 / (λ * 10^6)^2 - 0.0155 (λ * 10^6)^2];
(*BBO Sellmeier Equation for Ordinary Index, co-efficients in micron and micron squared*)
ne[λ_] := Sqrt[2.3730 + 0.0128 / (λ * 10^6)^2 - 0.0044 (λ * 10^6)^2];
(*BBO Sellmeier Equation for Extra-Ordinary Index, co-efficients in micron and micron squared*)
```

$$\Delta kz[\lambda p\_, \lambda s\_] := \frac{ne[\lambda p]\,\omega[\lambda p]}{c} - \frac{no[\lambda s]\,\omega[\lambda s]}{c} - \frac{no\left[\frac{\lambda p\,\lambda s}{\lambda s - \lambda p}\right](\omega[\lambda p] - \omega[\lambda s])}{c};$$

$$A1[Wp\_, Ws\_, Wi\_] := \frac{1}{Wp^2} + \frac{1}{Ws^2} + \frac{1}{Wi^2};$$

```
(*Assuming core diameters of both SMFs for signal and idler are the same as W and θs=θi = 0 for collinear emission*)
```

$$ne\phi[\lambda p\_, \lambda s\_, \phi\_] := \left(\frac{Sin[\phi]^2}{ne[\lambda p]^2} + \frac{Cos[\phi]^2}{no[\lambda p]^2}\right)^{-1/2}$$

$$\phi 0[\phi\_, \lambda p\_, \lambda s\_] := \phi /. FindRoot\left[\frac{1}{no[\lambda s]^2} == \frac{Sin[\phi]^2}{ne[\lambda p]^2} + \frac{Cos[\phi]^2}{no[\lambda p]^2}, \{\phi, 0.5\}\right];$$

$$\Delta kz\phi[\lambda p\_, \lambda s\_, \phi\_] := \frac{ne\phi[\lambda s, \lambda p, \phi]\,\omega[\lambda p]}{c} - \frac{no[\lambda s]\,\omega[\lambda s]}{c} - \frac{no\left[\frac{\lambda p\,\lambda s}{\lambda s - \lambda p}\right](\omega[\lambda p] - \omega[\lambda s])}{c};$$

```
ϕ2[λp_, λs_] := ϕ /. FindRoot[Δkzϕ[λp, λs, ϕ] == 0, {ϕ, 1}];
Δkzϕ[355 × 10^-9, 710 × 10^-9, ϕ2[355 × 10^-9, 710 × 10^-9]];
ϕc = ϕ2[355 × 10^-9, 710 × 10^-9];
```

$$Integrate\left[Exp[i\,z\,k], \left\{z, \frac{-L}{2}, \frac{L}{2}\right\}\right] // FullSimplify$$

$$\frac{2\,Sin\left[\frac{k\,L}{2}\right]}{k} /. k \to \Delta kz\phi[\lambda p, \lambda s, \phi]$$

```
f[L_, Wp_, Ws_, Wi_, λp_, λs_, ϕ_] :=
 (2 Sin[1/2 L (-(2 π Sqrt[2.7405` - 1.55`*^10 λs^2 + 0.0184`/(-0.0179` + 1000000000000 λs^2)])/λs -
      1/300000000 (600000000 π/λp - 600000000 π/λs))
    Sqrt[2.7405` - 1.55`*^10 λp^2 λs^2/(-λp + λs)^2 + 0.0184`/(-0.0179` + 1000000000000 λp^2 λs^2/(-λp + λs)^2)] +
   (2 π)/(λp Sqrt[Cos[ϕ]^2/(2.7405` - 1.55`*^10 λs^2 + 0.0184`/(-0.0179` + 1000000000000 λs^2)) +
      Sin[ϕ]^2/(2.373` - 4.4`*^9 λs^2 + 0.0128`/(-0.0156` + 1000000000000 λs^2))])]/
  (-(2 π Sqrt[2.7405` - 1.55`*^10 λs^2 + 0.0184`/(-0.0179` + 1000000000000 λs^2)])/λs -
    1/300000000 (600000000 π/λp - 600000000 π/λs))
   Sqrt[2.7405` - 1.55`*^10 λp^2 λs^2/(-λp + λs)^2 + 0.0184`/(-0.0179` + 1000000000000 λp^2 λs^2/(-λp + λs)^2)] +
  (2 π)/(λp Sqrt[Cos[ϕ]^2/(2.7405` - 1.55`*^10 λs^2 + 0.0184`/(-0.0179` + 1000000000000 λs^2)) +
     Sin[ϕ]^2/(2.373` - 4.4`*^9 λs^2 + 0.0128`/(-0.0156` + 1000000000000 λs^2))]);
(*Overlap Integral without co-efficients as calculated from previous substitutions*)

ϕ1[L_, Wp_, Ws_, Wi_, λp_, λs_, ϕ_] := 2^1.5/(Pi A1[Wp, Ws, Wi]) f[L, Wp, Ws, Wi, λp, λs, ϕ];
(*Normalized overlap function assuming Δky=0 for collinear case*)

Rωs[L_, Wp_, Ws_, Wi_, λp_, λs_, P_, ϕ_] := d^2 P 2 π c/λs (2 π c/λp - 2 π c/λs)/(16 ϵ0 π^5 c^3 Ws Wi Wp^2 ne[λp] no[λs] no[λp λs/(λs - λp)]) Abs[ϕ1[L, Wp, Ws, Wi, λp, λs, ϕ]]^2;
(*Joint spectral emission rate of the SPDC source*)
Φrad[L_, Wp_, Ws_, Wi_, λp_, λs_, P_, ϕ_] := hbar 2 π c/λs Rωs[L, Wp, Ws, Wi, λp, λs, P, ϕ]; (*Radiant Flux*)

RT[L_?NumericQ, W_?NumericQ, Wp_?NumericQ] :=
  NIntegrate[2 Pi c^2/(λs + δ)^2 Rωs[L, Wp, W, W, 355 × 10^-9, λs + δ, 1 × 10^-3, ϕc] /. λs → 710 × 10^-9,
   {δ, -2.5 10^-9, 2.5 × 10^-9}, WorkingPrecision → 15];
(*Total pair-generation rate by integrating over signal bandwidth*)
rtlcol = DiscretePlot[RT[L * 10^-3, W, Wp] /. {W → 50 × 10^-6, Wp → 35.350 × 10^-5}, {L, 0.01, 5, 0.2}, PlotRange → All,
  Filling → False, Joined → True, LabelStyle → 36, PlotStyle → {Black, Thickness[0.01]}, ImageSize → 800,
  Frame → True, FrameLabel → {Style["Crystal Length [mm]", 32], Style["Total Rate R_T [Counts s^-1]", 32]}]
```

Ling Integral Evaluation

(SI units used)

```
Clear["Global`*"]
$Assumptions = {n0 > 0, ωp ∈ Reals, m > 0, 0 < u < 1, 0 < v < 1, L > 0, k ∈ Reals, Δ > 0, W > 0, Wp > 0};
(*Lengths in m, susceptibility in m/V, angles in rad*)
```

L = Crystal length,
W = Signal/Idler SMF mode radius
Wp = Pump beam radius
$\theta s = \theta i = \theta$ = Angles of the overlapping signal and idler fiber modes used in calculation of overlap integral
λp = Pump Wavelength
λs = Signal Wavelength
$\lambda i = \frac{1}{\frac{1}{\lambda s} - \frac{1}{\lambda p}}$ = Idler Wavelength
z = Distance from crystal along propagation direction (= 1m here)
ϕ = Overlap Integral
$R\omega s$ = Joint Spectral Emission Rate
Φrad = Spectral Radiant Flux
Erad = Spectral Irradiance (at the detector/fiber) (Can also calculate it for the source by replacing the differential area with that of the source)
Irad = Spectral Radiometric Intensity
Lrad = Spectral Brightness or Spectral Radiance

Degenerate SPDC With Type-I Phase-Matching for collimated signal, idler and pump beams

```
c = 3 × 10^8; d = 2.4 × 10^-12;
ϵ0 = 8.85 × 10^-12; hbar = 1.054 × 10^-34;
λp0 = 355. × 10^-9;
λs0 = 710. × 10^-9;
θ0 = 0.01;
θ1 = 3.1 * Pi / 180;
ω[λ_] := (2 Pi c) / λ ;
no[λ_] := Sqrt[2.7405 + 0.0184 / (λ * 10^6)^2 - 0.0179 - 0.0155 (λ * 10^6)^2];
(*BBO Sellmeier Equation for Ordinary Index, co-efficients in micron and micron squared*)
ne[λ_] := Sqrt[2.3730 + 0.0128 / (λ * 10^6)^2 - 0.0156 - 0.0044 (λ * 10^6)^2];
(*BBO Sellmeier Equation for Extra-Ordinary Index, co-efficients in micron and micron squared*)
refdata = Plot[{no[λ * 10^-9], ne[λ * 10^-9]}, {λ, 300, 1000}, PlotRange → Automatic,
  LabelStyle → 24, PlotStyle → {{Black, Thickness[0.007]}, {Red, Thickness[0.007]}}, ImageSize → 800,
  Frame → True, FrameLabel → {Style["Wavelength [nm]", Large], Style["Refractive Index", Large]},
  PlotLegends → Placed[LineLegend[{"n_o[λ]", "n_e[λ]"}, LegendFunction → "Frame", LegendMargins → 0], {0.9, 0.86}]]
  (*Plotting refractive indices*)
```

```
Δkz[λp_, λs_, θs_, θi_] := ne[λp] ω[λp] / c - no[λs] ω[λs] / c Cos[θs] - no[λp λs / (λs - λp)] (ω[λp] - ω[λs]) / c Cos[θi];
(*Phase-mismatch along z for non-collinear propagation*)
Δky[λp_, λs_, θs_, θi_] := no[λs] ω[λs] / c Sin[θs] - no[λp λs / (λs - λp)] (ω[λp] - ω[λs]) / c Sin[θi];
(*Phase-mismatch along y for non-collinear propagation*)
A1[Wp_, W_] := 1 / Wp^2 + 2 / W^2; (*Assuming core diameters of both SMFs for signal and idler are the same as W and θs=θi*)

C1[Wp_, W_, θs_, θi_] := 1 / Wp^2 + (Cos[θs]^2 + Cos[θi]^2) / W^2;(*Defining parameters as described in Ling's paper*)
D1[W_, θs_, θi_] := (Sin[2 θs] - Sin[2 θi]) / W^2;
F1[W_, θs_, θi_] := (Sin[θs]^2 + Sin[θi]^2) / W^2;
(*Φ1[λp_,λs_,θs_,θi_,Wp_,W_,l_]:=
  Integrate[Exp[-H1[Wp,W,θs,θi] z^2 + i Δkz[λp,λs,θs,θi] z +i Δky [λp,λs,θs,θi] D1[W,θs,θi] / (2 C1[Wp,W,θs,θi]) z] ,
   {z, -1/2, 1/2},Assumptions→{l>0,H1[Wp,W,θs,θi]∈Reals,Δkz[λp,λs,θs,θi]∈Reals,
     Δky [λp,λs,θs,θi] ∈Reals,D1[W,θs,θi]∈Reals,C1[Wp,W,θs,θi],W>0,Wp>0}];*)
H1[W_, Wp_, θs_, θi_] := F1[W, θs, θi] - D1[W, θs, θi]^2 / (4 C1[Wp, W, θs, θi]);
θic[λp_, λs_, θs_] := ArcSin[no[λs] ω[λs] Sin[θs] / no[λp λs / (λs - λp)] (ω[λp] - ω[λs])]; (*Transverse Phase-Matching Angle*)
(*Angle-tuning for Longitudinal Phase-Matching*)

neϕ[λp_, ϕ_] := (Sin[ϕ]^2 / ne[λp]^2 + Cos[ϕ]^2 / no[λp]^2)^(-1/2)
Δkzϕ[λp_, λs_, θs_, θi_, ϕ_] := neϕ[λp, ϕ] ω[λp] / c - no[λs] ω[λs] / c Cos[θs] - no[λp λs / (λs - λp)] (ω[λp] - ω[λs]) / c Cos[θi];
K[λp_, λs_, θs_, θi_, ϕ_, W_, Wp_] := Δkzϕ[λp, λs, θs, θi, ϕ] + Δky[λp, λs, θs, θi] D1[W, θs, θi] / C1[Wp, W, θs, θi];
ΦΔk[λp_, λs_, θs_, θi_, ϕ_, L_] := Δkzϕ[λp, λs, θs, θi, ϕ] L;
ϕ2[λp_, λs_, θs_, θi_] := ϕ /. FindRoot[Δkzϕ[λp, λs, θs, θi, ϕ] == 0, {ϕ, 0.6}];
θic2 = θic[λp0, λs0, θ0];
```

Non-collinear opening angle for different phase-matching angles

```
θs2[λp_, λs_, ϕ_] := θs /. FindRoot[Δkzϕ[λp, λs, θs, θic[λp, λs, θs], ϕ] == 0, {θs, θ0}];

θs22[λp_, λs_, ϕ_] := ArcSin[no[λs] Sin[θs2[λp, λs, ϕ]]];

cone = Plot[{180 * θs22[λp0, 10^-9 * λs, ϕc2] / Pi, 180 * θs22[λp0, 10^-9 * λs, ϕc] / Pi, ArcSin[no[λs0] Sin[θ0]] * 180 / Pi},
  {λs, 600, 850}, PlotRange → All, LabelStyle → 32,
  PlotStyle → {{Thickness[0.005]}, {Pink, Thickness[0.005]}, {Black, Dashed, Thickness[0.003]}},
  ImageSize → 800, Frame → True, FrameLabel → {Style["Signal Wavelength [nm]", 32], Style["θs(°)", 32]},
  PlotLegends → Placed[LineLegend[{"Collinear", "θs = 0.953°"}, LegendFunction → "Frame", LegendMargins → 0],
    {0.64, 0.84}]] (*Plotting emission angles*)

Integrate[Exp[i z k] Exp[-A z^2], {z, -L/2, L/2}] // FullSimplify (*Integrating to get the overlap function*)
```

$$\frac{e^{-\frac{k^2}{4A}} \sqrt{\pi} \left(\text{Erf}\left[\frac{i k + A L}{2\sqrt{A}}\right] - i\, \text{Erfi}\left[\frac{k + i A L}{2\sqrt{A}}\right]\right)}{2\sqrt{A}}$$

```
e^(-k^2/(4 A)) Sqrt[π] (Erf[(i k + A L)/(2 Sqrt[A])] - i Erfi[(k + i A L)/(2 Sqrt[A])])/(2 Sqrt[A]) /. {A → H1[W, Wp, θs, θi], k → K[λp, λs, θs, θi, ϕ, W, Wp]}
```

```
(*Substituting the parameters for noncollinear emission*)
```

```
(*Defining unnormalized Overlap function by substituting the result of previous substitution*)
```

```
f[θs_, θi_, L_, W_, Wp_, λp_, λs_, ϕ_] := 1/(2 Sqrt[(Sin[θi]^2 + Sin[θs]^2)/W^2 - (-Sin[2 θi] + Sin[2 θs])^2/(4 W^4 (1/Wp^2 + (Cos[θi]^2 + Cos[θs]^2)/W^2))])
```

```
-((((600 000 000 π)/λp - (600 000 000 π)/λs) Sqrt[2.7405` - (1.55`*^10 λp^2 λs^2)/(-λp + λs)^2 + 0.0184`/(-0.0179` + (1 000 000 000 000 λp^2 λs^2)/(-λp + λs)^2)] Cos[θi])/300 000 000 - (2 π Sqrt[2.7405` - 1.55`*^10 λs^2 + 0.0184`/(-0.0179` + 1 000 000 000 000 λs^2)] Cos[θs])/λs + ((((600 000 000 π)/λp - (600 000 000 π)/λs) Sqrt[2.7405` - 1.5
```

```
-
```

```
4 (Si
```

```
e
```

```
Sqrt[π] (Erf[1/(2 Sqrt[(Sin[θi]^2 + Sin[θs]^2)/W^2 - (-Sin[2 θi] + Sin[2 θs])^2/(4 W^4 (1/Wp^2 + (Cos[θi]^2 + Cos[θs]^2)/W^2))])
(L[(Sin[θi]^2 + Sin[θs]^2)/W^2 - (-Sin[2 θi] + Sin[2 θs])^2/(4 W^4 (1/Wp^2 + (Cos[θi]^2 + Cos[θs]^2)/W^2))] +
i (-1/300 000 000 ((600 000 000 π)/λp - (600 000 000 π)/λs) Sqrt[(2.7405` - (1.55`*^10 λp^2 λs^2)/(-λp + λs)^2 + 0.0184`/(-0.0179` + (1 000 000 000 000 λp^2 λs^2)/(-λp + λs)^2)] Cos[θi] -
(2 π Sqrt[2.7405` - 1.55`*^10 λs^2 + 0.0184`/(-0.0179` + 1 000 000 000 000 λs^2)] Cos[θs])/λs + 1/(W^2 (1/Wp^2 + (Cos[θi]^2 + Cos[θs]^2)/W^2)) (-1/300 000 000
((600 000 000 π)/λp - (600 000 000 π)/λs) Sqrt[(2.7405` - (1.55`*^10 λp^2 λs^2)/(-λp + λs)^2 + 0.0184`/(-0.0179` + (1 000 000 000 000 λp^2 λs^2)/(-λp + λs)^2)] Sin[θi] + 1/λs
2 π Sqrt[2.7405` - 1.55`*^10 λs^2 + 0.0184`/(-0.0179` + 1 000 000 000 000 λs^2)] Sin[θs]) (-Sin[2 θi] + Sin[2 θs]) + (2 π)/
(λp Sqrt[(Cos[ϕ]^2)/(2.7405` - 1.55`*^10 λp^2 + 0.0184`/(-0.0179` + 1 000 000 000 000 λp^2)) + (Sin[ϕ]^2)/(2.373` - 4.4`*^9 λp^2 + 0.0128`/(-0.0156` + 1 000 000 000 000 λp^2))])))] -
i Erfi[1/(2 Sqrt[(Sin[θi]^2 + Sin[θs]^2)/W^2 - (-Sin[2 θi] + Sin[2 θs])^2/(4 W^4 (1/Wp^2 + (Cos[θi]^2 + Cos[θs]^2)/W^2))])
(-1/300 000 000 ((600 000 000 π)/λp - (600 000 000 π)/λs)
```

$$\sqrt{2.7405` - \frac{1.55`*^10\,\lambda p^2\,\lambda s^2}{(-\lambda p+\lambda s)^2} + \frac{0.0184`}{-0.0179` + \frac{1\,000\,000\,000\,000\,\lambda p^2\,\lambda s^2}{(-\lambda p+\lambda s)^2}}}\ \text{Cos}[\theta i] -$$

$$\frac{2\pi\sqrt{2.7405` - 1.55`*^10\,\lambda s^2 + \frac{0.0184`}{-0.0179` + 1\,000\,000\,000\,000\,\lambda s^2}}\ \text{Cos}[\theta s]}{\lambda s} + \frac{1}{W^2\left(\frac{1}{Wp^2} + \frac{\text{Cos}[\theta i]^2+\text{Cos}[\theta s]^2}{W^2}\right)}$$

$$\left(-\frac{1}{300\,000\,000}\left(\frac{600\,000\,000\,\pi}{\lambda p} - \frac{600\,000\,000\,\pi}{\lambda s}\right)\sqrt{\left(2.7405` - \frac{1.55`*^10\,\lambda p^2\,\lambda s^2}{(-\lambda p+\lambda s)^2} + \frac{0.0184`}{-0.0179` + \frac{1\,000\,000\,000\,000\,\lambda p^2\,\lambda s^2}{(-\lambda p+\lambda s)^2}}\right)}\right.$$

$$\left.\text{Sin}[\theta i] + \frac{1}{\lambda s}2\pi\sqrt{2.7405` - 1.55`*^10\,\lambda s^2 + \frac{0.0184`}{-0.0179` + 1\,000\,000\,000\,000\,\lambda s^2}}\ \text{Sin}[\theta s]\right)$$

$$(-\text{Sin}[2\,\theta i] + \text{Sin}[2\,\theta s]) + i\,L\left(\frac{\text{Sin}[\theta i]^2 + \text{Sin}[\theta s]^2}{W^2} - \frac{(-\text{Sin}[2\,\theta i] + \text{Sin}[2\,\theta s])^2}{4\,W^4\left(\frac{1}{Wp^2} + \frac{\text{Cos}[\theta i]^2+\text{Cos}[\theta s]^2}{W^2}\right)}\right) +$$

$$(2\pi)\Big/\left(\lambda p\sqrt{\left(\frac{\text{Cos}[\phi]^2}{2.7405` - 1.55`*^10\,\lambda p^2 + \frac{0.0184`}{-0.0179` + 1\,000\,000\,000\,000\,\lambda p^2}} + \frac{\text{Sin}[\phi]^2}{2.373` - 4.4`*^9\,\lambda p^2 + \frac{0.0128`}{-0.0156` + 1\,000\,000\,000\,000\,\lambda p^2}}\right)}\right)\Bigg];$$

```
ϕ1[θs_, θi_, L_, Wp_, W_, λp_, λs_, ϕ_] :=
  ((2^1.5 Exp[-Δky[λp, λs, θs, θi]^2/(4 C1[Wp, W, θs, θi])])/(Pi W^2 Wp Sqrt[A1[Wp, W] C1[Wp, W, θs, θi]]
      (*Normalizing by including pre-factors*))) f[θs, θi, L, W, Wp, λp, λs, ϕ] ; (*Δky=0*)
```

$$\text{Rωs}[\theta s\_, \theta i\_, L\_, Wp\_, W\_, \lambda p\_, \lambda s\_, P\_, \phi\_] := \frac{d^2\,P\,\frac{2\pi c}{\lambda s}\left(\frac{2\pi c}{\lambda p} - \frac{2\pi c}{\lambda s}\right)}{16\,\epsilon 0\,\pi^5\,c^3\ \text{ne}[\lambda p]\ \text{no}[\lambda s]\ \text{no}\left[\frac{\lambda p\,\lambda s}{\lambda s-\lambda p}\right]}\text{Abs}[\phi 1[\theta s, \theta i, L, Wp, W, \lambda p, \lambda s, \phi]]^2;$$

```
(*Joint spectral emission rate of the SPDC source*)
```

$$\text{Ɛrad}[\theta s\_, \theta i\_, L\_, Wp\_, W\_, \lambda p\_, \lambda s\_, P\_, \phi\_] := \text{hbar}\,\frac{2\pi c}{\lambda s}\,\text{Rωs}[\theta s, \theta i, L, Wp, W, \lambda p, \lambda s, P, \phi]; \text{(*Radiant Flux*)}$$

```
Rtγ[γ_, W_] := 10^12 Rωs[0.01, θic2, 0.002, γ W, W, 355 × 10^-9, 710 × 10^-9, 1 × 10^-3, ϕc];
max = {γ /. Last@#, First@#} &[FindMaximum[Rtγ[γ, 50 × 10^-6], γ]]
(*Finding value of γ where the maximuam spectral rate occurs*)
```

```
RT2[L_?NumericQ, W_?NumericQ, Wp_?NumericQ] :=
  NIntegrate[(2 Pi c)/(λs + δ)^2 Rωs[0.01, θic2, L, Wp, W, 355 × 10^-9, λs + δ, 2 × 10^-3, ϕc] /. λs → 710 × 10^-9,
    {δ, -2.5 10^-9, 2.5 × 10^-9}, WorkingPrecision → 10];
(*Total rate by numcarially integrating over the signal bandwidth*)
```

```
ƐradT[L_?NumericQ, W_?NumericQ, Wp_?NumericQ] :=
  NIntegrate[(2 Pi c^2)/(λs + δ)^2 Ɛrad[0.01, θic, L, Wp, W, 355 × 10^-9, λs + δ, 1 × 10^-3, ϕc] /. λs → 710 × 10^-9,
    {δ, -10 10^-9, 10 × 10^-9}, WorkingPrecision → 10]; (*Total radiant flux*)
```

Spectral Radiometric Parameters Calculation

Using the Friis Transmission formula for Radiance, we have $A_t\,\Omega_t = (1.22\,\pi\,\lambda s)^2$ for the signal photon. The 1.22 π factor is present because of the pump being a Gaussian of diameter Wp, which for this case of a diffracting signal beam can be assumed to be a circular aperture of diameter Wp and the 1.22 π being the

diameter of the Airy disk thus produced. The Radiance will be conserved between the source and the detector. But the power received by the detector cannot be simply obtained by multiplying Radiance (Lrad) with λs^2 as this would imply that all the power is collected by the detector. Instead, we need to find the solid angle subtended by the source on the detector instead and multiply with the area of detector to get the throughput, which in turn is multiplied with the Lrad to get received power.

```
Lrad[θs_, θi_, L_, Wp_, W_, λp_, λs_, P_, ϕ_] := 1/(1.22 Pi λs)^2 ℇrad[θs, θi, L, Wp, W, λp, λs, P, ϕ]; (*Spectral radiance*)
```

```
Erad[θs_, θi_, L_, Wp_, W_, λp_, λs_, P_, ϕ_] := 1/((Pi Wp^2) Cos[ArcSin[no[λs] Sin[θs]]]) ℇrad[θs, θi, L, Wp, W, λp, λs, P, ϕ];
(*Spectral irradiance*)
```

```
Irad[θs_, θi_, L_, Wp_, W_, λp_, λs_, P_, ϕ_] := (Pi Wp^2 Cos[ArcSin[no[λs] Sin[θs]]])/1 Lrad[θs, θi, L, Wp, W, λp, λs, P, ϕ];
(*Spectral Radiant Intensity*)
```

Total Radiometric Parameters Calculation

```
LradT[L_?NumericQ, W_?NumericQ, Wp_?NumericQ] :=
  NIntegrate[(2 Pi c)/(λs + δ)^2 Lrad[0.01, θic2, L, Wp, W, 355 × 10^-9, λs + δ, 1 × 10^-3, ϕc] /. λs → 710 × 10^-9,
    {δ, -2.5 10^-9, 2.5 × 10^-9}, WorkingPrecision → 10]; (*Total radiance*)
```

```
EradT[L_?NumericQ, W_?NumericQ, Wp_?NumericQ] :=
  NIntegrate[(2 Pi c^2)/(λs + δ)^2 Erad[0.01, θic, L, Wp, W, 355 × 10^-9, λs + δ, 1 × 10^-3, ϕc] /. λs → 710 × 10^-9,
    {δ, -2.5 10^-9, 2.5 × 10^-9}, WorkingPrecision → 10]; (*Total irradiance*)
```

```
IradT[L_?NumericQ, W_?NumericQ, Wp_?NumericQ] :=
  NIntegrate[(2 Pi c^2)/(λs + δ)^2 Irad[0.01, θic, L, Wp, W, 355 × 10^-9, λs + δ, 1 × 10^-3, ϕc] /. λs → 710 × 10^-9,
    {δ, -2.5 10^-9, 2.5 × 10^-9}, WorkingPrecision → 10]; (*Total radiant intensity*)
```

Heralding Efficiency after post-selecting spatial mode on a SMF

```
gW[x_, y_, W_] := (2/(Pi W^2))^0.5 Exp[-(x^2 + y^2)/W^2];
(*W and Wf are 1/e^2 mode-field diameters of the freely propagating signal beam and the SMF fiber respectively*)
Ig[W_] := Integrate[gW[x, y, W]^2, {x, -∞, ∞}, {y, -∞, ∞}, Assumptions → {W > 0}];
Ig1[W_, Wf_] := Integrate[gW[x, y, W] gW[x, y, Wf], {x, -∞, ∞},
   {y, -∞, ∞}, Assumptions → {{W, Wf} > 0, {W, Wf} → Reals}, GenerateConditions → False];
(Ig1[W, Wf])^2
Ig[W] Ig[Wf]
```

$$\frac{4.\,W^2\,Wf^4}{\left(W^2+Wf^2\right)^2\,\text{Abs}[Wf]^2}$$

```
ηi = 1; (*Quantum Efficiency of APD detectors*)
η1[W_, Wf_] := ηi 4.0 W^2 Wf^2/(W^2 + Wf^2)^2;
```

```
hereffsmf = Plot[η1[γ * W, W] /. W → 5 × 10^-6, {γ, 0, 6}, PlotRange → All, PlotPoints → 400,
  MaxRecursion → 4, LabelStyle → 32, PlotStyle → {Pink, Thickness[0.007]}, ImageSize → 800, Frame → True,
  FrameLabel → {Style["[W/W_f]", 32], Style["Heralding Efficiency", 32]}] (*Plotting heralding efficiency w.r.t. W/Wf*)
```

Diffraction in pump with collimated signal and idler beams for non-collinear geometry

The beams are assumed to have their waists at the centre of the crystal for maximum overlap of the beams.

L = Crystal length,
W = Signal / Idler SMF mode radius
Wp = Pump waist size
θs = θi = θ = Angles of the overlapping signal and idler fiber modes used in calculation of overlap integral
λp = Pump Wavelength
λs = Signal Wavelength
λi = $\frac{1}{\frac{1}{\lambda s}-\frac{1}{\lambda p}}$ = Idler Wavelength
z = Distance from crystal along propagation direction (= 1 m here)
ϕ = Overlap Integral
Rωs = Joint Spectral Emission Rate

```
Clear["Global`*"]

c = 3 × 10^8; d = 2.4 × 10^-12;
ϵ0 = 8.85 × 10^-12; hbar = 1.054 × 10^-34;
λs0 = 710. × 10^-9;
λp0 = 355. × 10^-9;
θ0 = 3.1 * Pi / 180;
W0 = 50. × 10^-6;
Wp0 = 0.707 * W0;
θ1 = 0.01;
W1 = 2.5 × 10^-6;
Wp1 = 0.707 * W1;
ω[λ_] := (2 Pi c) / λ ;
no[λ_] := Sqrt[2.7405 + 0.0184/((λ * 10^6)^2 - 0.0179) - 0.0155 (λ * 10^6)^2];
(*BBO Sellmeier Equation for Ordinary Index, co-efficients in micron and micron squared*)
ne[λ_] := Sqrt[2.3730 + 0.0128/((λ * 10^6)^2 - 0.0156) - 0.0044 (λ * 10^6)^2];
(*BBO Sellmeier Equation for Extra-Ordinary Index, co-efficients in micron and micron squared*)
```

Diffraction only in pump:

```
Δkz[λp_, λs_, θs_, θi_] := ne[λp] ω[λp] / c - no[λs] ω[λs] / c Cos[θs] - no[λp λs / (λs - λp)] (ω[λp] - ω[λs]) / c Cos[θi];

Δky[λp_, λs_, θs_, θi_] := no[λs] ω[λs] / c Sin[θs] - no[λp λs / (λs - λp)] (ω[λp] - ω[λs]) / c Sin[θi];

zr[W_, λ_] := Pi W^2 / (λ);

A1[Wp_, W_, z_, λs_, λp_] := 1 / (Wp^2 (1 + i z / zr[Wp, λp])) + 2 / W^2;

(*Assuming core diameters of both SMFs for signal and idler are the same as W and θs=θi*)

B1[Wp_, W_, z_, λs_, λp_, θ_] := 1 / (Wp^2 (1 + i z / zr[Wp, λp])) + 2 Cos[θ]^2 / W^2;

H1[W_, z_, λs_, θ_] := 2 Sin[θ]^2 / W^2;

θic[λp_, λs_, θs_] := ArcSin[no[λs] ω[λs] Sin[θs] / no[λp λs / (λs - λp)] (ω[λp] - ω[λs])]; (*Transverse Phase-Matching Angle*)

(*Angle-tuning for Longitudinal Phase-Matching*)

neϕ[λp_, ϕ_] := (Sin[ϕ]^2 / ne[λp]^2 + Cos[ϕ]^2 / no[λp]^2)^-1/2

Δkzϕ[λp_, λs_, θs_, θi_, ϕ_] := neϕ[λp, ϕ] ω[λp] / c - no[λs] ω[λs] / c Cos[θs] - no[λp λs / (λs - λp)] (ω[λp] - ω[λs]) / c Cos[θi];

Wξ[L_, λ_, ξ_] := (λ L / (2 Pi ξ))^0.5 ;

ξ[L_, λ_, W_] := λ L / (2 Pi W^2);

Φ[Δk[λp_, λs_, θs_, θi_, ϕ_, L_] := Δkzϕ[λp, λs, θs, θi, ϕ] L;
ϕ2[λp_, λs_, θs_, θi_] := ϕ /. FindRoot[Δkzϕ[λp, λs, θs, θi, ϕ] == 0, {ϕ, 0.6}];


Integrate[Exp[i z k] Exp[- A x^2 - B y^2 - H z^2], {x, -∞, ∞}, {y, -∞, ∞}, Assumptions → {A > 0, B > 0, H > 0, {A, B, H} ∈ Reals}]

e^(z (i k - H z)) π / Sqrt[A B] /. {A → A1[Wp, W, z, λs, λp], B → B1[Wp, W, z, λs, λp, θ], H → H1[W, z, λs, θ], k → Δkzϕ[λp, λs, θ, θ, ϕ]}

f1[z_, W_, Wp_, λs_, λp_, θ_, ϕ_] := 2^1.5 / (Pi W^2 Wp (1 + i z / zr[Wp, λp])) 1 / Sqrt[(2 / W^2 + 1 / (Wp^2 (1 + i z λp / (π Wp^2)))) (1 / (Wp^2 (1 + i z λp / (π Wp^2))) + 2 Cos[θ]^2 / W^2)]

e^(z (-2 z Sin[θ]^2 / W^2 + i (-(2 π Sqrt[2.7405^ - 1.55^ * ^10 λs^2 + 0.0184^ / (-0.0179^ + 1000000000000 λs^2)] Cos[θ]) / λs - ((600000000 π / λp - 600000000 π / λs) Sqrt[2.7405^ - 1.55^ * ^10 λp^2 λs^2 / (-λp + λs)^2 + 0.0184^ / (-0.0179^ + 1000000000000 λp^2 λs^2 / (-λp + λs)^2)] Cos[θ]) / 300000000 + (

    π; (*Defining overlap integral after integrating w.r.t. x and y*)
Φ[W_?NumericQ, Wp_?NumericQ, λs_?NumericQ, λp_?NumericQ, L_?NumericQ, θ_?NumericQ, ϕ_?NumericQ] :=
  NIntegrate[f1[z, W, Wp, λs, λp, θ, ϕ], {z, -0.5 L, 0.5 L}, WorkingPrecision → 15];
 (*Integrating w.r.t. z over the length of the crystal*)

Rωs[θ_, L_, Wp_, W_, λp_, λs_, P_, ϕ_] := d^2 P 2 π c / λs (2 π c / λp - 2 π c / λs) / (16 ∈0 π^5 c^3 ne[λp] no[λs] no[λp λs / (λs - λp)]) Abs[Φ[W, Wp, λs, λp, L * 10^-3, θ, ϕ]]^2;

(*Joint spectral rate*)
```

```
f11[z_, W_, Wp_, λs_, λp_, θ_] := 1/(W^2 Wp (1 + i z/zr[Wp, λp])) e^(-2 z^2 Sin[θ]^2/W^2) π / Sqrt[(2/W^2 + 1/(Wp^2 (1 + i z λp/(π Wp^2)))) (1/(Wp^2 (1 + i z λp/(π Wp^2))) + 2 Cos[θ]^2/W^2)];

(*Overlap function defined not considering phase-mismatch*)

Φ11[W_?NumericQ, Wp_?NumericQ, λs_?NumericQ, λp_?NumericQ, L_?NumericQ, θ_?NumericQ] :=
  NIntegrate[f11[z, W, Wp, λs, λp, θ], {z, -0.5 L, 0.5 L}, WorkingPrecision → 15];
(*Overlap after integrating over crystal length*)

Rωs[W_, Wp_, λs_, λp_, L_, θ_, ϕ_, P_] := 8 d^2 P 2 π c/λs (2 π c/λp - 2 π c/λs)/(ε0 π^4 c^3 ne[λp] no[λs] no[λp λs/(λs - λp)]) Abs[Φ[W, Wp, λs, λp, L, θ, ϕ]]^2;

(*Joint spectral emission rate of the SPDC source*)
```

Collinear Geometry with diffraction only in pump

```
e^(z (i k - H z)) π / Sqrt[A B] /. {A → A1[Wp, W, z, λs, λp], B → A1[Wp, W, z, λs, λp], H → 0, k → Δkzϕ[λp, λs, 0, 0, ϕ]}

f2[z_, W_, Wp_, λs_, λp_, ϕ_] := 1/(Wp W^2 (1 + i z λp/(π Wp^2))) 1/(2/W^2 + 1/(Wp^2 (1 + i z λp/(π Wp^2))))

e^(i z (-(2 π Sqrt[2.7405` - 1.55`*^-10 λs^2 + 0.0184`/(-0.0179`*^-10 + 1 000 000 000 000 λs^2)])/λs - (600 000 000 π/λp - 600 000 000 π/λs) Sqrt[2.7405` - 1.55`*^-10 λp^2 λs^2/(-λp + λs)^2 + 0.0184`/(-0.0179`*^-10 + 1 000 000 000 000 λp^2 λs^2/(-λp + λs)^2)]/300 000 000) + 2 π/(λp Sqrt[Cos[ϕ]^2/(2.7405` - 1.55`*^-10 λp^2 + 0.0184`/(-0.0179`*^-10 + 1 000 000 000 000 λp^2)) +

  π
Φ2[W_?NumericQ, Wp_?NumericQ, λs_?NumericQ, λp_?NumericQ, L_?NumericQ, ϕ_?NumericQ] :=
  NIntegrate[f2[z, W, Wp, λs, λp, ϕ], {z, -0.5 L, 0.5 L}, WorkingPrecision → 15];
```

Ryan Bennink's expression for collinear pump, signal and idler

```
Fi[ξk_, Φlk_, L_] := ξk^0.5 Exp[i Φlk L/2]/(1 - i ξk L);
F[ξk_?NumericQ, Φlk_?NumericQ] := NIntegrate[Fi[ξk, Φlk, L], {L, -1, 1}, WorkingPrecision → 10];
t3 = Table[{Φlk, ξk, Abs[F[10^ξk, Φlk * Pi]]^2/4}, {Φlk, -3, 3, 0.1}, {ξk, -3, 2, 0.1}];

ξlog = FindMaximum[Abs[F[10^ξk, -Pi]]^2, ξk]

{4.26866, {ξk → 0.442492}}

ϕma2x = FindMaximum[Abs[F[2.7700794745992146`, ϕk]]^2, ϕk]

{4.27019, {ϕk → -3.21925}}

-3.2192508363998877` / Pi

-1.02472

max1 = {-1.0247193673315214`, 0.44249222620772155`};

phixiryan = ListDensityPlot[Partition[Flatten[t3]/1.2, 3], PlotRange → All, ColorFunction → "AvocadoColors",
  PlotLegends → BarLegend[Automatic, LabelStyle → {FontSize → 30}], InterpolationOrder → 6,
  FrameLabel → {Style["ϕ/π", 32], Style["Log10 [ξ]", 32]}, LabelStyle → 32, ImageSize → 800,
  PlotLabel → Style["Overlap Function [arb. u.]", 32], Epilog → {PointSize[.01], Black, Point[max1]}]
```

Collinear geometry with diffraction only in pump in terms of focussing parameter

ξ

```
Ai[λp_, u_, ξ3_, L_, W_] := 2 Pi ξ3 / L * 1 / (λp (1 + i u ξ3)) + 2 / W^2;
Fi2[λp_, u_, ξ3_, ϕ4_, L_, W_] := 4 (ξ3)^0.5 Exp[i ϕ4 u / 2] / (W^2 (L λp)^0.5 (1 + i u ξ3) Ai[λp, u, ξ3, L, W]
F2[λp_?NumericQ, ξ3_?NumericQ, ϕ4_?NumericQ, L_?NumericQ, W_?NumericQ] :=
  NIntegrate[Fi2[λp, u, ξ3, ϕ4, L, W], {u, -1, 1}, WorkingPrecision → 15];
t4 = Table[{ϕ4, ξ3, Abs[F2[λp0, 10^ξ3, ϕ4 * Pi, 0.001, 3 × 10^-6]]^2 / (3.905 * 10^10)}, {ϕ4, -3, 3, 0.2}, {ξ3, -3, 2, 0.2}];

ξlog = FindMaximum[Abs[F2[λp0, ξk, ϕk * Pi, 0.001, 3 × 10^-6]]^2, ξk, ϕk]

{3.90471 × 10^10, {ξk → 2.43439, ϕk → 0.877292}}
```

Collinear geometry with diffraction in all 3 beams (our formulation)

```
Ai2[λp_, λs_, u_, ξ3_, L_] := 2 Pi ξ3 / L (1 / (λp (1 + i u ξ3)) + 2 / (λs (1 - i u ξ3)));
Ai4[λp_, λs_, u_, ξs3_, ξp3_, L_] := 2 Pi / L (ξp3 / (λp (1 + i u ξp3)) + 2 ξs3 / (λs (1 - i u ξs3)));
Fi3[λp_, λs_, u_, ξ3_, ϕ4_, L_] := (ξ3^3)^0.5 Exp[i ϕ4 u / 2] / ((L λp λs^2)^0.5 (1 + i u ξ3) (1 - i u ξ3)^2 Ai2[λp, λs, u, ξ3, L]
Fi4[λp_, λs_, u_, ξs3_, ξp3_, ϕ4_, L_] := (ξp3 ξs3^2)^0.5 Exp[i ϕ4 u / 2] / ((L λp λs^2)^0.5 (1 + i u ξp3) (1 - i u ξs3)^2 Ai4[λp, λs, u, ξs3, ξp3, L]
F4[λp_?NumericQ, λs_?NumericQ, ξs3_?NumericQ, ξp3_?NumericQ, ϕ4_?NumericQ, L_?NumericQ] :=
  NIntegrate[Fi4[λp, λs, u, ξs3, ξp3, ϕ4, L], {u, -1, 1}, WorkingPrecision → 15];


t5 = Table[{ϕ4, ξ3, Abs[F3[λp0, λs0, 10^ξ3, ϕ4 * Pi, 0.001]]^2 / 19.05}, {ϕ4, -3, 3, 0.1}, {ξ3, -3, 2, 0.1}];

t7 = Table[{ξs3, ξp3, Abs[F4[λp0, λs0, 10^ξs3, 10^ξp3, -1.03614 * Pi, 0.001]]^2 / 19.05}, {ξs3, -2, 2, 0.1}, {ξp3, -2, 2, 0.1}];

t6 = Table[{L, ξ3, Abs[F3[λp0, λs0, ξ3, -1.03614 * Pi, L * 10^-3]]^2}, {L, 0.01, 10, 0.1}, {ξ3, 0.01, 10, 0.1}];

Phicolxisxip = ListDensityPlot[Partition[Flatten[t7], 3], PlotRange → All, ColorFunction → "AvocadoColors",
  PlotLegends → BarLegend[Automatic, LabelStyle → {FontSize → 32}], InterpolationOrder → 6,
  FrameLabel → {Style["Log10 [ξs]", 32], Style["Log10 [ξp]", 32]}, LabelStyle → 32, ImageSize → 800,
  PlotLabel → Style["Overlap Function [arb. u.]", 32], Epilog → {PointSize[.01], Black, Point[max5]}]

phixicol3 = ListDensityPlot[Partition[Flatten[t5], 3], PlotRange → All, ColorFunction → "AvocadoColors",
  PlotLegends → BarLegend[Automatic, LabelStyle → {FontSize → 30}], InterpolationOrder → 6,
  FrameLabel → {Style["ϕ/π", 32], Style["Log10 [ξ]", 32]}, LabelStyle → 32, ImageSize → 800,
  PlotLabel → Style["Overlap Function [arb. u.]", 32], Epilog → {PointSize[.01], Black, Point[max6]}]
```

Non-collinear case with diffraction in all beams

```
g[y_, z_, θ_, λs_, λp_, W_, Wp_] :=
 (1/Sqrt[1/(Wp^2 (1 + i z/zr[Wp, λp])) + 1/(W^2 (1 + i (y Sin[θ] - z Cos[θ])/zr[W, λs])) + 1/(W^2 (1 - i (y Sin[θ] + z Cos[θ])/zr[W, λs]))]) 1/(W (1 + i (y Sin[θ] - z Cos[θ])/zr[W, λs]))
  1/(W (1 - i (y Sin[θ] + z Cos[θ])/zr[W, λs])) 1/(Wp (1 + i z/zr[Wp, λp])) Exp[-(1/(Wp^2 (1 + i z/zr[Wp, λp])) + Cos[θ]^2/(W^2 (1 + i (y Sin[θ] - z Cos[θ])/zr[W, λs])) + Cos[θ]^2/(W^2 (1 - i (y Sin[θ] + z Cos[θ])/zr[W, λs]))) y^2 -
   (Sin[θ]^2/(W^2 (1 + i (y Sin[θ] - z Cos[θ])/zr[W, λs])) + Sin[θ]^2/(W^2 (1 - i (y Sin[θ] + z Cos[θ])/zr[W, λs]))) z^2];
```

Perfect phase-matching assumed

```
Φ5[L_?NumericQ, W_?NumericQ, Wp_?NumericQ, θ_?NumericQ, λs_?NumericQ, λp_?NumericQ] :=
 NIntegrate[g[y, z, θ, λs, λp, W, Wp], {y, -∞, ∞}, {z, -L/2, L/2}, Exclusions → {0, 0}, Method → "PrincipalValue"]

Rωsdsip[θ_, L_, Wp_, W_, λp_, λs_, P_] := 8 d^2 P 2πc/λs (2πc/λp - 2πc/λs)/(ε0 π^4 c^3 ne[λp] no[λs] no[λp λs/(λs - λp)]) Abs[Φ5[L, W, Wp, θ, λs, λp]]^2;

(*Joint spectral emission rate*)

lentab = Table[10^10 Rωsdsip[θ, L*10^-3, Wp, W, λp, λs, P] /.
    {W → 10 × 10^-6, Wp → 0.707 × 10 × 10^-6, λs → λs0, λp → λp0, θ → 0.01, P → 0.001}, {L, 0.5, 15, 0.5}];

crylen3 = ListLinePlot[lentab, PlotRange → All, PlotStyle → Thickness[0.01], Joined → True,
  Filling → False, LabelStyle → 24, PlotStyle → Thickness[0.01], ImageSize → 800, Frame → True,
  FrameLabel → {Style["Signal mode width [μm]", Large], Style["dR_ωs/dω_s [10^-8 (Counts s^-1)/Hz]", Large]}]

crylen =
 DiscretePlot[10^10 Rωsdsip[θ, L*10^-3, Wp, W, λp, λs, P] /. {W → W0/2, Wp → Wp0/2, λs → λs0, λp → λp0, θ → 0.01, P → 0.001},
  {L, 0.5, 15, 0.5}, PlotRange → All, PlotStyle → Thickness[0.01], Joined → True,
  Filling → False, LabelStyle → 24, PlotStyle → Thickness[0.01], ImageSize → 800, Frame → True,
  FrameLabel → {Style["Crystal Length L [mm]", Large], Style["dR_ωs/dω_s [(Counts s^-1) s^-1]", Large]}]

cryslen = Show[cry, FrameLabel → {Style["Crystal Length L [mm]", Large], Style["dR_ωs/dω_s [10^-14 (Counts s^-1)/Hz]", Large]}]

tWdiff = Table[{W, 10^8 Rωsdsip[θ, L*10^-3, 0.707*W*10^-6, W*10^-6, λp, λs, P] /. {L → 1, λs → λs0, λp → λp0, θ → 0.01, P → 0.001}},
   {W, 4, 40, 0.5}];

sigwid = ListLinePlot[Partition[Flatten[tWdiff], 2], PlotRange → All, PlotStyle → Thickness[0.01],
  Joined → True, Filling → False, LabelStyle → 24, PlotStyle → Thickness[0.01], ImageSize → 800, Frame → True,
  FrameLabel → {Style["Signal mode width [μm]", Large], Style["dR_ωs/dω_s [10^-8 (Counts s^-1)/Hz]", Large]}]
```

Rewriting in terms of focussing parameters ξs, ξi and ξp

```
Aξ[y_, u_, ξ_, L_, θ_, λp_, λs_] :=
  2 Pi ξ / L ( 1 / (λp (1 + i u ξ)) + 1 / (λs (1 - i u ξ Cos[θ] + 2 i ξ y Sin[θ] / L)) + 1 / (λs (1 - i u ξ Cos[θ] - 2 i ξ y Sin[θ] / L)) );
Bξ[y_, u_, ξ_, L_, θ_, λp_, λs_] :=
  2 Pi ξ / L ( 1 / (λp (1 + i u ξ)) + Cos[θ]^2 / (λs (1 - i u ξ Cos[θ] + 2 i ξ y Sin[θ] / L)) + Cos[θ]^2 / (λs (1 - i u ξ Cos[θ] - 2 i ξ y Sin[θ] / L)) );
Hξ[y_, u_, ξ_, L_, θ_, λp_, λs_] := 2 Pi ξ / L ( Sin[θ]^2 / (λs (1 - i u ξ Cos[θ] + 2 i ξ y Sin[θ] / L)) + Sin[θ]^2 / (λs (1 - i u ξ Cos[θ] - 2 i ξ y Sin[θ] / L)) );
fξ[y_, u_, ξ_, L_, θ_, λp_, λs_, ϕ_] :=
  ( 2 Pi^2 ξ^3 / (L λp λs^2 Aξ[y, u, ξ, L, θ, λp, λs]) )^0.5 Exp[- Bξ[y, u, ξ, L, θ, λp, λs] y^2 - Hξ[y, u, ξ, L, θ, λp, λs] u^2 L^2 / 4 + i ϕ u / 2];

Φ6[L_?NumericQ, ξ_?NumericQ, θ_?NumericQ, λs_?NumericQ, λp_?NumericQ, ϕ_?NumericQ] :=
  NIntegrate[fξ[y, u, ξ, L, θ, λp, λs, ϕ], {y, -∞, ∞},
   {u, -1, 1}, Exclusions → {0, 0}, Method → "PrincipalValue"];

phixi6 = DiscretePlot[Abs[Φ6[L * 10^-3, 10^ξ, θ, λs, λp, 0]]^2 /. {L → 5, λs → λs0, λp → λp0, θ → 0.01}, {ξ, -1, 0.75, 0.025},
  PlotRange → All, PlotStyle → Thickness[0.01], Joined → True, Filling → False, LabelStyle → 24, PlotStyle → Thickness[0.01],
  ImageSize → 800, Frame → True, FrameLabel → {Style["Focussing Parameter ξ", Large], Style["Overlap Function", Large]}]

ListLinePlot[tfocus, PlotRange → All, PlotStyle → Thickness[0.01], Joined → True,
 Filling → False, LabelStyle → 24, PlotStyle → Thickness[0.01], ImageSize → 800, Frame → True,
 FrameLabel → {Style["Signal mode width [μm]", Large], Style["dR_ωs / dω_s [10^-8 (Counts s^-1) s^-1]", Large]}]
```

```
Clear["Global`*"]
```

Calculating Schmidt distribution of signal and idler photons being projected on LG basis using the method described in [79]

```
LGlp[ρ_, ϕ_, W_, l_, p_] :=
  (-1)^p (W^2 Factorial[p] / (2 Pi Factorial[p + Abs[l]]))^0.5 (ρ W / √2)^Abs[l] Exp[-ρ^2 W^2 / 4] LaguerreL[p, Abs[l], ρ^2 W^2 / 2] Exp[i l (ϕ + Pi/2)];

A[ρi_, ρs_, ϕi_, ϕs_, W_, L_, λ_] := W / (2 Pi)^0.5 Exp[(-W^2 / 4) (ρi^2 + ρs^2 + 2 ρi ρs Cos[ϕi - ϕs])] (λ L / Pi^3)^0.5
  Sinc[L λ (ρi^2 + ρs^2 - 2 ρi ρs Cos[ϕi - ϕs]) / (8 Pi)] Exp[-i L λ (ρi^2 + ρs^2 - 2 ρi ρs Cos[ϕi - ϕs]) / (8 Pi)];

Klp[pi_, ps_, l_] := Factorial[pi + ps + Abs[l]] / (Factorial[pi] Factorial[ps] Factorial[ps + Abs[l]] Factorial[pi + Abs[l]])^0.5;

B[t_, Wi_, Ws_, Wp_, L_, λp_] := -(λp t / (Pi Wi Ws) + L λp / (2 Pi Wi Ws) + i Wp^2 / (Wi Ws));

SI[t_, W_, Wp_, L_, λp_] := Wp^2 / (2 W^2) + 1/2 + i t λp / (2 Pi W^2) + i L λp / (4 Pi W^2);

T[t_, Wi_, Ws_, Wp_, L_, λp_] := 4 SI[t, Ws, Wp, L, λp] SI[t, Wi, Wp, L, λp] + B[t, Wi, Ws, Wp, L, λp]^2;

csi[L_, Ws_, Wi_, Wp_, λp_, ps_, pi_, l_, t_] :=
  B[t, Wi, Ws, Wp, L, λp]^Abs[l] (1 - 4 SI[t, Wi, Wp, L, λp] / T[t, Wi, Ws, Wp, L, λp])^ps (1 - 4 SI[t, Ws, Wp, L, λp] / T[t, Wi, Ws, Wp, L, λp])^pi
  / (T[t, Wi, Ws, Wp, L, λp])^(Abs[l] + 1) Hypergeometric2F1[-pi, -ps, -pi - ps - Abs[l],
    (T[t, Wi, Ws, Wp, L, λp] (T[t, Wi, Ws, Wp, L, λp] - 4 SI[t, Wi, Wp, L, λp] - 4 SI[t, Ws, Wp, L, λp] + 4)) /
     ((T[t, Wi, Ws, Wp, L, λp] - 4 SI[t, Ws, Wp, L, λp]) (T[t, Wi, Ws, Wp, L, λp] - 4 SI[t, Wi, Wp, L, λp])))];

Csi[L_?NumericQ, Ws_?NumericQ, Wi_?NumericQ, Wp_?NumericQ, λp_?NumericQ, ps_?NumericQ, pi_?NumericQ, l_?NumericQ] :=
  Klp[pi, ps, l] NIntegrate[csi[L, Ws, Wi, Wp, λp, ps, pi, l, t], {t, -L/2, L/2},
    AccuracyGoal → 5, Method → "GaussKronrodRule", WorkingPrecision → 10];
```

Variation of Schmidt probabilities with mode width W (Ws = Wi = Wp)

```
W0 = 25 × 10^-6; (*Signal mode waist size*)
λp0 = 355 × 10^-9;
λs0 = 710 × 10^-9;

Cpsum0 = Sum[Abs[Csi[L, Ws, Wi, Wp, λp, ps, pi, l]]^2, {ps, 0, 10, 1}, {pi, 0, 10, 1}, {l, -10, 10}] /.
   {L → 0.001, Ws → W0, Wi → W0, Wp → W0, λp → λp0};

Cprange = Table[Abs[Csi[L, Ws, Wi, Wp, λp, ps, pi, l]]^2 / Cpsum0 /.
    {L → 0.001, Ws → W0, Wi → W0, Wp → W0, λp → 355 × 10^-9, l → 0}, {ps, 0, 10, 1}, {pi, 0, 10, 1}];

p0l0 = MatrixPlot[Cprange, FrameTicks → {{Table[{ps, ps - 1}, {ps, 11}], None}, {Table[{pi, pi - 1}, {pi, 11}], None}},
  PlotRange → All, ColorFunction → "DeepSeaColors", PlotLegends → BarLegend[Automatic, LabelStyle → {FontSize → 24}],
  FrameLabel → {Style["ps", Large], Style["pi", Large]}, LabelStyle → 24, ImageSize → 400]

Spiralbw0 = Table[
   {1, Abs[Csi[L, Ws, Wi, Wp, λp, 0, 0, l]]^2 / Cpsum0 /. {L → 0.001, Ws → W0, Wi → W0, Wp → W0, λp → 355 × 10^-9}}, {l, -6, 6, 1}];

Cpsum1 = Sum[Abs[Csi[L, Ws, Wi, Wp, λp, ps, pi, l]]^2, {ps, 0, 10, 1}, {pi, 0, 10, 1}, {l, -10, 10}] /.
   {L → 0.001, Ws → 15 × 10^-6, Wi → 15 × 10^-6, Wp → 15 × 10^-6, λp → λp0};

Spiralbw1 = Table[{1, Abs[Csi[L, Ws, Wi, Wp, λp, 0, 0, l]]^2 / Cpsum1 /.
     {L → 0.001, Ws → 15 × 10^-6, Wi → 15 × 10^-6, Wp → 15 × 10^-6, λp → 355 × 10^-9}}, {l, -6, 6, 1}];

Cpsum2 = Sum[Abs[Csi[L, Ws, Wi, Wp, λp, ps, pi, l]]^2, {ps, 0, 10, 1}, {pi, 0, 10, 1}, {l, -10, 10}] /.
   {L → 0.001, Ws → 25 × 10^-6, Wi → 25 × 10^-6, Wp → 25 × 10^-6, λp → λp0};
```

```
Spiralbw2 = Table[{l, Abs[Csi[L, Ws, Wi, Wp, λp, 0, 0, l]]^2 1/Cpsum2 /.
      {L → 0.001, Ws → 25 × 10^-6, Wi → 25 × 10^-6, Wp → 25 × 10^-6, λp → 355 × 10^-9}}, {l, -6, 6, 1}] ;

Cpsum3 = Sum[Abs[Csi[L, Ws, Wi, Wp, λp, ps, pi, l]]^2, {ps, 0, 10, 1}, {pi, 0, 10, 1}, {l, -10, 10}] /.
   {L → 0.001, Ws → 50 × 10^-6, Wi → 50 × 10^-6, Wp → 50 × 10^-6, λp → λp0};

Spiralbw3 = Table[{l, Abs[Csi[L, Ws, Wi, Wp, λp, 0, 0, l]]^2 1/Cpsum3 /.
      {L → 0.001, Ws → 50 × 10^-6, Wi → 50 × 10^-6, Wp → 50 × 10^-6, λp → 355 × 10^-9}}, {l, -6, 6, 1}] ;

Cpsum4 = Sum[Abs[Csi[L, Ws, Wi, Wp, λp, ps, pi, l]]^2, {ps, 0, 10, 1}, {pi, 0, 10, 1}, {l, -10, 10}] /.
   {L → 0.001, Ws → 100 × 10^-6, Wi → 100 × 10^-6, Wp → 100 × 10^-6, λp → λp0};

Spiralbw4 = Table[{l, Abs[Csi[L, Ws, Wi, Wp, λp, 0, 0, l]]^2 1/Cpsum4 /.
      {L → 0.001, Ws → 100 × 10^-6, Wi → 100 × 10^-6, Wp → 100 × 10^-6, λp → 355 × 10^-9}}, {l, -6, 6, 1}] ;

SchmidtWplot = ListPlot[{Spiralbw0, Spiralbw1, Spiralbw2, Spiralbw3, Spiralbw4},
  PlotRange → All, Joined → True, PlotLabel → "p_s = p_i = 0", ImageSize → 600, Frame → True,
  FrameLabel → {Style["Azimuthal index [l]", 24], Style["Schmidt Probability", 24]}, LabelStyle → 24,
  PlotMarkers → {Automatic, 22}, PlotStyle → {{Dashed, Thickness[0.003]}}, PlotLegends → Placed[
    LineLegend[{"10 μm", "15 μm", "25 μm", "50 μm", "100 μm"}, LegendFunction → "Frame", LegendMargins → 0], {0.84, 0.64}]]
  (*Plotting probability distribution for ps = pi = 0*)
```

Variation of Schmidt probabilities with crystal length L for Ws = Wi = Wp = 25 μm

```
CLsum0 = Sum[Abs[Csi[L, Ws, Wi, Wp, λp, ps, pi, l]]^2, {ps, 0, 10, 1}, {pi, 0, 10, 1}, {l, -10, 10}] /.
   {L → 0.0001, Ws → 25 × 10^-6, Wi → 25 × 10^-6, Wp → 25 × 10^-6, λp → λp0};
CLsum1 = Sum[Abs[Csi[L, Ws, Wi, Wp, λp, ps, pi, l]]^2, {ps, 0, 10, 1}, {pi, 0, 10, 1}, {l, -10, 10}] /.
   {L → 0.0005, Ws → 25 × 10^-6, Wi → 25 × 10^-6, Wp → 25 × 10^-6, λp → λp0};
CLsum2 = Sum[Abs[Csi[L, Ws, Wi, Wp, λp, ps, pi, l]]^2, {ps, 0, 10, 1}, {pi, 0, 10, 1}, {l, -10, 10}] /.
   {L → 0.001, Ws → 25 × 10^-6, Wi → 25 × 10^-6, Wp → 25 × 10^-6, λp → λp0};
CLsum3 = Sum[Abs[Csi[L, Ws, Wi, Wp, λp, ps, pi, l]]^2, {ps, 0, 10, 1}, {pi, 0, 10, 1}, {l, -10, 10}] /.
   {L → 0.0025, Ws → 25 × 10^-6, Wi → 25 × 10^-6, Wp → 25 × 10^-6, λp → λp0};
CLsum4 = Sum[Abs[Csi[L, Ws, Wi, Wp, λp, ps, pi, l]]^2, {ps, 0, 10, 1}, {pi, 0, 10, 1}, {l, -10, 10}] /.
   {L → 0.005, Ws → 25 × 10^-6, Wi → 25 × 10^-6, Wp → 25 × 10^-6, λp → λp0};

SpiralL0 = Table[{l, Abs[Csi[L, Ws, Wi, Wp, λp, 0, 0, l]]^2 1/CLsum0 /.
      {L → 0.0001, Ws → 25 × 10^-6, Wi → 25 × 10^-6, Wp → 25 × 10^-6, λp → λp0}}, {l, -6, 6, 1}] ;
SpiralL1 = Table[{l, Abs[Csi[L, Ws, Wi, Wp, λp, 0, 0, l]]^2 1/CLsum1 /.
      {L → 0.0005, Ws → 25 × 10^-6, Wi → 25 × 10^-6, Wp → 25 × 10^-6, λp → λp0}}, {l, -6, 6, 1}] ;
SpiralL2 = Table[{l, Abs[Csi[L, Ws, Wi, Wp, λp, 0, 0, l]]^2 1/CLsum2 /.
      {L → 0.001, Ws → 25 × 10^-6, Wi → 25 × 10^-6, Wp → 25 × 10^-6, λp → λp0}}, {l, -6, 6, 1}] ;
SpiralL3 = Table[{l, Abs[Csi[L, Ws, Wi, Wp, λp, 0, 0, l]]^2 1/CLsum3 /.
      {L → 0.0025, Ws → 25 × 10^-6, Wi → 25 × 10^-6, Wp → 25 × 10^-6, λp → λp0}}, {l, -6, 6, 1}] ;
SpiralL4 = Table[{l, Abs[Csi[L, Ws, Wi, Wp, λp, 0, 0, l]]^2 1/CLsum4 /.
      {L → 0.005, Ws → 25 × 10^-6, Wi → 25 × 10^-6, Wp → 25 × 10^-6, λp → λp0}}, {l, -6, 6, 1}] ;

CLrange = Table[Abs[Csi[L, Ws, Wi, Wp, λp, ps, pi, l]]^2 1/Cpsum2 /.
    {L → 0.001, Ws → 25 × 10^-6, Wi → 25 × 10^-6, Wp → 25 × 10^-6, λp → λp0, l → 0}, {ps, 0, 10, 1}, {pi, 0, 10, 1}] ;

SchmidtLplot = ListPlot[{SpiralL0, SpiralL1, SpiralL2, SpiralL3, SpiralL4},
  PlotRange → All, Joined → True, PlotLabel → "p_s = p_i = 0", ImageSize → 600, Frame → True,
  FrameLabel → {Style["Azimuthal index [l]", 24], Style["Schmidt Probability", 24]}, LabelStyle → 24,
  PlotMarkers → {Automatic, 22}, PlotStyle → {{Dashed, Thickness[0.003]}}, PlotLegends → Placed[
    LineLegend[{"0.1 mm", "0.5 mm", "1 mm", "2.5 mm", "5 mm"}, LegendFunction → "Frame", LegendMargins → 0], {0.84, 0.6}]]
```

Variation of Schmidt probabilities with crystal length Pump focussing (γ = Wp/W,

Ws = Wi = W)

```
Cgsum0 = Sum[Abs[Csi[L, W, W, γW, λp, ps, pi, l]]^2, {ps, 0, 10, 1}, {pi, 0, 10, 1}, {l, -10, 10}] /.
    {L → 0.001, W → 25 × 10^-6, γ → 0.5, λp → λp0};
Cgsum1 = Sum[Abs[Csi[L, W, W, γW, λp, ps, pi, l]]^2, {ps, 0, 10, 1}, {pi, 0, 10, 1}, {l, -10, 10}] /.
    {L → 0.001, W → 25 × 10^-6, γ → 0.707, λp → λp0};
Cgsum2 = Sum[Abs[Csi[L, W, W, γW, λp, ps, pi, l]]^2, {ps, 0, 10, 1}, {pi, 0, 10, 1}, {l, -10, 10}] /.
    {L → 0.001, W → 25 × 10^-6, γ → 1, λp → λp0};
Cgsum3 = Sum[Abs[Csi[L, W, W, γW, λp, ps, pi, l]]^2, {ps, 0, 10, 1}, {pi, 0, 10, 1}, {l, -10, 10}] /.
    {L → 0.001, W → 25 × 10^-6, γ → 1.5, λp → λp0};
Cgsum4 = Sum[Abs[Csi[L, W, W, γW, λp, ps, pi, l]]^2, {ps, 0, 10, 1}, {pi, 0, 10, 1}, {l, -10, 10}] /.
    {L → 0.001, W → 25 × 10^-6, γ → 2, λp → λp0};
Cgsum5 = Sum[Abs[Csi[L, W, W, γW, λp, ps, pi, l]]^2, {ps, 0, 10, 1}, {pi, 0, 10, 1}, {l, -10, 10}] /.
    {L → 0.001, W → 25 × 10^-6, γ → 5, λp → λp0};

Spiralg0 =
  Table[{l, Abs[Csi[L, W, W, γW, λp, 0, 0, l]]^2 1/Cgsum0 /. {L → 0.001, W → 25 × 10^-6, γ → 0.5, λp → λp0}}, {l, -6, 6, 1}];
Spiralg1 = Table[{l, Abs[Csi[L, W, W, γW, λp, 0, 0, l]]^2 1/Cgsum1 /. {L → 0.001, W → 25 × 10^-6, γ → 0.707, λp → λp0}},
    {l, -6, 6, 1}];
Spiralg2 = Table[{l, Abs[Csi[L, W, W, γW, λp, 0, 0, l]]^2 1/Cgsum2 /. {L → 0.001, W → 25 × 10^-6, γ → 1, λp → λp0}}, {l, -6, 6, 1}];
Spiralg3 =
  Table[{l, Abs[Csi[L, W, W, γW, λp, 0, 0, l]]^2 1/Cgsum3 /. {L → 0.001, W → 25 × 10^-6, γ → 1.5, λp → λp0}}, {l, -6, 6, 1}];
Spiralg4 = Table[{l, Abs[Csi[L, W, W, γW, λp, 0, 0, l]]^2 1/Cgsum4 /. {L → 0.001, W → 25 × 10^-6, γ → 2, λp → λp0}}, {l, -6, 6, 1}];
Spiralg5 = Table[{l, Abs[Csi[L, W, W, γW, λp, 0, 0, l]]^2 1/Cgsum5 /. {L → 0.001, W → 25 × 10^-6, γ → 5, λp → λp0}}, {l, -6, 6, 1}];

Schmidtgplot = ListPlot[{Spiralg0, Spiralg1, Spiralg2, Spiralg3, Spiralg4, Spiralg5},
  PlotRange → All, Joined → True, PlotLabel → "p_s = p_i = 0", ImageSize → 600, Frame → True,
  FrameLabel → {Style["Azimuthal index [l]", 24], Style["Schmidt Probability", 24]}, LabelStyle → 24,
  PlotMarkers → {Automatic, 22}, PlotStyle → {{Dashed, Thickness[0.003]}}, PlotLegends →
   Placed[LineLegend[{"0.5", "0.707", "1", "1.5", "2", "5"}, LegendFunction → "Frame", LegendMargins → 0], {0.84, 0.6}]]

ξ[λ_, W_, L_] := L λ / (2 Pi W^2); (*Focussing parameter of signal*)
Ks[λ_, W_, L_] := 1/4 ((ξ[λ, W, L])^0.5 + 1/(ξ[λ, W, L])^0.5)^2; (*Schmidt Number*)
```

Calculation of coupling probability of each LG mode in a MMF by first solving for b values for each l and p value

```
Wm = 25 × 10^-6; (*Signal/idler beam waist after lens*)
a0 = 25. × 10^-6; (*Core radius = 25 μm*)
NA = 0.1; (*Numerical Aperture*)

V0 = 2 Pi a0 NA / λs0; (*V-parameter*)

N0 = V0^2/2; (*Approximate number of modes*)

LaguerreGauss[ρ_, Wa_, l_, p_, ϕ_] := 1/Wa (ρ √2 / Wa)^Abs[l] Exp[-ρ^2/Wa^2] LaguerreL[p, Abs[l], 2 ρ^2/Wa^2] Exp[i l ϕ];
(*Defining Signal/Idler modes in LG basis at z=0 or the entry face of the fiber*)
Elma[ρ1_, ϕ1_, U_, a_, m_] := BesselJ[Abs[m], U ρ1/a] / BesselJ[Abs[m], U] Exp[i m ϕ1]; (*Defining Fiber mode within the core*)
Elmo[ρ1_, ϕ1_, W_, a_, m_] := BesselK[Abs[m], W ρ1/a] / BesselK[Abs[m], W] Exp[i m ϕ1]; (*Defining tail of the fiber mode in the cladding*)
```

```
lhs1[V_, b_] := V Sqrt[1 - b] BesselJ[1, V Sqrt[1 - b]] / BesselJ[0, V Sqrt[1 - b]]; (*Fundamental fiber mode*)

rhs1[V_, b_] := V Sqrt[b] BesselK[1, V Sqrt[b]] / BesselK[0, V Sqrt[b]];


lhs1[V_, b_, l_] := V Sqrt[1 - b] BesselJ[1 - 1, V Sqrt[1 - b]] / BesselJ[1, V Sqrt[1 - b]];(*Higher order fiber modes*)

rhs1[V_, b_, l_] := -V Sqrt[b] BesselK[1 - 1, V Sqrt[b]] / BesselK[1, V Sqrt[b]];
```

Coupling probability of all l=0 modes (p = 0 to 10) to all fiber modes $E_{m,n}$ where m is the azimuthal index and n is the radial index

Finding all fiber modes and the normalizing factors for each mode

```
b0 = List[0.1, 0.5, 0.7, 0.8, 0.92, 0.98, 0.99] ;
(*Defining starting points to define roots of transcendental equation for m =
 0. This gives the fiber modes E_{m, n} with indices m and n. Here m is taken as 0. Later,
the overlap of each l (of the LG free space mode) is calculated for all the other m modes*)
bm0 = b /. Table[FindRoot[lhs1[V0, b] == rhs1[V0, b], {b, b0}], {b0, b0}] ;
(*Finding roots of the transcendental equation for m=0*)

Um0 = V0 Sqrt[1 - bm0] ;
Wm0 = V0 Sqrt[bm0] ;

fiberm0 = Integrate[ρ1 Abs[Elma[ρ1, ϕ1, U, a, m]]^2 /. {U → Um0, a → a0, m → 0},
    {ρ1, 0, a0}, {ϕ1, 0, 2 Pi}, Assumptions → {{ρ1, ϕ1} > 0}] + Integrate[
    ρ1 Abs[Elmo[ρ1, ϕ1, W, a, m]]^2 /. {W → Wm0, a → a0, m → 0}, {ρ1, a0, ∞}, {ϕ1, 0, 2 Pi}, Assumptions → {{ρ1, ϕ1} > 0}];
 (*The integral in the denominator of coupling efficiency in equation (4.82)*)

fiberm = {fiberm0};

b1 = List[0.1, 0.4, 0.6, 0.7, 0.8, 0.97, 0.99] ;(*m = 1*)
bm1 = b /. Table[FindRoot[lhsl[V0, b, 1] == rhsl[V0, b, 1], {b, b11}], {b11, b1}] ;

Um0 = Join[{Um0}, {V0 Sqrt[1 - bm1]}];
Wm0 = Join[{Wm0}, {V0 Sqrt[bm1]}];

fiberm1 = Integrate[ρ1 Abs[Elma[ρ1, ϕ1, U, a, m]]^2 /. {U → V0 Sqrt[1 - bm1], a → a0, m → 1},
    {ρ1, 0, a0}, {ϕ1, 0, 2 Pi}, Assumptions → {{ρ1, ϕ1} > 0}] + Integrate[
    ρ1 Abs[Elmo[ρ1, ϕ1, W, a, m]]^2 /. {W → V0 Sqrt[bm1], a → a0, m → 1}, {ρ1, a0, ∞}, {ϕ1, 0, 2 Pi}, Assumptions → {{ρ1, ϕ1} > 0}];


fiberm = Join[fiberm, {fiberm1}];

b2 = List[0.2, 0.5, 0.65, 0.8, 0.92, 0.98]; (*m = 2*)

bm2 = b /. Table[FindRoot[lhsl[V0, b, 2] == rhsl[V0, b, 2], {b, b22}], {b22, b2}];

Um0 = Join[Um0, {V0 Sqrt[1 - bm2]}];
Wm0 = Join[Wm0, {V0 Sqrt[bm2]}];
```

```
fiberm2 = Integrate[ρ1 Abs[Elma[ρ1, ϕ1, U, a, m]]^2 /. {U → V0 Sqrt[1 - bm2], a → a0, m → 2},
    {ρ1, 0, a0}, {ϕ1, 0, 2 Pi}, Assumptions → {{ρ1, ϕ1} > 0}] + Integrate[
    ρ1 Abs[Elmo[ρ1, ϕ1, W, a, m]]^2 /. {W → V0 Sqrt[bm2], a → a0, m → 2}, {ρ1, a0, ∞}, {ϕ1, 0, 2 Pi}, Assumptions → {{ρ1, ϕ1} > 0}];

fiberm = Join[fiberm, {fiberm2}];

b3 = List[0.2, 0.4, 0.5, 0.7, 0.85, 0.96]; (*m = 3*)

bm3 = b /. Table[FindRoot[lhsl[V0, b, 3] == rhsl[V0, b, 3], {b, b22}], {b22, b3}];

Um0 = Join[Um0, {V0 Sqrt[1 - bm3]}];
Wm0 = Join[Wm0, {V0 Sqrt[bm3]}];

fiberm3 = Integrate[ρ1 Abs[Elma[ρ1, ϕ1, U, a, m]]^2 /. {U → V0 Sqrt[1 - bm3], a → a0, m → 3},
    {ρ1, 0, a0}, {ϕ1, 0, 2 Pi}, Assumptions → {{ρ1, ϕ1} > 0}] + Integrate[
    ρ1 Abs[Elmo[ρ1, ϕ1, W, a, m]]^2 /. {W → V0 Sqrt[bm3], a → a0, m → 3}, {ρ1, a0, ∞}, {ϕ1, 0, 2 Pi}, Assumptions → {{ρ1, ϕ1} > 0}];

fiberm = Join[fiberm, {fiberm3}];

b4 = List[0.25, 0.5, 0.68, 0.8, 0.92]; (*m = 4*)

bm4 = b /. Table[FindRoot[lhsl[V0, b, 4] == rhsl[V0, b, 4], {b, b22}], {b22, b4}];

Um0 = Join[Um0, {V0 Sqrt[1 - bm4]}];
Wm0 = Join[Wm0, {V0 Sqrt[bm4]}];

fiberm4 = Integrate[ρ1 Abs[Elma[ρ1, ϕ1, U, a, m]]^2 /. {U → V0 Sqrt[1 - bm4], a → a0, m → 4},
    {ρ1, 0, a0}, {ϕ1, 0, 2 Pi}, Assumptions → {{ρ1, ϕ1} > 0}] + Integrate[
    ρ1 Abs[Elmo[ρ1, ϕ1, W, a, m]]^2 /. {W → V0 Sqrt[bm4], a → a0, m → 4}, {ρ1, a0, ∞}, {ϕ1, 0, 2 Pi}, Assumptions → {{ρ1, ϕ1} > 0}];

fiberm = Join[fiberm, {fiberm4}];

b5 = List[0.2, 0.4, 0.6, 0.8, 0.87]; (*m = 5*)

bm5 = b /. Table[FindRoot[lhsl[V0, b, 5] == rhsl[V0, b, 5], {b, b22}], {b22, b5}];

Um0 = Join[Um0, {V0 Sqrt[1 - bm5]}];
Wm0 = Join[Wm0, {V0 Sqrt[bm5]}];

fiberm5 = Integrate[ρ1 Abs[Elma[ρ1, ϕ1, U, a, m]]^2 /. {U → V0 Sqrt[1 - bm5], a → a0, m → 5},
    {ρ1, 0, a0}, {ϕ1, 0, 2 Pi}, Assumptions → {{ρ1, ϕ1} > 0}] + Integrate[
    ρ1 Abs[Elmo[ρ1, ϕ1, W, a, m]]^2 /. {W → V0 Sqrt[bm5], a → a0, m → 5}, {ρ1, a0, ∞}, {ϕ1, 0, 2 Pi}, Assumptions → {{ρ1, ϕ1} > 0}];

fiberm = Join[fiberm, {fiberm5}];

b6 = List[0.3, 0.5, 0.7, 0.85]; (*m = 6*)

bm6 = b /. Table[FindRoot[lhsl[V0, b, 6] == rhsl[V0, b, 6], {b, b22}], {b22, b6}];

Um0 = Join[Um0, {V0 Sqrt[1 - bm6]}];
Wm0 = Join[Wm0, {V0 Sqrt[bm6]}];
```

```
fiberm6 = Integrate[ρ1 Abs[Elma[ρ1, ϕ1, U, a, m]]^2 /. {U → V0 Sqrt[1 - bm6], a → a0, m → 6},
     {ρ1, 0, a0}, {ϕ1, 0, 2 Pi}, Assumptions → {{ρ1, ϕ1} > 0}] + Integrate[
     ρ1 Abs[Elmo[ρ1, ϕ1, W, a, m]]^2 /. {W → V0 Sqrt[bm6], a → a0, m → 6}, {ρ1, a0, ∞}, {ϕ1, 0, 2 Pi}, Assumptions → {{ρ1, ϕ1} > 0}];

fiberm = Join[fiberm, {fiberm6}];

b7 = List[0.2, 0.4, 0.6, 0.8]; (*m = 7*)

bm7 = b /. Table[FindRoot[lhsl[V0, b, 7] == rhsl[V0, b, 7], {b, b22}], {b22, b7}];

Um0 = Join[Um0, {V0 Sqrt[1 - bm7]}];
Wm0 = Join[Wm0, {V0 Sqrt[bm7]}];

fiberm7 = Integrate[ρ1 Abs[Elma[ρ1, ϕ1, U, a, m]]^2 /. {U → V0 Sqrt[1 - bm7], a → a0, m → 7},
     {ρ1, 0, a0}, {ϕ1, 0, 2 Pi}, Assumptions → {{ρ1, ϕ1} > 0}] + Integrate[
     ρ1 Abs[Elmo[ρ1, ϕ1, W, a, m]]^2 /. {W → V0 Sqrt[bm7], a → a0, m → 7}, {ρ1, a0, ∞}, {ϕ1, 0, 2 Pi}, Assumptions → {{ρ1, ϕ1} > 0}];

fiberm = Join[fiberm, {fiberm7}];

b8 = List[0.1, 0.3, 0.6, 0.77]; (*m = 8*)

bm8 = b /. Table[FindRoot[lhsl[V0, b, 8] == rhsl[V0, b, 8], {b, b22}], {b22, b8}];

Um0 = Join[Um0, {V0 Sqrt[1 - bm8]}];
Wm0 = Join[Wm0, {V0 Sqrt[bm8]}];

fiberm8 = Integrate[ρ1 Abs[Elma[ρ1, ϕ1, U, a, m]]^2 /. {U → V0 Sqrt[1 - bm8], a → a0, m → 8},
     {ρ1, 0, a0}, {ϕ1, 0, 2 Pi}, Assumptions → {{ρ1, ϕ1} > 0}] + Integrate[
     ρ1 Abs[Elmo[ρ1, ϕ1, W, a, m]]^2 /. {W → V0 Sqrt[bm8], a → a0, m → 8}, {ρ1, a0, ∞}, {ϕ1, 0, 2 Pi}, Assumptions → {{ρ1, ϕ1} > 0}];

fiberm = Join[fiberm, {fiberm8}];

b9 = List[0.22, 0.5, 0.7]; (*m = 9*)

bm9 = b /. Table[FindRoot[lhsl[V0, b, 9] == rhsl[V0, b, 9], {b, b22}], {b22, b9}]
  (*Finding roots of the transcendental equation*)
{0.201714, 0.448067, 0.667436}

Um0 = Join[Um0, {V0 Sqrt[1 - bm9]}];
Wm0 = Join[Wm0, {V0 Sqrt[bm9]}];

fiberm9 = Integrate[ρ1 Abs[Elma[ρ1, ϕ1, U, a, m]]^2 /. {U → V0 Sqrt[1 - bm9], a → a0, m → 9},
     {ρ1, 0, a0}, {ϕ1, 0, 2 Pi}, Assumptions → {{ρ1, ϕ1} > 0}] + Integrate[
     ρ1 Abs[Elmo[ρ1, ϕ1, W, a, m]]^2 /. {W → V0 Sqrt[bm9], a → a0, m → 9}, {ρ1, a0, ∞}, {ϕ1, 0, 2 Pi}, Assumptions → {{ρ1, ϕ1} > 0}];

fiberm = Join[fiberm, {fiberm9}];

b10 = List[0.15, 0.4, 0.62]; (*m = 10*)

bm10 = b /. Table[FindRoot[lhsl[V0, b, 10] == rhsl[V0, b, 10], {b, b22}], {b22, b10}];
```

```
Um0 = Join[Um0, {V0 Sqrt[1 - bm10]}];
Wm0 = Join[Wm0, {V0 Sqrt[bm10]}];

fiberm10 = Integrate[ρ1 Abs[Elma[ρ1, ϕ1, U, a, m]]^2 /. {U → V0 Sqrt[1 - bm10], a → a0, m → 10},
    {ρ1, 0, a0}, {ϕ1, 0, 2 Pi}, Assumptions → {{ρ1, ϕ1} > 0}] + Integrate[
    ρ1 Abs[Elmo[ρ1, ϕ1, W, a, m]]^2 /. {W → V0 Sqrt[bm10], a → a0, m → 10}, {ρ1, a0, ∞}, {ϕ1, 0, 2 Pi}, Assumptions → {{ρ1, ϕ1} > 0}];

fiberm = Join[fiberm, {fiberm10}];

b11 = List[0.1, 0.4, 0.6]; (*m = 11*)

bm11 = b /. Table[FindRoot[lhsl[V0, b, 11] == rhsl[V0, b, 11], {b, b22}], {b22, b11}];

Um0 = Join[Um0, {V0 Sqrt[1 - bm11]}];
Wm0 = Join[Wm0, {V0 Sqrt[bm11]}];

fiberm11 = Integrate[ρ1 Abs[Elma[ρ1, ϕ1, U, a, m]]^2 /. {U → V0 Sqrt[1 - bm11], a → a0, m → 11},
    {ρ1, 0, a0}, {ϕ1, 0, 2 Pi}, Assumptions → {{ρ1, ϕ1} > 0}] + Integrate[
    ρ1 Abs[Elmo[ρ1, ϕ1, W, a, m]]^2 /. {W → V0 Sqrt[bm11], a → a0, m → 11}, {ρ1, a0, ∞}, {ϕ1, 0, 2 Pi}, Assumptions → {{ρ1, ϕ1} > 0}];

fiberm = Join[fiberm, {fiberm11}];

b12 = List[0.21, 0.5]; (*m = 12*)

bm12 = b /. Table[FindRoot[lhsl[V0, b, 12] == rhsl[V0, b, 12], {b, b22}], {b22, b12}];

Um0 = Join[Um0, {V0 Sqrt[1 - bm12]}];
Wm0 = Join[Wm0, {V0 Sqrt[bm12]}];

fiberm12 = Integrate[ρ1 Abs[Elma[ρ1, ϕ1, U, a, m]]^2 /. {U → V0 Sqrt[1 - bm12], a → a0, m → 12},
    {ρ1, 0, a0}, {ϕ1, 0, 2 Pi}, Assumptions → {{ρ1, ϕ1} > 0}] + Integrate[
    ρ1 Abs[Elmo[ρ1, ϕ1, W, a, m]]^2 /. {W → V0 Sqrt[bm12], a → a0, m → 12}, {ρ1, a0, ∞}, {ϕ1, 0, 2 Pi}, Assumptions → {{ρ1, ϕ1} > 0}];

fiberm = Join[fiberm, {fiberm12}];

b13 = List[0.15, 0.42]; (*m = 13*)

bm13 = b /. Table[FindRoot[lhsl[V0, b, 13] == rhsl[V0, b, 13], {b, b22}], {b22, b13}];

Um0 = Join[Um0, {V0 Sqrt[1 - bm13]}];
Wm0 = Join[Wm0, {V0 Sqrt[bm13]}];

fiberm13 = Integrate[ρ1 Abs[Elma[ρ1, ϕ1, U, a, m]]^2 /. {U → V0 Sqrt[1 - bm13], a → a0, m → 13},
    {ρ1, 0, a0}, {ϕ1, 0, 2 Pi}, Assumptions → {{ρ1, ϕ1} > 0}] + Integrate[
    ρ1 Abs[Elmo[ρ1, ϕ1, W, a, m]]^2 /. {W → V0 Sqrt[bm13], a → a0, m → 13}, {ρ1, a0, ∞}, {ϕ1, 0, 2 Pi}, Assumptions → {{ρ1, ϕ1} > 0}];

fiberm = Join[fiberm, {fiberm13}];

b14 = List[0.1, 0.4]; (*m = 14*)

bm14 = b /. Table[FindRoot[lhsl[V0, b, 14] == rhsl[V0, b, 14], {b, b22}], {b22, b14}];
```

```
Um0 = Join[Um0, {V0 Sqrt[1 - bm14]}];
Wm0 = Join[Wm0, {V0 Sqrt[bm14]}];

fiberm14 = Integrate[ρ1 Abs[Elma[ρ1, ϕ1, U, a, m]]^2 /. {U → V0 Sqrt[1 - bm14], a → a0, m → 14},
    {ρ1, 0, a0}, {ϕ1, 0, 2 Pi}, Assumptions → {{ρ1, ϕ1} > 0}] + Integrate[
    ρ1 Abs[Elmo[ρ1, ϕ1, W, a, m]]^2 /. {W → V0 Sqrt[bm14], a → a0, m → 14}, {ρ1, a0, ∞}, {ϕ1, 0, 2 Pi}, Assumptions → {{ρ1, ϕ1} > 0}];

fiberm = Join[fiberm, {fiberm14}];

b15 = List[0.3]; (*m = 15*)

bm15 = b /. Table[FindRoot[lhsl[V0, b, 15] == rhsl[V0, b, 15], {b, b22}], {b22, b15}];

Um0 = Join[Um0, {V0 Sqrt[1 - bm15]}];
Wm0 = Join[Wm0, {V0 Sqrt[bm15]}];

fiberm15 = Integrate[ρ1 Abs[Elma[ρ1, ϕ1, U, a, m]]^2 /. {U → V0 Sqrt[1 - bm15], a → a0, m → 15},
    {ρ1, 0, a0}, {ϕ1, 0, 2 Pi}, Assumptions → {{ρ1, ϕ1} > 0}] + Integrate[
    ρ1 Abs[Elmo[ρ1, ϕ1, W, a, m]]^2 /. {W → V0 Sqrt[bm15], a → a0, m → 15}, {ρ1, a0, ∞}, {ϕ1, 0, 2 Pi}, Assumptions → {{ρ1, ϕ1} > 0}];

fiberm = Join[fiberm, {fiberm15}];

b16 = List[0.2]; (*m = 16*)

bm16 = b /. Table[FindRoot[lhsl[V0, b, 16] == rhsl[V0, b, 16], {b, b22}], {b22, b16}];

Um0 = Join[Um0, {V0 Sqrt[1 - bm16]}];
Wm0 = Join[Wm0, {V0 Sqrt[bm16]}];

fiberm16 = Integrate[ρ1 Abs[Elma[ρ1, ϕ1, U, a, m]]^2 /. {U → V0 Sqrt[1 - bm16], a → a0, m → 16},
    {ρ1, 0, a0}, {ϕ1, 0, 2 Pi}, Assumptions → {{ρ1, ϕ1} > 0}] + Integrate[
    ρ1 Abs[Elmo[ρ1, ϕ1, W, a, m]]^2 /. {W → V0 Sqrt[bm16], a → a0, m → 16}, {ρ1, a0, ∞}, {ϕ1, 0, 2 Pi}, Assumptions → {{ρ1, ϕ1} > 0}];

fiberm = Join[fiberm, {fiberm16}];

b17 = List[0.1]; (*m = 17*)

bm17 = b /. Table[FindRoot[lhsl[V0, b, 17] == rhsl[V0, b, 17], {b, b22}], {b22, b17}];

Um0 = Join[Um0, {V0 Sqrt[1 - bm17]}];
Wm0 = Join[Wm0, {V0 Sqrt[bm17]}];

fiberm17 = Integrate[ρ1 Abs[Elma[ρ1, ϕ1, U, a, m]]^2 /. {U → V0 Sqrt[1 - bm17], a → a0, m → 17},
    {ρ1, 0, a0}, {ϕ1, 0, 2 Pi}, Assumptions → {{ρ1, ϕ1} > 0}] + Integrate[
    ρ1 Abs[Elmo[ρ1, ϕ1, W, a, m]]^2 /. {W → V0 Sqrt[bm17], a → a0, m → 17}, {ρ1, a0, ∞}, {ϕ1, 0, 2 Pi}, Assumptions → {{ρ1, ϕ1} > 0}];

fiberm = Join[fiberm, {fiberm17}];

ll = Length[Um0];

Cpl = ConstantArray[0, {10, 6}];
```

```
k = 6;
l0 = -5;

For[i = 1; p = 0, i ≤ 10, i++; p++,
 LGl0p = Integrate[ρ Abs[LaguerreGauss[ρ, Wa, l, p1, ϕ]]^2 /. {Wa → Wm, l → l0, p1 → p},
    {ϕ, 0, 2 Pi}, {ρ, 0, ∞}, Assumptions → {{ρ, ϕ} > 0}];
 cfl0 = 0;
 Clear[Overlap];
 For[j = 1; m1 = 0, j ≤ 18, j++; m1++,
  Overlap =
   Abs[NIntegrate[ρ LaguerreGauss[ρ, Wa, l, p1, ϕ] Conjugate[Elma[ρ, ϕ, U, a, m]] /. {Wa → Wm, l → l0, p1 → p, a → a0, U →
          Um0[[j]], m → m1}, {ϕ, 0, 2 Pi}, {ρ, 0, a0}, AccuracyGoal → 5, Method → "GaussKronrodRule",
       WorkingPrecision → 10] + NIntegrate[ρ LaguerreGauss[ρ, Wa, l, p1, ϕ] Conjugate[Elmo[ρ, ϕ, W, a, m]] /.
        {Wa → Wm, l → l0, p1 → p, a → a0, W → Wm0[[j]], m → m1}, {ϕ, 0, 2 Pi},
       {ρ, a0, ∞}, AccuracyGoal → 5, Method → "GaussKronrodRule", WorkingPrecision → 10]]^2;
  (*Overlap integral for a given LG_p^l mode with a given fiber mode*)
  cfl0 = cfl0 + Total[Overlap / (LGl0p fiberm[[j]])];
  (*Summation of overlap integrals normalized w.r.t. the fiber and LG modes gives the coupling efficiency*)
 ];

 Cpl[[i, k]] = If[cfl0 ≤ 1, cfl0, 1];
]
```

Coupling Efficiencies of different modes to the fiber thus calculated

```
Cpls = {{1, 0.829737, 0.33735, 0.141208, 0.050943, 0.0167476}, {0.584431, 0.52452, 0.35403, 0.235403, 0.117284, 0.0478963},
   {0.485785, 0.327861, 0.236245, 0.231579, 0.165513, 0.0886458}, {0.488412, 0.29166, 0.189519,
    0.193057, 0.179031, 0.122702}, {0.342745, 0.229941, 0.176142, 0.158078, 0.166263, 0.140987},
   {0.374587, 0.234571, 0.176185, 0.142522, 0.144396, 0.142765}, {0.355327, 0.186618, 0.17462, 0.141435,
    0.126792, 0.13334}, {0.374903, 0.173941, 0.156931, 0.144166, 0.118551, 0.120007}, {0.432758, 0.169838,
    0.141116, 0.14288, 0.118014, 0.108668}, {0.399513, 0.162559, 0.127486, 0.162882, 0.120527, 0.10223}};
 (*Coupling efficiencies so calculated for Signal (l≥0)*)

Cpli =
  {{1, 0.15020529906496036`, 0.06013137315973533`, 0.023885501100694057`, 0.011938754279906729`, 0.0032898589235849677`},
   {0.5844306546558052`, 0.1349963452173048`, 0.028964693242052482`, 0.007194571266581146`, 0.001784365860818548`,
    0.0003809311153156359`}, {0.4857848843655344`, 0.062327408997316466`, 0.043246356241143584`, 0.002402396702911231`,
    0.000265899436887722`, 7.079100142597121`*^-6}, {0.4884118284817411`, 0.11908579747250472`,
    0.005525593803072322`, 0.0002289600321089388`, 0.00001143529986874111`, 1.8345932148939509`*^-6},
   {0.342744807760159`, 0.02608343569639584`, 0.009175231553395788`, 0.0001595885259568241 44`,
    0.000012710613023244387`, 5.1518546922563 45`*^-7}, {0.3745867206662126`, 0.025420960895490438`,
    0.001744629154249503 5`, 0.00023235585484184 1482`, 1.994604910987247`*^-6, 2.455386028361884`*^-7},
   {0.35532719791062556`, 0.03187397168256764`, 0.000984698069456007`, 0.00009136506290242658`,
    8.131228962056591`*^-7, 2.7665147020639187`*^-11}, {0.3749028621070899`, 0.02941589632102434`,
    0.001492944948658 5425`, 0.00001824405691330714`, 7.997946545949486`*^-8, 1.428673421758852`*^-14},
   {0.43275755884778244`, 0.017618804565085133`, 0.0002176045514999871`, 8.694480159780901`*^-8,
    1.076064607619614`*^-7, 2.5561520052475468`*^-8}, {0.3995133250420719`, 0.020359649708943106`,
    0.0004384733396280752`, 0.00002718745 3075567223`, 2.3347641413564686`*^-7, 7.230348875838416`*^-15}};
(*Coupling efficiencies so calculated for Signal (l<0)*)
```

Finding the coincidence probability $P_{ps,\,pi}^{l,-l}$

```
Wc = 25 × 10^-6; (*Collection mode waist*)
γ = 30;
L0 = 2.5 × 10^-3;

Csum0 = Sum[Abs[Csi[L, W, W, γW, λp, ps, pi, l]]^2, {ps, 0, 10, 1}, {pi, 0, 10, 1}, {l, -10, 10}] /. {L → L0, W → Wc, λp → λp0};

Ppspil1 =
  Table[Abs[Csi[L, W, W, γW, λp, ps, pi, l]]^2 1/Csum0 /. {L → L0, W → Wc, λp → λp0}, {ps, 0, 9, 1}, {pi, 0, 9, 1}, {l, 0, 5, 1}];
(*Matrix of Schmidt probability distribution for 0≤p≤9 and l≥0*)

Ppspil2 = Table[Abs[Csi[L, W, W, γW, λp, ps, pi, l]]^2 1/Csum0 /. {L → L0, W → Wc, λp → λp0}, {ps, 0, 9, 1},
   {pi, 0, 9, 1}, {l, 0, -5, -1}] ;(*Matrix of Schmidt probability distribution for 0≤p≤9 and l≤0*)
```

Singles probability

```
Ppsl1 = Total[Ppspil1, {2}];
Ppsl2 = Total[Ppspil2, {2}];
```

Heralding Efficiency calculation

```
Denom = Total[Total[Ppsl1 * Cpls]] + Total[Total[Ppsl2 * Cpli]] - Total[Ppsl1[[All, 1]] * Cpls[[All, 1]]];


Numer = Total[Total[Table[Total[Transpose[Transpose[Ppspil1[[All, i, All]] * Cpls] * Cpli[[i, All]]]], {i, 1, 10}]]] +
   Total[Total[Table[Total[Transpose[Transpose[Ppspil2[[All, i, All]] * Cpli] * Cpls[[i, All]]]], {i, 1, 10}]]] -
   Total[Total[Ppspil1[[All, All, 1]] * Cpls[[All, 1]] * Cpli[[All, 1]]]];

HE = Numer / Denom;
```

```
Clear["Global`*"]
```

```
n1 = 1.6645;
W0 = 50 × 10^-6; (*Signal waist at the centre of crystal*)
f1 = -0.025; (*Focal length of objective*)
f2 = 0.025; (*Focal Length of eyepiece*)
L = 0.001; (*Crystal Length = 1 mm*)
λ0 = 710. × 10^-9;
s1 = Abs[f1] - n1 L/2; (*Distance of beam expander from the rear face of the crystal*)

m = -f2/f1;

W1 = m W0 + (f2 + f1) Tan[λ0/(m Pi W0)];(*Signal waist size after beam expander*)
```

Schmidt distribution using the method described in [79]

```
LGlp[ρ_, ϕ_, W_, l_, p_] :=
  (-1)^p (W^2 Factorial[p]/(2 Pi Factorial[p + Abs[l]]))^0.5 (ρ W/√2)^Abs[l] Exp[-ρ^2 W^2/4] LaguerreL[p, Abs[l], ρ^2 W^2/2] Exp[i l (ϕ + Pi/2)];

A[ρi_, ρs_, ϕi_, ϕs_, W_, L_, λ_] := W/(2 Pi)^0.5 Exp[-W^2/4 (ρi^2 + ρs^2 + 2 ρi ρs Cos[ϕi - ϕs])] (λ L/Pi^3)^0.5
   Sinc[L λ (ρi^2 + ρs^2 - 2 ρi ρs Cos[ϕi - ϕs])/(8 Pi)] Exp[-i L λ (ρi^2 + ρs^2 - 2 ρi ρs Cos[ϕi - ϕs])/(8 Pi)];

Klp[pi_, ps_, l_] := Factorial[pi + ps + Abs[l]]/(Factorial[pi] Factorial[ps] Factorial[ps + Abs[l]] Factorial[pi + Abs[l]])^0.5;

B[t_, Wi_, Ws_, Wp_, L_, λp_] := -(λp t/(Pi Wi Ws) + L λp/(2 Pi Wi Ws) + i Wp^2/(Wi Ws));

SI[t_, W_, Wp_, L_, λp_] := Wp^2/(2 W^2) + 1/2 + i t λp/(2 Pi W^2) + i L λp/(4 Pi W^2);

T[t_, Wi_, Ws_, Wp_, L_, λp_] := 4 SI[t, Ws, Wp, L, λp] SI[t, Wi, Wp, L, λp] + B[t, Wi, Ws, Wp, L, λp]^2;

csi[L_, Ws_, Wi_, Wp_, λp_, ps_, pi_, l_, t_] :=
  ((B[t, Wi, Ws, Wp, L, λp]^Abs[l] (1 - 4 SI[t, Wi, Wp, L, λp]/T[t, Wi, Ws, Wp, L, λp])^ps (1 - 4 SI[t, Ws, Wp, L, λp]/T[t, Wi, Ws, Wp, L, λp])^pi)/
    (T[t, Wi, Ws, Wp, L, λp])^(Abs[l]+1)) Hypergeometric2F1[-pi, -ps, -pi - ps - Abs[l],
   (T[t, Wi, Ws, Wp, L, λp] (T[t, Wi, Ws, Wp, L, λp] - 4 SI[t, Wi, Wp, L, λp] - 4 SI[t, Ws, Wp, L, λp] + 4))/
    ((T[t, Wi, Ws, Wp, L, λp] - 4 SI[t, Ws, Wp, L, λp]) (T[t, Wi, Ws, Wp, L, λp] - 4 SI[t, Wi, Wp, L, λp])))];

Csi[L_?NumericQ, Ws_?NumericQ, Wi_?NumericQ, Wp_?NumericQ, λp_?NumericQ, ps_?NumericQ, pi_?NumericQ, l_?NumericQ] :=
  Klp[pi, ps, l] NIntegrate[csi[L, Ws, Wi, Wp, λp, ps, pi, l, t], {t, -L/2, L/2},
    AccuracyGoal → 5, Method → "GaussKronrodRule", WorkingPrecision → 10];
```

Finding coupling efficiencies of LG^{l}_{p} modes to a photodetector defined by circular aperture of diameter 'a'

```
a = 0.001; (*1 mm diameter of active area*)

LaguerreGauss[ρ_, Wa_, l_, p_, ϕ_] := 1/Wa (ρ √2/Wa)^Abs[l] Exp[-ρ^2/Wa^2] LaguerreL[p, Abs[l], 2 ρ^2/Wa^2] Exp[i l ϕ];

Cpl = ConstantArray[0, {10, 6}];
p = 0;
l = 0;
```

2 |

```
For[i = 1, i ≤ 10, i++; p++,
  For[j = 1 ; l = 0, j ≤ 6, j++; l++,
    C1 = Integrate[ρ Abs[LaguerreGauss[ρ, Wa, l1, p1, ϕ]]^2 /. {Wa → W1, l1 → l, p1 → p},
      {ϕ, 0, 2 Pi}, {ρ, 0, a / 2}, Assumptions → {{ρ, ϕ} > 0}];
    C2 = Integrate[ρ Abs[LaguerreGauss[ρ, Wa, l1, p1, ϕ]]^2 /. {Wa → W1, l1 → l, p1 → p},
      {ϕ, 0, 2 Pi}, {ρ, 0, ∞}, Assumptions → {{ρ, ϕ} > 0}];
    Cpl[[i, j]] = C1/C2;
    (*Finding coupling efficiency of each LG_p^l mode to the photodetector*)
   ];
 ];

Cpls = Cpl;

Cpli = Cpls;

Csum0 = Sum[Abs[Csi[L1, W, W, γ W, λp, ps, pi, l]]^2, {ps, 0, 15, 1}, {pi, 0, 15, 1}, {l, -10, 10}] /.
   {L1 → L, W → W0, λp → λ0 / 2, γ → 1};

Ppspil1 = Table[Abs[Csi[L1, W, W, γ W, λp, ps, pi, l]]^2 1/Csum0 /. {L1 → L, W → W0, λp → λ0 / 2, γ → 1},
  {ps, 0, 9, 1}, {pi, 0, 9, 1}, {l, 0, 5, 1}] ; (*Matrix of Schmidt distribution for signal l≥0*)

Ppspil2 = Table[Abs[Csi[L, W, W, γ W, λp, ps, pi, l]]^2 1/Csum0 /. {L1 → L, W → W0, λp → λ0 / 2, γ → 1},
  {ps, 0, 9, 1}, {pi, 0, 9, 1}, {l, 0, -5, -1}] ; (*Matrix of Schmidt distribution for signal l≤0*)

Ppsl1 = Total[Ppspil1, {2}];
Ppsl2 = Total[Ppspil2, {2}]; (*Singles probabilities*)

Denom = Total[Total[Ppsl1 * Cpls]] + Total[Total[Ppsl2 * Cpli]] - Total[Ppsl1[[All, 1]] * Cpls[[All, 1]]];

Numer = Total[Total[Table[Total[Transpose[Transpose[Ppspil1[[All, i, All]] * Cpls] * Cpli[[i, All]]]], {i, 1, 10}]]] +
   Total[Total[Table[Total[Transpose[Transpose[Ppspil2[[All, i, All]] * Cpli] * Cpls[[i, All]]]], {i, 1, 10}]]] -
   Total[Total[Ppspil1[[All, All, 1]] * Cpls[[All, 1]] * Cpli[[All, 1]]]];

HE = Numer / Denom;
```

Bibliography

[1] T. H. Maiman. Stimulated optical radiation in ruby. *Nature*, 187(4736):493–494, 08 1960.

[2] P. A. Franken, A. E. Hill, C. W. Peters, and G. Weinreich. Generation of optical harmonics. *Phys. Rev. Lett.*, 7:118–119, Aug 1961.

[3] R. H. Dicke. Coherence in spontaneous radiation processes. *Phys. Rev.*, 93:99–110, Jan 1954.

[4] R. Bonifacio and L. A. Lugiato. Cooperative radiation processes in two-level systems: Superfluorescence. *Phys. Rev. A*, 11:1507–1521, May 1975.

[5] M. Gross and S. Haroche. Superradiance: An essay on the theory of collective spontaneous emission. *Physics Reports*, 93(5):301 – 396, 1982.

[6] N. E. Rehler and J. H. Eberly. Superradiance. *Phys. Rev. A*, 3:1735–1751, May 1971.

[7] A. V. Andreev, V. I. Emel'yanov, and Y. A. Il'inski. Collective spontaneous emission (dicke superradiance). *Soviet Physics Uspekhi*, 23(8):493, 1980.

[8] N. Skribanowitz, I. P. Herman, J. C. MacGillivray, and M. S. Feld. Observation of dicke superradiance in optically pumped hf gas. *Phys. Rev. Lett.*, 30:309–312, Feb 1973.

[9] Q. H. F. Vrehen, H. M. J. Hikspoors, and H. M. Gibbs. Quantum beats in superfluorescence in atomic cesium. *Phys. Rev. Lett.*, 38:764–767, Apr 1977.

[10] H. M. Gibbs, Q. H. F. Vrehen, and H. M. J. Hikspoors. Single-pulse superfluorescence in cesium. *Phys. Rev. Lett.*, 39:547–550, Aug 1977.

[11] A. Crubellier, S. Liberman, D. Mayou, and P. Pillet. Experimental evidence for collision-induced superradiance. *Opt. Lett.*, 8(2):105–107, Feb 1983.

[12] A. Flusberg, T. Mossberg, and S. R. Hartmann. *Cooperative Effects in Matter and Radiation*. Springer US, Boston, MA, 1977.

[13] M. Gross, P. Goy, C. Fabre, S. Haroche, and J. M. Raimond. Maser oscillation and microwave superradiance in small systems of rydberg atoms. *Phys. Rev. Lett.*, 43:343–346, Jul 1979.

[14] S. Inouye, A. P. Chikkatur, D. M. Stamper-Kurn, J. Stenger, D. E. Pritchard, and W. Ketterle. Superradiant rayleigh scattering from a bose-einstein condensate. *Science*, 285(5427):571–574, 1999.

[15] R. G. DeVoe and R. G. Brewer. Observation of superradiant and subradiant spontaneous emission of two trapped ions. *Phys. Rev. Lett.*, 76:2049–2052, Mar 1996.

[16] J. A. Mlynek, A. A. Abdumalikov, C. Eichler, and A. Wallraff. Observation of dicke superradiance for two artificial atoms in a cavity with high decay rate. *Nat Commun*, 5, 11 2014.

[17] M. O. Scully. Collective lamb shift in single photon dicke superradiance. *Phys. Rev. Lett.*, 102:143601, Apr 2009.

[18] J. E. Sipe and J. Van Kranendonk. Macroscopic electromagnetic theory of resonant dielectrics. *Phys. Rev. A*, 9:1806–1822, May 1974.

[19] I. Sersic, M. Frimmer, E. Verhagen, and A. F. Koenderink. Electric and magnetic dipole coupling in near-infrared split-ring metamaterial arrays. *Phys. Rev. Lett.*, 103:213902, Nov 2009.

[20] Y.R. Shen. *Principles of nonlinear optics*. Wiley-Interscience, New York, NY, USA, Jan 1984.

[21] N. Gisin, G. Ribordy, W. Tittel, and H. Zbinden. Quantum cryptography. *Rev. Mod. Phys.*, 74:145–195, Mar 2002.

[22] F. Steinlechner, P. Trojek, M. Jofre, H. Weier, D. Perez, T. Jennewein, R. Ursin, J. Rarity, M. W. Mitchell, J. P. Torres, H. Weinfurter, and V. Pruneri. A high-brightness source of polarization-entangled photons optimized for applications in free space. *Optics Express*, 20(9):9640–9649, 2012.

[23] P. J. Mosley, J. S. Lundeen, B. J. Smith, P. Wasylczyk, A. B. U'Ren, C. Silberhorn, and I. A. Walmsley. Heralded generation of ultrafast single photons in pure quantum states. *Phys. Rev. Lett.*, 100:133601, Apr 2008.

[24] C. K. Hong and L. Mandel. Theory of parametric frequency down conversion of light. *Phys. Rev. A*, 31:2409–2418, Apr 1985.

[25] A. Dragan. Efficient fiber coupling of down-conversion photon pairs. *Phys. Rev. A*, 70:053814, Nov 2004.

[26] R. S. Bennink. Optimal collinear gaussian beams for spontaneous parametric down-conversion. *Phys. Rev. A*, 81:053805, May 2010.

[27] C. Cohen-Tannoudji, B. Diu, and F. Laloe. *Quantum Mechanics*, volume 2. Wiley, 1991.

[28] A. Ling, A. Lamas-Linares, and C. Kurtsiefer. Absolute emission rates of spontaneous parametric down-conversion into single transverse gaussian modes. *Phys. Rev. A*, 77:043834, Apr 2008.

[29] R. W. Boyd. *Nonlinear Optics, Third Edition*. Academic Press, 3rd edition, 2008.

[30] R. Hellwarth, J. Cherlow, and T. T. Yang. Origin and frequency dependence of nonlinear optical susceptibilities of glasses. *Phys. Rev. B*, 11:964–967, Jan 1975.

[31] J. K. Wright. Nonlinear optics. *Contemporary Physics*, 6:1–14, 1964.

[32] N. Bloembergen. *Nonlinear Optics*. World Scientific, 1996.

[33] R. W. Terhune, P. D. Maker, and C. M. Savage. Measurements of nonlinear light scattering. *Phys. Rev. Lett.*, 14:681–684, Apr 1965.

[34] N. Van Tran, J. Spalter, J. Hanus, J. Ernest, and D. Kehl. Generation of the difference frequency by non-collinear light beams in k.d.p. crystal. *Physics Letters*, 19(4):285 – 287, 1965.

[35] K. Dolgaleva, N. Lepeshkin, and R. W. Boyd. Frequency doubling. *Encyclopaedia of Nonlinear Science*, 2004.

[36] David C. Burnham and Donald L. Weinberg. Observation of simultaneity in parametric production of optical photon pairs. *Phys. Rev. Lett.*, 25:84–87, Jul 1970.

[37] S. E. Harris, M. K. Oshman, and R. L. Byer. Observation of tunable optical parametric fluorescence. *Phys. Rev. Lett.*, 18:732–734, May 1967.

[38] Morton H. Rubin, David N. Klyshko, Y. H. Shih, and A. V. Sergienko. Theory of two-photon entanglement in type-ii optical parametric down-conversion. *Phys. Rev. A*, 50:5122–5133, Dec 1994.

[39] Paul G. Kwiat, Klaus Mattle, Harald Weinfurter, Anton Zeilinger, Alexander V. Sergienko, and Yanhua Shih. New high-intensity source of polarization-entangled photon pairs. *Phys. Rev. Lett.*, 75:4337–4341, Dec 1995.

[40] J. E. Midwinter and J. Warner. The effects of phase matching method and of uniaxial crystal symmetry on the polar distribution of second-order nonlinear optical polarization. *British Journal of Applied Physics*, 16(8):1135, 1965.

[41] G. D. Boyd and D. A. Kleinman. Parametric interaction of focused gaussian light beams. *Journal of Applied Physics*, 39(8), 1968.

[42] D. A. Kleinman. Theory of second harmonic generation of light. *Phys. Rev.*, 128:1761–1775, Nov 1962.

[43] D. A. Kleinman, A. Ashkin, and G. D. Boyd. Second-harmonic generation of light by focused laser beams. *Phys. Rev.*, 145:338–379, May 1966.

[44] J. A. Armstrong, N. Bloembergen, J. Ducuing, and P. S. Pershan. Interactions between light waves in a nonlinear dielectric. *Phys. Rev.*, 127:1918–1939, Sep 1962.

[45] S. J. Bentley, R. W. Boyd, W. E. Butler, and A. C. Melissinos. Measurement of the thermal contribution to the nonlinear refractive index of air at 1064nm. *Optics Letters*, 25:1192–1194, August 2000.

[46] S. J. Bentley, R. W. Boyd, W. E. Butler, and A. C. Melissinos. Spatial patterns induced in a laser beam by thermal nonlinearities. *Opt. Lett.*, 26(14):1084–1086, Jul 2001.

[47] M. Sheik-Bahae, A. A. Said, T. H. Wei, D. J. Hagan, and E. W. Van Stryland. Sensitive measurement of optical nonlinearities using a single beam. *IEEE Journal of Quantum Electronics*, 26(4):760–769, Apr 1990.

[48] Nick N. Lepeshkin, Aaron Schweinsberg, Giovanni Piredda, Ryan S. Bennink, and Robert W. Boyd. Enhanced nonlinear optical response of one-dimensional metal-dielectric photonic crystals. *Phys. Rev. Lett.*, 93:123902, Sep 2004.

[49] M. Moran, Chiao-Yao She, and R. Carman. Interferometric measurements of the nonlinear refractive-index coefficient relative to cs2in laser-system-related materials. *IEEE Journal of Quantum Electronics*, 11(6):259–263, Jun 1975.

[50] S. Friberg and P. Smith. Nonlinear optical glasses for ultrafast optical switches. *IEEE Journal of Quantum Electronics*, 23(12):2089–2094, Dec 1987.

[51] R. Adair, L. L. Chase, and S. A. Payne. Nonlinear refractive-index measurements of glasses using three-wave frequency mixing. *J. Opt. Soc. Am. B*, 4(6):875–881, Jun 1987.

[52] A. Owyoung. Ellipse rotation studies in laser host materials. *IEEE Journal of Quantum Electronics*, 9(11):1064–1069, Nov 1973.

[53] W. E. Williams, M. J. Soileau, and E. W. Van Stryland. Optical switching and n2 measurements in {CS2}. *Optics Communications*, 50(4):256 – 260, 1984.

[54] P. L. Kelley. Self-focusing of optical beams. *Phys. Rev. Lett.*, 15:1005–1008, Dec 1965.

[55] R. Y. Chiao, E. Garmire, and C. H. Townes. Self-trapping of optical beams. *Phys. Rev. Lett.*, 13:479–482, Oct 1964.

[56] G. Fibich and A. L. Gaeta. Critical power for self-focusing in bulk media and in hollow waveguides. *Opt. Lett.*, 25(5):335–337, Mar 2000.

[57] A. J. Campillo, S. L. Shapiro, and B. R. Suydam. Relationship of self-focusing to spatial instability modes. *Applied Physics Letters*, 24(4):178–180, 1974.

[58] B. Suydam. Self-focusing of very powerful laser beams ii. *IEEE Journal of Quantum Electronics*, 10(11):837–843, Nov 1974.

[59] G. Fibich, S. Eisenmann, B. Ilan, Y. Erlich, M. Fraenkel, Z. Henis, A. L. Gaeta, and A. Zigler. Self-focusing distance of very high power laser pulses. *Opt. Express*, 13(15):5897–5903, Jul 2005.

[60] G. I. Stegeman and M. Segev. Optical spatial solitons and their interactions: Universality and diversity. *Science*, 286(5444):1518–1523, 1999.

[61] K. D. Moll, A. L. Gaeta, and G. Fibich. Self-similar optical wave collapse: Observation of the townes profile. *Phys. Rev. Lett.*, 90:203902, May 2003.

[62] G. Fibich and B. Ilan. Self-focusing of elliptic beams: an example of the failure of the aberration-less approximation. *J. Opt. Soc. Am. B*, 17(10):1749–1758, Oct 2000.

[63] B. Gross and J. T. Manassah. Numerical solution for the propagation of an elliptic gaussian beam in a kerr medium. *Physics Letters A*, 169(5):371 – 378, 1992.

[64] Taylor D. Grow, Amiel A. Ishaaya, Luat T. Vuong, Alexander L. Gaeta, Nir Gavish, and Gadi Fibich. Collapse dynamics of super-gaussian beams. *Opt. Express*, 14(12):5468–5475, Jun 2006.

[65] J. E. Bjorkholm and A. A. Ashkin. cw self-focusing and self-trapping of light in sodium vapor. *Phys. Rev. Lett.*, 32:129–132, Jan 1974.

[66] A. Barthelemy, S. Maneuf, and C. Froehly. Propagation soliton et auto-confinement de faisceaux laser par non linearit optique de kerr. *Optics Communications*, 55(3):201 – 206, 1985.

[67] J. S. Aitchison, K. Al-Hemyari, C. N. Ironside, R. S. Grant, and W. Sibbett. Observation of spatial solitons in algaas waveguides. *Electronics Letters*, 28(20):1879–1880, Sept 1992.

[68] J. Beeckman, K. Neyts, X. Hutsebaut, C. Cambournac, and M. Haelterman. Simulations and experiments on self-focusing conditions in nematic liquid-crystal planar cells. *Opt. Express*, 12(6):1011–1018, Mar 2004.

[69] V. E. Zakharov and A. B. Shabat. Exact Theory of Two-dimensional Self-focusing and One-dimensional Self-modulation of Waves in Nonlinear Media. *Soviet Journal of Experimental and Theoretical Physics*, 34:62, 1972.

[70] G. P. Agrawal. *Nonlinear Fiber Optics*. Academic Press, 2007.

[71] A. Hasegawa and F. Tappert. Transmission of stationary nonlinear optical pulses in dispersive dielectric fibers. i. anomalous dispersion. *Applied Physics Letters*, 23(3):142–144, 1973.

[72] L. F. Mollenauer, R. H. Stolen, and J. P. Gordon. Experimental observation of picosecond pulse narrowing and solitons in optical fibers. *Phys. Rev. Lett.*, 45:1095–1098, Sep 1980.

[73] L. Mollenauer, J. Gordon, and M. Islam. Soliton propagation in long fibers with periodically compensated loss. *IEEE Journal of Quantum Electronics*, 22(1):157–173, Jan 1986.

[74] V. I. Bespalov and V. I. Talanov. Filamentary Structure of Light Beams in Nonlinear Liquids. *Soviet Journal of Experimental and Theoretical Physics Letters*, 3:307, June 1966.

[75] R. S. Bennink, V. Wong, A. M. Marino, D. L. Aronstein, R. W. Boyd, C. R. Stroud, S. Lukishova, and D. J. Gauthier. Honeycomb pattern formation by laser-beam filamentation in atomic sodium vapor. *Phys. Rev. Lett.*, 88:113901, Feb 2002.

[76] D. Kip, M. Soljacic, M. Segev, E. Eugenieva, and D. N. Christodoulides. Modulation instability and pattern formation in spatially incoherent light beams. *Science*, 290(5491):495–498, 2000.

[77] L. Bergé, S. Skupin, F. Lederer, G. Méjean, J. Yu, J. Kasparian, E. Salmon, J. P. Wolf, M. Rodriguez, L. Wöste, R. Bourayou, and R. Sauerbrey. Multiple filamentation of terawatt laser pulses in air. *Phys. Rev. Lett.*, 92:225002, Jun 2004.

[78] A. Couairon and A. Mysyrowicz. *Self-focusing: Past and Present: Fundamentals and Prospects*. Springer New York, New York, NY, 2009.

[79] A. Dubietis, G. Tamosauskas, G. Fibich, and B. Ilan. Multiple filamentation induced by input-beam ellipticity. *Opt. Lett.*, 29(10):1126–1128, May 2004.

[80] G. Méchain, A. Couairon, M. Franco, B. Prade, and A. Mysyrowicz. Organizing multiple femtosecond filaments in air. *Phys. Rev. Lett.*, 93:035003, Jul 2004.

[81] F. Vidal and T. W. Johnston. Electromagnetic beam breakup: Multiple filaments, single beam equilibria, and radiation. *Phys. Rev. Lett.*, 77:1282–1285, Aug 1996.

[82] H. Schroeder, J. Liu, and S. L. Chin. From random to controlled small-scale filamentation in water. *Opt. Express*, 12(20):4768–4774, Oct 2004.

[83] L. T. Vuong, T. D. Grow, A. Ishaaya, A. L. Gaeta, G. W. 't Hooft, E. R. Eliel, and G. Fibich. Collapse of optical vortices. *Phys. Rev. Lett.*, 96:133901, Apr 2006.

[84] A. Schweinsberg, J. Kuper, and R. W. Boyd. Loss of spatial coherence and limiting of focal plane intensity by small-scale laser-beam filamentation. *Phys. Rev. A*, 84:053837, Nov 2011.

[85] K. Dolgaleva and R. W. Boyd. Local-field effects in nanostructured photonic materials. *Adv. Opt. Photon.*, 4(1):1–77, Mar 2012.

[86] N. Bloembergen, E. M. Purcell, and R. V. Pound. Relaxation effects in nuclear magnetic resonance absorption. *Phys. Rev.*, 73:679–712, Apr 1948.

[87] George L. Fischer, Robert W. Boyd, Russell J. Gehr, Samson A. Jenekhe, John A. Osaheni, J. E. Sipe, and Laura A. Weller-Brophy. Enhanced nonlinear optical response of composite materials. *Phys. Rev. Lett.*, 74:1871–1874, Mar 1995.

[88] R. W. Boyd and J. E. Sipe. Nonlinear optical susceptibilities of layered composite materials. *J. Opt. Soc. Am. B*, 11(2):297–303, Feb 1994.

[89] R. L. Nelson and R. W. Boyd. Enhanced electro-optic response of layered composite materials. *Applied Physics Letters*, 74(17):2417–2419, 1999.

[90] T. Tokizaki, A. Nakamura, S. Kaneko, K. Uchida, S. Omi, H. Tanji, and Y. Asahara. Subpicosecond time response of third?order optical nonlinearity of small copper particles in glass. *Applied Physics Letters*, 65(8):941–943, 1994.

[91] F. Hache, D. Ricard, C. Flytzanis, and U. Kreibig. The optical kerr effect in small metal particles and metal colloids: The case of gold. *Applied Physics A*, 47(4):347–357.

[92] V. M. Shalaev. *Nonlinear Optics of Random Media: Fractal Composites and Metal-Dielectric Films*. Springer Berlin Heidelberg, 1999.

[93] J. C. Maxwell Garnett. Colours in Metal Glasses and in Metallic Films. *Philosophical Transactions of the Royal Society of London Series A*, 203:385–420, 1904.

[94] D. A. G. Bruggeman. Berechnung verschiedener physikalischer konstanten von heterogenen substanzen. i. dielektrizitätskonstanten und leitfähigkeiten der mischkörper aus isotropen substanzen. *Annalen der Physik*, 416:636–664, 1935.

[95] R. J. Gehr, G. L. Fischer, and R. W. Boyd. Nonlinear-optical response of porous-glass-based composite materials. *J. Opt. Soc. Am. B*, 14(9):2310–2314, Sep 1997.

[96] M. J. Bloemer and M. Scalora. Transmissive properties of ag/mgf2 photonic band gaps. *Applied Physics Letters*, 72(14):1676–1678, 1998.

[97] R. S. Bennink, Y. K. Yoon, R. W. Boyd, and J. E. Sipe. Accessing the optical nonlinearity of metals with metal–dielectric photonic bandgap structures. *Opt. Lett.*, 24(20):1416–1418, Oct 1999.

[98] D. D. Smith, G. Fischer, R. W. Boyd, and D. A. Gregory. Cancellation of photoinduced absorption in metal nanoparticle composites through a counterintuitive consequence of local field effects. *J. Opt. Soc. Am. B*, 14(7):1625–1631, Jul 1997.

[99] M. Kauranen and A. V. Zayats. Nonlinear plasmonics. *Nat Photon*, 6(11):737–748, 11 2012.

[100] M. I. Stockman. Nanoplasmonics: past, present, and glimpse into future. *Opt. Express*, 19(22):22029–22106, Oct 2011.

[101] J. Homola. Surface plasmon resonance sensors for detection of chemical and biological species. *Chemical Reviews*, 108(2):462–493, 2008. PMID: 18229953.

[102] C. Anceau, S. Brasselet, J. Zyss, and P. Gadenne. Local second-harmonic generation enhancement on gold nanostructures probed by two-photon microscopy. *Opt. Lett.*, 28(9):713–715, May 2003.

[103] C. K. Chen, A. R. B. de Castro, and Y. R. Shen. Surface-enhanced second-harmonic generation. *Phys. Rev. Lett.*, 46:145–148, Jan 1981.

[104] I. I. Smolyaninov, A. V. Zayats, and C. C. Davis. Near-field second harmonic generation from a rough metal surface. *Phys. Rev. B*, 56:9290–9293, Oct 1997.

[105] A. Wokaun, J. G. Bergman, J. P. Heritage, A. M. Glass, P. F. Liao, and D. H. Olson. Surface second-harmonic generation from metal island films and microlithographic structures. *Phys. Rev. B*, 24:849–856, Jul 1981.

[106] E. M. Kim, S. S. Elovikov, T. V. Murzina, A. A. Nikulin, O. A. Aktsipetrov, M. A. Bader, and G. Marowsky. Surface-enhanced optical third-harmonic generation in ag island films. *Phys. Rev. Lett.*, 95:227402, Nov 2005.

[107] J. I. Dadap, J. Shan, K. B. Eisenthal, and T. F. Heinz. Second-harmonic rayleigh scattering from a sphere of centrosymmetric material. *Phys. Rev. Lett.*, 83:4045–4048, Nov 1999.

[108] A. Bouhelier, M. Beversluis, A. Hartschuh, and L. Novotny. Near-field second-harmonic generation induced by local field enhancement. *Phys. Rev. Lett.*, 90:013903, Jan 2003.

[109] A. Nahata, R. A. Linke, T. Ishi, and K. Ohashi. Enhanced nonlinear optical conversion from a periodically nanostructured metal film. *Opt. Lett.*, 28(6):423–425, Mar 2003.

[110] T. Hanke, J. Cesar, V. Knittel, A. Trgler, U. Hohenester, A. Leitenstorfer, and R. Bratschitsch. Tailoring spatiotemporal light confinement in single plasmonic nanoantennas. *Nano Letters*, 12(2):992–996, 2012. PMID: 22268812.

[111] S. Linden, F. B. P. Niesler, J. Förstner, Y. Grynko, T. Meier, and M. Wegener. Collective effects in second-harmonic generation from split-ring-resonator arrays. *Phys. Rev. Lett.*, 109:015502, Jul 2012.

[112] H. TUOVINEN, M. KAURANEN, K. JEFIMOVS, P. VAHIMAA, T. VALLIUS, J. TURUNEN, N. V. TKACHENKO, and H. LEMMETYINEN. Linear and second-order nonlinear optical properties of arrays of noncentrosymmetric gold nanoparticles. *Journal of Nonlinear Optical Physics and Materials*, 11(04):421–432, 2002.

[113] I. De Leon, Z. Shi, A. C. Liapis, and R. W. Boyd. Measurement of the complex nonlinear optical response of a surface plasmon-polariton. *Opt. Lett.*, 39(8):2274–2277, Apr 2014.

[114] L. Brillouin and H. S. W. Massey. *Wave Propagation and Group Velocity*. Elsevier Science, 2013.

[115] D. Gauthier and R. W. Boyd. *Progress in Optics*. Number v. 42. Elsevier, 2002.

[116] R. Y. Chiao and P. W. Milonni. Fast light, slow light. *Opt. Photon. News*, 13(6):26–30, Jun 2002.

[117] J. A. Carruthers and T. Bieber. Pulse velocity in a self?locked he?ne laser. *Journal of Applied Physics*, 40(1):426–428, 1969.

[118] Lene Vestergaard Hau, S. E. Harris, Zachary Dutton, and Cyrus H. Behroozi. Light speed reduction to 17 metres per second in an ultracold atomic gas. *Nature*, 397(6720):594–598, 02 1999.

[119] M. S. Bigelow, N. N. Lepeshkin, and R. W. Boyd. Superluminal and slow light propagation in a room-temperature solid. *Science*, 301(5630):200–202, 2003.

[120] M. S. Bigelow, N. N. Lepeshkin, and R. W. Boyd. Observation of ultraslow light propagation in a ruby crystal at room temperature. *Phys. Rev. Lett.*, 90:113903, Mar 2003.

[121] Y. Okawachi, M. S. Bigelow, J. E. Sharping, Z. Zhu, A. Schweinsberg, D. J. Gauthier, R. W. Boyd, and A. L. Gaeta. Tunable all-optical delays via brillouin slow light in an optical fiber. *Phys. Rev. Lett.*, 94:153902, Apr 2005.

[122] A. Schweinsberg, N. N. Lepeshkin, M. S. Bigelow, R. W. Boyd, and S. Jarabo. Observation of superluminal and slow light propagation in erbium-doped optical fiber. *EPL (Europhysics Letters)*, 73(2):218, 2006.

[123] K. Y. Song, M. G. Herráez, and L. Thévenaz. Observation of pulse delaying and advancement in optical fibers using stimulated brillouin scattering. *Opt. Express*, 13(1):82–88, Jan 2005.

[124] Y. Okawachi, M. A. Foster, J. E. Sharping, A. L. Gaeta, Q. Xu, and M. Lipson. All-optical slow-light on a photonic chip. *Opt. Express*, 14(6):2317–2322, Mar 2006.

[125] A. Yariv, Y. Xu, R. K. Lee, and A. K. Scherer. Coupled-resonator optical waveguide:?a proposal and analysis. *Opt. Lett.*, 24(11):711–713, Jun 1999.

[126] S. E. Harris, J. E. Field, and A. Imamoğlu. Nonlinear optical processes using electromagnetically induced transparency. *Phys. Rev. Lett.*, 64:1107–1110, Mar 1990.

[127] D. Budker, D. F. Kimball, S. M. Rochester, and V. V. Yashchuk. Nonlinear magneto-optics and reduced group velocity of light in atomic vapor with slow ground state relaxation. *Phys. Rev. Lett.*, 83:1767–1770, Aug 1999.

[128] C. Liu, Z. Dutton, C. H. Behroozi, and L. V. Hau. Observation of coherent optical information storage in an atomic medium using halted light pulses. *Nature*, 409(6819):490–493, 01 2001.

[129] A. M. Akulshin, S. Barreiro, and A. Lezama. Steep anomalous dispersion in coherently prepared rb vapor. *Phys. Rev. Lett.*, 83:4277–4280, Nov 1999.

[130] S. E. Schwarz and T. Y. Tan. Wave interactions in saturable absorbers. *Applied Physics Letters*, 10(1):4–7, 1967.

[131] L. W. Hillman, R. W. Boyd, J. Krasinski, and C.R. Stroud Jr. Observation of a spectral hole due to population oscillations in a homogeneously broadened optical absorption line. *Optics Communications*, 45(6):416 – 419, 1983.

[132] I. L. Fabelinskii. Molecular scattering of light . Plenum Press, New York, 1968, pp. xxvii+622. *Journal of Molecular Structure*, 1969.

[133] R. P. Feynman. *The Feynman Lectures on Physics: The New Millennium Edition*. Basic Books, 2013.

[134] R. W. Hellwarth. Theory of stimulated raman scattering. *Phys. Rev.*, 130:1850–1852, Jun 1963.

[135] L.I. Mandelstam. Light scattering by inhomogeneous media. *Zh. Russ. Fiz-Khim. Ova.*, 58(381), 1926.

[136] L. Brillouin. Diffusion de la lumiere et des rayonnes x par un corps transparent homogene influence del'agitation thermique. *Ann. Phys. (Paris)*, 17(88), 1922.

[137] E. Gross. Modification of light quanta by elastic heat oscillations in scattering media. *Nature*, 129:722–723, 1932.

[138] C. V. Raman. A new radiation. *Proceedings of the Indian Academy of Sciences - Section A*, 37(3):333–341.

[139] E. Garmire, F. Pandarese, and C. H. Townes. Coherently driven molecular vibrations and light modulation. *Phys. Rev. Lett.*, 11:160–163, Aug 1963.

[140] G. S. Kruglik and P. A. Apanasevich. *Izv. Akad. Nauk SSSE, Ser. Fiz.*, 483(27), 1963.

[141] C. Gerry and P. Knight. *Introductory Quantum Optics*. Cambridge University Press, 2005.

[142] B. H. Bransden and C. J. Joachain. *Quantum Mechanics*. Prentice Hall, 2000.

[143] E. Merzbacher. Quantum mechanics. 1998.

[144] R. H. Dicke. The coherence brightened laser. *Quantum Electronics III; Grivet P, Bloembergen N, editors. Proceedings of the third international congress, Paris*, page 35, 1964.

[145] L. Allen and G.I. Peters. Superradiance, coherence brightening and amplified spontaneous emission. *Physics Letters A*, 31(3):95 – 96, 1970.

[146] J. D. Jackson. *Classical Electrodynamics Third Edition*. Wiley, third edition, Aug 1998.

[147] L. Novotny and D. Hecht. *Principles of Nano-Optics*. Cambridge University Press, 2006. Cambridge Books Online.

[148] M. Gross, P. Goy, C. Fabre, S. Haroche, and J. M. Raimond. Maser oscillation and microwave superradiance in small systems of rydberg atoms. *Phys. Rev. Lett.*, 43:343–346, Jul 1979.

[149] F. Gounand, M. Hugon, P. R. Fournier, and J. Berlande. Superradiant cascading effects in rubidium rydberg levels. *Journal of Physics B: Atomic and Molecular Physics*, 12(4):547, 1979.

[150] M. Gross, C. Fabre, P. Pillet, and S. Haroche. Observation of near-infrared dicke superradiance on cascading transitions in atomic sodium. *Phys. Rev. Lett.*, 36:1035–1038, Apr 1976.

[151] C. Dahmen, B. Schmidt, and G. von Plessen. Radiation damping in metal nanoparticle pairs. *Nano Letters*, 7(2):318–322, 02 2007.

[152] M. Scheibner, T. Schmidt, L. Worschech, A. Forchel, G. Bacher, T. Passow, and D. Hommel. Superradiance of quantum dots. *Nat Phys*, 3(2):106–110, 02 2007.

[153] S. Filipp, M. Göppl, J. M. Fink, M. Baur, R. Bianchetti, L. Steffen, and A. Wallraff. Multimode mediated qubit-qubit coupling and dark-state symmetries in circuit quantum electrodynamics. *Phys. Rev. A*, 83:063827, Jun 2011.

[154] A. F. van Loo, A. Fedorov, K. Lalumière, B. C. Sanders, A. Blais, and A. Wallraff. Photon-mediated interactions between distant artificial atoms. *Science*, 342(6165):1494–1496, 2013.

[155] R. Röhlsberger, K. Schlage, B. Sahoo, S. Couet, and R. Rüffer. Collective lamb shift in single-photon superradiance. *Science*, 328(5983):1248–1251, 2010.

[156] U. Kreibig and M. Vollmer. *Optical Properties of Metal Clusters*, volume 25. Springer, Berlin, 1995.

[157] M. L. Brongersma. Plasmonics: Engineering optical nanoantennas. *Nat Photon*, 2(5):270–272, 05 2008.

[158] L. Novotny and N. van Hulst. Antennas for light. *Nat Photon*, 5(2):83–90, 02 2011.

[159] P.K. Jain, W. Huang, and M. El-Sayed. On the universal scaling behavior of the distance decay of plasmon coupling in metal nanoparticle pairs: A plasmon ruler equation. *Nano Letters*, 7(7):2080–2088, 2007.

[160] C. Dahmen, B. Schmidt, , and G. von Plessen. Radiation damping in metal nanoparticle pairs. *Nano Letters*, 7(2):318–322, 2007. PMID: 17243751.

[161] F. Hao, Y. Sonnefraud, P. Van Dorpe, S. A. Maier, N. J. Halas, and P. Nordlander. Symmetry breaking in plasmonic nanocavities: Subradiant lspr sensing and a tunable fano resonance. *Nano Letters*, 8(11):3983–3988, 2008. PMID: 18831572.

[162] Y. Sonnefraud, N. Verellen, H. Sobhani, G. A. E Vandenbosch, V. V. Moshchalkov, P. V. Dorpe, P. Nordlander, and S. A. Maier. Experimental realization of subradiant, superradiant, and fano resonances in ring/disk plasmonic nanocavities. *ACS Nano*, 4(3):1664–1670, 2010. PMID: 20155967.

[163] O. L. Muskens, V. Giannini, J. A. Sánchez-Gil, and J. Gómez Rivas. Optical scattering resonances of single and coupled dimer plasmonic nanoantennas. *Opt. Express*, 15(26):17736–17746, Dec 2007.

[164] Phillip Olk, Jan Renger, Marc Tobias Wenzel, and Lukas M. Eng. Distance dependent spectral tuning of two coupled metal nanoparticles. *Nano Letters*, 8(4):1174–1178, 2008.

[165] S. Linden, C. Enkrich, M. Wegener, J. Zhou, T. Koschny, and C. M. Soukoulis. Magnetic response of metamaterials at 100 terahertz. *Science*, 306(5700):1351–1353, 2004.

[166] C. Rockstuhl, T. Zentgraf, H. Guo, N. Liu, C. Etrich, I. Loa, K. Syassen, J. Kuhl, F. Lederer, and H. Giessen. Resonances of split-ring resonator metamaterials in the near infrared. *Applied Physics B*, 84(1-2):219–227, 2006.

[167] M. Decker, N. Feth, C. M. Soukoulis, S. Linden, and M. Wegener. Retarded long-range interaction in split-ring-resonator square arrays. *Phys. Rev. B*, 84:085416, Aug 2011.

[168] B. S. Simpkins, J. P. Long, O. J. Glembocki, J. Guo, J. D. Caldwell, and J. C. Owrutsky. Pitch-dependent resonances and near-field coupling in infrared nanoantenna arrays. *Opt. Express*, 20(25):27725–27739, Dec 2012.

[169] P. Lunnemann, I. Sersic, and A. F. Koenderink. Optical properties of two-dimensional magnetoelectric point scattering lattices. *Phys. Rev. B*, 88:245109, Dec 2013.

[170] R. Taubert, R. Ameling, T. Weiss, A. Christ, and H. Giessen. From near-field to far-field coupling in the third dimension: Retarded interaction of particle plasmons. *Nano Letters*, 11(10):4421–4424, 2011. PMID: 21879724.

[171] T. Iida. Control of plasmonic superradiance in metallic nanoparticle assembly by light-induced force and fluctuations. *The Journal of Physical Chemistry Letters*, 3(3):332–336, 2012. PMID: 26285847.

[172] S. Tokonami, S. Hidaka, K. Nishida, Y. Yamamoto, H. Nakao, and T. Iida. Multipole superradiance from densely assembled metallic nanoparticles. *The Journal of Physical Chemistry C*, 117(29):15247–15252, 2013.

[173] P. A. Belov and C. R. Simovski. Homogenization of electromagnetic crystals formed by uniaxial resonant scatterers. *Phys. Rev. E*, 72:026615, Aug 2005.

[174] Sergei Tretyakov. *Analytical modeling in applied electromagnetics*. Artech House, 2003.

[175] W. Feng, Y. Li, and S. Y. Zhu. Effect of atomic distribution on cooperative spontaneous emission. *Phys. Rev. A*, 89:013816, Jan 2014.

[176] P. B. Johnson and R. W. Christy. Optical constants of the noble metals. *Phys. Rev. B*, 6:4370–4379, Dec 1972.

[177] H.C. van de Hulst. *Light Scattering by Small Particles*. Dover Books on Physics. Dover Publications, 2012.

[178] R. E. Collin. *Field Theory of Guided Waves*. Wiley-IEEE Press, 1991.

[179] N. Gisin and R. Thew. Quantum communication. *Nat Photon*, 1(3):165–171, 03 2007.

[180] Tomasz Paterek, Alessandro Fedrizzi, Simon Gröblacher, Thomas Jennewein, Marek Żukowski, Markus Aspelmeyer, and Anton Zeilinger. Experimental test of nonlocal realistic theories without the rotational symmetry assumption. *Phys. Rev. Lett.*, 99:210406, Nov 2007.

[181] y. Shih. *An introduction to quantum optics : photon and biphoton physics*. Taylor and Francis, 2011.

[182] B. G. Christensen, K. T. McCusker, J. B. Altepeter, B. Calkins, T. Gerrits, A. E. Lita, A. Miller, L. K. Shalm, Y. Zhang, S. W. Nam, N. Brunner, C. C. W. Lim, N. Gisin, and P. G. Kwiat. Detection-loophole-free test of quantum nonlocality, and applications. *Phys. Rev. Lett.*, 111:130406, Sep 2013.

[183] F. A. Bovino, P. Varisco, A. Maria Colla, G. Castagnoli, G. Di Giuseppe, and A. V. Sergienko. Effective fiber-coupling of entangled photons for quantum communication. *Optics Communications*, 227(4–6):343–348, 11 2003.

[184] D. Ljunggren and M. Tengner. Optimal focusing for maximal collection of entangled narrow-band photon pairs into single-mode fibers. *Phys. Rev. A*, 72:062301, Dec 2005.

[185] H. E. Guilbert and D. J. Gauthier. Enhancing heralding efficiency and biphoton rate in type-i spontaneous parametric down-conversion. *IEEE Journal of Selected Topics in Quantum Electronics*, 21(3):215–224, 2015.

[186] Bahaa E. A. Saleh, Ayman F. Abouraddy, Alexander V. Sergienko, and Malvin C. Teich. Duality between partial coherence and partial entanglement. *Phys. Rev. A*, 62:043816, Sep 2000.

[187] F. M. Miatto, A. M. Yao, and S. M. Barnett. Full characterization of the quantum spiral bandwidth of entangled biphotons. *Phys. Rev. A*, 83:033816, Mar 2011.

[188] M. A. Nielsen and I. L. Chuang. *Quantum Computation and Quantum Information: 10th Anniversary Edition*. Cambridge University Press, New York, NY, USA, 10th edition, 2011.

[189] A. Ghatak and K. Thyagarajan. *An Introduction to Fiber Optics*. Cambridge University Press, 1998.

[190] J. Niu and J. Xu. Coupling efficiency of laser beam to multimode fiber. *Optics Communications*, 274(2):315 – 319, 2007.

[191] Ryan S. Bennink, Sean J. Bentley, and Robert W. Boyd. "two-photon" coincidence imaging with a classical source. *Phys. Rev. Lett.*, 89:113601, Aug 2002.

[192] Alejandro Ferrero, Joaquin Campos, Alicia Pons, and Antonio Corrons. New model for the internal quantum efficiency of photodiodes based on photocurrent analysis. *Appl. Opt.*, 44(2):208–216, Jan 2005.

[193] R. W. Boyd. *Radiometry and the detection of optical radiation*. New York : Wiley, 1983.

[194] C. A. Balanis. *Antenna Theory: Analysis and Design*. Wiley-Interscience, 2005.